Fall 2009

Redox behavior of magnetite in the environment: moving towards a semiconductor model

Christopher Aaron Gorski
University of Iowa

REDOX BEHAVIOR OF MAGNETITE IN THE ENVIRONMENT: MOVING TOWARDS A SEMICONDUCTOR MODEL

by

Christopher Aaron Gorski

An Abstract

Of a thesis submitted in partial fulfillment
of the requirements for the Doctor of
Philosophy degree in Civil and Environmental Engineering
in the Graduate College of
The University of Iowa

December 2009

Thesis Supervisor: Associate Professor Michelle M. Scherer

ABSTRACT

Magnetite (Fe_3O_4) is a commonly found in the environment and can form via several pathways, including biotic and abiotic reduction of Fe^{3+} oxides and the oxidation of Fe^{2+} and Fe^0. Despite extensive research, the redox behavior of magnetite is poorly understood. In previous work, the extent and kinetics of contaminant reduction by magnetite varied by several orders of magnitude between studies, two fundamentally different models are used to explain magnetite oxidation (i.e., core-shell diffusion and redox-driven), and reported reduction potentials vary by almost 1 V. In other fields of science (e.g., physics), magnetite stoichiometry ($x = Fe^{2+}/Fe^{3+}$) is a commonly measured property, however, in environmental studies, the stoichiometry is rarely measured.

The stoichiometry of magnetite can range from 0.5 (stoichiometric) to 0 (completely oxidized), with intermediate values ($0 < x < 0.5$) referred to as nonstoichiometric or partially oxidized magnetite. To determine the relationship between magnetite stoichiometry and contaminant fate, the reduction rates of three substituted nitrobenzenes ($ArNO_2$) were measured. The kinetic rates varied over five orders of magnitude as the particle stoichiometry increased from $x = 0.31$ to 0.50. Apparent ^{15}N kinetic isotope effects (^{15}N-AKIE) values for $ArNO_2$ were greater than unity for all magnetite stoichiometries investigated, and indicated that mass transfer processes are not controlling the reaction rate. To determine if the reaction kinetics were redox-driven, magnetite open circuit potentials (E_{OCP}) were measured. E_{OCP} values were linearly related to the stoichiometry, with more stoichiometric magnetite having a lower potential, in good agreement with redox-driven models.

The reaction of aqueous Fe^{2+} and magnetite was investigated. Similar to previous findings for other Fe^{3+} oxides, the formation of a stable sorbed Fe^{2+} species was not observed; instead, the sorbed Fe^{2+} underwent interfacial electron transfer to form a partially oxidized magnetite phase, which was accompanied by reduction of the

underlying magnetite. The lack of a stable sorbed Fe^{2+} species on magnetite indicated that the traditional surface complexation model was incorrect; instead, the uptake of Fe^{2+} by magnetite appeared to be limited by the whole particle (i.e., the sorbed and underlying phases combined) reaching a stoichiometry of 0.5.

Abstract Approved: _____
Thesis Supervisor

_____
Title and Department

_____
Date

REDOX BEHAVIOR OF MAGNETITE IN THE ENVIRONMENT: MOVING TOWARDS A SEMICONDUCTOR MODEL

by

Christopher Aaron Gorski

A thesis submitted in partial fulfillment of the
requirements for the Doctor of
Philosophy degree in Civil and Environmental Engineering
in the Graduate College of
The University of Iowa

December 2009

Thesis Supervisor: Associate Professor Michelle M. Scherer

Graduate College
The University of Iowa
Iowa City, Iowa

CERTIFICATE OF APPROVAL

_____

PH.D. THESIS

_____

This is to certify that the Ph.D. thesis of

Christopher Aaron Gorski

has been approved by the Examining Committee
for the thesis requirement for the Doctor of Philosophy
degree in Civil and Environmental Engineering at the December 2009
graduation.

Thesis Committee: _____
Michelle M. Scherer, Thesis Supervisor

_____
Edward G. Gillan

_____
Richard L. Valentine

_____
Timothy E. Mattes

_____
Kevin M. Rosso

To my parents for providing framework
And to Shirley for supplying context

For what use will it be on the Day of Judgment, when all of human achievements are weighed, to offer up three articles on formic acid, or even thirty? On the other hand, what do we know of the Day of Judgment if we do not even know what may have become of formic acid by then?

Robert Musil, The Man Without Qualities

ACKNOWLEDGMENTS

There was an excellent short act on the radio show *This American Life* about the Vienna sausage company (episode 241; “20 Acts in 60 Minutes”). In the story, we hear about how the Vienna sausage company moved from their old, “Rube Goldberg” manufacturing plant in the south side of Chicago to a new, efficient plant in northern Chicago. In the new plant, where each machine was brand new stainless steel and the processes were made more efficient, the hot dogs were simply not as good as those made in the old plant; the new hot dogs did not have the same “snap” and the color was not red enough. The employees struggled with the problem for about a year and half before they figured out the cause.

A man named Ervine used to transport the uncooked sausages to the smoke house in the old plant, a process that took about a half hour. In the new plant, the smoke house was placed near the assembly line to avoid the apparent inefficiencies. It turned out that this 30 minute commute, where the sausages warmed prior to being smoked, was the reason the sausages developed their trademark characteristics. Ervine’s job was critical to making the Vienna sausages.

Of course, this is no surprise to anyone who has experience doing experimental research, where seemingly arbitrary changes drastically affect the outcome of experiments. The scope of the anecdote is much broader though, and it is an excellent parallel to life: The truth is that we often have no idea of what makes us succeed or fail in our pursuits.

As a result, I cannot properly acknowledge all those who helped me through this degree, but I will try. Michelle Scherer became my advisor through a series of seemingly random steps, and I am incredibly grateful that life worked out as it did. Michelle has been a perfect advisor in every sense of the word, which is a claim that very few students can honestly make. David Cwiertny and Philip Larese-Casanova were also excellent

teachers and friends when I began my graduate education. My progress is largely due to having these excellent influences to steer me in the right direction.

My family has also been an incredible source of encouragement and support throughout this process. I am very thankful for the conversations, debates, arguments, microscope, telescope, pets, hikes, camping trips, and experiences I was generously provided that led me to become the curious person I am today. I would also like to thank Shirley Stern, who has had such a profound effect on my life. She constantly keeps my life in perspective, and has patiently kept me from pursuing a Faustian future. I am an incredibly lucky person to have such a supportive partner.

Lastly, I would like to thank all the Ervines who have surely affected and directed me throughout my life. Thank you.

ABSTRACT

Magnetite (Fe_3O_4) is a commonly found in the environment and can form via several pathways, including biotic and abiotic reduction of Fe^{3+} oxides and the oxidation of Fe^{2+} and Fe^0. Despite extensive research, the redox behavior of magnetite is poorly understood. In previous work, the extent and kinetics of contaminant reduction by magnetite varied by several orders of magnitude between studies, two fundamentally different models are used to explain magnetite oxidation (i.e., core-shell diffusion and redox-driven), and reported reduction potentials vary by almost 1 V. In other fields of science (e.g., physics), magnetite stoichiometry ($x = Fe^{2+}/Fe^{3+}$) is a commonly measured property, however, in environmental studies, the stoichiometry is rarely measured.

The stoichiometry of magnetite can range from 0.5 (stoichiometric) to 0 (completely oxidized), with intermediate values ($0 < x < 0.5$) referred to as nonstoichiometric or partially oxidized magnetite. To determine the relationship between magnetite stoichiometry and contaminant fate, the reduction rates of three substituted nitrobenzenes ($ArNO_2$) were measured. The kinetic rates varied over five orders of magnitude as the particle stoichiometry increased from $x = 0.31$ to 0.50. Apparent ^{15}N kinetic isotope effects (^{15}N-AKIE) values for $ArNO_2$ were greater than unity for all magnetite stoichiometries investigated, and indicated that mass transfer processes are not controlling the reaction rate. To determine if the reaction kinetics were redox-driven, magnetite open circuit potentials (E_{OCP}) were measured. E_{OCP} values were linearly related to the stoichiometry, with more stoichiometric magnetite having a lower potential, in good agreement with redox-driven models.

The reaction of aqueous Fe^{2+} and magnetite was investigated. Similar to previous findings for other Fe^{3+} oxides, the formation of a stable sorbed Fe^{2+} species was not observed; instead, the sorbed Fe^{2+} underwent interfacial electron transfer to form a partially oxidized magnetite phase, which was accompanied by reduction of the

underlying magnetite. The lack of a stable sorbed Fe^{2+} species on magnetite indicated that the traditional surface complexation model was incorrect; instead, the uptake of Fe^{2+} by magnetite appeared to be limited by the whole particle (i.e., the sorbed and underlying phases combined) reaching a stoichiometry of 0.5.

TABLE OF CONTENTS

LIST OF TABLES

LIST OF FIGURES

CHAPTER I. INTRODUCTION

Iron Chemistry

Iron (Fe) is ubiquitous in the environment, and is the most abundant redox-active element found in the Earth's crust (1). It occurs naturally as iron metal (Fe^0), ferrous iron (Fe^{2+}), and ferric iron (Fe^{3+}). Iron can be found in many forms in the environment, which can be broadly classified into aqueous, sorbed, and structural phases. Iron also has several industrial applications, including solar cells (2), pigments (3), catalysis (4), medicinal drug transport (5, 6), and drinking water treatment (7). As a result, the physicochemical properties of many iron minerals have been investigated and applied to several areas of research (1, 8, and refs. therein).

The formation, persistence, and reactivity of Fe^{2+} is of particular interest to the biogeochemical and environmental communities due to its reactivity with several groundwater constituents, including many natural and anthropogenic contaminants. When oxygen is limited or absent in groundwater, Fe^{2+} can be produced from Fe^{3+}-bearing minerals either directly by dissimilatory iron reducing bacteria (DIRB) (9), or by indirect mechanisms, such as reduction by sulfide (10). Structural and sorbed Fe^{2+} has been shown to reduce several environmental contaminants which are not reactive with aqueous Fe^{2+}, including halogenated aliphatics (11, 12), nitroaromatics (13-15), pesticides (16), heavy metals (17), and radionuclides (18, 19).

Fe^{2+} Uptake by Fe Oxides

Many studies has examined how Fe^{2+} interacts with Fe^{3+} oxides under anaerobic conditions for two primary reasons: (*i*) contaminant reduction can be very rapid when aqueous Fe^{2+} is exposed to Fe^{3+} oxide surfaces, and (*ii*) a limited understand exists regarding the fundamental processes involved when Fe^{2+} is removed from solution by ferric oxides. Previously, researchers thought that Fe^{2+} adsorbed to the surface of oxides formed stable surface complexes (i.e., ≡O-Fe^{2+} and ≡O-Fe^{2+}-OH), with the relative site

abundance dependent upon pH, solution conditions, and the oxide surface (20-22). Modeling the speciation and density of the surface sites was done using surface complexation modeling (SCM). Such models fit experimental data very accurately, and were often used to explain model contaminant fate (20-23).

Recent work, however, has found that a stable sorbed Fe^{2+} complex does not exist on the surface of iron oxides. Using the isotopic selectivity of ^{57}Fe Mössbauer spectroscopy, researchers have synthesized Fe^{3+} oxides from ^{56}Fe, which is invisible to Mössbauer spectroscopy, and exposed the oxides to a solution containing $^{57}Fe^{2+}$ to measure only the spectra of the sorbed phase. This approach showed unambiguously that all the $^{57}Fe^{2+}$ was oxidized to $^{57}Fe^{3+}$, with the $^{57}Fe^{3+}$ phase being the same as the underlying oxide (i.e., goethite grew on goethite, hematite grew on hematite) (22, 24-26). In these experiments, a stoichiometric number of Fe^{2+} atoms could be recovered upon acidic dissolution of the oxide, indicating that a trace oxidant was not responsible for the observations (24). Additionally, when the experiment was switched (i.e., $^{56}Fe^{2+}$ sorbed on $^{57}Fe^{3+}$ oxide), the underling oxide showed signs that the electrons are present within the underlying oxide phase (24, 27).

Interfacial electron transfer (i.e., an electron transferred from the sorbed phase to the underling oxide) has also been observed using other techniques. When isotopic tracers were used to track the isotopic composition of the solid Fe phase and the aqueous Fe^{2+} phase, two studies observed significant atomic exchange (28, 29), indicating that dissolution of structural iron far from the particle surface occurred over the course of the experiment. In another study, Fe^{2+} utpake on a single crystal of hematite was explored (30); the researchers found that Fe^{2+} was taken up at the (001) crystal face, while dissolution occurred at (hk0) faces. This resulted in a reshaping of the oxide, with the appearance of pyramidal growth at the (100) face, and pitting observed at the (hk0) faces. Currently, it is thought that once the electron is transferred from the aqueous Fe^{2+}, it is capable of conducting through the solid to another area of the crystal (29, 30).

Studies examining contaminant fate have also brought SCMs into question. When nitrobenzene ($ArNO_2$) is exposed to a solution containing goethite and aqueous Fe^{2+}, rapid reduction of the $ArNO_2$ to aniline ($ArNH_2$) occurs (14, 31, 32); note that similar observations have been made for several other oxides and contaminants (e.g., 12). Under the previous paradigm, this was interpreted as $ArNO_2$ reduction by sorbed Fe^{2+} at the goethite system. To test this hypothesis, researchers removed the aqueous Fe^{2+} from solution by replacing the buffer, leaving only the goethite with sorbed Fe^{2+}, and exposed the new solution to $ArNO_2$ (24). Negligible reduction of $ArNO_2$ was observed, which indicated that aqueous Fe^{2+} was necessary to promote rapid contaminant reduction, and that the reaction mechanism was likely more complex than previously thought. In another study examining O_2 reduction by aqueous Fe^{2+} and ferrihydrite, a similar conclusion was drawn, and it was argued that O_2 reduction kinetics could only be accurately described using both the sorbed and aqueous Fe^{2+} concentrations (33).

In light of these observation, two different approaches have been taken; one has attempted to incorporate electron-transfer reactions into traditional SCMs (21-23), while the other has started afresh with a semiconductor model (33-35). For the latter model, an iron oxide particle acts as a semiconductor, and electrons transferred to the particle from sorbed Fe^{2+} atoms (or DIRB) effectively dope the semiconductor with additional electrons; this results in electron rich sites (i.e., anode sites) and electron poor sites (i.e., cathode sites). These sites may be relatively near each other at the oxide surface (35), or may be present at different crystallographic faces (30).

Electronic Properties of Iron Oxides

It is worth briefly providing a background on the semiconducting properties of iron oxides. Solids can be broadly classified into three types based on their ability to conduct electricity. At one end of the spectrum, metals can conduct electricity very well, with little to no energy required for an electron to migrate from one atom to another.

Insulators, in contrast, are very poor conductors, with the amount of energy required to ionize an electron from one atom to another too great to observe conductivity under normal potentials. The last type of solid is the semiconductor, which exhibits electron conductivity in ranges between that of a metal and an insulator.

Band theory can be described as an expansion of molecular orbital theory to explain the behavior of solid structures. Band theory is used to illustrate the locations of electrons in orbitals of solid structures, and the ability for valence electrons to migrate between neighboring atoms (Figure 1.2). The valence band contains electrons in the highest energy orbitals of the solid, and is filled to the highest occupied molecular orbital (HOMO). The conduction band, however, is unoccupied by electrons, and is the lowest energy orbital that is unfilled, which is also known as the lowest unoccupied molecular orbital (LUMO). The Fermi level is the energy level equally between the valence and conduction bands.

In order for conduction to occur, an electron must become excited from the HOMO to the LUMO, which can be accomplished via several mechanisms, such as thermal energy or the absorption of light. For a metal, the valence band and conduction band overlap; as a result, no external energy is needed for an electron to become excited from the HOMO to the LUMO, making the material very conductive. In a semiconductor, however, the energy between the valence band and the conduction band, known as the band gap, is larger, and traditionally includes solids with band gaps ranging from 0.5 to 3 eV. As a result, it is much more difficult to excite an electron from the HOMO to the LUMO, which results in conductivities several orders of magnitude lower than in metals. Insulators are the final case, characterized as solids with band gaps greater than 3 eV.

Semiconductors can be doped with other elements to change their electrical properties. A semiconductor that is doped with another element to change electronic properties is referred to as an extrinsic semiconductor, whereas the unmodified analog is known as an intrinsic semiconductor. There are two primary methods for doping a crystal

structure: negative doping, or *n* doping, which occurs when elements with similar atomic size and an additional electron are added into the crystal lattice (e.g., doping N or P into a Si lattice); and positive doping, or *p* doping, where similarly sized elements with one less electron are added into the crystal lattice (e.g., doping Al or B in a Si lattice). Both *n* and *p* doping can decrease the band gap in the structure by either lowering the conduction band energy level (*n* doping), or by increasing the valence band energy nearer to the conduction band (*p* doping).

Most of the Fe oxides, such as goethite, hematite, lepidocrocite, and maghemite are semiconductors, whereas magnetite exhibits properties closer to that of a metal (Table 1.1). A 2 eV band gap corresponds to the absorption of light with a wavelength shorter than ~620 nm, resulting in reflected red and orange light, with adsorption of yellow to violet light in the visible spectrum, providing the Fe oxides with their characteristic colors. Studies to characterize the electrochemical behavior of Fe oxides are more complicated than just the band gap, however, as surface effects and particle treatment tend to strongly influence the behavior of the oxide (36, 37).

Iron oxides can be doped with Fe^{2+} using three methods: (*i*) sorption of Fe^{2+} followed by electron transfer, (*ii*) electrochemical reduction of the Fe^{3+} oxide, and (*iii*) the introduction of dopant elements with higher valence charges (e.g., Ti^{4+}) (38). Several previous studies have doped Fe oxides with elements commonly found in the environment, such as Al^{3+} and Mn^{2+}, focusing primarily on the observed structural changes (1 and refs. therein). Blako and Clarkson (38) showed that when hematite was doped with Sn^{4+} or Ti^{4+}, Fe^{2+} was present structurally to neutralize the charge balance within the crystal lattice. The doped hematite was capable of oxygen reduction, indicating that the reduction potential had increased with the addition of the dopant. The measured open circuit potential of the doped hematite ranged from -0.12 to -0.17 V at pH 9, which is theoretically low enough to reduce several environmental contaminants.

Magnetite

The implications of the semiconductor model have remained largely unexplored for magnetite (Fe_3O_4), a common iron oxide. Magnetite is important to several areas of research due to its unique physical, chemical, and magnetic properties; it is used in several medicinal and industrial processes as a ferrofluid (5, 6), it is of interest to physicists due to its conducting properties and the Verwey transition (39-42), it is used as a sorbent for drinking water decontamination (7), and is a common corrosion product of steel (37). Additional applications and interests of magnetite are shown in Figure 1.1. Magnetite is also of great importance in environmental studies, as it is a common product of Fe^{3+} oxide reduction by biological and abiotic mechanisms, and can form by Fe^{2+} oxidation (43-45). Magnetite has also been shown to reduce several contaminants in laboratory studies, such as carbon tetrachloride (CCl_4) (46, 47), hexavalent chromium (Cr^{6+}) (48), hexavalent uranium (U^{6+}) (49), and several other compounds (e.g., 17). In a field study, magnetite has been suggested as the dominant reductant of *cis*-dichloroethene (cis-DCE) in a chlorinated ethene plume at the Twin Cities Army Ammunition Plant (TCAAP) in Minnesota (50).

Despite extensive research, the redox behavior of magnetite remains poorly understood, especially in environmental studies: (*i*) the extent and kinetics of contaminant reduction by magnetite varied by several orders of magnitude between studies (e.g., CCl_4 (46, 47)), (*ii*) Fe^{2+} sorption ranges from significant to negligible under similar experimental conditions (12, 14, 31, 51, 52), (*iii*) two fundamentally different models are used to explain magnetite oxidation (i.e., core-shell diffusion and redox-driven) (53-60), (*iv*) and reported redox potentials vary by almost 1 V (54, 60, 61). Additionally, it has been concluded that sorbed Fe^{2+} on magnetite is reactive with nitroaromatics, while magnetite alone is not (14, 51), which is a puzzling conclusion considering the recent paradigm shift for other iron oxides mentioned above. In other fields of science (e.g., physics), some of these anomalies have been explained by changes in the magnetite

stoichiometry ($x = Fe^{2+}/Fe^{3+}$); slight changes in stoichiometry have shown to change magnetite conductivity by several orders of magnitude (62, 63), and influence the redox reactivity (54, 60). Little attention has been paid to stoichiometry in the environmental community, however, making it difficult to access the role of stoichiometry on environmentally relevant reactions.

The stoichiometry of magnetite can range from 0.5 (stoichiometric) to 0 (completely oxidized; maghemite, γ-Fe_2O_3), with intermediate values ($0 < x < 0.5$) referred to as nonstoichiometric or partially oxidized magnetite. Some notable differences exist between stoichiometric magnetite and maghemite: magnetite is essentially a conductor (band gap ≈ 0.1 eV), while maghemite is a semiconductor (band gap ≈ 2.0 eV) (1); this results in magnetite appearing black, while maghemite has a dark red color. Both magnetite and maghemite have cubic crystalline symmetry, and both contain iron in octahedral (Oct; 6-coordinate) and tetrahedral (Tet; 4-coordinate) sites. The magnetite formula (Fe_3O_4) can be written more precisely as $^{Tet}Fe^{3+}[^{Oct}Fe^{2+}Fe^{3+}]O_4$.Within the unit cell, there are eight $^{Tet}Fe^{3+}$, eight $^{Oct}Fe^{2+}$, eight $^{Oct}Fe^{3+}$, and 32 oxygen atoms. The maghemite (γ-Fe_2O_3) formula can be expressed as $^{Tet}Fe^{3+}[^{Oct}Fe^{3+}_{1.66}\ \square_{0.33}]O_4$, where $\square$ are vacancies formed in the crystal structure to account for charge balance. A schematic of the magnetite unit cell can be found in Figure 2.1 (Chapter 2). Magnetite has a slightly larger unit cell (~8.4 Å) than maghemite (~8.34 Å) due to vacancies which exist within the maghemite crystal lattice (1).

Nonstoichiometric magnetite ($0 < x < 0.5$) often contains a combination of the properties listed above. For example, the unit cell length of magnetite is linearly related to stoichiometry (x) (Chapter 2). Other properties, such as the redox potential, have only been explored in a qualitative manner (64). It is also unclear as to what nonstoichiometric magnetite even is: some studies have proposed that a maghemite shell forms around a magnetite core, with the change in properties due to the ability for Fe^{2+} to diffuse through

the maghemite shell (54, 56), while other work has concluded that a homogenous or heterogeneous solid solution of magnetite and maghemite exists (53, 55).

Objectives and Hypotheses

Objectives

The primary objective of this work was to gain insight into the redox reactions of magnetite at a series of stoichiometries in light of the recent paradigm shift of Fe^{2+}-iron oxide reactions. Experiments were conducted on several batches of magnetite with stoichiometries spanning the range of 0 to 0.5, while the range of specific surface areas between batches was held as narrow as possible. The redox potential, contaminant reduction rates, and reaction with aqueous Fe^{2+} were investigated to quantitatively determine the role of stoichiometry in these reactions, and to determine how magnetite should be best modeled in environmental reactions. The applicability of the conclusions drawn for magnetite was also explored for hematite exposed to aqueous Fe^{2+}.

Hypotheses

1. The uptake of Fe^{2+} on Fe oxides is best described using a semiconductor model.
    a. Interfacial electron transfer occurs when Fe^{2+} is taken up by magnetite, with the sorbed phase being oxidized, and the underlying oxide phase being reduced.
    b. The extent of Fe^{2+} uptake by magnetite is controlled by the bulk stoichiometry, not the specific surface area.
    c. The extent of Fe^{2+} uptake on other iron oxides is also controlled by bulk properties.
2. Contaminant reduction by the aqueous Fe^{2+}-Fe^{3+}-oxide system is due to the particle becoming a doped semiconductor.

   a. The extent and kinetics of contaminant reduction are directly related to the magnetite stoichiometry.
   b. Addition of aqueous Fe^{2+} to a suspension of nonstoichiometric magnetite favors contaminant reduction because the aqueous Fe^{2+} reduces the magnetite to a higher stoichiometry, and not because of sorbed Fe^{2+}.

3. Fe^{2+} sorbed on non-redox active surfaces, such as Al and Ti oxides, can be identified using Mössbauer spectroscopy, and can provide insight into the adsorption reaction.
   a. Sorbed Fe^{2+} can be distinguished from other forms of Fe^{2+} found in the environment by the presence of CS-QS coupling, or spectral asymmetry where the two peaks have equal areas.
   b. Sorption of Fe^{2+} on complex surfaces (e.g., cells) can be interpreted on a molecular level by collecting Mössbauer hyperfine parameters of simplified analogs.
   c. Observed relative trends between observed CS values and expected ^{57}Fe electron densities exhibit good agreement.
   d. The CS and QS appear to follow a general positive linear correlation for sorbed Fe^{2+} samples.

Thesis Overview

The thesis is outlined with respect to the above hypotheses. Chapters II-IV addresses hypotheses 1-2 with respect to magnetite. Chapter V is coupled to chapters II-IV, and uses the models produced for magnetite to explain the reactivity of dissolved Fe^{2+} with hematite (α-Fe_2O_3) and explore hypotheses 1-2. Chapter VI is an investigation of Fe^{2+} sorbed to redox inactive surfaces as a function of bulk solution conditions (e.g., pH, amount of Fe^{2+}) (hypothesis 3).

Chapter II contains a review of the three most common techniques used to determine magnetite stoichiometry: acidic dissolution, Mössbauer spectroscopy, and powder X-ray diffraction (pXRD). In this chapter, we found good agreement between all three techniques, providing compelling evidence that magnetite stoichiometry could be accurately and reproducibly determined. Additionally, we provide outlines for how these measurements should be carried out for other researchers investigating the properties of magnetite.

Chapter III investigates the interaction of dissolved Fe^{2+} with magnetite using bulk measurements, and Mössbauer spectroscopy coupled with isotopically enriched phases. Here, we found that the uptake of dissolved Fe^{2+} was controlled and limited by the particle initial stoichiometry, where uptake was limited by the formation of stoichiometric magnetite. Mössbauer spectroscopy confirmed that Fe^{2+} taken up by magnetite became structurally incorporated, with interfacial electron transfer reactions occurring. This observation explained why there were inconsistencies in the literature regarding the extent of Fe^{2+} uptake and the effect of 'sorbed Fe^{2+}' on contaminant reduction in the presence of magnetite.

Chapter IV examines the effect of stoichiometry on the reduction rate of nitroaromatics by magnetite. It was found that as the magnetite stoichiometry ranged from stoichiometric ($x = Fe^{2+}/Fe^{3+} = 0.50$) to significantly oxidized ($x = 0.31$), the observed reaction rate shifted over five orders of magnitude. Using compound-specific stable isotope measurements for nitrobenzene and direct redox measurements of the magnetite, we found that the shift in reaction kinetics was likely due to a shift in the Fe^{2+}/Fe^{3+} redox couple for the magnetite. Using this information, we produced a quantitative structure activity relationship (QSAR) which could be used to accurately predict the rates of nitrobenzene reduction using the measured corrosion potential of magnetite.

Chapter V uses the principle ideas outlined in chapters II-IV to determine if the reaction of Fe^{2+} and hematite could be better explained using the models developed for magnetite as opposed to more traditional surface complexation models. These experiments were conducted using viologen radicals, which are a one-electron transfer, pH independent redox probe. Using these measurements, the measured potential of the Fe^{2+}-hematite system appeared to exhibit Nernstian behavior, and may be better modeled as a charged semiconductor.

Chapter VI develops the relationship between bulk observations of sorption with measurable hyperfine (i.e., nucleus-electron interactions) parameters using Mössbauer spectroscopy. Here, uptake of Fe^{2+} was conducted on several environmentally relevant surfaces, including Al and Ti oxides, cells, clay minerals, and functionalized polystyrene beads. The hyperfine parameters were related to more traditionally reported values, such as the amount of Fe^{2+} taken up from solution and the pH. This work demonstrates that additional spectroscopic techniques can extend our understanding of basic processes occurring at the solid-solution interface.

Appendix A contains supplemental information referenced in chapters III and IV. Appendix B contains a manuscript published in *Environmental Science and Technology* which I provided Mössbauer characterization of hematite samples exposed to Fe^{2+}.

Background of Mössbauer Spectroscopy

A brief background on Mössbauer spectroscopy is provided here to help interpret discussion in the subsequent chapters. ^{57}Fe Mössbauer spectroscopy is a technique that is commonly used for iron characterization. Mössbauer spectroscopy can be used to detect oxidation state, magnetic behavior, electron density, and distortions in the local bonding environment of a nucleus (65). In the past few decades, it has become a standard instrument in geosciences, as iron's abundance and multiple oxidation states offer new insights into a wide spectrum of geochemical processes. Many iron phases can be easily

fingerprinted, making quantification of multiple phases in a sample possible, even if the phases have amorphous structures. Mössbauer spectroscopy is specifically useful to this study in that anaerobic samples can be analyzed, ^{57}Fe isotopic labeling can be used advantageously, and temperature dependent magnetic behavior can be used to better understand local Fe environments on an atomic scale.

Mössbauer spectroscopy relies upon the common phenomenon of resonance absorption of radiation, which is the fundamental principle of many spectroscopic techniques. Here, excited source nuclei lose their energy via the release of γ-radiation, and a sample isotope absorbs the γ-ray of a specific energy characteristic of the isotope. In the case of ^{57}Fe, a radioactive ^{57}Co decays to form an excited ^{57}Fe* isotope, where the nuclear spin quantum of ^{57}Fe*, I, is equal to 3/2. The excited ^{57}Fe* nucleus then decays to its ground state via the emission of a γ-ray of 14.4 keV, where I = ½ is the ground state of ^{57}Fe. This process occurs in the radiation source of the instrument, which is aligned with the sample and detector. When the characteristic 14.4 keV γ-ray interacts with a ^{57}Fe atom in the sample, it can be absorbed by the sample in two unique ways. The nuclei may recoil in order to conserve momentum, with the emitted γ-ray energy being the initial energy minus the kinetic energy lost to momentum. The second option is that the nucleus does not recoil when it absorbs the γ-ray, which is known as recoilless absorption, and is the measurable phenomenon of the experiment.

The recoilless fraction, *f*, is the fraction of the ^{57}Fe in the sample that undergoes recoilless absorption. It is dependent on both temperature and the crystal lattice of the Fe atom, with strongly-bound atoms and lower temperatures increasing the observed *f*. As a result, both the number of ^{57}Fe nuclei present and a sufficiently high *f* must be present for an interpretable spectrum to be collected. Additionally, the recoilless fraction must be considered when quantifying the relative abundance of multiple phases in a given sample, as it may strongly influence the relative abundance of phases in an observed spectrum.

As nuclei can be in different chemical and physical environments, these nuclear and electronic changes will influence the specific energy at which a nucleus will absorb the γ-ray. As a result, a spectrum of energy is needed to measure the interaction of the emitted γ-rays. This is achieved by mounting the ^{57}Co source on a small motor that oscillates forward and backward, advantageously using Doppler effect to add or subtract kinetic energy produced from the motion of the motor. Note that the energy shift being detected is on the order of 10^{-12} the energy of the γ-ray (66). Spectra are typically collected over a small range of velocities, with the x axis of a spectrum ranging from –X mm/s to X mm/s, which can be adjusted on the motor to optimize the quality of the spectrum.

A Mössbauer spectrum is primarily described using three hyperfine interactions: the isomer shift (δ, CS), the quadrupole split or shift (Δ, QS), and the hyperfine field (H). Each parameter can be used to interpret the interactions between the ^{57}Fe nucleus and surrounding electrons. The nuclear energy levels become shifted by the nuclear electronic environment, which provides relative changes, allowing for characterization and interpretation of spectra. A schematic relating the changes in the local nuclear environment to the observed spectrum is shown in Figure 1.3.

If a collected Mössbauer spectrum is of sufficient intensity and is well resolved, it can be fit to extract the hyperfine parameters. The three primary hyperfine parameters which are typically extracted are the center shift (CS; mm/s), the quadrupole splitting or shift (QS; mm/s), and the hyperfine field interaction (H; Teslas). A schematic relating the changes in the local nuclear environment to the observed spectrum is shown in Figure 1.3.

The CS is the most understood of the three, and is consequently the easiest to interpret. When the local environments of the source and absorber (i.e., the sample) atoms are not the same, the observed spectrum will be shifted by some energy, known as the isomer shift. Spectra are calibrated to a known material, setting the observed

transition of a standard at room temperature as zero, with α-Fe metal being the most common choice. The observed isomer shift is directly related to the ns electron density at the nucleus, as the wave functions of s electrons have a nonzero probability of being in the nucleus (65). The isomer shift is a temperature independent phenomenon since the wave functions of electrons do not include temperature. For ^{57}Fe, the observed isomer shift *decreases* with increasing s electron density. Other electron orbitals may indirectly influence the s electrons via electron shielding, making p, d, and f electrons, as well as the bonding environment, have an influence on the isomer shift. The observed shift in a spectrum, known as the chemical shift, is a combination of the isomer shift and a temperature dependent second order Doppler shift, which is caused by atomic vibrations. This value can be approximated, but is traditionally ignore. Typically the observed chemical shift is reported, and is often confused for the isomer shift. For ^{57}Fe, a typical isomer shift from Fe(III) is in the range of 0.3-0.5 mm/s; the isomer shift of Fe(II) is much larger usually, in the range of 0.8-1.4 mm/s, although structural changes can cause exceptions (8).

The second hyperfine interaction is the electric field gradient, which produces quadrupole splitting. This splitting is due to non-cubic symmetry of the local electronic environment, creating a gradient in the electric field, which is analogous to 3d electron splitting to t_{2g} and e_g orbitals in transition metals (66). This information can be used to gain understanding of the local asymmetries and distortions in the nuclear environment, but is much less trivial than the isomer shift to interpret. Possible observable distortions include flattening, counter-rotation, bond scaling, and bond lengths (67, 68). If quadrupole splitting occurs in a paramagnetic sample, a ‘doublet’ is observed in the spectrum, which is observed as two equal intensity peaks separated by the QS (middle portion of Figure 1.3).

The final parameter is known as the hyperfine field interaction (H), which is the effective magnetic field felt by the nucleus. Such a magnetic field can be applied

externally, or can be present internally if the sample is magnetically ordered. Many iron minerals will magnetically order at a characteristic temperature, aiding in fingerprinting procedures. H is modeled using five terms, making fundamental interpretation very difficult (65). When a sample magnetically orders, six peaks are observed which is known as a 'sextet' (right side of Figure 1.3). The larger the magnetic field felt by the active nuclei, the larger the splitting in the spectrum, which is quantified by the energy difference between the first and sixth peak. Quadrupole shifts can be present when there is a hyperfine field interaction, which is observed as QS = $(l_6-l_5) - (l_2-l_1)$. In some samples, such as magnetically ordered ferrous minerals, octets can be observed, with extra peaks resulting from spin-forbidden transitions (65).

It is important to note that much of the interpretation of Mössbauer spectra is done empirically. First principles cannot be used to calculate an expected spectrum of an Fe environment, making interpretation difficult and controversial in some cases. Exciting attempts have been made recently to address this issue (67, 68), but further work is still needed. Additionally, real spectra are much more complicated than just characterizing these parameters, as several features can affect the observed spectra, such as particle size, sample thickness, non-static interactions between electrons and the probe nuclei, and the presence of several different electronic environments coexisting within a single phase can severely complicate interpretation (65). Finally, the approach of fitting a spectrum using computer modeling is still a controversial subject, with various underlying assumptions strongly influencing the extracted data (65, 69, 70). As a result, caution must be taken in the extent of interpretation of collected spectra without complementary techniques.

To model spectra, fitting is typically done using computer software using a least-squares fitting approach (71). Individual parameters can be floated or fixed to allow for the most realistic fit. Fitting of spectra is nontrivial, and is dependent upon the model assumed for fitting. The ideal lineshape in a Mossbauer spectrum is the Lorentzian, which arises from the excitation time and the Heisenberg uncertainty principle. Spectra

typically display linewidths broader than the predicted ones, which has accounted for using different models. The broadening can occur by a sample which is too thick, or by distributions of sites (i.e., different stresses and strains for each atom) (69, 70). It has been concluded previously that for samples with a distribution of sites, a broader Lorentzian line is not an accurate descriptor by several researchers; instead, it is common to assume a Gaussian distribution of Lorentzian peaks, which is referred to as a Voigt distribution (70).

Table 1.1. Reported band gaps for iron oxides (1)

Mineral	**Band Gap (eV)**
Conductor	*≤ 0 (overlap)*
Magnetite (Fe_3O_4)	0.1
Semiconductor	*0.5-3*
Feroxyhyte (δ-FeOOH)	1.94
Maghemite (γ-Fe_2O_3)	2.03
Lepidocrocite (γ-FeOOH)	2.06
Goethite (α-FeOOH)	2.10
Akaganeite (β-FeOOH)	2.12
Hematite (α-Fe_2O_3)	2.20
Insulator	*> 3*

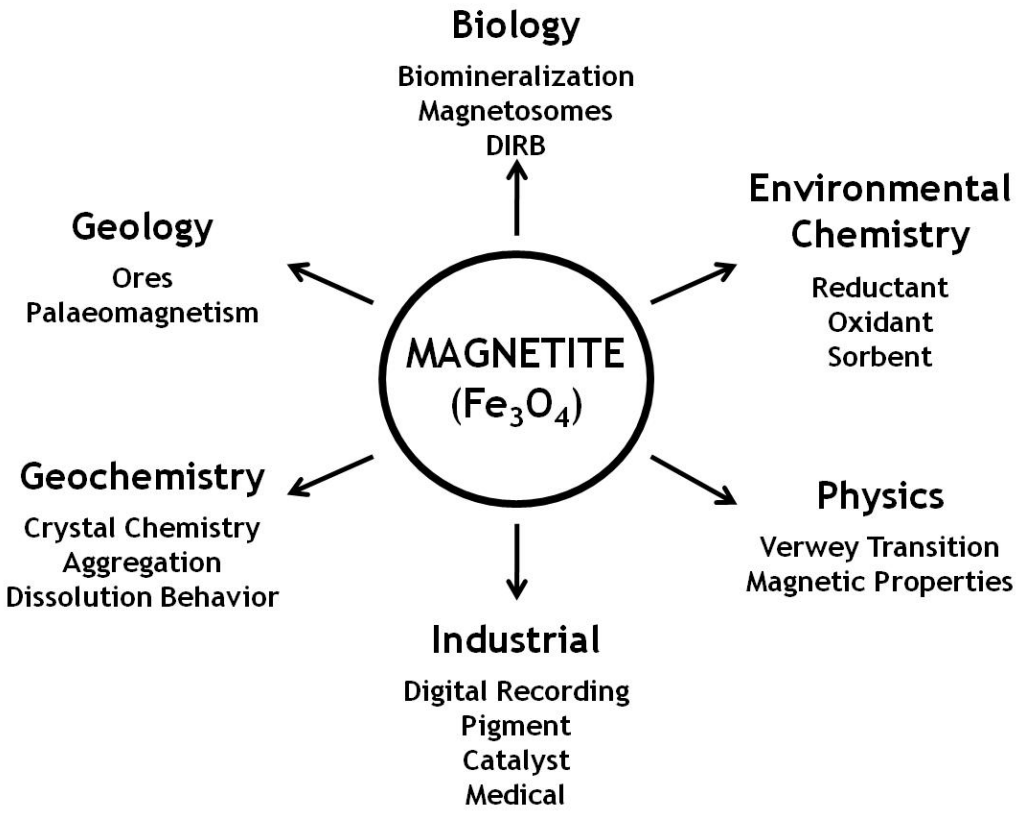

Figure 1.1. The diverse scientific realm of the magnetite.

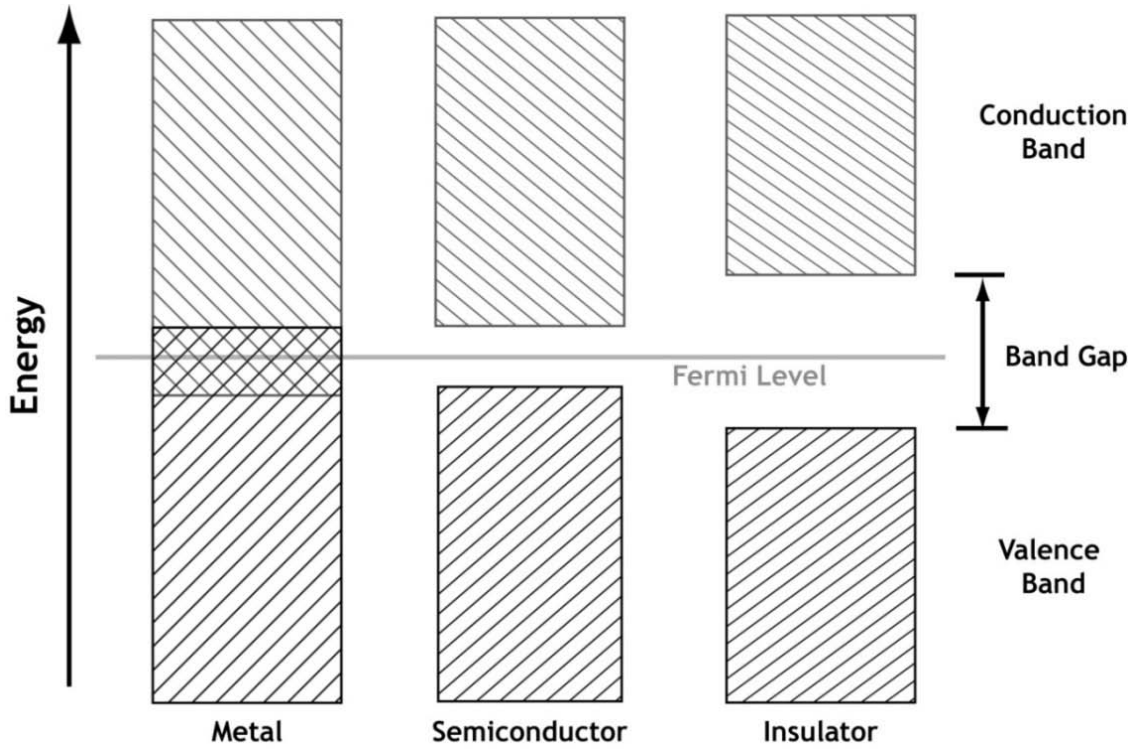

Figure 1.2. Schematic representation of the three types of electronic properties commonly exhibited in solids.

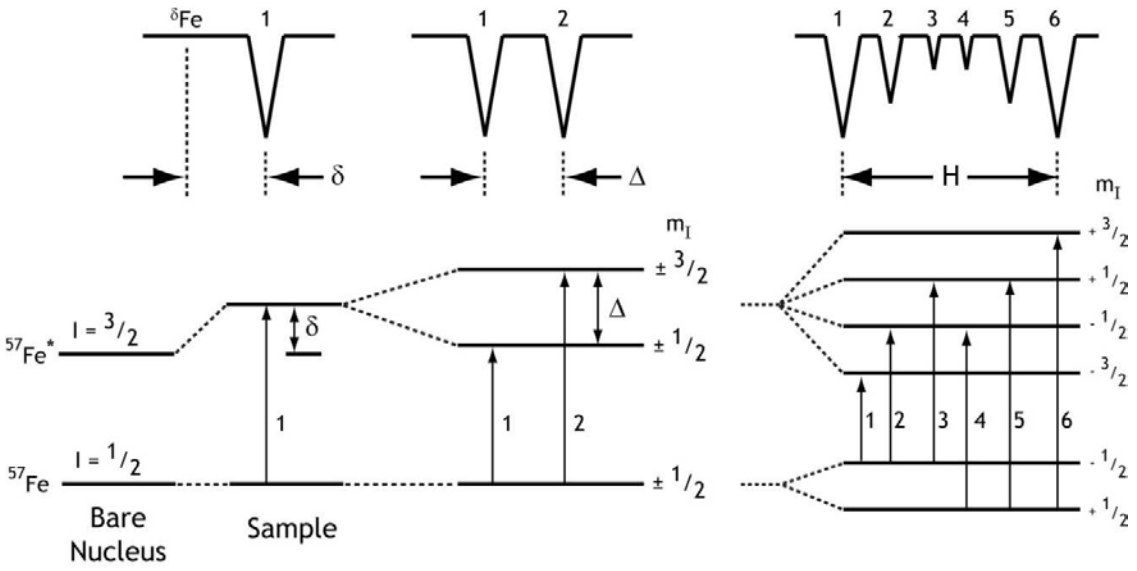

Figure 1.3. Schematic diagram of the ^{57}Fe Mössbauer energy levels as a function of local environment (Adapted from 72).

CHAPTER II: MÖSSBAUER AND XRD CHARACTERIZATION OF MAGNETITE STOICHIOMETRY

Abstract

A solid solution can exist of magnetite (Fe_3O_4) and maghemite (γ-Fe_2O_3), which is commonly referred to as nonstoichiometric or partially oxidized magnetite. The degree of stoichiometry in magnetite is quantitatively measured by determining the ratio of Fe^{2+} to Fe^{3+}. Magnetite stoichiometry ($x = Fe^{2+}/Fe^{3+}$) strongly influences several physical properties, including the coercitivity, sorption capacity, reduction potential, and crystalline structure. Nanoparticulate magnetite has been extensively studied in geochemical and industrial fields, but magnetite stoichiometry is rarely reported, or, when measured, it is not validated with a secondary technique. Here, we review the three most common techniques to determine magnetite stoichiometry: (*i*) acidic dissolution, (*ii*) Mössbauer spectroscopy, and (*iii*) powder X-ray diffraction (pXRD). Eight samples of nonstoichiometric magnetite were synthesized with x ranging from 0 to 0.5 and with the particle size kept as similar as possible (BET specific surface area = 63 ± 7 m^2g^{-1}). Our measurements indicate excellent agreement between stoichiometries determined from Mössbauer spectra and by acidic dissolution, suggesting that Mössbauer spectroscopy may be a useful means for estimating magnetite stoichiometry in multi-phases samples such as those found in the environment. A significant linear correlation was also observed between the unit cell length (a) of magnetite measured by pXRD and magnetite stoichiometry, indicating that pXRD may also be useful for determining particle stoichiometry, especially for mixed phased samples.

C.A. Gorski and M.M. Scherer. Mössbauer and XRD characterization of magnetite stoichiometry. *American Mineralogist.* Submitted.

Introduction

Magnetite (Fe_3O_4) is an important mineral to several fields of study. It has widespread uses in industrial processes as a ferrofluid, including digital media recording and drug delivery (5, 6). Magnetite is of great interest to physicists, as it has unique magnetic properties, undergoes the Verwey transition, and is a conductor (39-42). Magnetite is also widely used in water treatment as an effective sorbent for many contaminants that can be easily separated from water using an applied magnet field (7). In corrosive environments, magnetite is a frequently observed product of steel oxidation (37). In natural environments, magnetite is a common end product of biological and abiotic reduction of ferric (Fe^{3+}) oxides (43-45), and a facile reductant for several environmental contaminants found in groundwater (17, 18, 43, 73, 74).

Stoichiometric magnetite ($x = 0.5$) has an inverse spinel structure (space group *Fd*3*m*), which has an oxygen cubic closed-packed structure, and a 2:1 octahedral (Oct) to tetrahedral (Tet) site occupancy with Fe atoms. As a result, the magnetite formula can be written more precisely as $^{Tet}Fe^{3+}[^{Oct}Fe^{2+}Fe^{3+}]O_4$. In the literature, the ^{Tet}Fe is often referred to as the "A" site, and the ^{Oct}Fe is denoted as the "B" site. For clarity of discussion, we will refer to these sites as Oct and Tet throughout this paper. Within the unit cell, there are eight $^{Tet}Fe^{3+}$, eight $^{Oct}Fe^{2+}$, eight $^{Oct}Fe^{3+}$, and 32 oxygen atoms. Figure 2.1 contains a quarter of the magnetite unit cell with example bonding arrangements shown for each atom type. Note that $^1/_2$ of the available octahedral sites and $^1/_8$ of the tetrahedral sites are occupied by Fe atoms.

As magnetite becomes oxidized, the Fe^{2+}/Fe^{3+} ratio decreases ($x < 0.5$), with this form denoted as nonstoichiometric or partially-oxidized magnetite. When the magnetite is completely oxidized ($x = 0$), the mineral is known as maghemite. For nonstoichiometric magnetite, the structure is often written as $Fe_{3-\delta}O_4$, where δ can range from zero (stoichiometric magnetite) to $^1/_3$ (completely oxidized). This formula can be expressed as $^{Tet}Fe^{3+}[^{Oct}Fe^{2+}{}_{1-3\delta}\ Fe^{3+}{}_{1+2\delta}\ \square_\delta]O_4$, where $\square$ are vacancies formed in the

crystal structure to account for charge balance. Note that this model assumes that all vacancies are Oct, which is a topic of debate in the literature (39, 75, 76). The stoichiometry can easily be converted to and from this form by the following relationship:

$$x = \frac{Fe^{2+}}{Fe^{3+}} = \frac{1-3\delta}{2+2\delta}. \quad (2.1)$$

The physical and chemical properties of magnetite, including the reduction potential (54, 64, 77), conductivity (62, 63), and crystalline structure (e.g., 78), are strongly influenced by particle stoichiometry ($x = Fe^{2+}/Fe^{3+}$). In our previous work, we demonstrated that stoichiometry dramatically influences the measured open-circuit potential (E_{OCP}), as well as the reactivity of magnetite with nitrobenzene and dissolved Fe^{2+} (74, 77). Magnetite stoichiometry is important to several other fields as well, as it influences the sorption capacity for heavy metals (48), affects the coercitivty, a property critical to digital data storage (39), and can influence the conductivity by orders of magnitude (62). Despite the significant influence of magnetite stoichiometry on particle properties and reactivity, little has been done to critically evaluate the most common measurement techniques.

The most common methods for measuring magnetite stoichiometry include (*i*) ^{57}Fe Mössbauer spectroscopy (79-82), (*ii*) complete acidic dissolution (74, 78, 79), and (*iii*) powder X-ray diffraction (pXRD) (53, 79, 80, 83-85). Other less common spectroscopic techniques have also been used to characterized stoichiometry, including X-ray magnetic circular dichroism (XMCD) and Fourier transform infrared spectroscopy (FTIR) (86, 87). The precision, accuracy, and reliability of these individual methods, however, are unclear, and little has been done to do compare stoichiometries determined by different methods on the same samples. In addition, most of the studies have been carried out on large particulate samples (several micron crystals), despite the fact that

many of the environmental and industrial samples studied are nanoparticulate (< 100 nm).

Here, we compared the stoichiometry of nanoparticulate magnetite samples using three measurement techniques. We measured the stoichiometry of eight nanoparticulate magnetite samples using acidic dissolution (x_d) and Mössbauer spectroscopy (x_{MS}). We also used pXRD to characterize the samples to determine relative peak intensity and the fitted unit cell length (a) as a function of x_d. Magnetite stoichiometries determine by Mössbauer spectroscopy (x_{MS}) are typically determined from room temperature (298 K) spectra, but nanoparticulate magnetite does not produced well-resolved spectra. We overcame this issue by selecting a colder temperature of 140 K to collect and fit spectra for nanoparticulate magnetite. We found excellent agreement between x_d and x_{MS}, with no observable bias in either method. We examined the general trends between stoichiometry and pXRD fitted results with our samples as well as literature values, and observed good agreement across studies, indicating that pXRD may also be useful for determining magnetite stoichiometry.

Materials and Methods

Magnetite Synthesis and Characterization

Stoichiometric nanoparticulate magnetite was synthesized by creating a 2:1 Fe^{2+}:Fe^{3+} acidic solution (pH < 1) in an anaerobic N_2/H_2 (94/6) glovebox. The solution was then titrated to an alkaline pH (10-11) using 5 M NaOH while being stirred, and allowed to mix overnight. To form nonstoichiometric magnetite, concentrated H_2O_2 was added to the solution after the overnight equilibration, and allowed to equilibrate an additional day. For all batches, the resultant solution was filtered within the glovebox, with minimal washing used (< 2 rinses), as additional washing resulted in oxidation of stoichiometric magnetite due to Fe^{2+} dissolution. The solids were then freeze-dried outside the glovebox, and were then returned to the glovebox for sieving (100 mesh) and

storage prior to characterization. Maghemite was synthesized from magnetite by baking it at 200 °C for two hours outside the glovebox (88).

Particles were characterized by acidic dissolution (x_d), ^{57}Fe Mössbauer spectroscopy (x_{MS}), pXRD, BET, and some samples were examined using surface and transmission electron diffraction (SEM & TEM). BET specific surfaces areas (SSA) were 63 ± 7 m^2g^{-1}, and have been provided for each batch in our previous works (74, 77). TEM images showed spherical particles that were approximately 20 nm in diameter, in good agreement with the size expected from the BET SSA (74, 77). There were no discernable trends between the stoichiometry and the particle morphology or size.

The large particulate magnetite was prepared from a natural magnetite single crystal from Minas Gerais, Brazil (Ward's Natural Science, Rochester, NY, USA). The sample was ground in a mortar and passed through a 100 mesh sieve in an anaerobic glovebox. The sample was characterized by dissolution, Mössbauer spectroscopy, and pXRD. The particle size was determined to be large (> 200 nm) based on the pXRD patterns using the Scherrer equation.

Acid Dissolution Method

The dissolution stoichiometries ($x_d = Fe^{2+}/Fe^{3+}$) were determined by dissolving the solids in 5 M HCl in an anaerobic N_2/H_2 glovebox. The total Fe concentration was aimed to be approximately 10 mM. The nanoparticulate solids took approximately 2-4 hours to completely dissolve, while the large particulate sample took several days. The Fe^{2+} and total Fe concentrations were then measured using the phenanthroline method (89). The standard deviation was low between replicate samples ($\sigma_d < 0.01$). Note that filtering the acidic Fe solutions at any stage of analysis significantly oxidized the dissolved Fe^{2+}, which was likely due to nitrate groups present on the filter paper.

Mössbauer Spectroscopy

Transmission Mössbauer spectroscopy was performed with a variable temperature He-cooled system with a 1024 channel detector. The ^{57}Co source used (~50 mCi) was in a Rh matrix at room temperature. All center shifts reported are relative to α-Fe foil at room temperature. Samples were prepared by sealing the powder specimen between two pieces of 5 mL Kapton Tape to avoid oxidation while mounting the sample.

Spectral fitting was done using Recoil Software (University of Ottawa, Ottawa, Canada). Lorentzian, Voigt, and extended-Voigt fits were used to model the spectra to determine the most accurate model. Unless noted, all fits presented were done with extended-Voigt fitting. For all fits, the relative sextet peak areas (3:2:1:1:2:3) was held constant. The Lorentzian linewidth was held at 0.12 mm/s for Voigt and extended-Voigt fitting, as it was the linewidth measured on the spectrometer for an ideally thick α -Fe foil. For all fits, unless otherwise noted, the center shift (CS), quadrupole shift (QS), hyperfine parameter (H), and relative areas were allowed to float during fitting. Both sextets had two hyperfine components that were allowed to float, as the fits were unacceptably poor when only one component was used. The CS and QS were fit with single components in all cases.

Powder X-Ray Diffraction

pXRD patterns were collected using a Rigaku MiniFlex II system equipped with a Co source (CoK_α = 1.78899 Å). Sample powders were mixed with a small amount of glycerol to form a thick paste in an aerobic glovebox to avoid inadvertent oxidation during analysis (90). Samples were analyzed from 5-80 °2θ with a 0.02 ° step size and a 1.2 second dwell time. Patterns were analyzed and fit using Jade 6 software (Materials Data, Incorporated, USA). For analysis, patterns were smoothed, background subtracted, and $K_{\alpha 2}$ stripped prior to analysis and fitting. A broad peak was observed at approximately 24 °2θ due to the glycerol, otherwise all the peaks were characteristic of

magnetite. Fitting was done using pseudo-Voigt peaks with allowable displacement error in order to minimize error as outlined elsewhere (91).

Results and Discussion

Mössbauer Characterization of Stoichiometric Magnetite.

Mössbauer spectra collected for a large particulate (> 200 nm) and a nanoparticulate (~20 nm) stoichiometric magnetite (x_d = 0.5) at a series of temperatures ranging from room temperature (298 K) to 13 K are shown in Figure 2.2. Mossbauer temperature profiles are a useful method for characterizing iron minerals because their magnetic behaviors, and subsequently observed spectra, are highly temperature dependent as can be seen by the change in peak localities and intensities in Figure 2.2.

For large particulate and single crystals of magnetite, two primary temperature domains exist at and below room temperature. From room temperature down to 121 K, a Mössbauer spectrum of magnetite is characterized by two sextets. For the large particulate magnetite spectrum at 298 K in Figure 2.2, the left-hand side of the spectrum shows two clearly defined sextets which overlap on the right-hand side of the spectrum. For stoichiometric (x = 0.5), these two sextets correspond to the $^{Tet}Fe^{3+}$ and the $^{Oct}Fe^{3+}$ and $^{Oct}Fe^{2+}$. Magnetite, which is a conductor, exhibits rapid electron hopping between the $^{Oct}Fe^{3+}$ and $^{Oct}Fe^{2+}$ at room temperature which is faster than the characteristic sample time for Mössbauer spectroscopy (10^{-8} s). As a result of this fast electron hopping, the ^{Oct}Fe atoms are observed with an average valence state of 2.5+, with the sextet referred to as $^{Oct}Fe^{2.5+}$. For samples that are partially oxidized (x < 0.5), an $^{Oct}Fe^{3+}$ sextet is present in the spectrum, which closely overlaps with the $^{Tet}Fe^{3+}$ sextet. When an external magnetic field is used with Mössbauer spectroscopy, the two signals ($^{Oct}Fe^{3+}$ and $^{Tet}Fe^{3+}$) can be discerned; however, in the absence of an external magnetic field, they are typically modeled as one site (81, 82, 92). In the absence of an external magnet, 298 K magnetite

spectra are often fit to extract the stoichiometry by comparing the relative areas of the $^{Oct,Tet}Fe^{3+}$ and the $^{Oct}Fe^{2.5+}$ using the following equation (80-82):

$$x_{MS} = \frac{Fe^{2+}}{Fe^{3+}} = \frac{{}^{1}/_{2}\,{}^{Oct}Fe^{2.5+}}{{}^{1}/_{2}\,{}^{Oct}Fe^{2.5+} + {}^{Oct,Tet}Fe^{3+}}. \quad (2.2)$$

It is unclear, however, how accurate this method is since it has rarely been compared to stoichiometries determined from acidic dissolution.

In Figure 2.2, the room temperature spectrum of the nanoparticulate magnetite is significantly different than the large particulate magnetite. For the nanoparticulate sample, two sextets are still visibly present, but the sextets are significantly broader and overlap considerably. The change in the Mössbauer spectrum is due to the small particle size, which can cause a greater distribution in magnetic behavior due to a higher percentage of surface atoms, additional stresses between atoms, and superparamagnetic behavior due to the small domain sizes (80, 93-95). Similar room temperature spectra have previously been observed for nanoparticulate magnetite (85, 96, 97). The overlapping sextets make it difficult to fit the spectrum, and our attempts to do so resulted in non-unique fits (i.e., different x_{MS} values) depending on the initial assumptions used. Note that some previous work has used 298 K fits of nanoparticulate magnetite to determine stoichiometry, despite the difficulty and ambiguity of fitting (85).

Upon cooling the magnetite sample, both the large particulate and nanoparticulate magnetite spectral features change considerably (Figure 2.2). At 200 K and 140 K, the large particulate magnetite spectra look similar to the room temperature spectrum, however the inner sextet broadens (i.e., the $^{Oct}Fe^{2.5+}$ sextet as discussed later). For the nanoparticulate sample, the spectra become better resolved upon cooling, as the size-dependent nano-effects become less pronounced. The 200 K and 140 K spectra look similar to those of the large particulate magnetite; however, the $^{Oct}Fe^{2.5+}$ sextet is broader for the nanoparticulate sample.

Upon cooling the magnetite sample further, a distinct change in the magnetic properties occurs at 121 K, which is known as the Verwey transition point (T_V). Below this temperature, the conductivity of magnetite is significantly reduced, and the magnetic behavior dramatically changes (41, 42). The cause for these changes is a controversial subject in the literature, and, despite extensive work, a consensus has yet to be reached. The effect of transition can be seen clearly for the large particulate magnetite in Figure 2.2, where several additional peaks can be seen in the 77 K and 13 K spectra. For the nanoparticulate magnetite, the 77 K and 13 K spectra also look considerably different with peaks absent which are present for the large particulate magnetite. It is unclear if the nanoparticulate magnetite does not undergo the Verwey transition, or, if it does, the resultant spectra are different due to the smaller particle size. In one study, it was shown that the Verwey transition is highly dependent upon stoichiometry, but not of particle size (98); however, in that study, their small particulate magnetite (0.22 µm) was not a nanoparticulate sample (< 100 nm), and was similar in size to our large particulate sample.

Determining Magnetite Stoichiometry from Mössbauer Spectra.

Based on the temperature dependent behavior shown in Figure 2.2, we chose to use spectra collected at 140 K to determine the stoichiometry of nanoparticulate magnetite. Our goal was to evaluate whether Mossbauer spectroscopy could be used to reliably estimate the stoichiometry of nanoparticulate magnetite by comparing the stoichiometry measured by acidic dissolution (x_d) and Mössbauer spectroscopy (x_{MS}). Note that for large particulate magnetite, a room temperature spectrum is often used and is sufficient to calculate the stoichiometry using the relative areas of the two sextets. For nanoparticulate magnetite, however, the room temperature spectrum is complicated and fitting does not provide a unique set of parameters. Spectra collected at 140 K were the

best candidate because the temperature was low enough to minimize the nanoparticulate superparamagnetic effects and high enough (> 121 K) to avoid complications arising from the Verwey transition. Figure 2.3 contains model fits for 140 K spectra for the large particulate and nanoparticulate magnetite. Despite the effects of cooling to reduce the effects of particle size, there are still discernable differences, such as the $^{Oct}Fe^{2.5+}$ sextet is much broader for the nanoparticulate sample.

In addition to the relative abundance of phases within a sample, spectral fitting provides additional parameters: the center shift (CS), the quadruple shift (QS), and the hyperfine field (H), which are collectively known as the hyperfine parameters, which measure the nucleus-electron interactions. Each hyperfine parameter is closely related to physical properties of the sample. The center shift is proportional to the electron density for the Fe atom, with an Fe^{2+} atom having a lower electron density than an Fe^{3+} atom due to extra d-electron reducing s-electron density, and thus the center shift of an Fe^{2+} atom is higher than an Fe^{3+} atom in most cases. For the $^{Oct}Fe^{2.5+}$ sextet, the observed center shift is a combination of the Fe^{2+} and Fe^{3+}, and is higher (~ 0.72 mm/s at 140 K) than the $^{Tet}Fe^{3+}$ sextet (~0.37 mm/s at 140 K). The quadrupole shift is proportional to the relative bond symmetry of an Fe atom, with higher stresses and strains resulting in a larger quadrupole shift. For a perfectly symmetrical atom, like the $^{Tet}Fe^{3+}$ in magnetite, the expected quadrupole shift should be zero. The hyperfine field is proportional to the strength of the internal magnetic field (in the absence of an applied field). For nanoparticles, the hyperfine field is typically smaller than their large particulate analogs due to poorer ordering of spins within the lattice (76). Here, we observe significantly smaller hyperfine field values for the nanoparticulate phases.

Two fundamentally different model exist for extracting the hyperfine parameters from a Mossbauer spectrum: Lorentzian and Voigt-based. For a Lorentzian fit, the width of the peaks is accounted for by broadening a single Lorentizan peak; in the Voigt model, however, the peak is modeled as a Gaussian distribution of several Lorentzian peaks

resulting from multiple unique atomic sites within the sample. This difference is not subtle, as it changes the shape of the peaks, and results in different fits and extractable parameters. Rancourt and co-workers have argued extensively for the merit of the Voigt-based model, citing that floating the Lorentzian linewidth is a physically incorrect assumption (70, 99-101). Previous work has often assumed a Lorentzian model to fit the peak profiles (81, 82, 102), which has worked well for large particulate magnetite due to the samples being well-crystalline, which results in a narrow distribution of sites (and negligible Voigt distribution). The Lorentzian fitting model could not be applied to the nanoparticulate magnetite in this study, however, because the peak shapes were distinctly non-Lorentzian in shape. A Voigt model was required to achieve reasonable fits that captured the peak shape and distributions of the spectra. For example, Lorentzian modeling of the spectra in Figure 2.3, resulted in x_{MS} values for both the large particulate and nanoparticulate magnetite that were lower than the x_d value of 0.50. The discrepancy was much greater for the nanoparticulate magnetite, with an x_{MS} of only 0.27, and an x_{MS} of 0.44 for the large particulate sample. Modeling the spectra with the Voigt model provided x_{MS} values of 0.50 (large particulate) and 0.47 (nanoparticulate), which were much closer to the x_d of 0.50 (Figure 2.3). Our results suggest that for nanoparticulate magnetite, it is important to use appropriate fitting models, such as Voigt-based models, when estimating stoichiometry from Mössbauer spectroscopy.

Another consideration is that the spectral areas in a Mössbauer spectrum do not always directly correlate to the relative abundance of sites because some of the sites are not completely rigid (i.e., they have some recoil). The percentage of Fe atoms that are rigid enough to undergo the necessary nuclear absorption and emission process which results in an absorption Mössbauer spectrum is known as the recoilless fraction (f). In a previous study, a room temperature recoilless fraction ratio ($f_{2.5+}/f_{3+}$) of 0.94 was determined (103). More recently, others have found the $f_{2.5+}/f_{3+}$ ratio is closer to 1.00 (78, 79). As the temperature cools in a sample, the f ratio should approach 1.00 (103),

although this has not been experimentally validated for magnetite. The *f* ratio is critical to for extracting x_{MS}, as the spectral areas would need to be corrected for the recoilless fraction. To determine the *f* ratio for our large particulate sample, the relative areas of the two sextets ($^{Oct}Fe^{2.5+}/^{Oct,Tet}Fe^{3+}$) were fit at 298 K, 200 K, and 140 K; the relative areas were modeled to be 1.976 (298 K), 1.955 (200 K), 1.976 (140 K) (data not shown), indicating that $f_{2.5+}/f_{3+}$ is independent of temperature using this fitting method, and is likely very near to 1.00 at temperatures up to 298 K for the large particulate sample. A similar method could not be applied to the nanoparticulate samples, because fitting could only be done in a narrow temperature range, so it must be assumed that a similar *f* ratio of 1.00 exists at 140 K.

Spectral Interpretation of Non-stoichiometric Magnetite.

Sample spectra from magnetite samples with varying stoichiometries collected at 140 K are presented in Figure 2.4. The Mössbauer fit parameters are shown in Table 2.1 with literature values at similar temperatures. As the sample becomes more oxidized (smaller *x*), the $^{Oct}Fe^{2.5+}$ sextet area decreases and the $^{Oct,Tet}Fe^{3+}$ sextet area increases. Model parameters found for the $x_d = 0.50$ magnetite were used as initial values for fits of the nonstoichiometric samples. For some spectra (indicated in Table 2.1), the center shift (CS) was fixed as 0.72 mm/s, as floating the value led to unrealistic values as discussed later.

A comparison of the stoichiometry determined by acidic dissolution (x_d) and by Mössbauer spectroscopy (x_{MS}) is shown in Figure 2.5. For the entire range of stoichiometry, the agreement between x_d and x_{MS} is excellent. The slope of the line is close to 1.0 indicating near-perfect agreement between x_d and x_{MS} ($m = 0.96 \pm 0.04$ ($\pm \sigma$); $R^2 = 0.998$, $n = 8$). There does not appear to be an indication of a systematic bias in either direction (i.e., over-estimation or under-estimation), suggesting that the fitting model

used is robust, and can be applied to samples over the full range of stoichiometry, that is, from maghemite to stoichiometric magnetite.

It is worth noting that in previous works, the reliability of determining the stoichiometry by acidic dissolution (x_d) has been questioned due to the possibility of inadvertent oxidation in the dissolution process (80, 104). As a result, the excellent agreement between x_{MS} and x_d observed here provides validation of both techniques concurrently. We suspect that since previous work was not done in an anaerobic chamber, that the inadvertent oxidation reactions would be more likely. We have also found that filtering the acidic suspensions can lead to significant oxidation of Fe^{2+} if nitrate groups are present on the filter. Additionally, the use of the 1,10-phenathroline method used to measure dissolved Fe^{2+} coupled with the use of fluoride to mask the presence of Fe^{3+} greatly increased the precision of x_d (89).

Note that we used a pair-localized model to fit the Mössbauer spectra which explicitly assumes discernable $^{Oct}Fe^{3+}$ and $^{Oct}Fe^{2.5+}$ sites. This, however, is a controversial topic. Three models have been proposed to explain the Mössbauer spectra of non-stoichiometric magnetite above the Verwey transition: (*i*) the "discrete" model, where a combination of stoichiometric magnetite and maghemite is present (76, 80); (*ii*) the "pair-localized" theory used here, where upon oxidation octahedral Fe^{2+} and Fe^{3+} atoms pair, with unpaired Fe^{3+} atoms resulting in the $^{Oct}Fe^{3+}$ signal (82, 83, 95); and (*iii*) the "band-delocalized" model, where a pool of valence electrons is shared between all ^{Oct}Fe atoms (105). The discrete and pair-localized models would result in the same observed spectra with discrete $^{Oct,Tet}Fe^{3+}$ and $^{Oct}Fe^{2.5+}$ sextets, whereas the band-delocalized model would result in a $^{Tet}Fe^{3+}$ sextet and an $^{Oct}Fe^{2.z+}$ sextet, where $5 < z < 10$. It has also been hypothesized that both the pair-localized and the band-delocalized mechanisms may both be occurring simultaneously (106). In our previous work where we characterized the redox properties and reactivity of magnetite, we concluded that the discrete model [i.e., a stoichiometric magnetite core ($x = 0.5$) with a maghemite shell ($x = 0$)] is an inaccurate

descriptor of nonstoichiometric nanoparticulate magnetite(74, 77), and thus, we used the pair-localized model to fit the spectra here.

The good agreement between stoichiometries determined from the Mossbauer spectra and the dissolution data, however, does not necessarily imply that the pair-localized model is correct.. Indeed, there are some indicators in the fit parameters (Table 2.1) that suggest that some band-delocalization may be occurring. For example, as the stoichiometry decreases, the $^{Oct}Fe^{2.5+}$ sextet has a lower average H, and the standard distribution (i.e., width of the sextets; std(H)) increases; this can also been seen visually in Figure 2.4. This suggests that the internal magnetic interactions between ^{Oct}Fe are smaller (decreasing H), and that there is a wider distribution of local ^{Oct}Fe environments (increasing std(H)). It has also been proposed that the larger std(H) is due to slowed electron hopping rates in the conduction band, which would also manifest in widening the sextet peaks (106, 107). Others, however, have argued that these observations are also consistent with the pair-localized model, as one would expect the vacancies and reordering that must occur as Fe^{2+} atoms become Fe^{3+} will cause local disorders (78, 94).

A second indication that suggests band delocalization may be occurring is that the CS had to be fixed at 0.72 mm/s for some of the more oxidized samples (Figure 2.4, Table 2.1) as noted earlier. Figure 2.6 shows the fitted spectrum for the $x_d = 0.25$ magnetite with the fixed CS (i.e., pair-localized) and without (i.e., band-delocalized). Note that the fitted areas shift substantially, and the CS drifts to 0.62 mm/s in the band-delocalized spectrum. If all the octahedral atoms were pooling electrons, an $^{Oct}Fe^{2.z+}$ sextet would be expected, and it should represent approximately two thirds of the spectral area with a minor shift due to vacancies. For the band-delocalized model, the $^{Oct}Fe^{2.z+}$ sextet accounts for only 52% of the area, so at least some of the ^{Oct}Fe is still being modeled as the $^{Oct,Tet}Fe^{3+}$ sextet. A quantitative means for comparing the fits is to examine the goodness-of-fit parameter, χ^2, where lower values represent a better fit. The χ^2 value is virtually identical between the samples: 1.087 for pair-localized and 1.089 for

band-delocalized, indicating that one fit does not appear to model the data any better than the other. As a result, from our data, we cannot determine if the pair-localized, band-delocalized, or a combination of the two is the most accurate model to describe nonstoichiometric magnetite. We can, however, conclude that fitting the data with the pair-localized model results in excellent agreement between x_d and x_{MS}. Not that the stoichiometries cannot be determined from the fitting the data with band-delocalized model because the sextet areas would not correspond to known Fe oxidation states (i.e., 3+ and 2.z+).

Characterization of Magnetite using Powder X-ray Diffraction

A third method that has been used to determine the stoichiometry of magnetite samples is pXRD. The pXRD pattern of magnetite has previously been shown to be dependent upon stoichiometry in several studies (53, 79, 80, 83-85). Stoichiometric magnetite, which has a cubic close-packed structure, has a reported unit-cell length (a) of 8.396-8.400 Å (1, 79, 86, 108, 109). As the magnetite becomes oxidized (lower x), the unit cell becomes smaller due to the formation of vacancies and the smaller atomic size of Fe^{3+} atoms as compared to Fe^{2+}. Maghemite (x = 0) has a similar cubic structure, but with a slightly smaller unit cell length (8.33-8.34 Å) (1, 78, 109). In these studies, the stoichiometry is determined by linear interpolation between the two extreme stoichiometries (i.e., 0 and 0.5) and their reference unit cell lengths. It has been proposed that the maghemite structure has additional symmetry due to the ordering of vacancies, which results in additional peaks observed in pXRD patterns (53, 75, 79). The method of maghemite preparation appears to influence the presence and intensity of these peaks, however, it has been suggested that there are structurally different forms of maghemite with varying degrees of vacancy ordering (78).

Selected pXRD patterns for magnetite over the range of stoichiometries (x_d = 0.50, 0.25, 0.00) are shown in Figure 2.7. The patterns have been smoothed, background-subtracted, and Kα_2-stripped to aid in interpretation. The eight most intense peaks have been labeled with their appropriate crystallographic planes (hkl). The patterns appear nearly identical as the changes in the unit cell are quite subtle and require fitting of peaks to extract. As the sample becomes oxidized, additional peaks are observed in both the x_d = 0.25 and 0.00 samples, which have been labeled with a star (*) for the x_d = 0.00 sample in Figure 2.7. Note that the small broad peak directly to the right of the (111) peak for the x_d = 0.00 is an artifact of using glycerol to avoid sample oxidation. The additional peaks observed here suggest that some vacancy ordering has occurred within the oxidized samples.

Diffraction patterns of the magnetites were fit to determine the relative peak localities and intensities to determine if they could be used to estimate the stoichiometry of the samples. For the samples in Figure 2.7, the fitted unit cell lengths were 8.394 Å (x_d = 0.50), 8.366 Å (0.25), and 8.339 Å (0.00). As expected, the unit cell length decreases upon the oxidation of magnetite (which manifests in a slight left-shift of peaks in Figure 2.7). The same trend has been observed by several studies in the past, however, the trends have never compared among papers, making the robustness of these methods difficult to determine.

The extracted unit cell lengths are shown as a function of stoichiometry determined by acidic dissolution (x_d) in Figure 2.8. The peak data and resultant fits are summarized in Table 2.2. The error bars used for the data markers are the standard deviations provided from the fitting software with the exception of the x_d = 0.50 batch where five replicate samples were prepared, and the error bars represent the standard deviation computed from these samples. Data from previous studies that related stoichiometry to the unit cell length are also shown in Figure 2.8 for comparison. A robust linear trend is observed between the studies using a linear regression (R^2 = 0.93, n

= 35). The fitted line yields the equation: a = 0.1148(± 0.0055)x_d + 8.3396(± 0.0020), where a(x_d = 0) = 8.3396 Å and a(x_d = 0.5) = 8.397 Å, both in excellent agreement with the reference values above. This method also validates the usage of pXRD to characterize stoichiometries between the two extremes (i.e., 0 and 0.5), which has previously been an assumption in the literature.

The relative intensity of the (111) peak has also been used to determine stoichiometry in the past. It has been proposed that as the magnetite becomes more oxidized (lower *x*), the (111) peak will decrease due to octahedral vacancies (i.e., less atoms to diffract). Linear relationships have been observed in the past (53, 75, 79), yet some studies have noticed no correlation (39, 78). As mentioned earlier, this apparent contradiction has been rationalized by the possibility that different nonstoichiometric magnetite and maghemite structures can exist, with vacancy location and structural ordering varying between samples synthesis methods (78). The peak intensities were measured for the seven most intense peaks in this study, with the data summarized in Table 2.3. In this work, there appears to be a slight positive trend between the (111) peak intensity and magnetite stoichiometry (R^2 = 0.57, n = 7); however, the noise of the data appears to be too great. For the five x_d = 0.50 replicates, the standard deviation was 3.1%, which was roughly the extent of change observed between the samples.

Applicability of Mössbauer spectroscopy and pXRD for determination of stoichiometry

Here, the three most common techniques for determining magnetite stoichiometry have been validated on the basis that there is good agreement among the three methods. Acidic dissolution is a simple, easy method for determining stoichiometry for synthesized samples, but care must be taken to avoid oxidation by air-exposure and filtration. There are many cases, however, when acidic dissolution of the sample is not a possibility. For example, natural and mixed-phased samples can contain other redox active components

(e.g., bacteria), and have functional groups adhered to the particle surface for stabilization. In these cases, spectroscopic techniques are preferred because the sample does not require any additional treatment (e.g., washing) to characterize.

One important limitation of these methods, however, is the effect of substituent elements within the magnetite crystal lattice. Aluminum can readily be substituted for ^{Tet}Fe atoms, and work has shown that it will influence the relative ratios of sextets in Mössbauer spectra, the unit cell length in pXRD, and the acidic dissolution values (1, 76). As a result, the stoichiometry could easily be misinterpreted using these techniques, especially when applied to natural samples where the source elements are unknown. Additional characterization will thus be needed in order to determine the content of substituent. Furthermore, the effects of the substituents on many of the physical properties of magnetite remain unexplored, especially with the magnetite stoichiometry in mind.

Despite this limitation, the strong trends observed among the three techniques suggest that acid dissolution, Mössbauer spectroscopy, and pXRD are all valid approaches for determining magnetite stoichiometry. Discrepancies between techniques observed in previous works are likely in part due to the several structural forms with which nonstoichiometric magnetite and maghemite can take. As a result, caution should be taken in further interpretation of spectra and pXRD patterns, as the Mössbauer hyperfine parameters or the (111) pXRD relative peak intensities are likely to be dependent upon factors besides stoichiometry. Acidic dissolution is thus a favorable characterization choice, as it will be independent of particle size and synthesis method, although it will not address sample impurities. The robust trend observed for the pXRD data, however, suggests that the unit cell length (a) is likely directly related to stoichiometry, and is thus probably immune to the influence of synthesis methods.

Table 2.1. Mössbauer Parameters for magnetite of varying stoichiometry ($x = Fe^{2+}/Fe^{3+}$) at T = 140 K.

			$^{Oct}Fe^{2.5+}$				$^{Tet}Fe^{3+}$, $^{Oct}Fe^{3+}$					
	x_d[a]	CS (mm/s)	ε (mm/s)	H (T)	std(H) (T)	Area (%)	CS (mm/s)	□ (mm/s)	ε (T)	std(H) (T)	Area (%)	x_{MS}[b]
This work	**0.00**	B.D.[c]	B.D.	B.D.	B.D.	0	0.42	0.00	49.8	2.5	100	**0.00**
	0.16	0.72[d]	-0.10	39.3	10.5	24.3	0.43	-0.01	48.1	3.2	75.7	**0.14**
	0.25	0.71	-0.03	44.0	8.4	37.7	0.40	0.00	48.8	2.3	62.3	**0.23**
	0.26	0.74	-0.02	46.4	4.4	41.3	0.39	-0.01	49.3	1.9	58.7	**0.26**
	0.36	0.72[d]	-0.01	45.8	3.2	56.4	0.39	0.00	48.9	1.1	43.6	**0.39**
	0.42	0.72	-0.02	46.8	2.5	58.5	0.37	0.00	49.5	0.8	41.5	**0.41**
	0.49	0.74	-0.02	46.0	3.8	62.3	0.38	0.00	49.3	0.8	37.7	**0.45**
	0.50	0.72	-0.02	47.4	2.8	64.1	0.38	0.00	50.2	0.1	35.9	**0.47**
	LP[e] (0.50)	0.76	0.00	48.2	2.1	66.4	0.37	0.00	50.4	0.6	33.6	**0.50**
References	**135 K[h]**	0.75	-0.01	47.9	-	65	0.35	0[f]	50.4	-	35	**0.48**
	150 K[i]	0.65	0[f]	46.7	-	54	0.37	0[f]	50.6	-	46	**0.37**
	130 K[j]	0.68	0	47.7	-	51	0.37	0	50.8	-	49	**0.34**
	120 K[k]	0.77	0	48.1[l]	-	38	0.34	0	50.3	-	63	**0.23**
	130 K[m]	0.76	0[f]	48.2	-[g]	64	0.35	0[f]	50.0	-	36	**0.47**

[a] x_d = stoichiometry determined by acidic dissolution. $\sigma_{xd} < 0.01$.

[b] $x_{Mössbauer} = (½\ ^{Oct}Fe^{2.5+})/(½\ ^{Oct}Fe^{2.5+} + {}^{Tet,Oct}Fe^{3+})$.

[c] B.D. = Below detection in fitting.

[d] The CS was fixed at 0.72 because floating led to unrealistic parameters.

[e] LP = Large particulate magnetite.

[f] Fixed at 0 during fitting.

[g] Not determined; this value is only available with Voigt based fitting. The reference spectra were fit using Lorentzian models.

[h] A synthetic well crystalline sample (95).

Table 2.1 Continued

[i] Nanoparticulate magnetite (avg. diameter from TEM = 21 nm) produced from oxidizing nanoparticulate Fe metal via exposure to air (110).

[j] Natural large particulate polycrystalline magnetite taken from the Gällivare iron mine (102).

[k] A natural soil sample containing magnetite as a constituent from Huangling, China (111).

[l] Fit using two signals, reported value is the weighted mean of the two sextets.

[m] Large particulate magnetite (particle size > 200 nm) (80).

Table 2.2. Observed pXRD peak locations from magnetite batches with varying stoichiometries. Whole pattern fits of the patterns were used to determine the magnetite unit cell parameter (a).

				Nanoparticulate magnetite (x_d)								
(hkl)	**Ref. 2θ[a]**	**Ref. d (Å)[a]**	**LP (0.50)[b]**	**0.00**	**0.16**	**0.25**	**0.26**	**0.33**	**0.36**	**0.42**	**0.49**	**0.50[d]**
(111)	21.29	4.8426	21.12	B.D.[c]	21.23	21.25	21.24	21.50	B.D.[c]	21.50	21.25	21.25 (0.067)[e]
(220)	35.11	2.9655	34.95	35.17	35.08	35.20	35.02	35.27	34.94	35.20	35.12	34.98 (0.111)
(311)	41.43	2.5289	41.19	41.52	41.38	41.38	41.28	41.56	41.14	41.42	41.38	41.24 (0.092)
(400)	50.50	2.0969	50.27	50.66	50.41	50.31	50.38	50.68	50.22	50.58	50.44	50.33 (0.093)
(422)	62.99	1.7121	62.77	63.31	62.83	63.17	62.79	63.14	63.03	63.06	62.81	62.82 (0.129)
(511)	67.30	1.6142	67.19	67.61	67.49	67.36	67.24	67.54	67.14	67.36	67.24	67.12 (0.092)
(440)	74.21	1.4827	74.01	74.58	74.21	74.20	74.16	74.40	73.96	74.24	74.16	74.02 (0.080)
a fit[f] (Å)		8.3958	8.3876	8.3390	8.3584	8.3662	8.3776	8.3677	8.3852	8.3921	8.3895	8.3942
σ_a[g] (Å)			0.0023	0.0034	0.0028	0.0031	0.0044	0.0029	0.0022	0.0054	0.0023	(0.0046)[e]

[a] Ref. (108)

[b] LP = Large particulate magnetite (x_d, x_{MS} = 0.50)

Table 2.2 Continued

[c] Below detection limit (< 3% of maximum intensity peak).

[d] Values reported are the average of five identically prepared samples. Parenthetic values are the standard deviation between samples.

[e] Parenthetic values are the standard deviation of five replicate samples for $x = 0.50$ magnetite.

[f] Fit done using Jade 6 software (described in the Materials and Methods).

[g] Standard deviation of a from the whole pattern fit.

Table 2.3. Relative peak intensities of fitted pXRD peaks for magnetites with varying stoichiometries (x_d).

			Nanoparticulate magnetite (x_d)								
(hkl)	**Ref.[a]**	**LP[b]**	**0.00**	**0.16**	**0.25**	**0.26**	**0.33**	**0.36**	**0.42**	**0.49**	**0.50[d]**
(111)	8.2	4.4	B.D.[c]	5.0	4.7	5.7	7.4	B.D.[c]	5.2	7.6	10.1 (3.1)
(220)	28.4	23.7	32.5	34.3	24.2	27.9	31.2	22.9	29.9	26.0	25.7 (2.2)
(311)	100.0	100.0	100.0	100.0	100.0	100.0	100.0	100.0	100.0	100.0	100.0 (0.0)
(400)	8.1	23.2	26.6	32.1	27.0	30.9	34.2	29.7	32.4	35.5	30.4 (2.3)
(422)	9.2	7.5	10.0	7.5	8.0	7.6	7.3	10.0	6.5	5.9	7.7 (1.2)
(511)	24.3	31.7	24.8	24.4	25.3	29.9	27.3	40.9	28.4	27.9	29.2 (7.7)
(440)	41.7	30.9	43.9	60.2	45.9	47.8	46.1	69.5	43.6	54.1	49.0 (11.0)

[a] Ref. (108)

[b] LP = Large particulate magnetite (x_d, x_{MS} = 0.50)

[c] Below detection limit (< 3% of maximum intensity peak).

[d] Values reported are the average of five identically prepared samples. Parenthetic values are the standard deviation between samples.

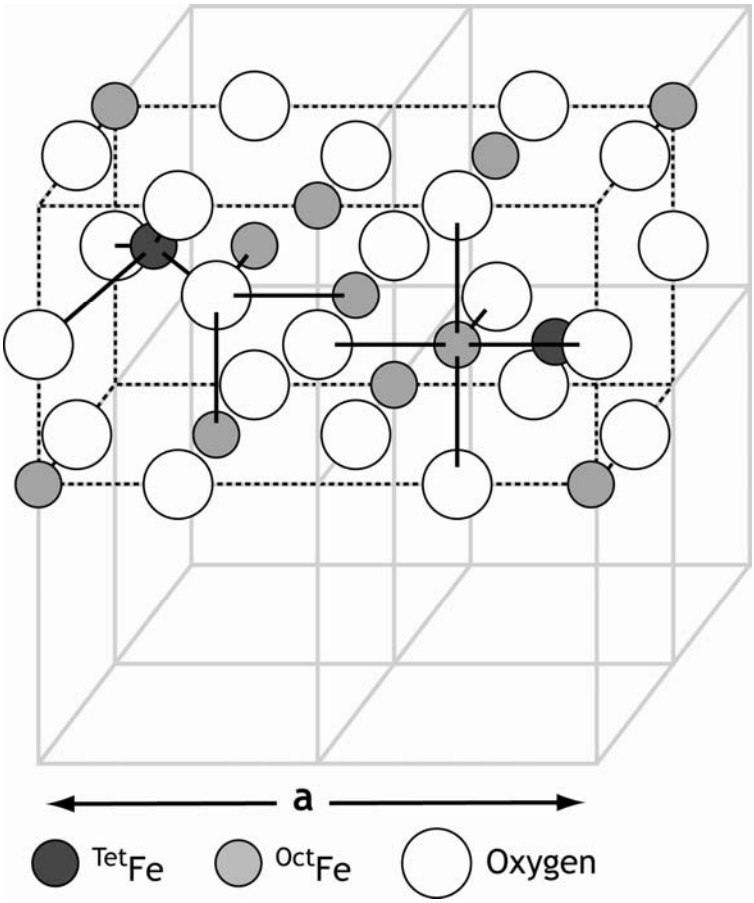

Figure 2.1. A schematic representing a portion of the magnetite (Fe_3O_4) unit cell. Magnetite has an inverse spinel structure, with $^2/_3$ of the Fe atoms in octahedral orientation, and $^1/_3$ in the tetrahedral configuration. $^1/_2$ of the available octahedral vacancies are filled, and $^1/_8$ of the available tetrahedral vacancies are occupied. The whole unit cell contains 16 ^{Oct}Fe atoms, 8 ^{Tet}Fe atoms, and 32 oxygen atoms. Example bonding structures are shown for each atom.

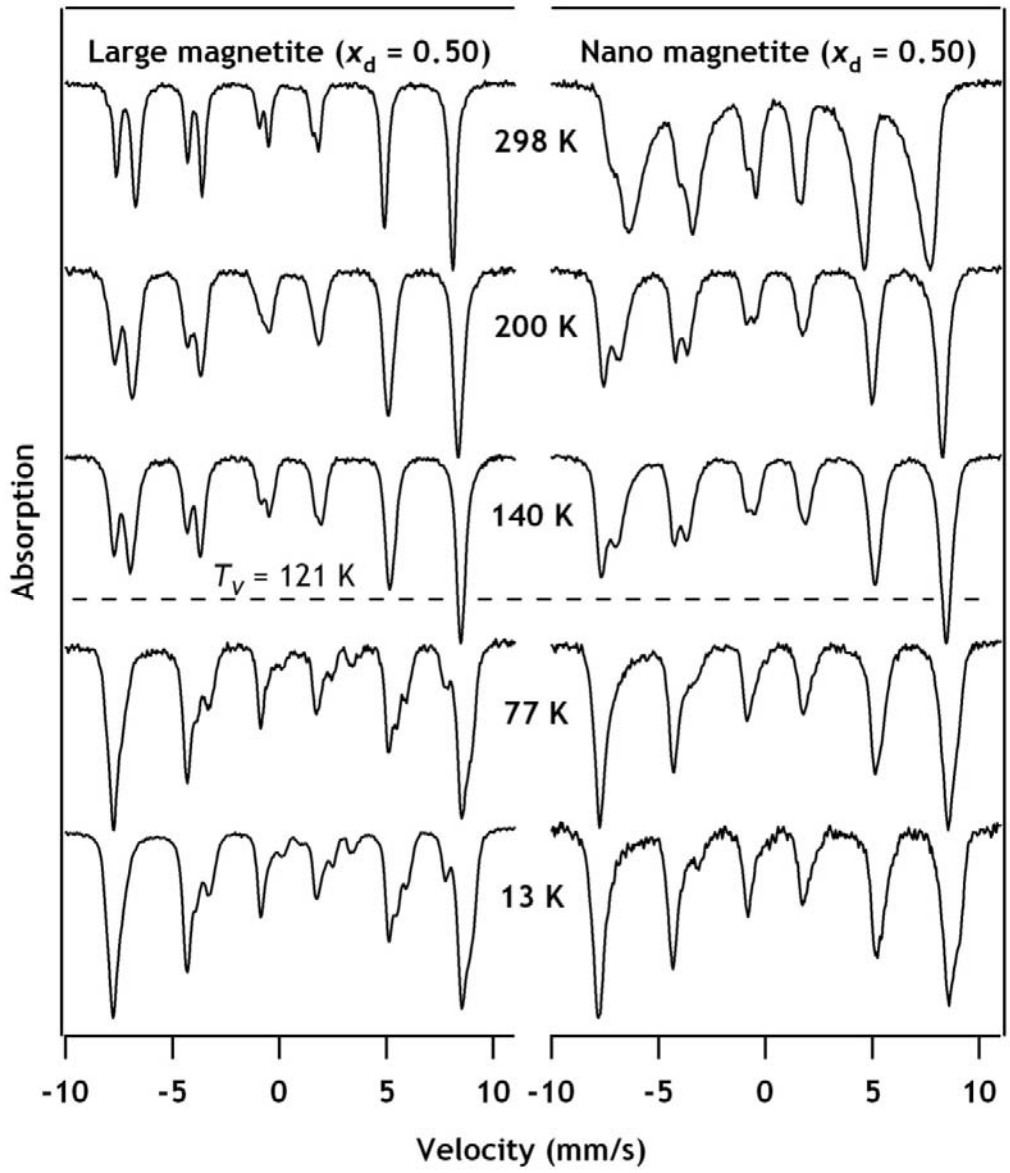

Figure 2.2. Mössbauer spectra of large particulate and nanoparticulate stoichiometric magnetite (x_d = 0.50) at several temperatures (298 K, 200 K, 140 K, 77 K, 13 K).

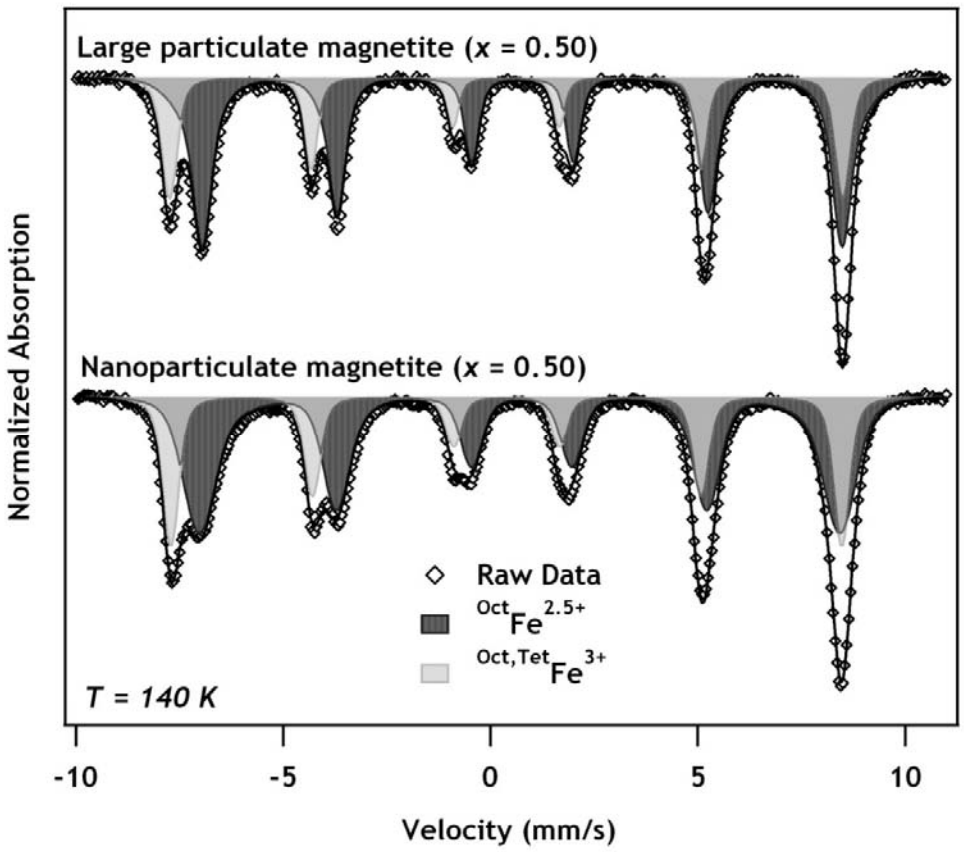

Figure 2.3. Fitted Mössbauer spectra of stoichiometric large particulate magnetite (top) and nanoparticulate magnetite (bottom) collected at 140 K. Fit parameters are shown in Table 2.1.

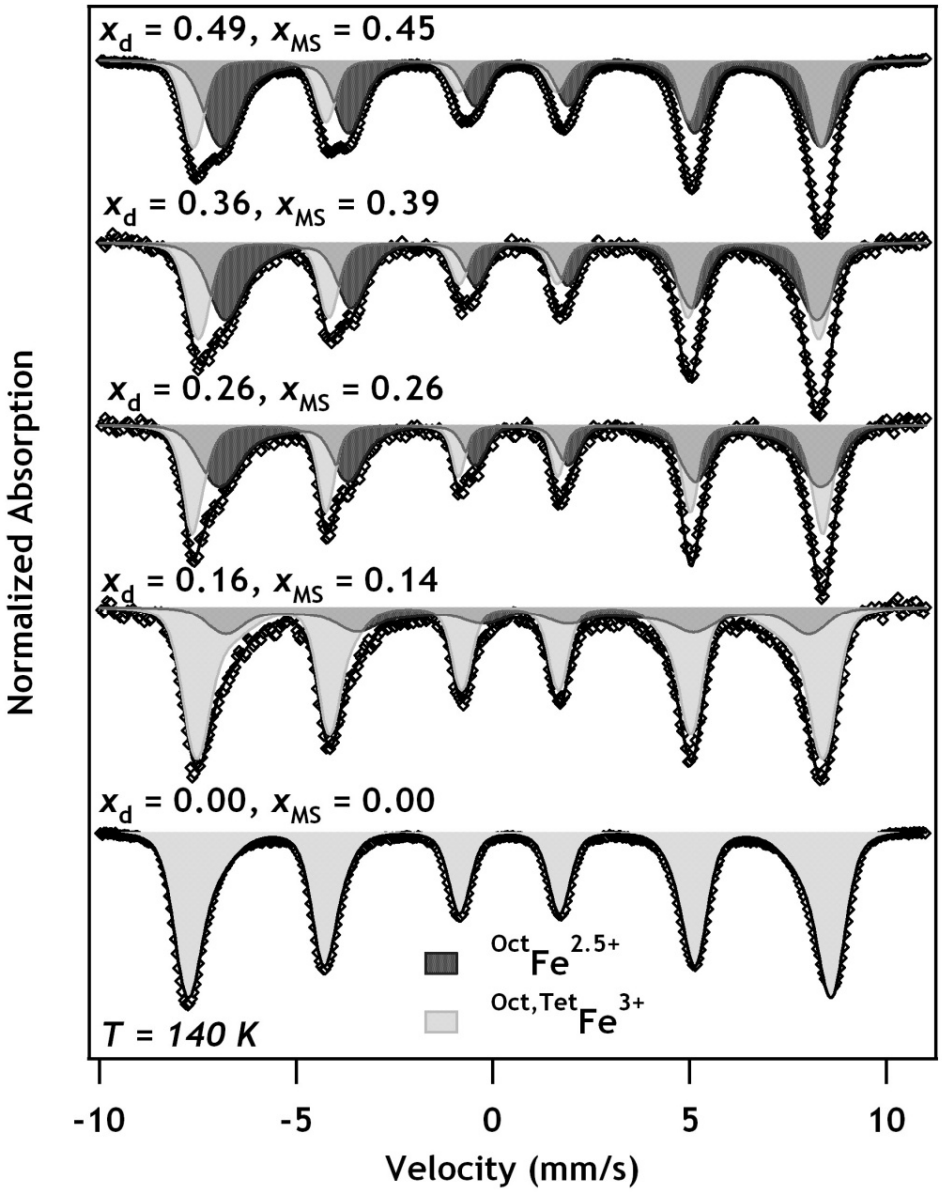

Figure 2.4. Mössbauer spectra of nanoparticulate magnetite with varying stoichiometries ($x = Fe^{2+}/Fe^{3+}$) at 140 K. Fit hyperfine parameters are shown in Table 2.1.

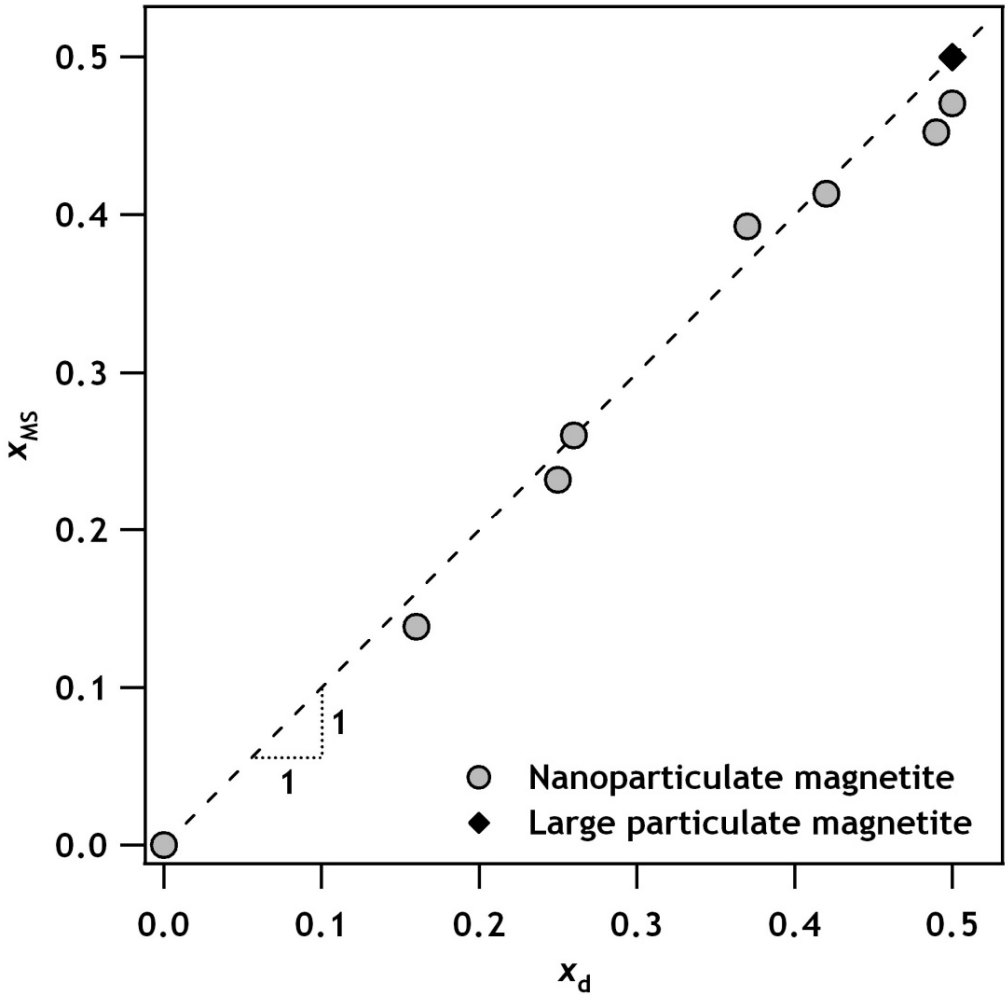

Figure 2.5. Comparison of magnetite stoichiometry determine by Mössbauer spectroscopy and acidic dissolution.

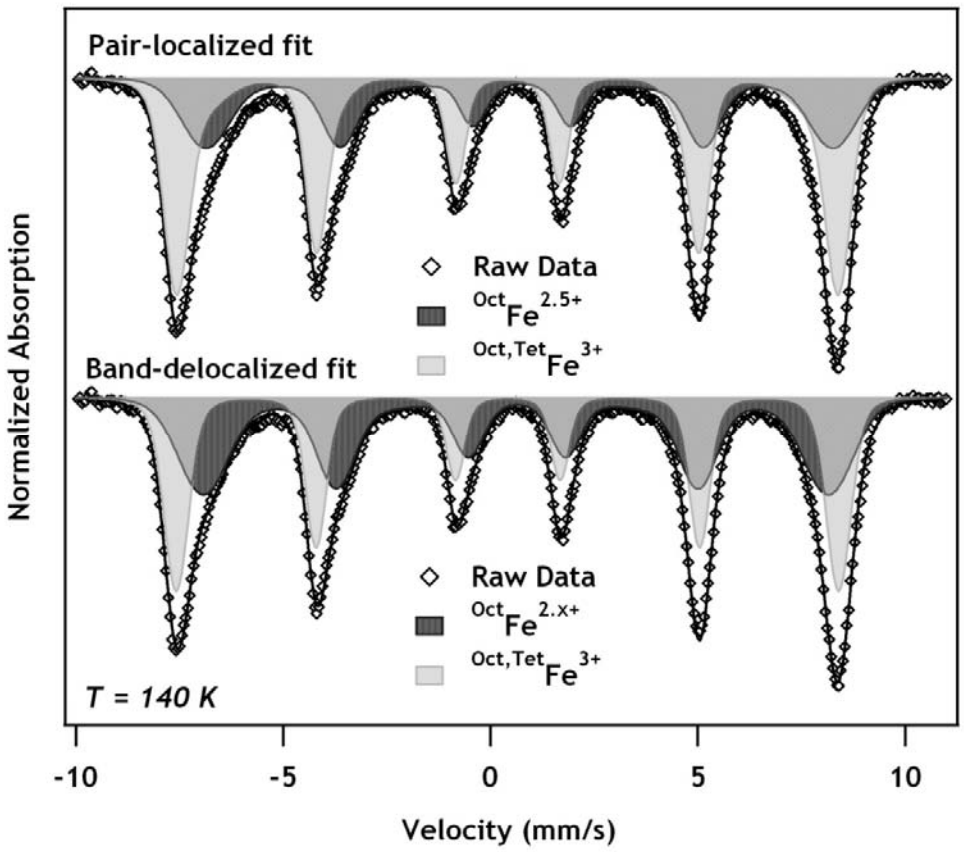

Figure 2.6. Fitted Mössbauer spectra of nonstoichiometric nanoparticulate magnetite (x_d = 0.22) collected at 140 K. The pair-localized fit assumes a CS of 0.72 mm/s, while the band-delocalized spectrum allows the CS to float (0.62 mm/s).

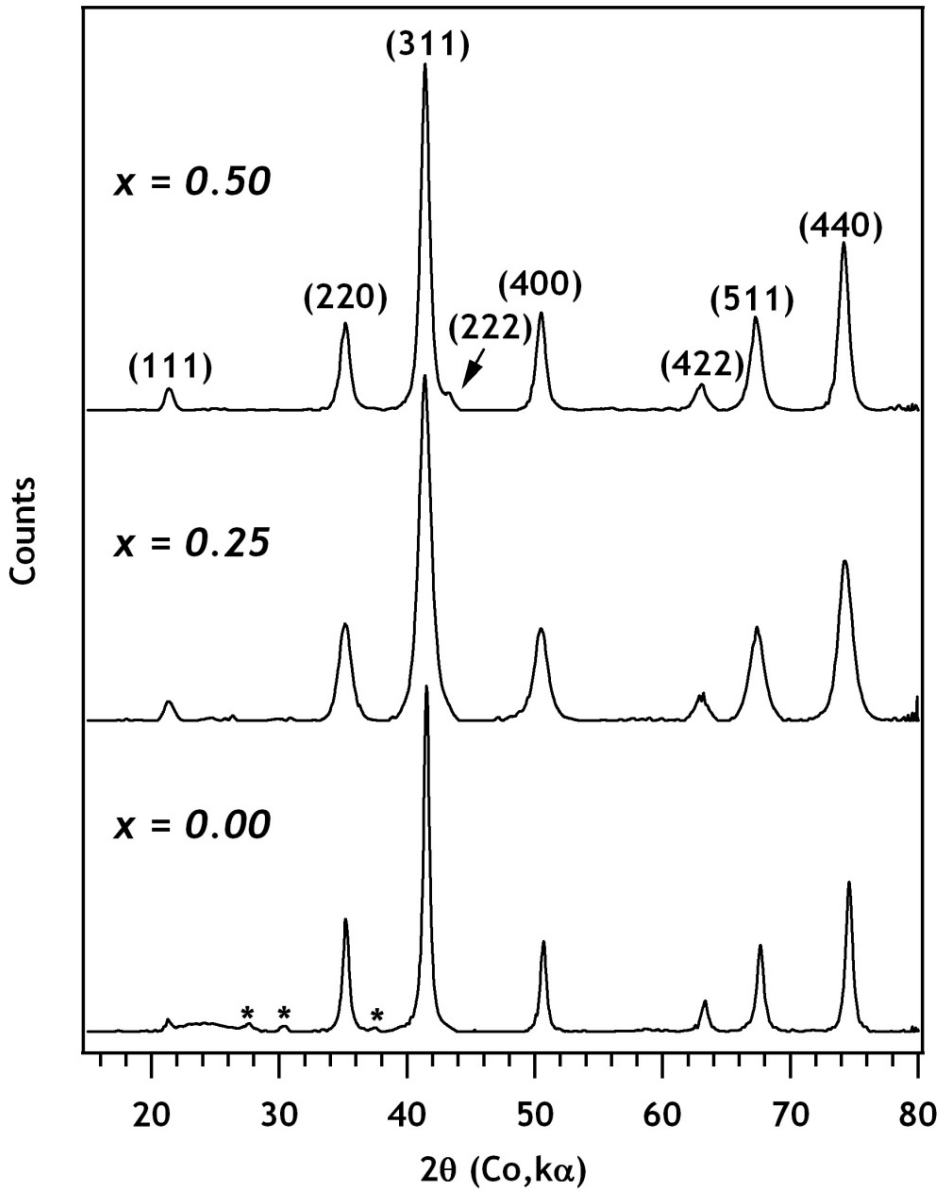

Figure 2.7. Powder X-ray diffraction of nanoparticulate stoichiometric (x = 0.50), significantly oxidized (x = 0.25), and completely oxidized (x = 0.00) magnetite. The patterns have been smoothed, background subtracted, and $k\alpha_2$ stripped to aid in interpretation. The eight most intense diffraction peaks are labeled with respect to their crystallographic planes (hkl). Stars (*) denote additional peaks observed in the completely oxidized sample.

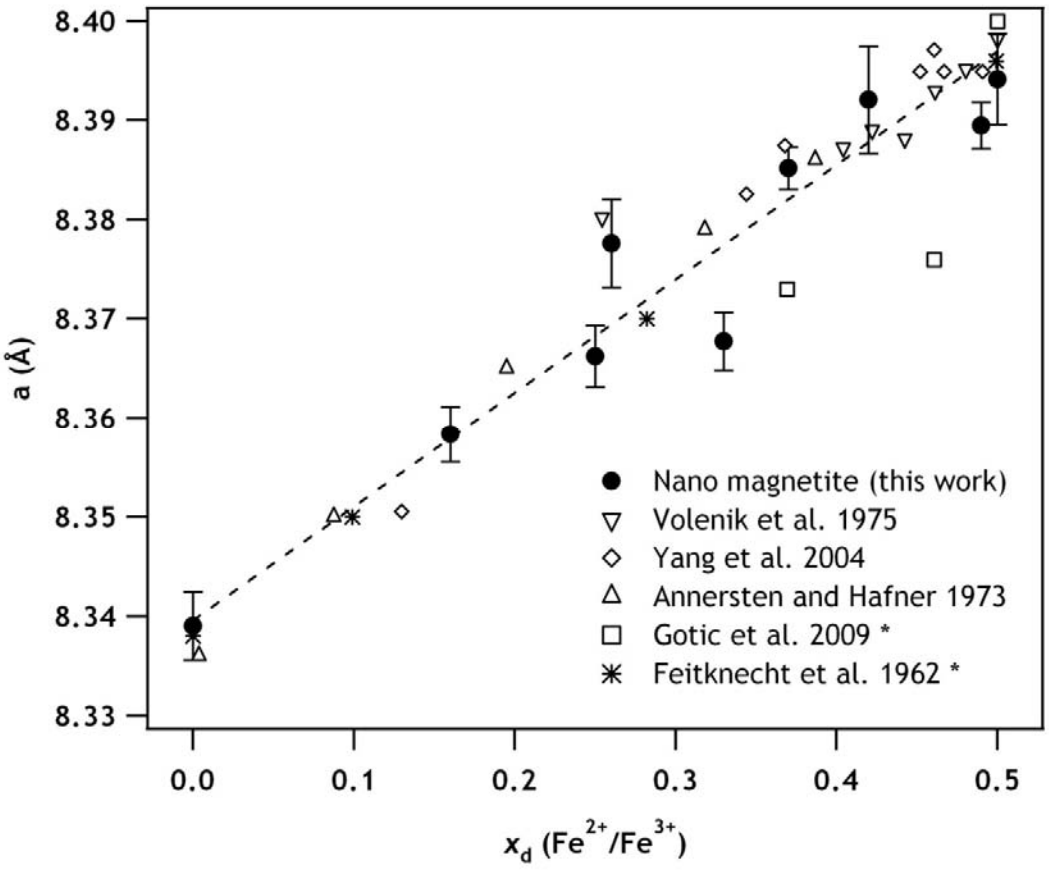

Figure 2.8. Unit cell length of magnetite derived from fitting pXRD patterns at varying stoichiometries (x_d). Error bars shown are the standard deviations provided from the full pattern fit. The black marker is the average of five identically prepared samples (x_d = 0.50), with the error bars calculated from the standard deviation of the five computed a values. The fit shown is a = 0.1148(±0.0055)x_d + 8.3396(±0.0020); R^2 = 0.93; n = 35. For literature values, *x* was determined by acidic dissolution except for samples denoted with a star (*), in which the stoichiometry was determined using Mössbauer spectroscopy.

CHAPTER III: INFLUENCE OF MAGNETITE STOICHIOMETRY ON Fe^{II} UPTAKE AND NITROBENZENE REDUCTION

Abstract

Magnetite (Fe_3O_4) is a common biomineralization product of microbial iron respiration and is often found in subsurface anoxic environments, such as groundwater aquifers where aqueous Fe^{II} is present. We investigated the reaction between aqueous Fe^{II} and magnetite using the isotopic selectivity of ^{57}Fe Mössbauer spectroscopy and revisited the reduction of nitrobenzene by magnetite. Similar to our previous findings with Fe^{3+} oxides, we did not observe the formation of a stable sorbed Fe^{II} species; instead, we observed oxidation of the Fe^{II} to a partially oxidized magnetite phase. Oxidation of Fe^{II} was accompanied by reduction of the octahedral Fe^{3+} atoms in the underlying magnetite to octahedral Fe^{2+} atoms. The lack of a stable, sorbed Fe^{II} species on magnetite prompted us to re-evaluate what is controlling the extent of Fe^{II} uptake on magnetite, as well as contaminant reduction in the presence of magnetite and Fe^{II}. Uptake of Fe^{II} by magnetite appears to be limited by the stoichiometry of the magnetite particles, rather than the surface area of the particles. More oxidized (or less stoichiometric) magnetite particles take up more Fe^{II}, with the formation of stoichiometric magnetite (Fe^{2+}/ Fe^{3+} = 0.5) limiting the extent of Fe^{II} uptake. We also show that stoichiometric magnetite, in the *absence* of aqueous Fe^{II}, can rapidly reduce nitrobenzene. Based on these results, we speculate that contaminant reduction that was previously attributed to Fe^{II} sorbed on magnetite is really due to a process similar to negative (*n*) doping of a solid, which increases the stoichiometry of the magnetite and alters the redox properties of the particle to make reduction more favorable.

C.A. Gorski M.M. Scherer. Influence of magnetite stoichiometry on Fe^{II} uptake and nitrobenzene reduction. *Environmental Science and Technology.* 2009, *43*, 3675-3680.

Introduction

Magnetite (Fe_3O_4) is a mixed-valent iron mineral that is ubiquitous in the environment as both a primary and secondary mineral phase (*1*). Magnetite can form via the reduction of Fe^{3+} oxides by dissimilatory iron reducing bacteria (DIRB) and aqueous Fe^{II} (1, 43, 45, 84, 85), and can also form by the oxidation of ferrous minerals and iron metal from both natural and anthropogenic sources (1, 37). Magnetite has widespread industrial uses (such as digital recording and drug delivery) because of its unique electronic, magnetic, structural, and redox properties (1, 17, 37, 54, 63).

Magnetite has been implicated as a potentially important reductant of environmental contaminants in Fe-rich subsurface environments. In the laboratory, chemically synthesized magnetite has been shown to reduce several contaminants, including carbon tetrachloride (CCl_4) (46, 47), hexavalent chromium (Cr^{VI}) (48), hexavalent uranium (U^{VI}) (49), and several other compounds (e.g., 17). In addition to chemically synthesized magnetite, biologically produced magnetite formed from microbial respiration of Fe^{3+} oxides has been shown to reduce carbon tetrachloride (CCl_4) (43). In the field, magnetite has been suggested as the dominant reductant of *cis*-dichloroethene (cis-DCE) in a chlorinated ethene plume at the Twin Cities Army Ammunition Plant (TCAAP) in Minnesota (50).

Surprisingly, magnetite has been shown to be relatively unreactive toward nitroaromatics, even though the reaction is thermodynamically favorable (14, 51). Addition of aqueous Fe^{II} to magnetite suspensions, however, resulted in rapid reduction of nitroaromatics, which was attributed to the formation of reactive surface Fe^{II} complexes (14, 51). For other contaminants, the addition of aqueous Fe^{II} appears to have varying effects, from no effect observed on the rate of chlorinated ethenes by magnetite (73), to a significant increase in the reported rate and extent of Cr^{VI} reduction (112). These inconsistencies reveal a significant gap in our understanding of the reaction of

aqueous Fe^{II} with magnetite, and how it influences rates of contaminant reduction by magnetite.

Recent work by our group, as well as others, has shown that the reaction of aqueous Fe^{II} with Fe^{3+} oxides is complex and involves sorption, electron transfer, and, in some cases, dissolution and secondary mineral transformation (22, 24, 26, 45). Similarly, Tronc and co-workers have shown that electron transfer occurs between Fe^{II} and magnetite using X-ray diffraction techniques (52, 85). Magnetite is markedly different from the Fe^{3+} oxides in that it contains both Fe^{2+} and Fe^{3+} in an inverse-spinel structure, where iron atoms occupy octahedral (Oct) and tetrahedral (Tet) sites in a 2:1 ratio. The Fe^{2+} content in magnetite is well known to dramatically alter its physical properties, including redox potential and conductivity (54, 62, 63). The influence of Fe^{2+} content, or the stoichiometry of magnetite (eq. 3.1), on Fe^{II} uptake and contaminant reduction rates, however, remains unclear despite compelling evidence that it affects the redox properties of magnetite (54).

$$x = \frac{Fe^{2+}}{Fe^{3+}} = \frac{{}^{Oct}Fe^{2+}}{{}^{Oct}Fe^{3+} + {}^{Tet}Fe^{3+}} \qquad (3.1)$$

Here, we investigated the reaction of aqueous Fe^{II} with magnetite to evaluate the influence of magnetite stoichiometry (x) on the capacity of magnetite to uptake Fe^{II} and to reduce nitrobenzene. We aimed to examine 'sorbed Fe^{II}' on magnetite spectroscopically, and determine the roll that this species had on reactivity with environmental contaminants. We found that stable, sorbed Fe^{II} species do not exist under the conditions of this study; instead, electron transfer occurs between the Fe^{II} and the underlying magnetite, similar to what we previously observed for Fe^{3+} oxides (24, 26). The extent of Fe^{II} uptake as well as the rate of nitrobenzene reduction appear to be determined by the initial stoichiometry (x) of the magnetite. To clarify our discussion, we use Roman numerals (e.g., Fe^{II}) to denote dissolved and adsorbed metal species, and Arabic numerals (e.g., Fe^{2+}) to indicate structural metal species.

Experimental Section

Magnetite Synthesis and Characterization

Magnetite was synthesized using methods to control both particle size and stoichiometry. In order to make small stoichiometric magnetite (~20 nm), a 1:2 Fe^{II}:Fe^{III} solution was prepared under anoxic conditions, then titrated to an alkaline pH (> 10) with NaOH and allowed to mix overnight (113). For partially oxidized magnetite, this solution was exposed to various amounts of H_2O_2 and allowed to equilibrate at least one additional day. Magnetite (x = 0.41 batch) was also synthesized by modifying the methods of Cornell and Schwertmann, specifically by oxidizing an alkaline anoxic Fe^{II} solution with nitrate at room temperature (*1*). For both syntheses, batches of magnetite were filtered anaerobically, with minimal washing to remove excess salts. It was found when synthesizing stoichiometric magnetite that excessive washing (> 2 rinse cycles) caused the magnetite to become oxidized, as structural-Fe^{2+} was removed in the rinse. Solids were freeze-dried, sieved anaerobically (100 mesh), and stored in an anaerobic glove box until use.

The particles synthesized using both techniques provided similar particle morphologies from transmission and scanning electron microscopy (TEM & SEM), similar BET surface areas (62 ± 8 m^2g^{-1}; n = 4), and indistinguishable primary crystallite sizes (~11 nm) using the Scherrer equation with powder X-ray diffraction (pXRD) patterns. BET specific surface areas were x = 0.28 (63 m^2g^{-1}), x = 0.33 (72 m^2g^{-1}), x = 0.41 (54 m^2g^{-1}), and x = 0.48 (58 m^2g^{-1}). A representative TEM image of the magnetite is shown in Figure A.1. Precautions were taken to avoid oxidation for all analyses, by storing samples in airtight vessels prior to analysis and by mixing pXRD samples with glycerol. ^{57}Fe Mössbauer spectroscopy was used to characterize the particles, as well as determine the stoichiometry from the relative areas of Mössbauer spectra ($x_{Mössbauer}$). Details of the fitting procedures used can be found in Appendix A. Magnetite

stoichiometry was also measured by complete dissolution of solids in 5 M HCl in an anaerobic glovebox ($x_{dissolution}$). Solids were allowed to dissolve for about two days, followed by measuring Fe^{II} and total Fe by the phenanthroline method (89).

Fe^{II} Uptake Experiments

All experiments were done in batch reactors in a N_2/H_2 glove box. Experiments with Fe^{II} were done in 50 mM 3-(N-morpholino)propanesulfonic acid buffer (MOPS, pK_a 7.2) adjusted to pH 7.2 with a solids loading of 1 g/L. Fe^{II} was equilibrated in solution overnight, and the solution was filtered through a 0.2 µM filter prior to the addition of solids in order to remove trace Fe^{III} and precipitated $Fe(OH)_2$. An initial Fe^{II} concentration was measured prior to the addition of the magnetite solids. The solids were then allowed to equilibrate with solution for 24 hours, then the solution was filtered (0.2 µM), and the final Fe^{II} concentration was measured. Kinetic experiments indicated that the Fe^{II} concentration was stable after 24 hours (data not shown).

Isotope Selective Mössbauer Spectroscopy

Isotopically enriched magnetite was synthesized from ^{56}Fe metal from Chemgas (Boulogne, France). A 1:2 Fe^{II}:Fe^{III} solution was created by dissolving ^{56}Fe metal in 1 M HCl, then dividing the solution into two portions and oxidizing the Fe^{III} component with a calculated amount of H_2O_2 prior to titrating to an alkaline pH. pXRD indicated that the solids collected were indistinguishable from solids prepared identically from isotopically normal Fe metal and as expected, the ^{56}magnetite gave little Mössbauer signal (Figure A.2). Sorption experiments were performed with a $^{57}Fe^{II}$ stock solution, with the solids collected after a 24-hour equilibration period for Mössbauer analysis. Similarly, naturally abundant magnetite (~2.2% ^{57}Fe) was exposed to a $^{56}Fe^{II}$ solution, with Mössbauer analysis performed on the filtered solids at a series of temperatures. Mössbauer spectroscopy measurements were made using the same system described in our previous work (26).

Nitrobenzene Reduction Experiments

Suspensions of 1 g/L magnetite at pH 7.2 were equilibrated for one hour prior to the addition of 40 µM nitrobenzene. Aqueous nitrobenzene and aniline concentrations were measured after reaction with magnetite using high-pressure liquid chromatography (HPLC) as previously described (24).

Results and Discussion

Mössbauer Spectroscopy of Fe^{II} Reacted with Magnetite

Similar to our previous approach with Fe^{3+} oxides (24, 26), we used isotopically labeled $^{57}Fe^{II}$ and ^{56}magnetite to investigate the fate of Fe^{II} after reaction with magnetite. The ^{56}magnetite alone results in negligible Mössbauer signal because ^{56}Fe is transparent to ^{57}Fe Mössbauer spectroscopy (Figure A.2). After reacting the ^{56}magnetite particles with $^{57}Fe^{II}$ (200 µM, ~1.6% total Fe), The Mössbauer spectrum of the solids revealed one primary sextet and one small secondary sextet that appears as a shoulder on the primary sextet. Both sextets are characteristic of magnetite spectra collected at temperatures above the Verwey transition temperature of 121 K (Figure 3.1A) (102, 111). Formation of a magnetite-like phase indicates that some of the $^{57}Fe^{II}$ was oxidized. No evidence for a sorbed or precipitated Fe^{2+} phase was observed. The sextet comprising most of the spectral area (≈ 79%) has a center shift (CS) and hyperfine splitting (H) consistent with $^{Tet}Fe^{3+}$ sites in magnetite (Table 3.1). The second, smaller sextet (≈ 21%) is consistent with $^{Oct}Fe^{2+}$ and $^{Oct}Fe^{3+}$ sites, which appear as one sextet with an average valence state of 2.5 (because the electron hopping rate between octahedral sites is faster than the Mössbauer characteristic time of about 10^{-8} s) (80).

Although the Mössbauer parameters of the two sextets are consistent with magnetite, the relative spectral areas indicate that the sample is oxidized relative to stoichiometric magnetite. A solid solution can exist between magnetite and maghemite ($0 < x < 0.5$), which can be referred to as non-stoichiometric magnetite, or partially oxidized

magnetite (82). A spectrum of nearly stoichiometric magnetite is shown in Figure 3.1B to illustrate the spectral differences between partially oxidized magnetite and stoichiometric magnetite. Stoichiometric magnetite ($x = 0.5$) contains two-thirds Fe^{3+} and one-third Fe^{2+}, resulting in 67% of the spectral area associated with the $^{Oct}Fe^{2.5+}$ sextet and 33% of the spectral area associated with the $^{Tet}Fe^{3+}$ sextet. The phase formed from oxidation of $^{57}Fe^{II}$ by ^{56}magnetite has significantly more $^{Tet}Fe^{3+}$ area (≈ 79% compared to 33%) and less $^{Oct}Fe^{2.5+}$ area (≈ 21% compared to 67%). Growth of the $^{Tet}Fe^{3+}$ sextet coupled with reduction of the $^{Oct}Fe^{2.5+}$ sextet results from the formation of unpaired $^{Oct}Fe^{3+}$ sites, which are indistinguishable from the $^{Tet}Fe^{3+}$ sites above the Verwey temperature (80, 82). The relative spectral areas can be used to calculate the stoichiometry of the phase, which results in a calculated Fe^{2+}/Fe^{3+} ratio ($x_{Mössbauer}$) of 0.12 for this spectra, which is significantly oxidized compared to stoichiometric magnetite ($x = 0.5$).

Whether this oxidized magnetite phase is a mixture of magnetite and maghemite or a solid solution of partially oxidized magnetite is difficult to determine and distinguishing between the two has been a controversial topic for many years (80-82, 92). Formation of a partially oxidized magnetite rather than a mixture of magnetite and maghemite is, however, consistent with a previous study using integrated low-energy electron Mössbauer spectroscopy (ILEEMS), a surface-sensitive Mössbauer technique, to show that non-stoichiometric magnetite has chiefly an Fe^{3+} surface coating, with little Fe^{2+} (114). Regardless of whether this phase is a mixture of magnetite and maghemite or a solid solution of partially oxidized magnetite, it is clear that it is a predominantly Fe^{3+} phase (79%), which indicates that most of the $^{57}Fe^{II}$ taken up was oxidized, similar to our previous findings of $^{57}Fe^{II}$ oxidation by goethite, hematite, and ferrihydrite (24, 26). Fe^{II} uptake accompanied by growth of a magnetite outer shell is also consistent with the structural model proposed by Tronc et al. based on acid-base titrations and structural modeling of pXRD patterns (52).

To investigate if the underlying magnetite particle is reduced after reaction with aqueous Fe^{II}, we reacted magnetite with aqueous $^{56}Fe^{II}$. Using $^{56}Fe^{II}$, rather than $^{57}Fe^{II}$, allowed us to track the redox changes to the underlying magnetite particles without interference from the reacted Fe^{II}. Mössbauer spectra of non-stoichiometric magnetite before and after reaction with $^{56}Fe^{II}$ are shown in Figure 3.2. Two magnetite sextets, similar to those in Figure 3.1, are observed in both spectra, but there is a distinct shift in the relative areas of the sextets after reaction with $^{56}Fe^{II}$. The area of the $^{Oct}Fe^{2.5+}$ sextet increases by 12% after reaction with $^{56}Fe^{II}$, indicating that some of the $^{Oct}Fe^{3+}$ atoms have been reduced. The 12% increase in the $^{Oct}Fe^{2.5+}$ sextet is accompanied by an 11% decrease in the $^{Oct}Fe^{3+}$ sextet (Table 3.1). The shift to more $^{Oct}Fe^{2.5+}$ sites and less $^{Oct}Fe^{3+}$ indicates that $^{Oct}Fe^{3+}$ in the magnetite lattice was reduced by the $^{56}Fe^{II}$.

Consistent with the structural data of Tronc et al. (52), the Mössbauer spectra indicate that Fe^{II} reduces structural $^{Oct}Fe^{3+}$ atoms in magnetite forming more stoichiometric magnetite with no indication in the spectra that stable Fe^{II} surface-complexes or secondary Fe^{2+} precipitates have formed. Tronc et al. further proposed that the electrons injected into magnetite could (*i*) stabilize as $^{Oct}Fe^{2+}$-Fe^{3+} pairs or (*ii*) delocalize in the conduction band of the magnetite. The good agreement between the observed shifts in spectral area (about 12% between the $^{Oct}Fe^{2.5+}$ and $^{Oct}Fe^{3+}$ sextets) and the estimated change in spectral area based on loss of Fe^{II} from solution (see Supporting Information, Appendix A for details of the calculation), suggests that the electrons localize as $^{Oct}Fe^{2+}$-Fe^{3+} pairs. The change in the spectral area would be much greater than the calculated change if the electrons had become delocalized, similar to what we observed previously in hematite (27); furthermore, we expect that the Mössbauer parameters (CS and H) would have changed more significantly if electrons were conducting through the solids (66). Stabilization of the injected electrons as $^{Oct}Fe^{2+}$-Fe^{3+} pairs to form more stoichiometric magnetite raises the interesting question of whether the

uptake of Fe^{II} from solution is limited by the initial Fe^{2+} content of the magnetite particles.

Effect of Magnetite Stoichiometry on Fe^{II} Uptake

To evaluate whether the capacity for Fe^{II} uptake on magnetite is influenced by particle stoichiometry, we measured Fe^{II} uptake on magnetite powders with Fe^{2+}/Fe^{3+} ratios (x) ranging from 0.28 to 0.48 (Figure 3.3). For comparison with previous work, we present the data as traditional sorption isotherms; note, however, that our Mössbauer data clearly indicate that Fe^{II} taken up by magnetite is not stable and that electron transfer between Fe^{II} and $^{Oct}Fe^{3+}$ in magnetite occurs. Among the four magnetite powders, the extent of Fe^{II} uptake varies widely despite similar BET surface areas (62 ± 8 m^2g^{-1}). The least stoichiometric magnetite (i.e., the most oxidized magnetite with $x = 0.28$) resulted in an Fe^{II} uptake up to 1500 µmole/g and the most stoichiometric magnetite ($x = 0.48$) took up only 370 µmole/g. In all cases, the maximum amount of Fe^{II} uptake exceeded the estimated monolayer coverage of 300 µmole/g magnetite (shown as a dashed line in Figure 3.3). Mössbauer spectra collected at similar $^{57}Fe^{II}$ concentrations (3 mM) on ^{56}magnetite confirmed that no Fe^{2+} precipitation occurred at the higher initial Fe^{II} concentrations (data not shown).

Greater than expected Fe^{II} uptake on non-stoichiometric magnetite is consistent with previous work comparing the uptake of Fe^{II} and Co^{II} on magnetite under similar conditions (52, 85). Co^{II} uptake behavior was well described by a surface complexation model, with a rapid, one-step, reversible adsorption reaction, whereas Fe^{II} uptake was three times greater than Co^{II} and could not be adequately described by adsorption. Tronc and co-workers proposed an alternative to one-step, reversible adsorption for Fe^{II} that suggested that the capacity of magnetite to take up Fe^{II} would be determined by the initial Fe^{2+} content of the particle, rather than surface area, similar to what we observed in Figure 3.3 (52, 85). Indeed, a plot of the maximum amount of Fe^{II} uptake versus the

initial magnetite stoichiometry reveals a significant linear relationship (R^2 = 0.98; n=4; Figure A.3), indicating that as the Fe^{2+} content of magnetite increases (as x approaches 0.5), less Fe^{II} uptake is observed, as predicted by Tronc and co-workers.

To confirm that Fe^{II} uptake is limited by the formation of stoichiometric magnetite, we measured the stoichiometry of the particles after complete dissolution in acid ($x_{dissolution}$) along the isotherms shown in Figure 3.3. Strikingly, all four Fe^{II} isotherms begin to plateau at about x = 0.5 ($x_{dissolution}$ = 0.51 ± 0.01, n = 4), providing compelling evidence to support Tronc and co-workers' proposal that the capacity for magnetite to uptake Fe^{II} is determined by the initial Fe^{2+} content. The extent of Fe^{II} uptake also agrees reasonably well with the calculated amount of Fe^{II} needed to reach stoichiometry (Figs. S3, S4, calculation in Supporting Information, Appendix A).

The significant influence of structural Fe^{2+} content (i.e., magnetite stoichiometry) on the extent of Fe^{II} uptake may explain why reports of Fe^{II} uptake on magnetite vary so much in the literature. Several studies have reported extensive uptake of Fe^{II} on magnetite (14, 51, 52) and, based on our results, we suspect that the magnetite particles in these studies were partially oxidized (x < 0.5). As an illustration, we plotted the isotherm collected by Klausen et al. (14) on Figure 3.3, and it falls somewhere between our x = 0.33 and x = 0.41 magnetite powders, implying that the particles may have been partially oxidized. In other studies where little uptake (31) or even net release of Fe^{II} (12) was observed, we suspect that the particles were less oxidized and closer to stoichiometric magnetite. At this point, however, magnetite stoichiometries are not reported in most of these studies, so we can only hypothesize that differences in magnetite stoichiometry are responsible for the discrepancies in reported amounts of Fe^{II} uptake on magnetite.

Nitrobenzene Reduction by Magnetite

To explore whether particle stoichiometry might also influence rates of contaminant reduction by magnetite, we measured the rate of nitrobenzene ($ArNO_2$)

reduction and the production of aniline ($ArNH_2$) by both non-stoichiometric magnetite (x = 0.31) and nearly stoichiometric magnetite (x = 0.48) (Figure 3.5). The nearly stoichiometric magnetite reduced nitrobenzene to aniline in less than an hour, with a first-order rate coefficient, k_{obs}, of 0.20 min^{-1}. In contrast, non-stoichiometric magnetite with a lower Fe^{2+} content resulted in negligible nitrobenzene reduction over the time scales of a few hours. We did observe some reduction of nitrobenzene by non-stoichiometric magnetite over longer time scales, with a first-order rate coefficient that was five orders of magnitude (k_{obs} = 5.36 x 10^{-6} min^{-1}) smaller than what we observed for the more stoichiometric magnetite (Figure A.5). Our results indicate that magnetite is capable of reducing nitrobenzene, but that the rate of reduction can span several orders of magnitude depending on the stoichiometry of the particle. At this point, it is unclear whether reduction rates are limited by a charge transfer process, such as a change in redox potential of the magnetite (e.g., 60), or a mass transfer process, such as diffusion of electrons through the magnetite structure (e.g., 46).

Our observation of nitrobenzene reduction by magnetite *in the absence* of added Fe^{II} is not consistent with previous work by Klausen et al. (14). We suspect, however, based on the Fe^{II} uptake data in Figure 3.3, that the magnetite used by Klausen et al. (14) was partially oxidized. Addition of Fe^{II} to a suspension of non-stoichiometric magnetite will result in the formation of stoichiometric magnetite (via electron transfer from the Fe^{II} to $^{Oct}Fe^{3+}$ sites in magnetite as shown in our Mössbauer and isotherm data). If this is the case, then non-stoichiometric magnetite reacted with Fe^{II} should reduce nitrobenzene at rates similar to stoichiometric magnetite. Indeed, after reaction with Fe^{II}, the magnetite used by Klausen et al. reduced nitrobenzene almost as fast as our stoichiometric magnetite (k_{obs} = 0.187 min^{-1} compared to 0.20 min^{-1}) despite different experimental conditions (14). We further tested this hypothesis by exposing non-stoichiometric magnetite (x = 0.31) to aqueous Fe^{II} and measuring the particle stoichiometry and rate of nitrobenzene reduction after removing aqueous Fe^{II}. Similar to what we observed in

Figure 3.4, the non-stoichoimetric magnetite became more stoichometric after reaction with Fe^{II} ($x_{dissolution}$ of 0.49). The stoichiometric magnetite created by reacting non-stoichiometric magnetite with Fe^{II} also reduced nitrobenzene at rates comparable to that of nearly stoichiometric magnetite with an initial *x* of 0.48 (k_{obs} = 0.20 min^{-1} compared to 0.21 min^{-1}) (Figure 3.5).

The similarity in rates of nitrobenzene reduction by stoichiometric magnetite and non-stoichiometric magnetite reacted with Fe^{II} indicates that particle stoichiometry (*x*), or Fe^{2+} content, is critical to predicting rates of contaminant reduction by magnetite. Based on our Mössbauer and isotherm data, it is clear that Fe^{II} is oxidized by magnetite and electrons are transferred into the underlying magnetite particle, a process that we propose is similar to negative (*n*) doping of a semiconductor particle (e.g., 115). The process of *n*-doping the non-stoichiometric magnetite particles by reaction with Fe^{II} results in more stoichiometric magnetite that is more facile at reducing nitrobenzene.

Implications for Magnetite Reactivity in the Environment

The significant influence of stoichiometry on the rate of nitrobenzene reduction observed here raises the interesting questions of (*i*) what is the stoichiometry of magnetite found in the environment, and (*ii*) what is the potential for contaminant reduction? Under iron-reducing conditions, magnetite has been shown to form from the reaction of Fe^{II} with other iron oxides (i.e., ferrihydrite, maghemite, lepidocrocite) (1, 44, 45, 84, 85), as well as from reduction by dissimilatory iron reducing bacteria (DIRB) (43). Based on our results here, it seems likely that in the presence of DIRB or aqueous Fe^{II}, stoichiometric magnetite would prevail; however, in two studies examining natural samples of magnetite found in the environment, the magnetite appeared to be significantly oxidized (*x* = 0.23 to 0.34) (102, 111).

The presence of excess Fe^{II} and DIRB has been shown to increase the kinetics of reduction by magnetite for nitroaromatics (14, 51), carbon tetrachloride (43, 116), and

Cr^{VI} (112). Under oxic conditions, however, magnetite will likely be oxidized by O_2, which may significantly inhibit rates of contaminant reduction. For example, Peterson et al. showed that exposing magnetite to air for various amounts of time (i.e., months) significantly slowed the rate of Cr^{VI} reduction (117). These results suggest that the presence of magnetite in natural environments may not be as important for contaminant reduction as the presence of an active reductant that can effectively "recharge" the magnetite (i.e., aqueous Fe^{II} or DIRB).

Table 3.1. Mössbauer parameters for magnetite and magnetite reacted with isotopically enriched aqueous Fe^{II}. Literature values for natural magnetite at similar temperatures are shown for reference.

	Sample	$^{Oct}Fe^{2.5+}$					$^{Tet}Fe^{3+}$, $^{Oct}Fe^{3+}$				$x_{Mössbauer}$ [g]
		Temp. (K)	CS (mm/s)	ε (mm/s)	H (T)	Area (%)	CS (mm/s)	ε (mm/s)	H (T)	Area (%)	
Figure 3.1	$^{57}Fe^{II}$ + ^{56}Magnetite[b]	140	0.72[c]	0.00	46.2	21.1	0.42	0.00	48.8	78.9	0.12
	Magnetite[a]	140	0.72	-0.02	46.6	63.0	0.37	0.00	49.5	37.0	0.46
Figure 3.2	Magnetite[d]	140	0.74	-0.02	46.0	52.9	0.37	0.00	48.8	47.1	0.36
	$^{56}Fe^{II}$ + Magnetite[e]	140	0.72	-0.02	46.3	65.3	0.36	0.00	49.5	35.7	0.48
Reference[h]	(102)	120	0.77	0	48.1[f]	38	0.34	0	50.3	63	0.23
	(102)	200	0.70	0	47.0[f]	40	0.33	0	50.0	60	0.25
	(111)	130	0.68	0	47.7	51	0.37	0	50.8	49	0.34

[a] Nearly stoichiometric magnetite, $x_{dissolution}$ = 0.48.

[b] 200 µM $^{57}Fe^{II}$ and 1 g/L ^{56}mag (all Fe^{II} sorbed), x = 0.31 for ^{56}mag.

[c] Value was fixed, since floating caused unrealistic fit parameters.

[d] non-stoichiometric magnetite, $x_{dissolution}$ = 0.31.

[e] 3000 µM $^{56}Fe^{II}$ initially, 1500 µM sorbed.

Table 3.1 Continued

[f] Fit using two signals, reported value is the weighted mean of the two sextets.

[g] $x_{Mössbauer} = ½Oct^{2.5+}/(½Oct^{2.5+} + Tet^{3+})$.

[h] Literature values for natural magnetite at similar temperatures shown for reference.

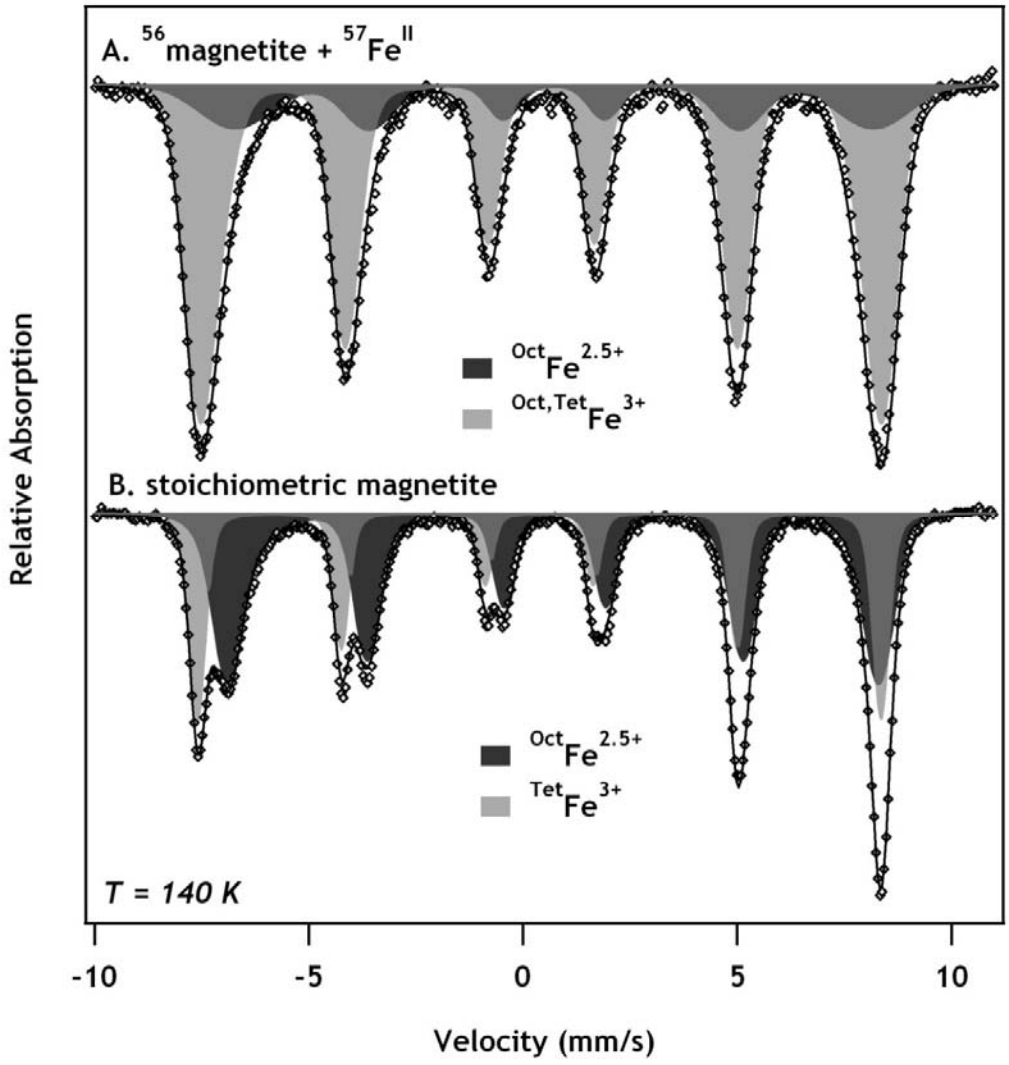

Figure 3.1. Mössbauer spectrum of ^{56}magnetite reacted with $^{57}Fe^{II}$ (**A**) compared to a spectrum for stoichiometric magnetite (**B**). The ^{56}magnetite had an initial stoichiometry of $x_{dissolution}$ = 0.31 before it was exposed to 200 µM aqueous $^{57}Fe^{II}$. The stoichiometric magnetite in spectrum **B** had an $x_{dissolution}$ of 0.48. Open markers represent the observed spectrum, with the total fit shown as a solid line.

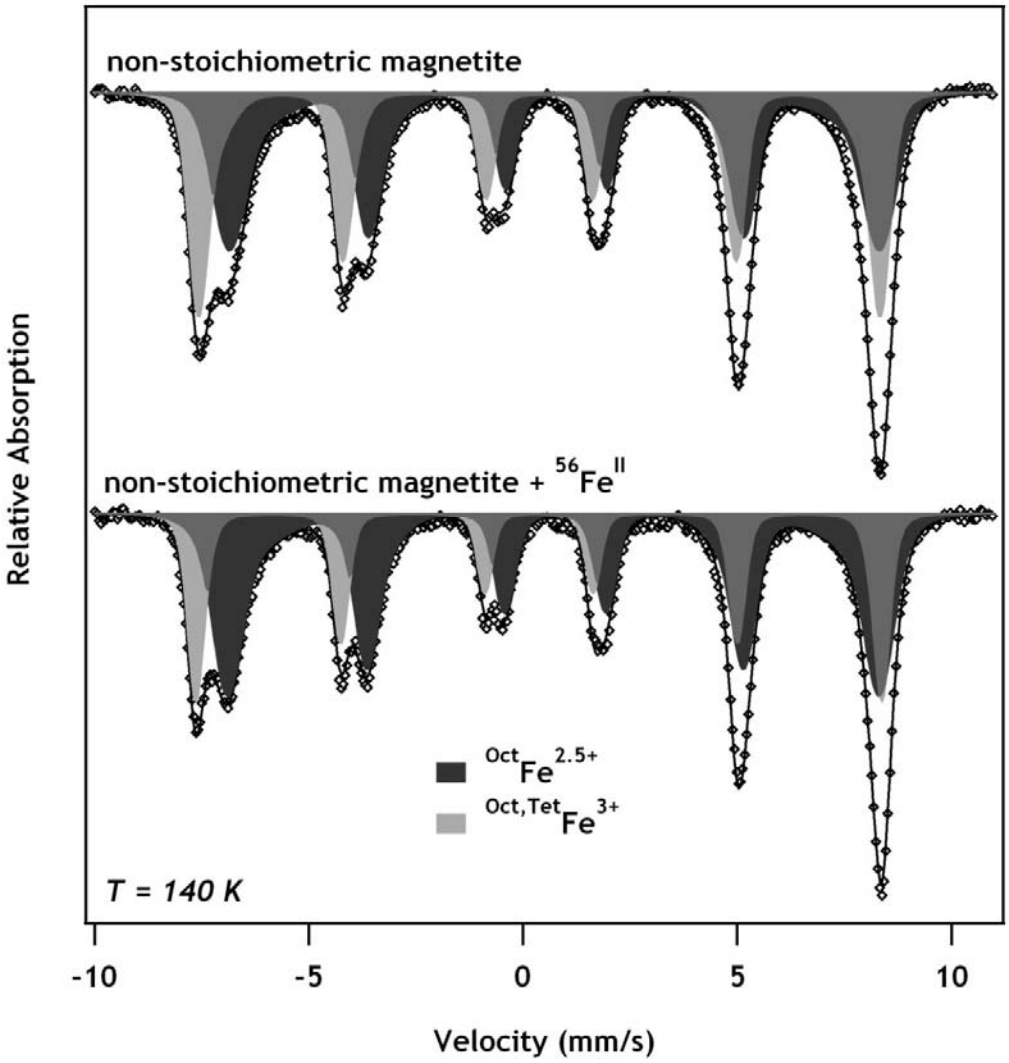

Figure 3.2. Mössbauer spectrum of non-stoichiometric magnetite ($x_{dissolution}$ = 0.31) before and after reaction with $^{56}Fe^{II}$. Initial concentration of aqueous $^{56}Fe^{II}$ was 3 mM. After 24 hours, 1.5 mM was taken up. Open markers represent the observed spectrum, with the total fit shown as a solid line.

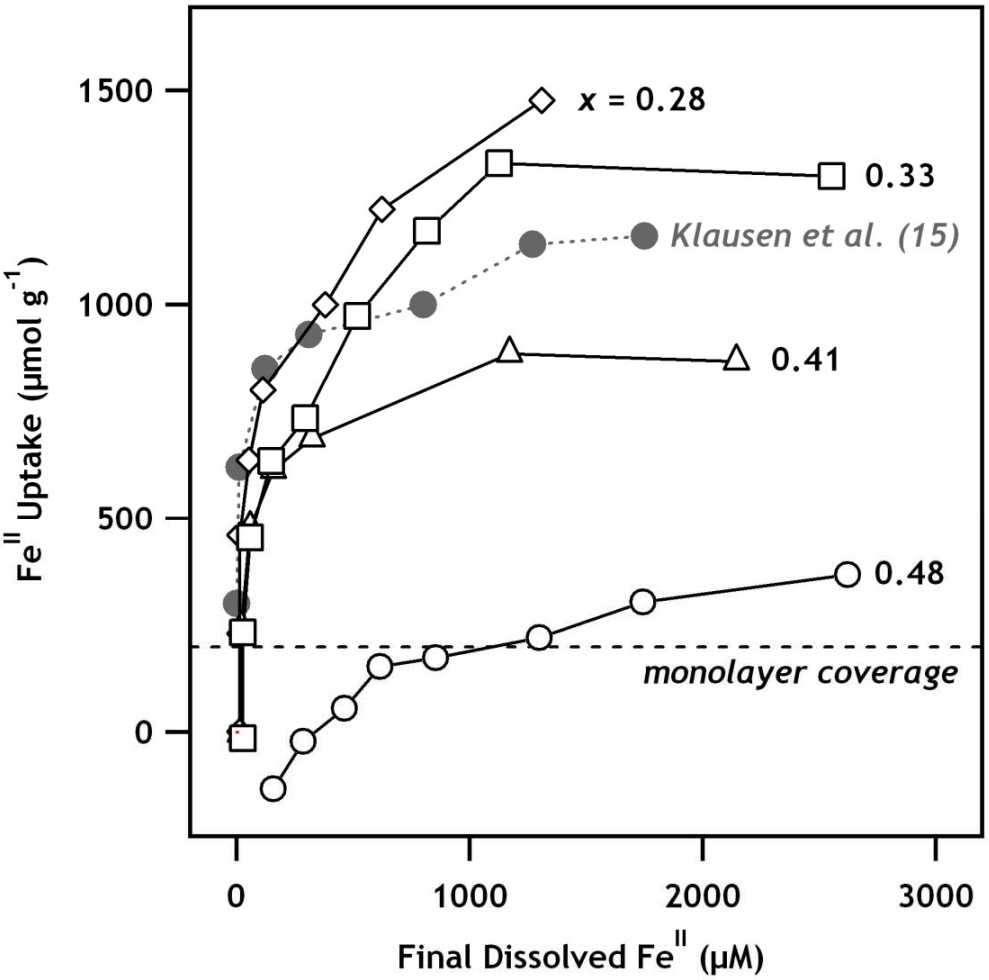

Figure 3.3. Effect of initial magnetite stoichiometry (x = Fe^{2+}/Fe^{3+}) on Fe^{II} uptake from solution (presented as sorption isotherms). The average surface area (62±8 m^2g^{-1}) and the average reported site density for magnetite (3.1 sites/nm^2) (118, 119) yield an estimated monolayer coverage of 200 µmol Fe^{II}/g. Experimental conditions: 1 g/L magnetite, pH 7.2, 50 mM MOPS buffer, 24 hour equilibration.

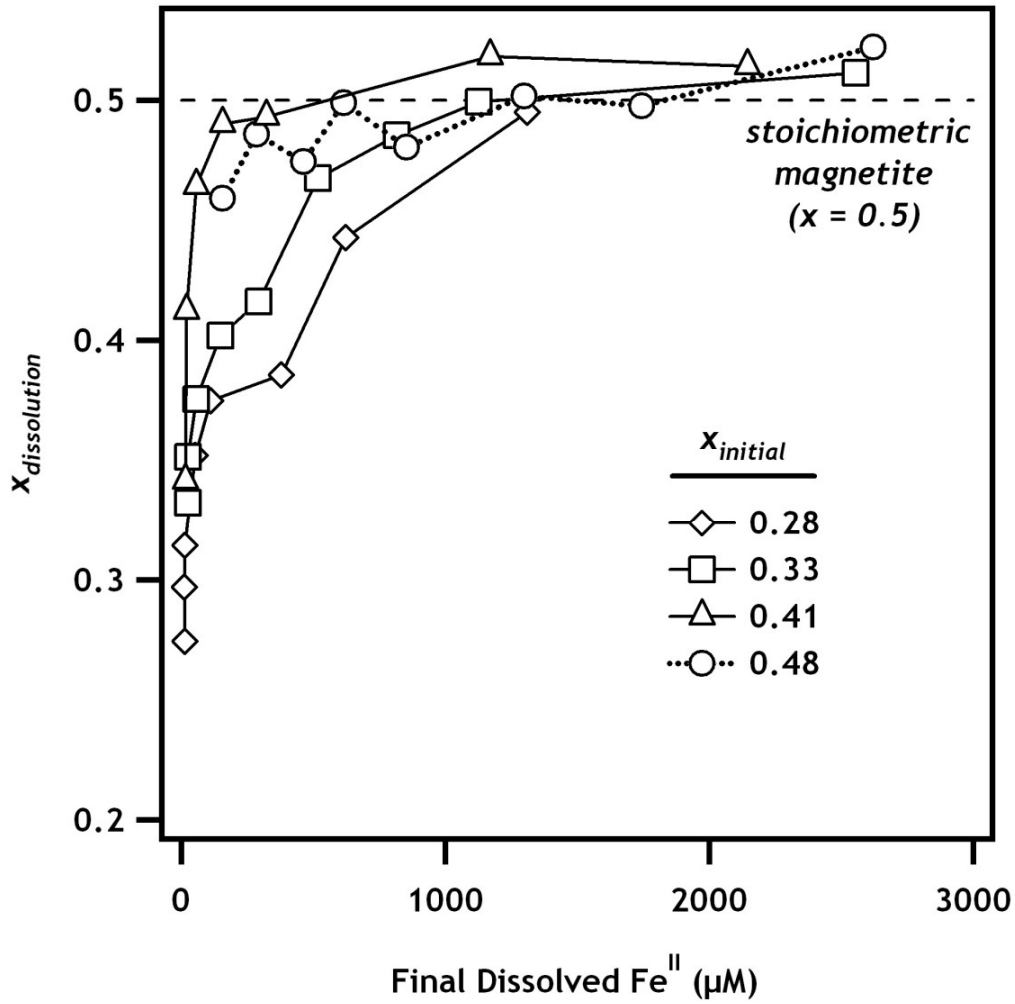

Figure 3.4. Magnetite stoichiometry measured by dissolution ($x_{dissolution}$) after reaction with aqueous Fe^{II}. The data is plotted as a function of final aqueous Fe^{II} concentration to facilitate comparison with Figure 3.3.

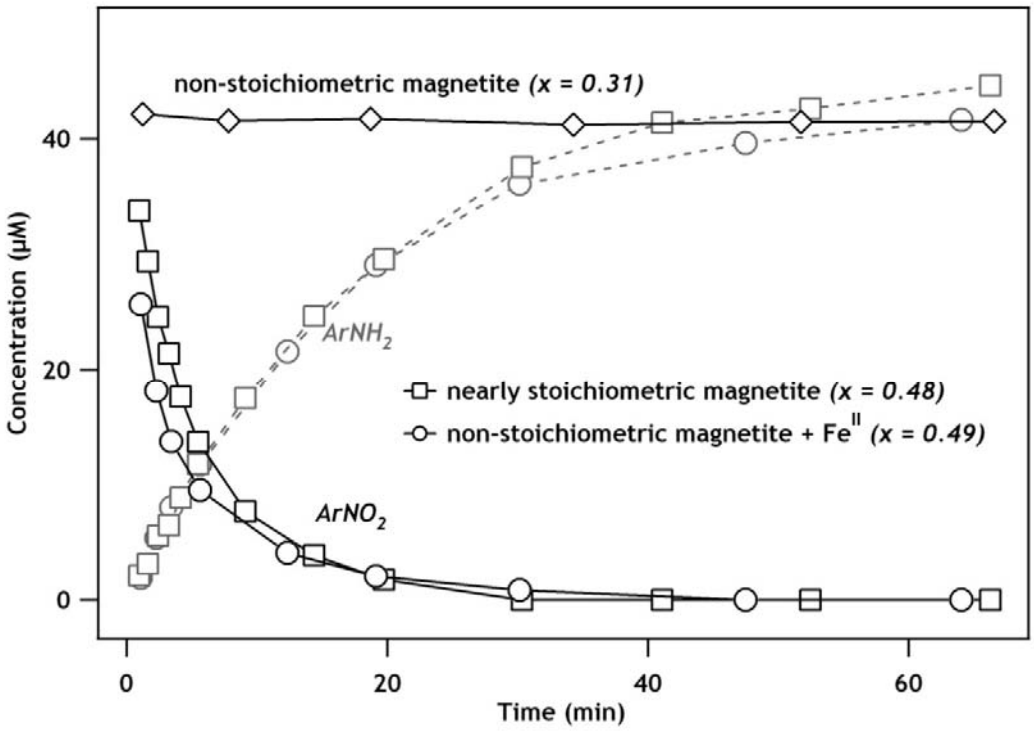

Figure 3.5. Reduction of nitrobenzene by nearly-stoichiometric magnetite ($x_{dissolution}$ = 0.48) and non-stoichiometric magnetite ($x_{dissolution}$ = 0.31) reduced by reaction with Fe^{II}. The "non-stoichiometric magnetite + Fe^{II}" sample was prepared by exposing x = 0.31 magnetite to 3 mM Fe^{II} for 24 hours. We observed an uptake of 1.5 mM Fe^{II}, and formation of a more stoichiometric magnetite ($x_{dissolution}$ = 0.49). The sample was then filtered and re-suspended in fresh buffer to remove the presence of aqueous Fe^{II}. Experimental conditions: 1 g/L magnetite, pH 7.2 50 mM MOPS buffer.

CHAPTER IV: REDOX BEHAVIOR OF MAGNETITE: IMPLICATIONS FOR CONTAMINANT REDUCTION

Abstract

The factors controlling rates of contaminant reduction by magnetite (Fe_3O_4) are poorly understood. Here, we measured the reduction rates of three $ArNO_2$ compounds by magnetite particles ranging from highly oxidized ($x = Fe^{2+}/Fe^{3+} = 0.31$) to fully stoichiometric ($x = 0.50$). Rates of $ArNO_2$ reduction became almost five orders of magnitude faster as the particle stoichiometry increased from $x = 0.31$ to 0.50. To evaluate what was controlling the rate of $ArNO_2$ reduction, we measured apparent ^{15}N kinetic isotope effects (^{15}N-AKIE) values for nitrobenzene and magnetite open-circuit potentials (E_{OCP}). ^{15}N-AKIE values were greater than unity for all magnetite stoichiometries investigated, indicating that mass transfer processes are not controlling the rate of $ArNO_2$ reduction by magnetite. E_{OCP} measurements showed that the E_{OCP} for magnetite was linearly related to the stoichiometry, with more stoichiometric magnetite having a lower potential. Based on these results, we propose that conceptual models that incorporate both redox and Fe^{2+} diffusion processes, rather than those that rely solely on diffusion of Fe^{2+}, are more appropriate for understanding contaminant reduction by magnetite. Our work indicates that particle stoichiometry should be considered when evaluating rates of contaminant reduction by magnetite.

Introduction

Magnetite (Fe_3O_4) is a common constituent of soils and sediments (1, 120). Magnetite can form naturally via several pathways including iron metal corrosion (121), Fe^{2+} oxidation (1), and chemical and biological reduction of Fe^{3+} oxides (43, 44). Due to

---

C.A. Gorski, J.T. Nurmi, P.G. Tratnyek, T.B. Hofstetter, M.M. Scherer. Redox behavior of magnetite: Implications for contaminant reduction. *Environmental Science and Technology. 2009, In Press.*

the ubiquity of magnetite in the environment, it has been implicated as a potentially important reductant for environmental contaminants, including several halogenated organics and heavy metals (e.g., 17, 18, 43, 73). Magnetite is also of great interest to the corrosion community, as it is a common oxidation product of steel (e.g., 121).

We have previously demonstrated that the degree of magnetite oxidation, measured as the ratio of structural Fe^{2+} and Fe^{3+} atoms ($x = Fe^{2+}/Fe^{3+}$), strongly influences the rate of nitrobenzene ($ArNO_2$) reduction (74). The extent of magnetite oxidation, or magnetite stoichiometry (x), can range from 0 to 0.5, where 0.5 corresponds to the most reduced form (stoichiometric magnetite), and 0 is the completely oxidized form (all Fe^{3+}), which is known as maghemite (γ-Fe_2O_3). In our previous work, we observed that stoichiometric magnetite could rapidly reduce $ArNO_2$ in the absence of dissolved Fe^{2+}, whereas reduction by partially oxidized magnetite was much slower; however, the factors controlling the rate of $ArNO_2$ reduction and magnetite oxidation were unclear.

Several models have been proposed to describe the kinetics of magnetite oxidation, with many derived from corrosion studies where magnetite and maghemite form passive films on iron metal (53-57, 60). Models based on diffusion of Fe^{2+} outward to the magnetite surface (53-56) are the most common, and have been invoked to explain carbon tetrachloride (CCl_4) reduction by magnetite (46). Although diffusion models can often describe the data well, the room temperature diffusion rates for Fe^{2+} estimated from these models vary by several orders of magnitude between studies (10^{-3} cm^2s^{-1} (53), 10^{-12}-10^{-16} cm^2s^{-1} (54), 2.1 x10^{-15} cm^2s^{-1} (55), 1.3 x 10^{-20} cm^2s^{-1} (56)), raising questions about the assumption of diffusion control on rates of magnetite oxidation (57-59). Others have proposed alternative models based on changes in magnetite redox potential upon oxidation (57, 60), and evidence for these models has been accumulating based on direct measurements of magnetite redox potentials upon oxidation (17, 60, 64).

To explore whether $ArNO_2$ reduction by oxidized magnetite is controlled by changes in the redox potential of the particle or by diffusion of Fe^{2+} to the magnetite surface, we measured the apparent ^{15}N kinetic isotope effects (^{15}N-AKIE) for $ArNO_2$ reduction and open-circuit potentials as a function of magnetite stoichiometry. We purposefully minimized the variation in specific surface areas among the batches of magnetite (~20 nm spheres, 63±7 m^2g^{-1}) in an attempt to isolate the influence of magnetite stoichiometry as the sole variable. $ArNO_2$ and its substituted analogs (3-Cl-$ArNO_2$, 2-Me-$ArNO_2$) were selected as model environmental contaminants due to the extensive body of knowledge available regarding their reactivity and substituent-dependent redox properties (122-126). We further apply this model to develop a quantitative structure activity relationship (QSAR) that may be useful for predicting rates of $ArNO_2$ reduction, and perhaps even other environmentally relevant contaminants.

Experimental Section

Magnetite Synthesis and Characterization

Details regarding the chemicals and instrumentation used can be found in the Appendix A. Magnetite batches were synthesized using methods to control particle size and stoichiometry; a detailed explanation of the synthesis can be found in our previous work (74). Briefly, magnetite was synthesized in a H_2/N_2 (6/94) anaerobic glovebox by mixing a 1:2 Fe^{2+}:Fe^{3+} acidic solution, with the pH titrated to at least 10 with NaOH. H_2O_2 was used to oxidize the stoichiometric magnetite to produce oxidized magnetite powders, and x was determined by complete dissolution in acid with $\sigma_x < 0.01$ (74).

Mössbauer spectroscopy and powder X-ray diffraction (pXRD) patterns indicated magnetite as the sole phase present, as shown in our previous work (74). BET specific surface areas (SSAs) were 59 m^2 g^{-1} (x = 0.50), 66 m^2 g^{-1} (x = 0.49), 58 m^2 g^{-1} (x = 0.48), 75 m^2 g^{-1} (x = 0.42), 64 m^2 g^{-1} (x = 0.36), and 58 m^2 g^{-1} (x = 0.31), with the average SSA being 63±7 m^2 g^{-1}. The SSAs were not measured for the x = 0.33, 0.22, and 0.17 batches,

but TEM images indicated particle sizes similar to the x = 0.36 batch from which they were synthesized. pXRD patterns also provided similar primary crystallite sizes (~11±1 nm) for all measured batches using the Scherrer equation. Transmission electron microscopy (TEM) images showed particles having spherical morphologies with diameters of approximately 20 nm (74); there was no evidence of any distinct phase separation (i.e., a core-shell structure).

Nitrobenzene Reduction Experiments

Reduction rates of three $ArNO_2$ compounds were investigated, including 3-Cl-nitrobenzene (3-Cl-$ArNO_2$, $E_h^{1'}$ = -0.405 V), nitrobenzene ($ArNO_2$, $E_h^{1'}$ = -0.485 V), and 2-methyl-nitrobenzene (2-Me-$ArNO_2$, $E_h^{1'}$ = -0.590 V) (122). All experiments were conducted in an anaerobic H_2/N_2 (6/94) glovebox measuring less than 1 ppm oxygen. For these experiments, 1.0±0.07 g/L magnetite was added to a solution containing 50 mM 3-(*N*-morpholino)propanesulfonic acid buffer (MOPS, pK_a 7.2) adjusted to pH 7.2, and allowed to equilibrate one hour prior to the addition of a methanolic $ArNO_2$ stock to achieve a final concentration of 40 µM $ArNO_2$; the MeOH concentration was approximately 50 mM. All reactors were run in duplicates, with reported rates being the average of the two experiments; agreement was generally within 10-15%. Samples were taken at time intervals by filtering the solution through an 0.2 µm PTFE filter, and measuring the aqueous concentration using high-pressure liquid chromatography (HPLC) with an eluent of 70:30 acetonitrile:1 g/L ammonium acetate in water (pH ≈ 7) passed through a Supelco LC-18 column at 1 mL/min. All $ArNO_2$ and aniline compounds were measured using UV absorbance detection at 254 nm and 235 nm, respectively.

Electrochemistry

Chronopotentiograms (CPs) of the open-circuit potential (E_{OCP}) were obtained in a two-electrode cell, containing a powder disk electrode (PDE) made with the synthesized magnetite samples and a Ag/AgCl reference electrode (values converted to

SHE). Details of the design and electrochemical properties of the PDE used in this study have been published previously (127, 128). Custom caps (Teflon or Kel-F) were used to cover the tip of a polished disk electrode made with high purity Fe^0, leaving a 1.4 mm diameter x 5.1 mm deep cavity that was filled by pressing the sample into the cavity with a small metal plunger (this compression was sufficient to hold sample in the cavity). All results presented here were obtained with a stationary PDE. Electrode potentials were recorded with a potentiostat (Autolab PGSTAT30; EcoChemie, Utrecht, The Netherlands) without built-in resistance compensation. The sampling rate for chronopotentiometry was 2.0 sec^{-1}. Linear sweep voltammetry (LSV) was also used to characterize the samples, but irreversible redox reactions occurred during the sweep, similar to previous observations on magnetite electrodes (54).

Nitrobenzene Stable Isotope Analysis

Nitrogen isotope fractionation associated with the reduction of $ArNO_2$ was examined in suspensions of 6.0±0.07 g/L magnetite and 400 µM initial $ArNO_2$ concentrations under conditions otherwise identical to those described above ([MeOH] = 12 mM). Magnetite stoichiometries (*x*) examined were 0.36, 0.42, 0.49, and 0.50. For each experiment (i.e., magnetite stoichiometry) up to seven individual reactors were prepared. Nitrogen isotope signatures of $ArNO_2$ at different extent of reactant conversion were obtained from compound-specific isotope analysis (CSIA). Following a procedure described earlier, individual reactors were sacrificed for solid-phase microextraction (SPME) and subsequent isotope analysis by GC/C/IRMS (gas chromatography isotope-ratio mass spectrometry with combustion interface) (129, 130).

All $\delta^{15}N$ values were derived from triplicate measurements and are reported relative to N_2 in air as $\delta^{15}N_{Air}$. All samples were diluted to the least concentrated nitrobenzene solution prior to analysis and measured at constant peak amplitudes (126).

Bulk ^{15}N enrichment factors (ε_N) of the $ArNO_2$ were derived from linear regression analysis of eq. 4.1.

$$\ln\left[\frac{\delta^{15}N_0 + \Delta\delta^{15}N_0 + 1000}{\delta^{15}N_0 + 1000}\right] = \frac{\varepsilon_N}{1000} \cdot \ln\left(\frac{c}{c_0}\right) \quad (4.1)$$

where $\delta^{15}N_0$ is the initial ^{15}N signatures of $ArNO_2$ (-3.96±0.48‰, ±1σ), $\Delta\delta^{15}N$ is its change during the reaction, and c_0 and c are the substrate's initial concentration and concentration following different extents of $ArNO_2$ reduction, respectively. Apparent ^{15}N kinetic isotope effects (^{15}N-AKIE) were calculated according to eq. 4.2.

$$^{15}N - AKIE = \left(\frac{1}{1 + {}^{\varepsilon_N}/_{1000}}\right) \quad (4.2)$$

Results & Discussion

Reduction of Substituted Nitrobenzene Compounds by Magnetite

We previously reported that the stoichiometry, or Fe^{2+}/Fe^{3+} ratio of magnetite (*x*), strongly influenced the kinetics of $ArNO_2$ reduction to aniline ($ArNH_2$) (74). Here, we further explored this by synthesizing several batches of magnetite with bulk stoichiometries ranging from *x* = 0.50 (stoichiometric) to *x* = 0.17 (significantly oxidized). Figure 4.1 shows a first order plot for the reduction of $ArNO_2$ by five batches of magnetite with different stoichiometries. $ArNO_2$ reduction rates become slower as the magnetite becomes more oxidized (decreasing *x*). For the stoichiometric magnetite (*x* = 0.50), the half-life of $ArNO_2$ is approximately a minute, whereas for the most oxidized magnetite (*x* = 0.31), the half-life is approximately three months. Mass balances ranged between 98-104% based on formation of the aniline product, as shown in Figure 4.2 for *x* = 0.42. Note that experiments with more oxidized magnetite (*x* = 0.26) were conducted, but the reduction rate was too slow to obtain a reliable rate estimate over a four month time period. Slower rates of contaminant reduction by oxidized magnetite are consistent

with earlier studies examining chromate reduction, where magnetite exposed to air for various time periods (i.e., months) slowed chromate reduction rates (117). These observations also agree with decreasing rates of $ArNO_2$ and chlorohydrocarbon reduction by structural Fe^{2+} in smectite minerals with decreasing Fe^{2+}-content in the octahedral clay sheets and decreasing Fe^{2+}/Fe^{3+} ratios (131, 132).

A similar trend of faster reduction rates with increasing magnetite stoichiometry was observed for two substituted $ArNO_2$ compounds (Figures A.6-A.8). As expected based on their one-electron potentials ($E_h^{1'}$), 3-Cl-$ArNO_2$ was reduced the fastest with a one-electron potential of $E_h^{1'}$ = -0.405 V, followed by $ArNO_2$ ($E_h^{1'}$ = -0.485 V), and 2-Me-$ArNO_2$ ($E_h^{1'}$ = -0.590 V) for all stoichiometries (Table 4.1). Comparison of reduction rates with existing work is difficult because the stoichiometry of magnetite is not reported in previous studies. As we noted in our previous work (74), we suspect that differences in magnetite stoichiometry can explain discrepancies in contaminant reduction rates found among earlier studies (e.g., CCl_4) (46, 47).

A plot of the natural log of the first-order rate coefficient (k_{obs}) versus x reveals a linear correlation (Figure 4.3; R^2 = 0.96 for regression of all of the compounds together, and $R^2 \geq 0.97$ for the individual compounds). Substituent effects on reduction rates are much less pronounced than the effect of stoichiometry, and only span up to about one order of magnitude, in comparison to the five orders of magnitude range observed as a function of magnetite stoichiometry (Table 4.1). In addition, the substituent effects appear to become more significant as the magnetite becomes more oxidized (x decreases); this is shown by the markers becoming more vertically spread out with smaller x values, which indicates a possible shift in the rate-limiting step.

Nitrobenzene Stable Isotope Analysis.

To evaluate whether the rate-limiting step in $ArNO_2$ reduction was shifting with magnetite stoichiometry, we determined apparent ^{15}N kinetic isotope effects (^{15}N-AKIE,

eq. 4.2) by measuring the enrichment of ^{15}N over the course of a reduction experiment. As found previously for solid-phase Fe^{2+} species (131, 132), ^{14}N in $ArNO_2$ is preferentially reduced, which leads to ^{15}N enrichment in the remaining $ArNO_2$, as observed in increasing $\delta^{15}N$ signatures (data not shown). Figure 4.4 shows that N isotope fractionation during $ArNO_2$ reduction was substantial, and most pronounced for $x = 0.36$. The magnitude of isotope fractionation, as quantified by its ^{15}N enrichment factors, ε_N (eq. 4.1), decreased with increasing rates of $ArNO_2$ reduction, and thus, with increasing stoichiometry (x) of magnetite. The corresponding ^{15}N-AKIE values were between 1.0176±0.0007 ($x = 0.50$) and 1.0481±0.0016 (x = 0.36) (Table 4.1). Note that transport processes, such as diffusion, only lead to negligible isotope fractionation; therefore, ^{15}N-AKIE values significantly different from unity for all magnetite stoichiometries rule out that mass-transfer processes fully governed the reaction kinetics of $ArNO_2$ reduction.

Experimental and computational evidence for nitroaromatic compound reduction by a variety of dissolved and mineral bound reductants imply that ^{15}N kinetic isotope effects greater than 1.03 are typical for reaction kinetics that are limited by the cleavage of the 1st N-O bond of substituted *N*,*N*-dihydroxyanilines after sequential transfer of electrons and protons to the Ar-NO_2 ($e^-/H^+/e^-/H^+$-pathway) (126, 129). The ^{15}N-AKIE of 1.048 and 1.041 for more oxidized magnetite samples ($x = 0.36$ and 0.42) are both greater than 1.03, and suggest that $ArNO_2$ reduction was limited by cleavage of the 1st N-O bond, not electron and proton transfers to the $ArNO_2$, nor by transport processes of aqueous $ArNO_2$ to the particle surface.

The decrease of ^{15}N isotope effects by 50% and more found for the more stoichiometric magnetites ($x = 0.49$ and 0.50) suggests that either a non-isotopic transport process, such as migration of Fe^{2+} outward to the magnetite surface or diffusion of $ArNO_2$ to the magnetite surface, may be masking the isotope fractioning bond cleavage, or a change in the initial reaction mechanism may be occurring. The fast reaction kinetics (half-life ≈ 1 min) suggests a non-isotropic transport process (i.e., diffusion of $ArNO_2$ to

a reactive site or solid state Fe^{2+} migration) may be responsible for the lack of fractioning bond cleavage. Shifts in ^{15}N-AKIE with increasing rates of nitroaromatic compound reduction in homogeneous solution have recently been observed due to changes in the initial reaction mechanisms. At more negative reduction potentials and under proton-limited conditions, substantially lower ^{15}N-AKIE values have been reported (126 and refs. therein), which have been attributed to the second electron transfer to the nitroaromatic radical anion becoming the rate-limiting step. Thus, ^{15}N-AKIE of 1.0235±0.0008 (x = 0.49) and 1.0176±0.0007 (x = 0.50) could also indicate that at least some of the $ArNO_2$ reduction at stoichiometric magnetite particles occurs via an $e^-/e^-/H^+/H^+$-pathway instead of the $e^-/H^+/e^-/H^+$-sequence. This interpretation of $ArNO_2$ reduction kinetics would require that for x = 0.49 and 0.50, some Fe^{2+} species have a more negative reduction potential than in partially oxidized magnetite.

Open Circuit Potential of Magnetite as a Function of Stoichiometry

To estimate redox potentials of magnetite as a function of stoichiometry, we used a powder disk electrode (PDE) to measure the self-induced potential, which is more commonly referred to as the open circuit potential (E_{OCP}). Powder electrode configurations have previously been used for characterizing the electrochemical properties of Fe^0 powders (128), goethite (α-FeOOH) (133), and other oxides (134 and refs. therein). Chronopotentiometric (CP) experiments were conducted where E_{OCP} values were measured without any applied potential for a 60 minute period for nine batches of magnetite with varied stoichiometries (Table A.2 and Figure A.10). The limiting value of E_{OCP} at 60 minutes varied linearly over more than 500 mV (-0.48 V to +0.05 V vs. SHE) as magnetite stoichiometry decreased from 0.5 to 0.17 (Figure 4.5). Stoichiometric magnetite had the lowest reduction potentials consistent with the faster nitroaromatic reduction rates shown in Figure 4.1 and the shift to lower ^{15}N-AKIE values shown in

Figure 4.4. Both the magnitudes and trend of E_{OCP} values as a function of magnetite oxidation are consistent with previous studies conducted with magnetite single crystals (54, 64). Note, however, that there is a wide range of measured magnetite redox potentials reported in the literature (e.g., at neutral pH: +0.66 V (61), +0.25 V (54), -0.38 V (60) vs. SHE), and we suspect that the range is due to differences magnetite stoichiometry, which is rarely reported.

Substituent Effects on Rates of Nitrobenzene Reduction by Magnetite

To evaluate the effect of structural substituents on rates of $ArNO_2$ reduction by different stoichiometry magnetites, we plotted the log of reaction rates for substituted nitroaromatic compounds versus their $E_h^{1'}$ values (Figure 4.6). Although plots of $\log(k_{obs})$ versus $E_h^{1'}$ are typically considered linear free energy relationships (LFERs), recall that the ^{15}N-AKIE values indicate that cleavage of the 1st N-O bond, rather than electron transfer, may be the rate limiting step for the more oxidized magnetite samples, potentially making $E_h^{1'}$ a less promising descriptor than it would be for a system where nitro reduction was entirely limited by the rate of electron transfer. The trends in slopes from the LFER plot are still nonetheless instructive to consider. The free energies of the first electron transfer ($E_h^{1'}/0.059$) co-correlate with the overall rate of $ArNO_2$ reduction (126), and thus provide a qualitative means to assess the effects of contaminant structure on its reactivity (129, 131).

For the range of magnetite stoichiometries investigated, the LFER slopes are all less than one and decrease from 0.42 to 0.08 as the magnetite becomes more stoichiometric, indicating that the rates of $ArNO_2$ reduction by magnetite are affected by the contaminant's structure (substituent effects), and thus its electron accepting properties. Shallower LFER slopes as the magnetite becomes more stoichiometric are consistent with the shift to lower ^{15}N-AKIE values shown in Figure 4.4, and provide

additional evidence that a change in the rate limiting step is occurring as the magnetite stoichiometry changes. LFER slopes significantly less than one have been reported for the reduction of other contaminants by Fe^{2+} associated with magnetite and other iron oxides, and have been interpreted to indicate transport limitations on the reaction rate (14, 15); however, as discussed above with regards to the shift to lower ^{15}N-AKIE values, we cannot distinguish whether the shallower LFER slopes observed for the more stoichiometric magnetite is due to a shift to a secondary reaction pathway (such as $e^-/e^-/H^+/H^+$, (124, 126)), or the onset of some transport limitation. Note that the LFER slopes including 2-Me-$ArNO_2$ may result in slightly underestimated slopes for x = 0.31 - 0.42 because 2-Me-$ArNO_2$ often reacts faster than predicted based on $E_h^{1'}$ values (14, 122, 132); the effect, however, would be identical for LFERs of all magnetite stoichiometries, and does not change the above interpretations.

Redox Behavior of Magnetite: Implications for Contaminant Reduction

Our findings that particle stoichiometry dramatically affects the reduction rates of mono-substituted nitrobenzene compounds have both fundamental and practical implications for understanding the redox behavior of magnetite with regards to contaminant fate. On a fundamental level, our work suggests that conceptual models for magnetite oxidation that rely solely on Fe^{2+} diffusion (53-56) or redox processes (60) may not be sufficient for describing contaminant reduction rates. Our ^{15}N-AKIE results indicate that transport limitations are not controlling the rate of $ArNO_2$ reduction by magnetite. This means that models based solely on diffusion, such as the core-shell diffusion model, where magnetite oxidation is limited by rates of Fe^{2+} migration from the core of the magnetite particle out through an oxidized maghemite shell (e.g., 54), are not applicable to contaminant reduction by magnetite. In addition, the strong linear correlation between E_{OCP} and magnetite stoichiometry (Figure 4.5) provides compelling

evidence that redox processes play an important role in controlling rates of $ArNO_2$ reduction by magnetite. We propose that conceptual models that incorporate both redox and diffusion processes, such as those developed to describe magnetite oxidation and Fe^0 corrosion oxidation (57-60), are more appropriate for understanding $ArNO_2$ reduction by magnetite. We suspect that this may be true for other contaminants as well (46).

On a more practical level, the strong correlation between magnetite stoichiometry and rates of $ArNO_2$ reduction (Figure 4.3) compelled us to explore whether a quantitative structure activity relationship (QSAR) could be used to predict rates of $ArNO_2$ reduction (123). Magnetite stoichoimetry can be measured by complete dissolution and colorimetric measurements, and could potentially serve as an accessible descriptor variable for contaminant reduction rates. The relationship between E_{OCP} and *x* in Figure 4.5 can then be used to estimate the E_{OCP} as a function of magnetite stoichiometry. By taking the difference between the one-electron reduction potentials ($E_h^{1'}$) as a proxy for the redox activity for the substituted $ArNO_2$ compounds and E_{OCP}, we can approximate the overpotential (ΔE), or thermodynamic driving force using eq. 4.3.

$$\Delta E(x) = E_h^{1'} - E_{OCP}(x) \tag{4.3}$$

In the absence of mass transfer effects, the overpotential can be used to estimate the rate of nitroaromatic reduction (calculation in Supporting Information, Appendix A). Figure 4.7 shows a comparison of the estimated rates and the experimentally measured rates. Agreement between the calculated and experimental values is quite good for $ArNO_2$ (within half an order of magnitude), but not as close for the two substituted $ArNO_2$ compounds (within two orders of magnitude). The QSAR systematically underpredicts the rate of 3-Cl-$ArNO_2$ and overpredicts the rate of 2-Me-$ArNO_2$, possibly due to mass transfers limitations or $E_h^{1'}$ not being an appropriate reaction descriptor. It is also possible that other thermodynamic values may prove to be better predictors of the reaction kinetics in the future (e.g., the bond dissociation enthalpy for the N-O cleavage)

(124). Nonetheless, the QSAR may provide a useful tool for estimating rates of contaminant reduction by magnetite.

Table 4.1. First-order rate coefficients (k_{obs}, min^{-1}), $t_{1/2}$ (min), LFER slope, and ^{15}N-AKIE of $ArNO_2$ reduction for different stoichiometry magnetites (x).

		k_{obs} (min^{-1})[b]					
Compound	**$E_h^{1'}$[a] (V)**	**x = 0.50[c]**	**x = 0.49[d]**	**x = 0.48**	**x = 0.42**	**x = 0.36**	**x = 0.31**
3-Cl-$ArNO_2$	-0.405	0.74	0.29	0.29	5.8×10^{-2}	3.4×10^{-4}	3.4×10^{-5}
$ArNO_2$	-0.485	0.57	0.16	0.20	9.4×10^{-3}	1.3×10^{-4}	5.4×10^{-6}
2-Me- $ArNO_2$	-0.590	0.43	0.10	0.13	5.6×10^{-3}	7.8×10^{-5}	1.6×10^{-6}
$t_{1/2}$, $ArNO_2$		1.2 min	4.5 min	3.5 min	74 min	3.8 day	90 day
LFER slope		0.08	0.14	0.11	0.22	0.20	0.42
^{15}N-AKIE ($\pm 1\sigma$)		1.0176 (0.0007)	1.0235 (0.0008)	n.d.[e]	1.0405 (0.0011)	1.0481 (0.0016)	n.d.

[a] Reduction potential of the half reaction $ArNO_2 + e^- = ArNO_2^{\bullet -}$ (122)

[b] Duplicate reactors were` used, with the average rate reported; agreement was generally within 10-15%.

[c] $\sigma_x < 0.01$.

[d] Data not shown in Figures 4.1 and 4.5 due to overlap with x = 0.48 (data shown in Figure A.8).

[e] Not determined due to lack of magnetite sample.

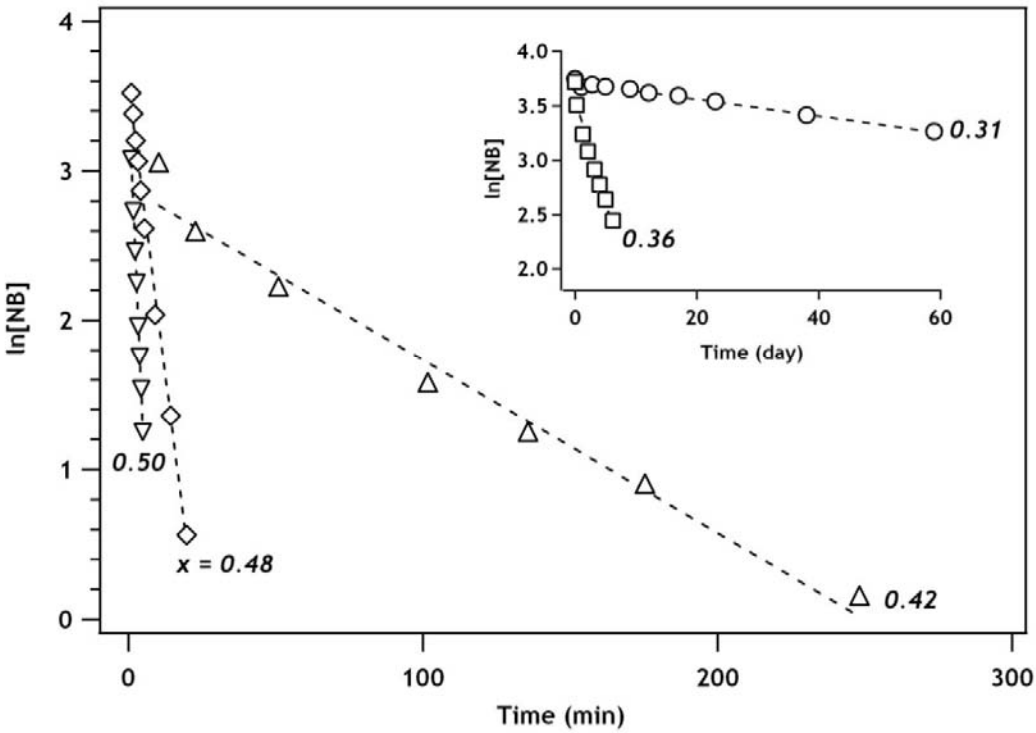

Figure 4.1. First-order plot for $ArNO_2$ reduction by magnetite with different stoichiometries ($x = Fe^{2+}/Fe^{3+}$). Legend: ▽ x = 0.50, ◇ x = 0.48, △ x = 0.42, □ x = 0.36, ○ x = 0.31. Experimental conditions: 1.0 g/L magnetite, pH 7.2, 50 mM MOPS buffer, 1 hour equilibration prior to addition of $ArNO_2$, $[ArNO_2]_0$ = 40 µM.

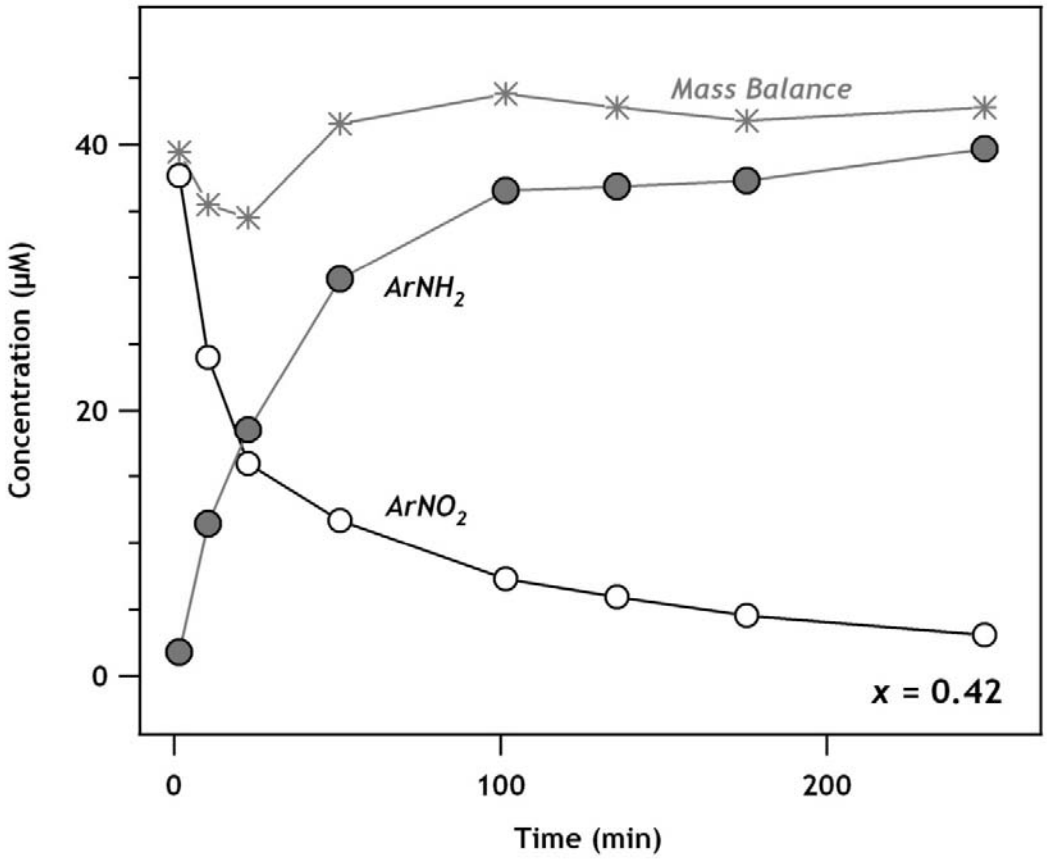

Figure 4.2. Reduction of $ArNO_2$ to $ArNH_2$ by x = 0.42 magnetite with the mass balance of $ArNO_2$ and $ArHN_2$ shown. Experimental conditions: 1.0 g/L magnetite, pH 7.2, 50 mM MOPS buffer, 1 hour equilibration prior to addition of $ArNO_2$, $[ArNO_2]_0$ = 40 µM.

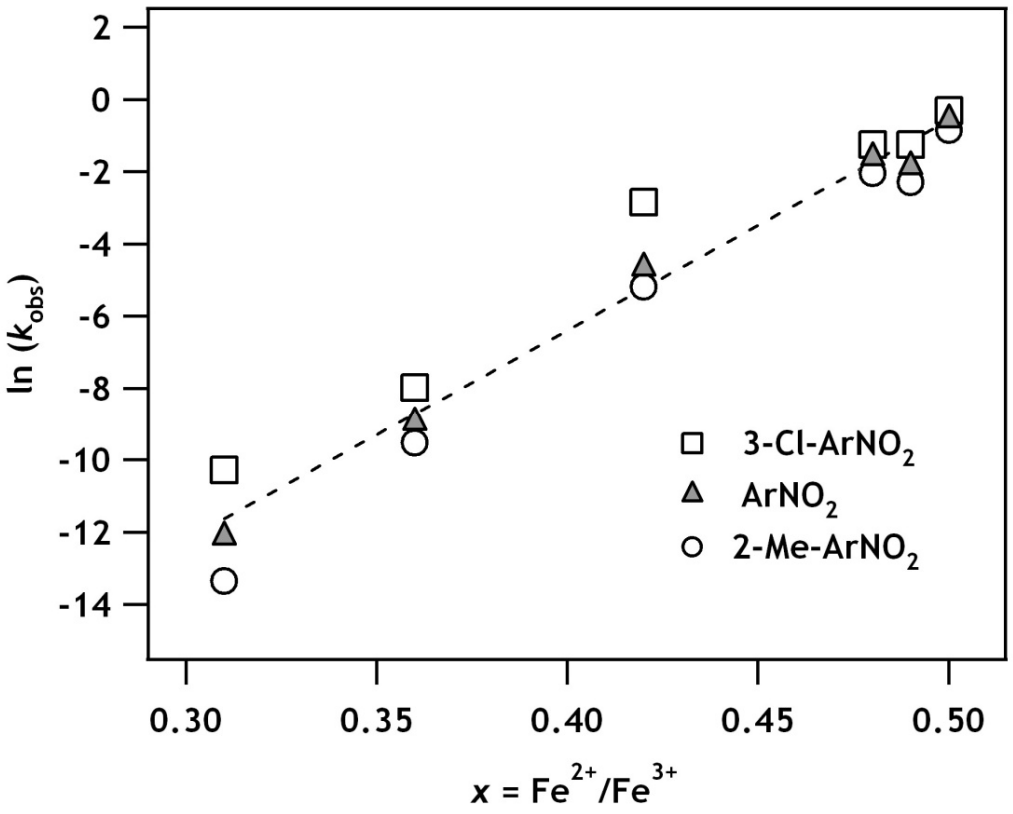

Figure 4.3. Natural log transformed observed kinetics for R-ArNO$_2$ compounds with different stoichiometry magnetites. The fitted line shown is for all R-ArNO$_2$ compounds vs. *x* (n = 15; R^2 = 0.96).

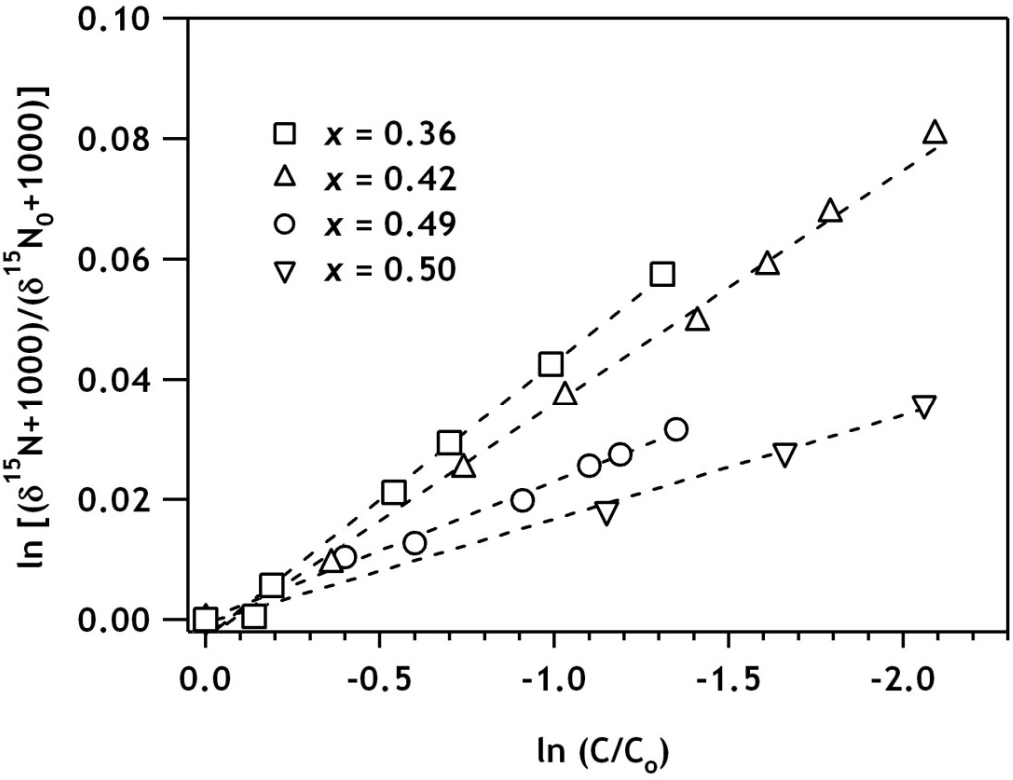

Figure 4.4. Linearized nitrogen isotope enrichment according to eq. 4.2 during the reduction of $ArNO_2$ in suspension of magnetites with varying *x*. The slopes of the dashed lines correspond to bulk ^{15}N enrichment factors, ε_N, which, in the sequence of increasing *x*, were -17.2±0.7‰, -23.0±0.8‰, -39.0±1.1‰, and -45.9±1.6‰ (±1σ). Error bars are smaller than the data markers. Legend: ▽ *x* = 0.50, ○ *x* = 0.49, △ *x* = 0.42, □ *x* = 0.36. Experimental conditions: 6.0 g/L magnetite, pH 7.2, 50 mM MOPS buffer, 1 hour equilibration prior to addition of $ArNO_2$, $[ArNO_2]_0$ = 400 µM.

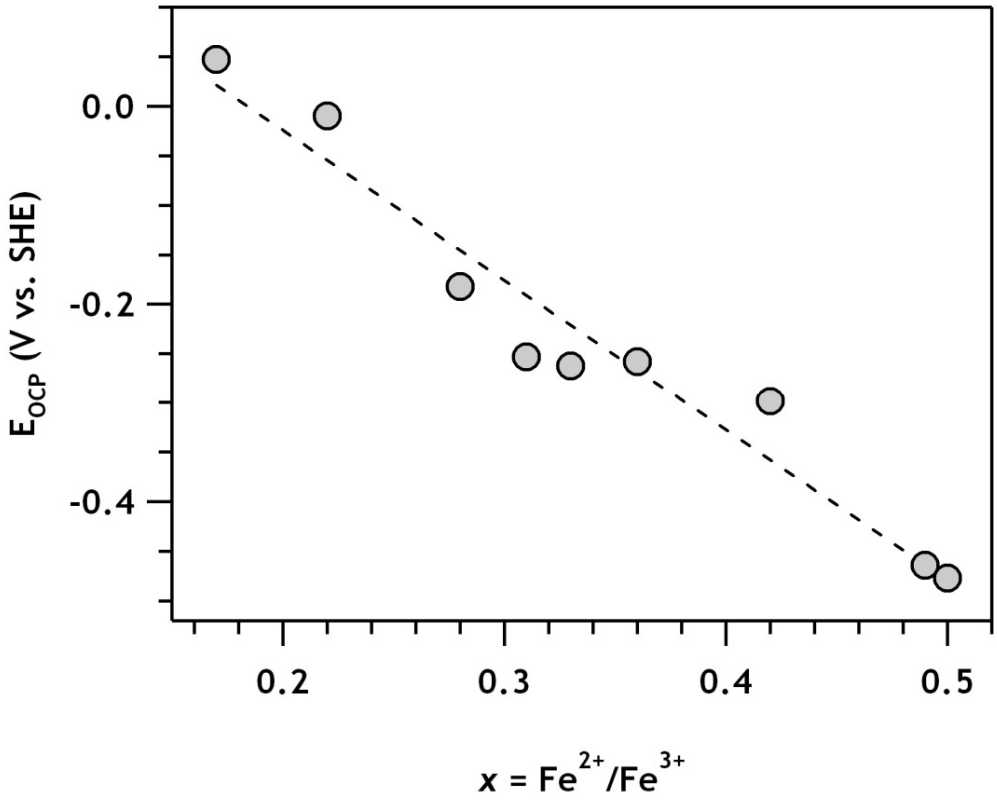

Figure 4.5. The E_{OCP} of each magnetite batch plotted against the measured stoichiometry. The fitted linear regression with n = 9 yields $E(x) = -1.52\pm0.14(x) + 0.28\pm0.05$ ($\pm\sigma$) vs. SHE; $R^2 = 0.95$.

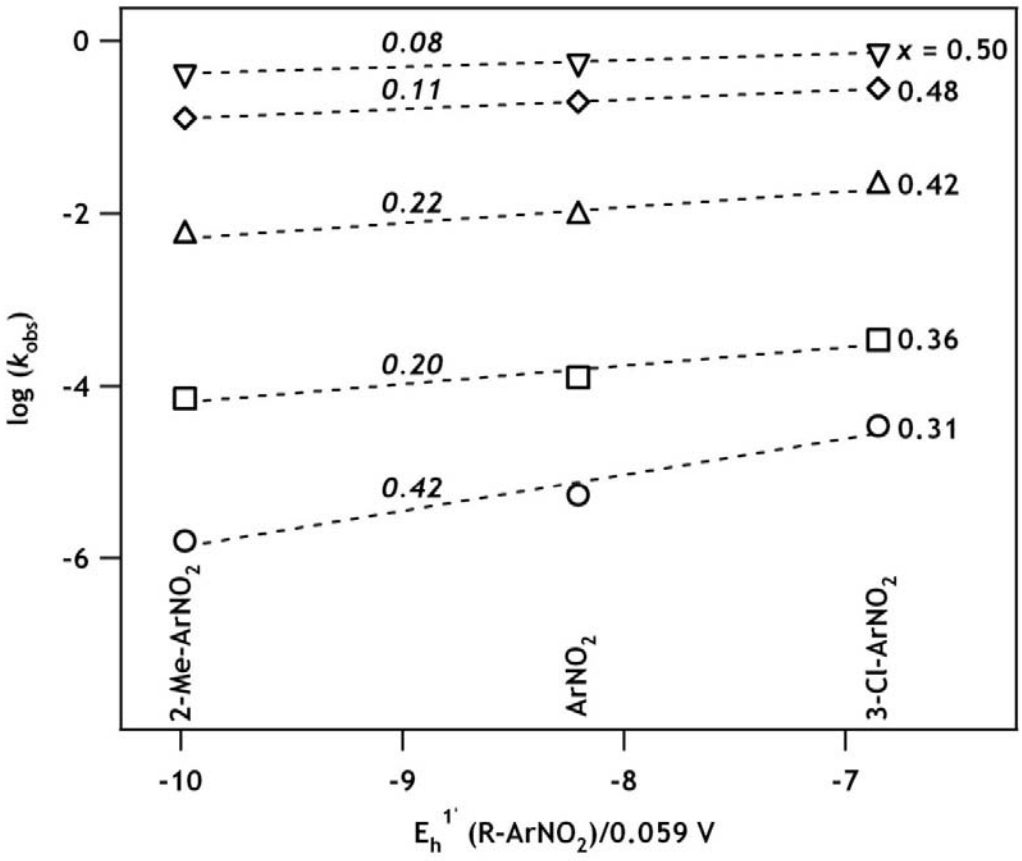

Figure 4.6. Linear free-energy relationship of magnetites with varying stoichiometries for three $ArNO_2$ analogs (3-Cl-$ArNO_2$, $ArNO_2$, 2-Me-$ArNO_2$). Legend: ▽ x = 0.50, ◇ x = 0.48, △ x = 0.42, □ x = 0.36, ○ x = 0.31. The values provided above the fitted lines are the LFER slopes. The data is also presented in Table 4.1.

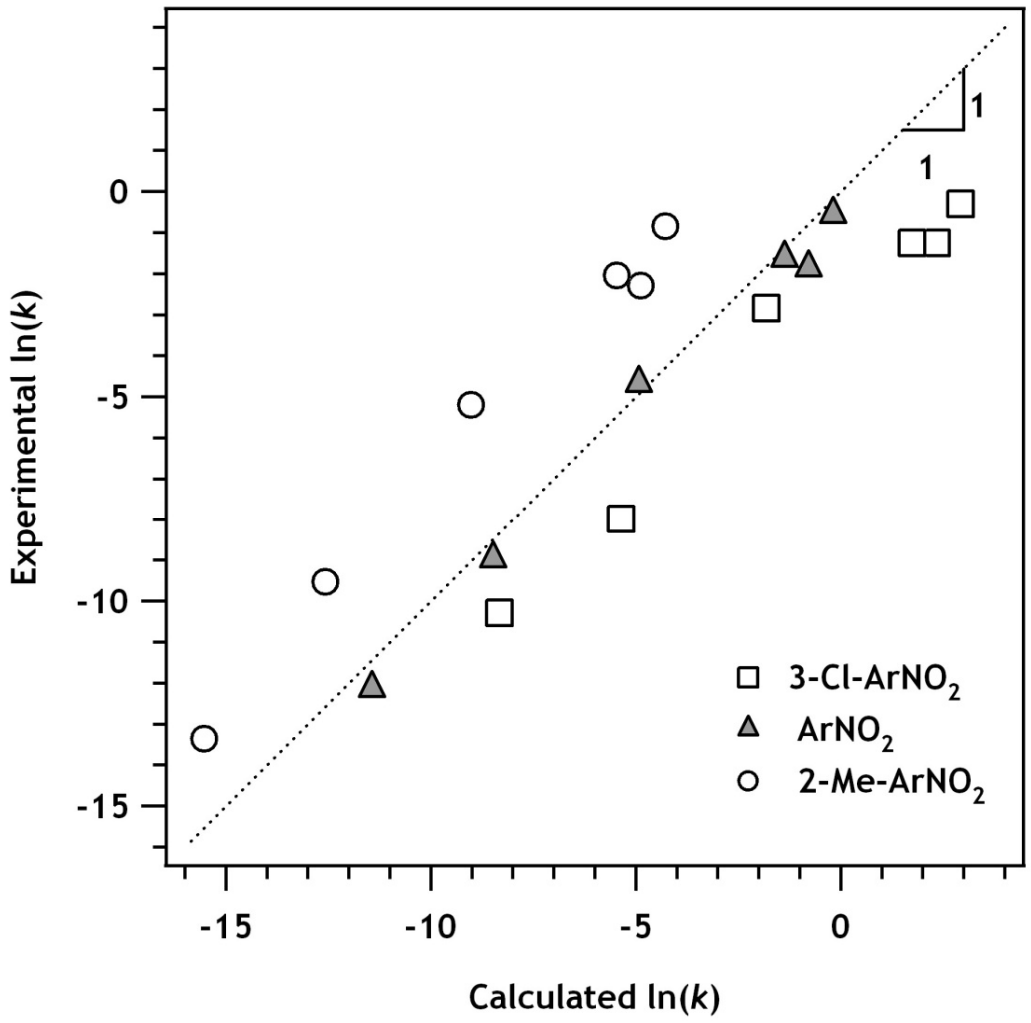

Figure 4.7. Comparison of experimentally measured k_{obs} values versus calculated k_{obs} values for R-$ArNO_2$ reduction by magnetites of varying stoichiometries. Experimental k_{obs} rates are the average of duplicate experiments. Calculated k_{obs} values were estimated from $E_h^{1'}$ values for R-$ArNO_2$ (Table 4.1) and E_{OCP} values for each magnetite stoichiometry (Table A.2). An example calculation is provided in Supporting Information, Appendix A.

CHAPTER V: A REDOX INDICATOR STUDY OF Fe^{2+}-DOPED Fe^{3+} OXIDES

Abstract

The interaction between dissolved Fe^{2+} and iron oxides is of great interest due to its relevance for subsurface biogeochemical reactions. Recent studies have brought traditional surface complexation models into question, providing researchers with the challenge of developing new models to incorporate more complex processes, such as interfacial electron transfer. Here, we explore Fe^{2+}-iron oxide reactions using viologen radicals as redox indicators to measure the redox potential of the system and the subsequent applicability of a semiconductor model. The presented work is in agreement with the semiconductor model, but cannot validate it with the contained information.

Introduction

Several studies have focused on Fe^{2+} uptake by iron oxides (20, 21, 26, 84, 135-142); the Fe^{2+}-iron oxide redox couple has been shown to be capable of reducing several environmental contaminants that are unreactive with dissolved Fe^{2+} alone, including nitroaromatics (14), heavy metals (20, 135), halogenated alphatics (143), pesticides (144), and disinfection byproducts (145). As a result, significant efforts have been made to model this system to interpret and predict contaminant fate in the environment. In the past, Fe^{2+} uptake by iron oxides was thought to be an adsorption reaction, where stable adsorbed Fe^{2+} atoms sit at the surface of an oxide, with their speciation (i.e., $\equiv$O-Fe^{2++} and $\equiv$O-Fe^{2+}-OH) dependent upon concentration and pH (20-22).

Recent studies, however, have questioned the accuracy of this model. Williams and Scherer demonstrated that Fe^{2+} taken up by several different iron oxides undergoes an interfacial electron transfer, where the Fe^{2+} atom becomes oxidized to Fe^{3+}, and the electron is transferred to the underlying oxide (24); this observation has been repeated elsewhere with identical conclusions (22, 26, 30, 146, 147). In this work, we have shown

that Fe^{2+} uptake by magnetite is controlled by a bulk property (i.e., the stoichiometry), and cannot be described using typical surface complexation models (SCMs).

SCMs have also been questioned in more practical experiments examining the fate of contaminants. In one study examining nitrobenzene reduction by Fe^{2+} reacted with goethite, the researchers found that nitrobenzene was rapidly reduced in the presence of dissolved Fe^{2+}, but if the dissolved Fe^{2+} was removed after sorption had occurred, the sorbed Fe^{2+} was unreactive with the nitrobenzene, which led to the conclusion that dissolved Fe^{2+} was necessary for the reaction to occur (24). In another study examining O_2 reduction by Fe^{2+} and ferrihydrite, the kinetics of O_2 reduction were dependent upon both the sorbed and dissolved Fe^{2+} concentrations (33). In both studies, the required presence of dissolved Fe^{2+} is a compelling line of evidence that reaction modeling cannot be done using only the sorbed Fe^{2+} concentration alone.

Researchers are now poised with two interesting questions: what controls the extent of Fe^{2+} uptake on an oxide if it is not the number of available surface sites, and what controls subsequent contaminant reduction rates? While some recent work has attempted to incorporate these new considerations into existing SCMs (21-23), other researchers have used more compelling approaches, including the application of a semiconductor model (33-35). In this model, an iron oxide particle acts as a semiconductor, and electrons transferred to the particle from Fe^{2+} atoms taken up from solution effectively dope the semiconductor with additional electrons; this results in electron rich sites (i.e., anode sites) and electron poor sites (i.e., cathode sites). These sites may be relatively near each other at the oxide surface (35), or may be present at different crystallographic faces (30).

If the semiconductor model were an accurate descriptor of the Fe^{2+}-iron oxide redox couple, it would have dramatic implications for simple sorption reactions. For example, the amount of Fe^{2+} taken up from solution by iron oxides typically increase as the particle size becomes smaller (i.e., the particle has higher surface area) (e.g., 148). In

the semiconductor model, however, the increased Fe^{2+} uptake on smaller particles can be explained an increase in crystalline defect trapping sites, a bulk crystalline parameter (149). Another common observation is that the amount of Fe^{2+} taken up by an oxide increases with increasing pH. In SCM, this is rationalized as the surface charge of the oxide becoming more negative as the pH increases (i.e., more OH^- surface groups), which results in an increased electrostatic attraction of Fe^{2+} atoms. In the semiconductor model, however, this shift could be due to the thermodynamic reactions occurring at the oxide surface upon sorption. A potential (*E*) would exist for the Fe^{2+}/Fe^{3+} redox couple occurring at the particle surface, a reaction which would be pH dependent, with the slope relating to the number of protons involved in the reaction. Note that such a model has already been applied with some success to redox measurements taken of the Fe^{2+}-iron oxide system, although it was explained using SCM (22).

In order to determine if the semiconductor model can accurately be used to describe the Fe^{2+}-iron oxide redox couple, validating experiments must be designed, specifically with respect to redox reactions occurring at the surface. Measuring the redox reactions occurring at the oxide-solution interface is, however, an experimentally difficult task. Using a potentiostat equilibrated with the particle suspension is challenging because it assumes that the equilibrium is reached and that there is no sorption onto the electrode. In a previous work, it was shown that for nanoparticulate suspensions, a potentiostat did not fulfill these assumptions (22). Another approach is the use of packed powder disk electrodes and electrodes coated with an oxide (127, 128, 150-153), both of these assume that the oxide is a good conductor, an assumption which is rarely validated. The use of contaminants with well-known reduction potentials is another redox probe that is commonly used (122-126), but these reactions are often irreversible and involve multiple electron transfer steps, which may complicate the interpretation of observations.

Previous work in the field of photochemistry has utilized soluble radical redox probes to determine the redox state of the solution (149, 154-159). The viologens (4,4'-

Bipyridine and its substituents) are commonly used due to their pH-independent one-electron reversible redox potentials which can be manipulated with functional groups (155, 160). A schematic representing the reduced and oxidized forms of methyl and benzyl viologen are shown in Figure 5.1. The viologens are also advantageous in that the reduced form ($V^{\bullet+}$) is blue, while the oxidized form (V^{2+}) is clear, making redox measurements simple with the use of a spectrophotometer (600 nm). The redox conditions of a solution can be determined using the Nernst equation:

$$E = E^{o} + \frac{RT}{nF} \ln \left({}^{C_R}/_{C_O} \right) \tag{5.1}$$

where E is the potential in V, E^o Is the standard potential (a constant for each viologen), R is the ideal gas constant, T is the absolute temperature, n is the number of electrons transferred (1 for viologen), F is Faraday's constant, C_R is the concentration of the reduced species ($V^{\bullet+}$), and C_O is the concentration of the oxidized species (V^{2+}). E^o for methyl viologen ($MV^{\bullet+}/MV^{2+}$) is -0.44 V vs. SHE, and E^o for benzyl viologen ($BV^{\bullet+}/BV^{2+}$) is -0.36 V vs. SHE. As a result, a redox equation for benzyl viologen can be written more simply as:

$$E = -0.36\,V - 0.0591 \times \log \left({}^{C_R}/_{C_O} \right) \tag{5.2}$$

where E can be solved if C_R and C_O are measured.

In this work, we found compelling evidence suggesting that viologen can indeed be used to measure the Fe^{2+}/Fe^{3+} redox couple at the oxide surface. Based on the fitted trend lines between E and solution conditions (e.g., pH), the relationships appear to be Nernstian, indicating that the semiconductor model may be accurately applied. Further work is needed, however, to accurately interpret the collected data.

Materials and Methods

The hematite and goethite samples used in this experiment were generously provided by Robert Handler; their synthesis was done using recipes found elsewhere (25,

88). The samples were both micron-scale particulates. The stoichiometric magnetite is described in Chapter IV.

All experiments were done within an N_2/H_2 (94/6) anaerobic chamber. Solids were allowed to equilibrate in the glovebox atmosphere several weeks prior to their use in experiments to avoid inadvertent oxidation. Solutions were buffered with 50 mM buffer, with the buffer selected to avoid complexation with Fe^{2+} atoms (MES, MOPS, PIPPS) (161). Isotherms were performed as described in Chapter III. After an equilibration period of 24 hours, viologen was added from a buffered stock solution to achieve the desired concentration. The viologen was added in the oxidized form (V^{2+}) to avoid the possibility of false-negatives (i.e., the appearance of reduction when there was no interaction between the solution and particle). The viologen concentration was measured with a spectrophotometer at 600 nm using a five point standard curve. The spectrophotometer was used within the glovebox, as the solutions were unstable in the presence of oxygen, even when the cuvettes were sealed. All potentials reported are in reference to the standard hydrogen electrode (SHE).

Results and Discussion

Validation of the use of viologen as a redox indicator

In order for viologen to be used as a redox indicator for the Fe^{2+}-iron oxide reaction, certain assumptions must be validated: (*i*) no sorption of the viologen can occur at the oxide surface, (*ii*) the measured C_R/C_O value must be independent of the initial concentration and speciation the added viologen, and (*iii*) the system must reach equilibrium and be reversible. Additionally, it is desirable to validate the method with a previously well-characterized system.

(*i*) To determine if viologen sorption was occurring at oxide surfaces, viologen isotherms were created with the concentration ranging from 25 to 1000 µM in buffered solutions at pH 7.8. The concentration of total viologen was measured before and after

the addition of the oxide. It was found that filtering the suspension resulted in significant sorption to the filter, so solids were separated using centrifugation. In these control experiments, there was no measurable shift in the soluble viologen concentration before and after the addition of the oxide, indicating that no sorption was occurring. Similar observations have been made in previous studies which used viologen and iron oxides (149, 157, 159). In all experiments, the amount of viologen added to a reactor was known, allowing for comparison between the theoretical and experimental total viologen concentrations; the viologen concentration was typically within 10 % of the expected value, with no bias in either direction (i.e., no consistent over- or under-estimation) (Tables 5.1-5.3).

(*ii*) If the measured *E* value were dependent upon the initial redox state and concentration of the added viologen, it would be difficult to determine what experimental conditions should be used. To determine if *E* was influenced by the viologen concentration, experiments were done in a model system of 1 g/L goethite with 1 mM Fe^{2+} at pH 7.8; benzyl viologen was added as BV^{2+} in concentrations ranging from 50 to 1000 µM (Figure 5.2). In these experiments, the amount of $BV^{\bullet+}$ measured was proportional to the total amount of benzyl viologen added, with the $BV^{\bullet+}/BV^{2+}$ appearing to be independent of the initial concentration. The measured *E* is a function of this ratio, and is shown to be consistent between samples (bottom panel of Figure 5.2, $\sigma = 0.002$ V). Note that the potential (-0.31 V) measured here is approximately 1100 mV lower than the aqueous Fe^{2+}/Fe^{3+} redox couple (+0.77 V).

(*iii*) Determining that a system has reached equilibrium is difficult to determine, as the kinetics of the reaction could be so slow that they would lead an observer to assume the reaction has stopped. In these experiments, the kinetics were measured qualitatively by the appearance of blue within the bottle. Typically, the color developed within a few seconds after the addition of the oxidized viologen, suggesting the kinetics were fast. A rapid kinetic study could not be done because reactors required 10 minutes

of centrifugation prior to measuring; experiments indicating that the equilibrium was reached within these 10 minutes (data not shown). Measurements were typically made after a 24 hour equilibration period where steady-state conditions based on solution measurements were achieved. In some experiments, measurements were taken at various time points, with no variation in results observed. Also, experiments where no viologen reduction was observed were not used, as the lack of reduction could have been either due to the redox conditions or slow kinetic rates; this was only observed for the hematite system at sufficiently low pHs that the expected potential was outside the measurable range with the benzyl viologen.

Discerning if the reaction is reversible requires that the reduced and oxidized states can transition between each other. Previous work has shown that hematite reduced by viologen is indeed a reversible reaction (149, 159); however, we could not conclusively determine if the reactions here were reversible. Because the $V^{\bullet+}/V^{2+}$ was stable with respect to time, it was assumed that a steady-state equilibrium had been reached. In other control experiments where Fe metal was used, this was not the case: rapid viologen reduction occurred over the first minute of exposure as observed by the solution turning dark blue, but when the reactors were examined after a few hours, the solution was clear. It is suspected that irreversible secondary reactions occurred for Fe^0, which is likely because the Fe^{1+} oxidation state is very unstable.

We have satisfied ourselves in demonstrating that viologen sorption, concentration-dependence measurements, and kinetics are not an issue when measuring *E*. The next step in validating this technique is to measure an already well-established redox potential. We chose stoichiometric magnetite, due to our previous work with the oxide. Magnetite is an ideal candidate for this validation because it is also a nanoparticulate suspension, and will likely address many similar potential problems for other particulate suspensions. For magnetite, *E* was measured as a function of pH values to compare with existing published values (Figure 5.3, Table 5.1). The fitted linear

regression of the data is E = 0.214 - 0.060[pH] V. The Pourbaix reference equation of magnetite oxidation is E = 0.221 - 0.059[pH], with the following half reaction (162):

$$Fe_3O_4 + {}^1/_2H_2O \leftrightarrow {}^3/_2Fe_2O_3 + H^+ + e^- \quad (5.3)$$

The excellent agreement between the two equations suggests that the use of viologens as a method to determine the redox state of suspended nanoparticles (Figure 5.4).

The Fe^{2+}-hematite redox couple

In this work, the interaction of Fe^{2+} and hematite was used as a model system, but it should be noted that the techniques outlined here could be applicable to other Fe^{2+}-iron oxide systems. In the hematite experiments, the pH, solids concentration, and Fe^{2+} concentration were varied to determine their affect on the measured redox potential. First, experiments were done with hematite exposed to Fe^{2+} as a function of pH (Figure 5.5, Table 5.2). Here, 1 mM Fe^{2+} was equilibrated with 2 g/L hematite prior to the addition of viologen. E decreases with increasing pH, as expected. The observed slope of the line is 0.120, near the slope expected for a system where the sorption of an Fe^{2+} atom displaced two H^+ (0.118). Silvester et al. have proposed the following model for Fe^{2+} sorption followed by electron transfer to the underlying oxide (22):

$$\equiv Fe^{3+}OFe^{2+} + \frac{3}{2}H_2O \leftrightarrow \equiv Fe^{3+}OH + \frac{1}{2}Fe_2O_3 + 2H^+ + e^- \quad (5.4)$$

To gain insight into how the amount of Fe^{2+} added influences the reaction, varying amounts of Fe^{2+} were equilibrated with hematite at a constant pH of 7.8. The amount of Fe^{2+} sorbed was measured for each reactor, with a traditional sorption isotherm created (Figure 5.6, Table 5.3). The behavior here is typical for the sorption of Fe^{2+} on hematite, where a steep slope is observed for lower concentrations of Fe^{2+}, and a shallower slope is observed at higher initial Fe^{2+} concentrations (26).

To gain a better understanding of the redox conditions in terms of the isotherm, benzyl or methyl viologen was added to each reactor in the isotherm in Figure 5.6; E was

then determined for each point. Determining how to relate *E* to the bulk conditions is, however, a difficult task because it is unclear what values to use for C_R and C_O. It is common to use only the dissolved species in determining a potential (22, 163), which would result in the following equation:

$$E = E^o - \frac{0.0591}{\mathrm{n}} \log\left(\mathrm{Fe}^{2+}_{\mathrm{dis}}\right) \tag{5.5}$$

where E_o and n can be determined by plotting *E* vs. log(Fe^{2+}). When this is done (Figure 5.7), a good linear fit is observed: E = -0.280 - 0.0298*log(Fe^{2+}_{dis}). The E_o value (-0.280 V) is approximately 1000 mV lower than for the Fe^{2+}/Fe^{3+} aqueous redox couple (+0.77 V). Also, the slope appears to agree incredibly well with that predicted for a Nernstian relationship where n = 2 (m_{theor} = 0.0296, m_{obs} = 0.0298). This slope indicates a two electron transfer, which seems unlikely, unless hyrodxyl ligands were also participating in the electron transfer reaction.

Another, less conventional model can also be used to interpret the data. Park and Dempsey argued that the kinetics of O_2 reduction by the sorbed Fe^{2+}-ferrihydrite system was best described with the following relationship (33):

$$R = \frac{d[Fe^{2+}]}{dt} = -\mathrm{k}\left[\mathrm{Fe}^{2+}_{\mathrm{dis}}\right]\left[\mathrm{Fe}^{2+}_{\mathrm{sorb}}\right][\mathrm{O}_2] \tag{5.6}$$

If this were an accurate model, it would appear that the sorbed Fe^{2+} is also influencing the redox state of the solution, and should thus be included in the Nernstian model. If the sorbed Fe^{2+} is "oxidized" phase, and the dissolved Fe^{2+} remains the "reduced phase," the following Nernstian equation can be used:

$$E = E^o - \frac{0.0591}{\mathrm{n}} \log\left[\frac{\mathrm{Fe}^{2+}_{\mathrm{dis}}}{\mathrm{Fe}^{2+}_{\mathrm{sorb}}}\right] \tag{5.7}$$

where E_o and n can be again be determined by plotting *E* vs. log(Fe^{2+}_{dis}/ Fe^{2+}_{sorb}). Note that the dissolved Fe^{2+} phase is the reduced phase, because it can become oxidized at the particle, but cannot undergo further reduction. Using this relationship, a strong linear trend is again observed (Figure 5.8). Despite the data being somewhat noisier than in

Figure 5.7 (R^2 = 0.85 (Figure 5.8) vs. 0.96 (Figure 5.7)), a strong linear correlation is still observed. The observed trend is E = -0.278 – 0.056*log[Fe^{2+}_{dis}/ Fe^{2+}_{sorb}] V. In this case, the observed slope is near that of a one electron transfer step (i.e., 0.059).

The trends observed in the models is both compelling and concerning. The observed slopes are similar to those expected using the Nernst equation, but that is not necessarily evidence to support their accuracy in describing the system. It is interesting, however, that both models yield virtually the same E^o (i.e., the y-intercept; -0.280 (Figure 5.7), -0.278 (Figure 5.8)). For the prior model, which only accounts for dissolved Fe^{2+}, there are some conceptually difficult issues to rectify: for example, if the oxide were not added to the system, then the dissolved Fe^{2+} concentration would be larger, yet the potential would be higher also. Some solid has to be present in the system, yet this model clearly cannot account for how much there is, as it is only examining the dissolved phase. As a result, the latter model appears to be better in this respect, although it there is not a good theoretical reason for incorporating the sorbed phase in these calculations (163).

It remains unclear if the trends observed here are indicative that this type of modeling can be a useful means for describing reversible environmental redox reactions. Good agreement between model and theory is not indicative in itself, although it is encouraging. Note that Silvester et al. used a method to explore the redox reactions occurring at oxide surfaces, but interpreted the data within the framework of SCM (22). The data does, however, confirm the capability of viologen radicals to make redox measurements that would be difficult using more conventional methods. Further work is still needed to determine if the measured potentials can in themselves be used to produce a theoretical sorption isotherm in good agreement with those measured experimentally.

Table 5.1. Viologen concentrations and measured redox potential for stoichiometric magnetite at varied pHs. Experimental conditions: [Fe_3O_4] = 1 g/L, [Viologen] ≈ 250 µM, Eq. time = 24 hrs. The data is presented in Figure 5.2.

pH	Viologen	$V^{\bullet+}$ (µM)	V^{2+} (µM)	V_{total} (µM)	$V^{\bullet+}/V^{2+}$	*E* (V)
7.40	BV	1.3	255.8	257.1	0.0050	-0.22
7.77	BV	2.6	258.6	261.2	0.0099	-0.24
8.10	BV	5.8	247.2	253.0	0.0235	-0.26
8.22	BV	7.9	234.3	242.2	0.0338	-0.27
8.83	BV	49.6	185.9	235.5	0.2668	-0.33
9.65	MV	16.2	230.1	246.3	0.0703	-0.37
10.15	MV	43.4	184.0	227.3	0.2357	-0.40
10.05	MV	46.5	207.8	254.4	0.2240	-0.40
12.68	MV	261.2	8.1	269.3	32.1667	-0.53

Table 5.2. Redox potential measured viologen at a series of pH values for the hematite-aqueous Fe^{2+} system. The data is also shown in Figure 5.3. Experimental conditions: [hematite] = 2 g/L; [Fe^{2+}] = 1 mM; [Viologen] = 250 µM; sorption eq. time = 24 hours, viologen eq. time = 24 hours. Note the pH and extent of Fe^{2+} uptake were not measured after equilibration.

pH	Viologen	$V^{\bullet+}$ (µM)	V^{2+} (µM)	$V^{\bullet+}/V^{2+}$	*E* (V)
7.4	BV	0.40	249.60	0.0016	-0.19
7.8	BV	1.46	248.54	0.0059	-0.23
8.2	BV	11.98	238.02	0.0503	-0.28
8.6	BV	62.82	187.18	0.3356	-0.33
8.2	MV	0.90	249.10	0.0036	-0.30
8.6	MV	3.32	246.68	0.0135	-0.33

Table 5.3. Isotherm and viologen redox data collected for the hematite-aqueous Fe^{2+} system. The data is also shown in Figures 5.6-5.8. Experimental conditions: [hematite] = 2 g/L; pH = 7.8, 50 mM PIPPS; [Viologen] = 200 µM (BV) or 450 µM (MV); sorption eq. time = 24 hours, viologen eq. time = 24 hours.

Fe^{2+}total (µM)	Fe^{2+} aq. (µM)	Fe^{2+} sorbed (µM)	Viologen	$V^{\bullet+}$ (µM)	V^{2+} (µM)	V_{total} (µM)	$V^{\bullet+}/V^{2+}$	*E* (V)	E^{oa} (V)
163	12	150	BV	6.4	193.9	200.3	0.033	-0.27	-0.208
338	12	327	MV	3.9	447.1	451.0	0.009	-0.32	-0.402
354	5	349	BV	14.9	193.5	208.4	0.077	-0.29	-0.398
540	24	516	BV	31.9	156.2	188.1	0.205	-0.32	-0.402
732	55	677	BV	7.1	439.4	446.5	0.016	-0.33	-0.399
753	45	708	MV	51.7	156.7	208.4	0.330	-0.33	-0.398
969	82	888	BV	72.3	171.3	243.6	0.422	-0.34	-0.404
1135	119	1016	MV	8.7	425.6	434.4	0.021	-0.34	-0.398
1155	152	1003	BV	85.4	127.1	212.4	0.672	-0.35	-0.395
1508	236	1272	MV	11.6	421.3	432.9	0.028	-0.35	-0.391
1713	292	1420	MV	14.2	427.8	441.9	0.033	-0.35	-0.393
2271	582	1688	MV	18.4	413.0	431.4	0.045	-0.36	-0.387

[a] E^o is calculated using the measured *E* for viologen and the $Fe^{2+}_{aq.}/Fe^{2+}_{sorbed}$ redox couple plugged into the Nernst equation. This value can be interpreted as the E^o of Fe^{2+} sorption on hematite at pH 7.8.

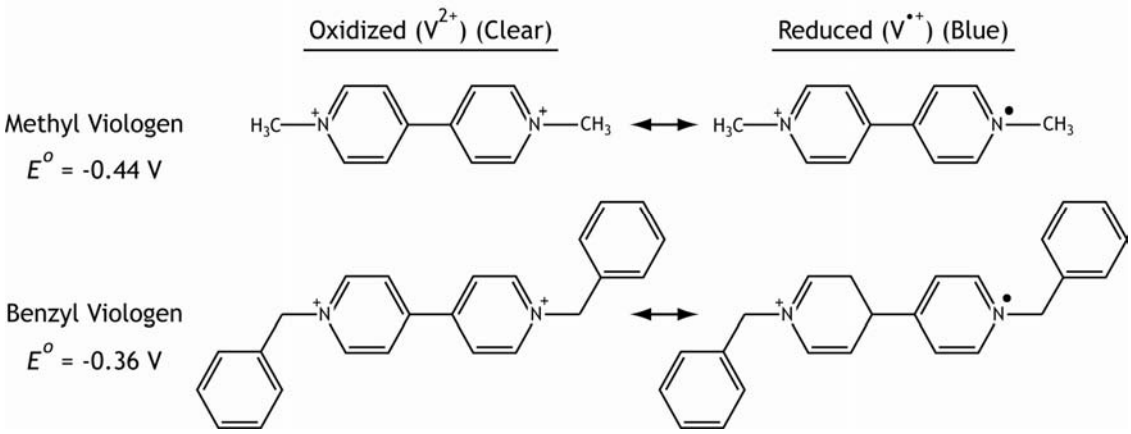

Figure 5.1. The oxidized ($V^{\bullet+}$) and reduced (V^{2+}) forms of methyl viologen (MV) and benzyl viologen (BV).

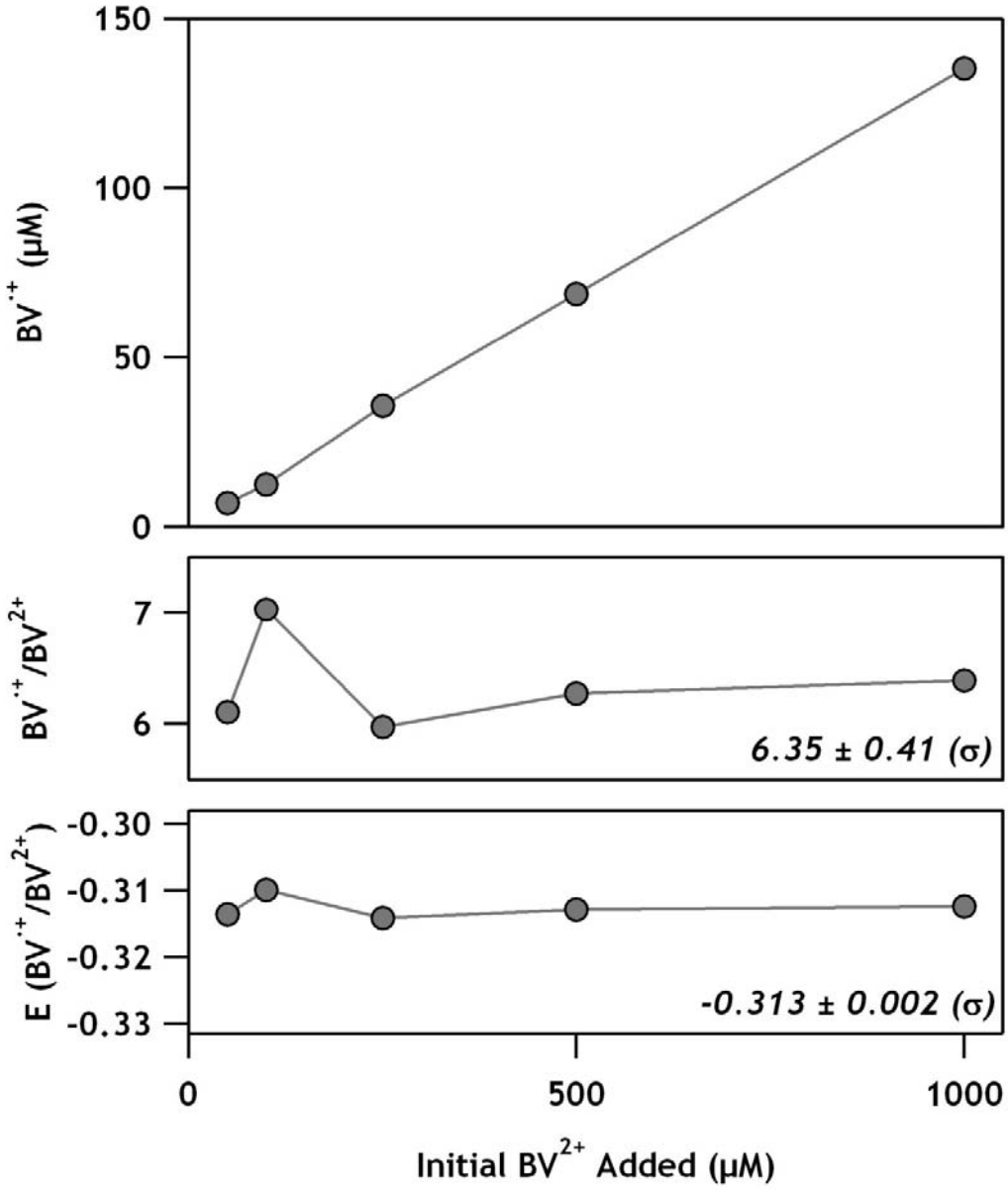

Figure 5.2. The amount (top) of $BV^{\bullet+}$ as a function of the amount of viologen added. (Middle) The ratio of reduced to oxidized benzyl viologen ($BV^{\bullet+}$ / BV^{2+}). (Bottom) The calculated *E* found by setting C_R/C_O = $BV^{\bullet+}$ / BV^{2+} in equation 5.2. Experimental conditions: 1 g/L goethite; 50 mM PIPPS, pH 7.8; [Fe^{2+}] = 1 mM; sorption eq. time = 24 hours, viologen eq. time = 24 hours.

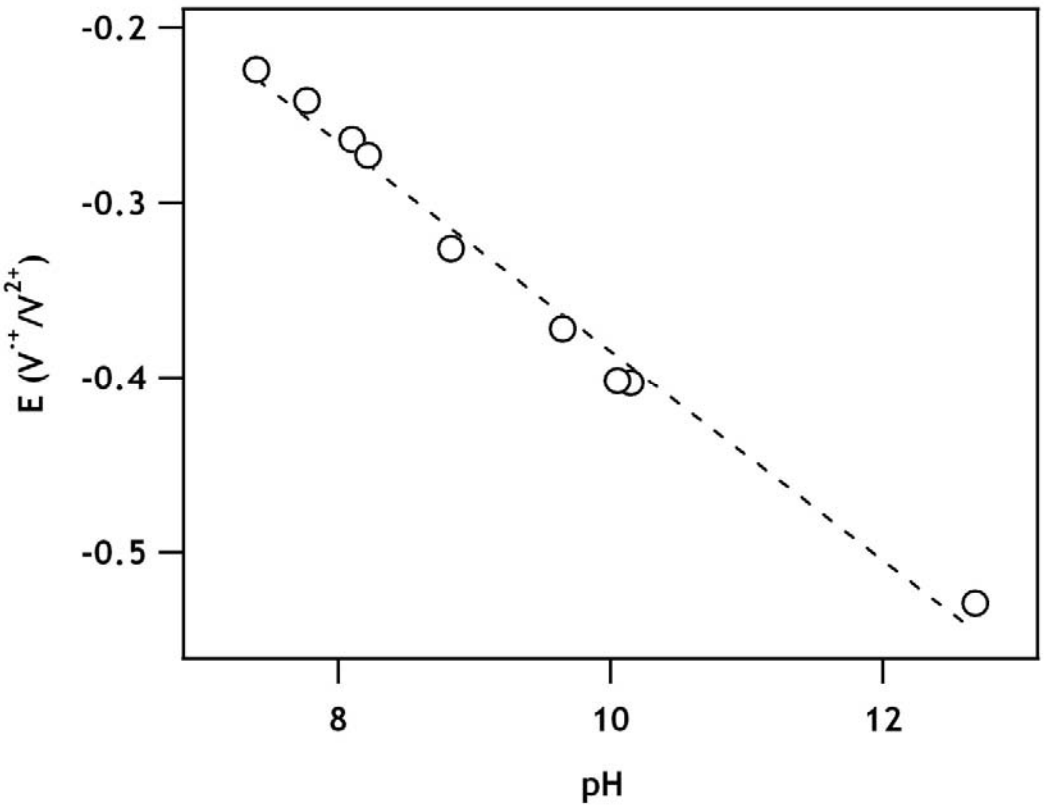

Figure 5.3. The measured potential (*E*) of stoichiometric magnetite as a function of pH using benzyl and methyl viologen as redox indicators. The linear regression shown is $E = 0.214 - 0.0598[pH]$; $R^2 = 0.99$. Experimental conditions: 1 g/L magnetite, 100 µM viologen as benzyl or methyl viologen. The viologen used for each data marker can be found in Table 6.1.

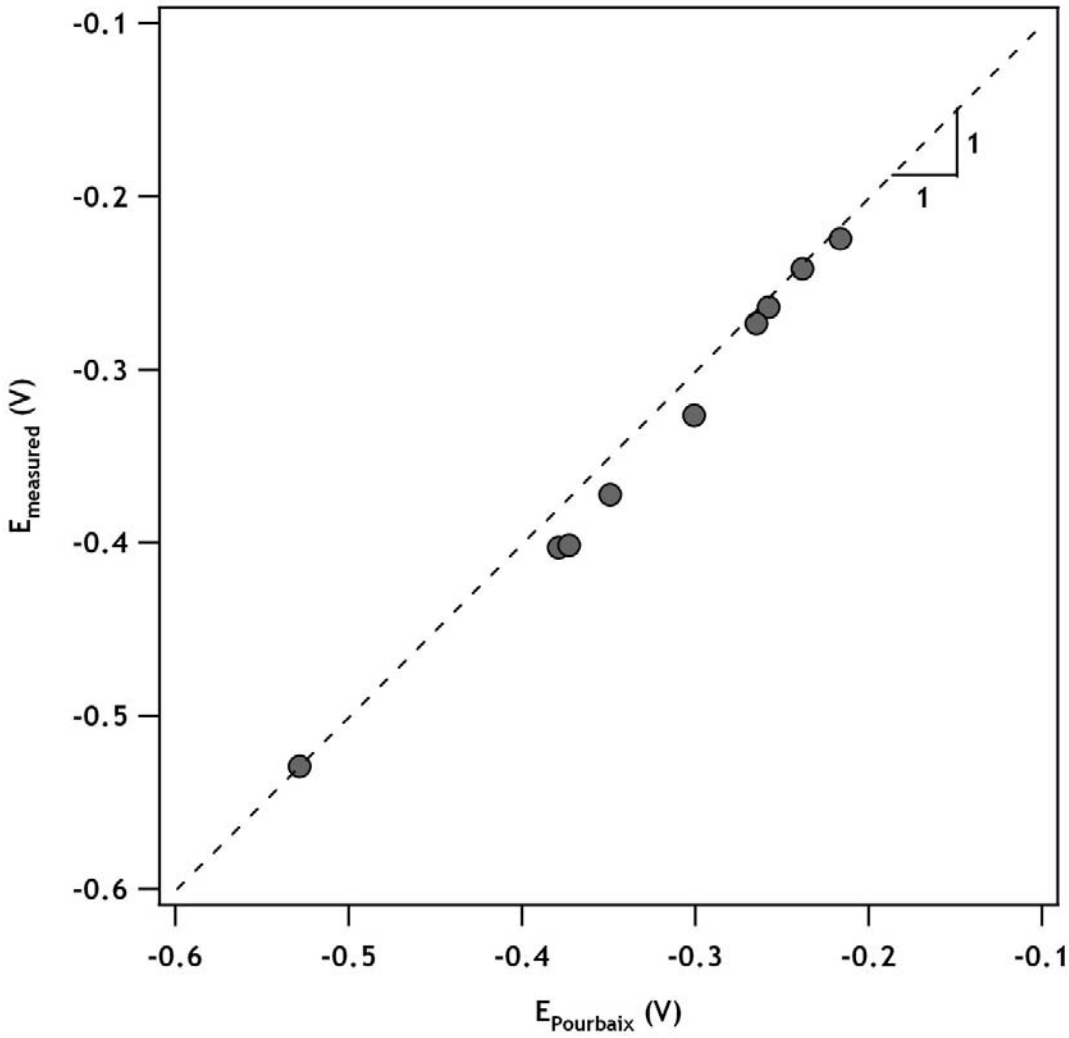

Figure 5.4. Redox potential measurements made using viologen ($E_{measured}$) compared the reference reference values calculated using the Pourbaix equation ($E_{Pourbaix}$).

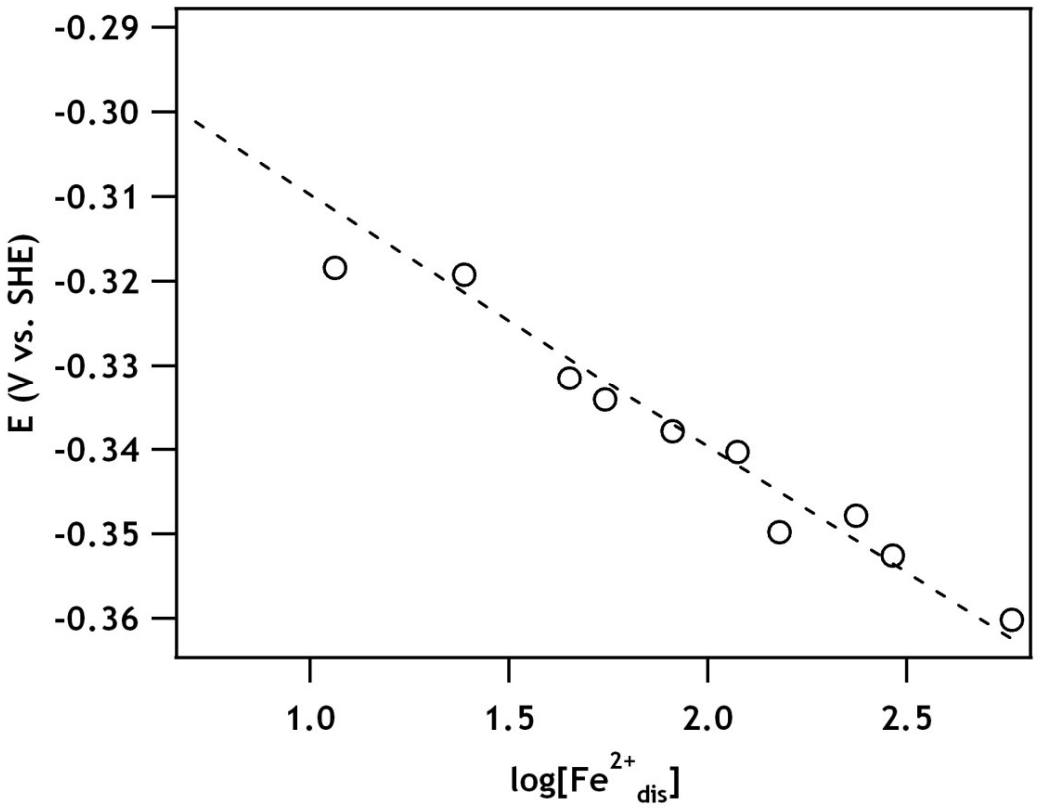

Figure 5.5.The potential using viologen of 1 mM Fe^{2+} equilibrated with 2 g/L hematite as a function of pH. The fitted line yields $E = -0.120[Fe^{2+}] + 0.57$; $R^2 = 0.99$.

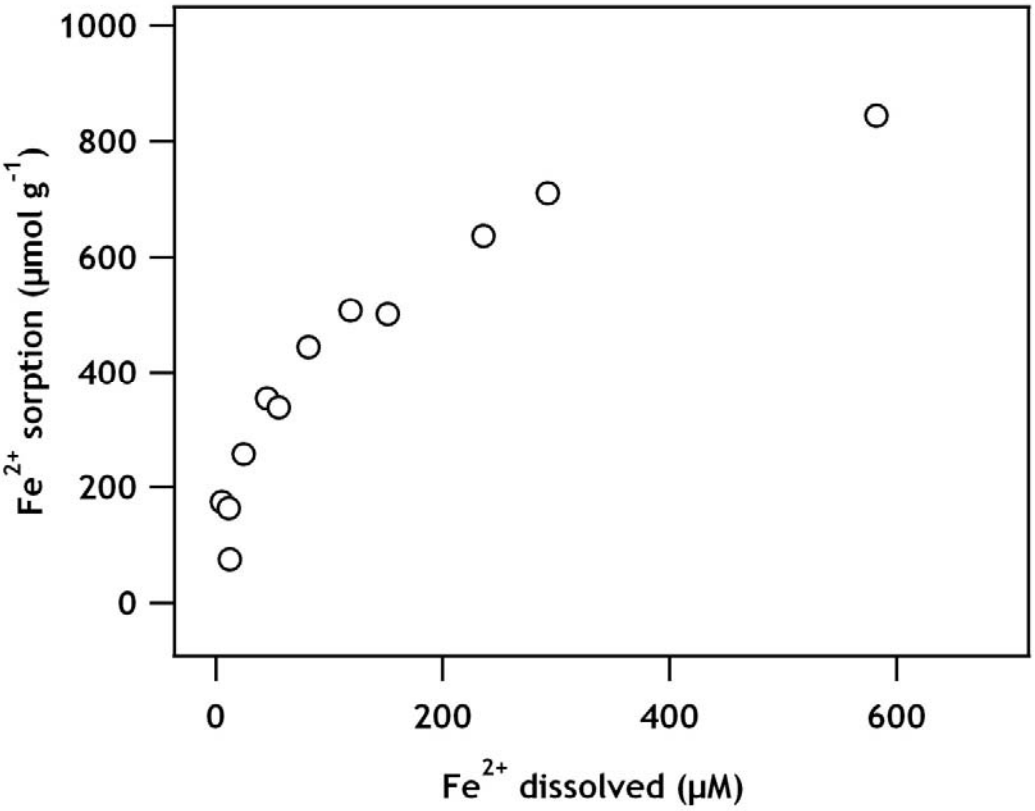

Figure 5.6. Fe^{2+} sorption isotherm for 2 g/L hematite at pH 7.8. Experimental conditions: 50 mM PIPPS buffer; eq. time = 24 hrs. The equilibrium concentrations of Fe^{2+} were measured after the addition of viologen, with slightly more Fe^{2+} being removed from solution as the viologen became reduced.

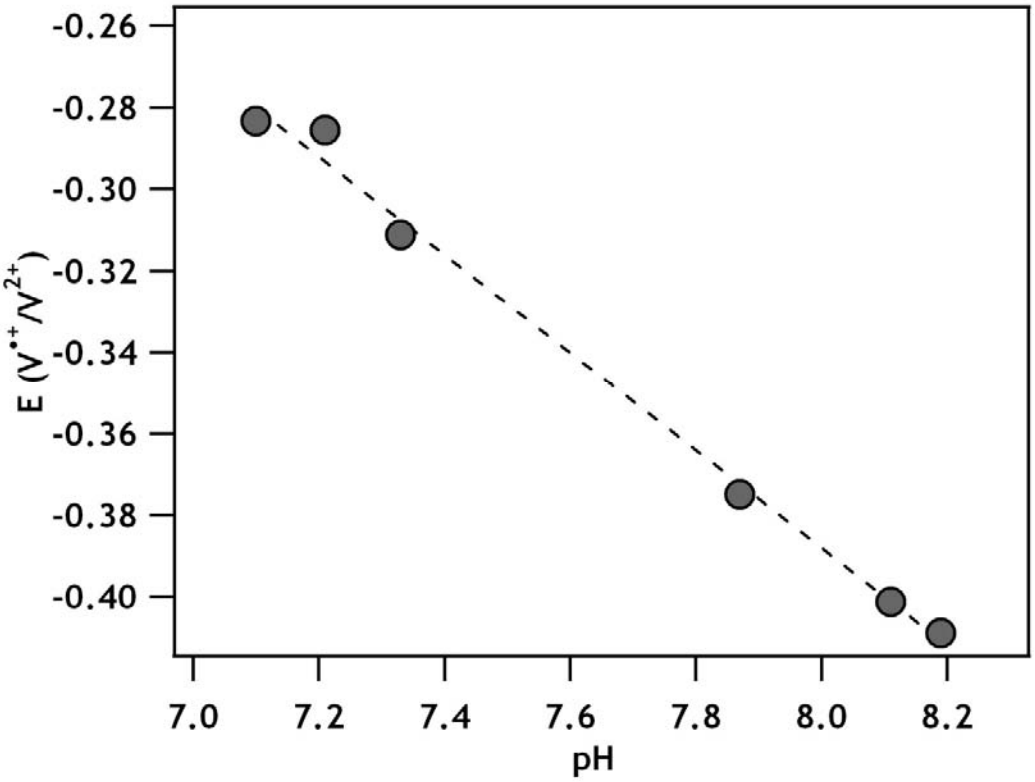

Figure 5.7. The measured potential using viologen vs. the log of the equilibrium dissolved Fe^{2+} concentration after sorption (same data set as Figure 5.6). The fitted line yields E = -0.0298[Fe^{2+}_{dis}] - 0.230; R^2 = 0.96. Experimental conditions: 2 g/L hematite, pH 7.8.

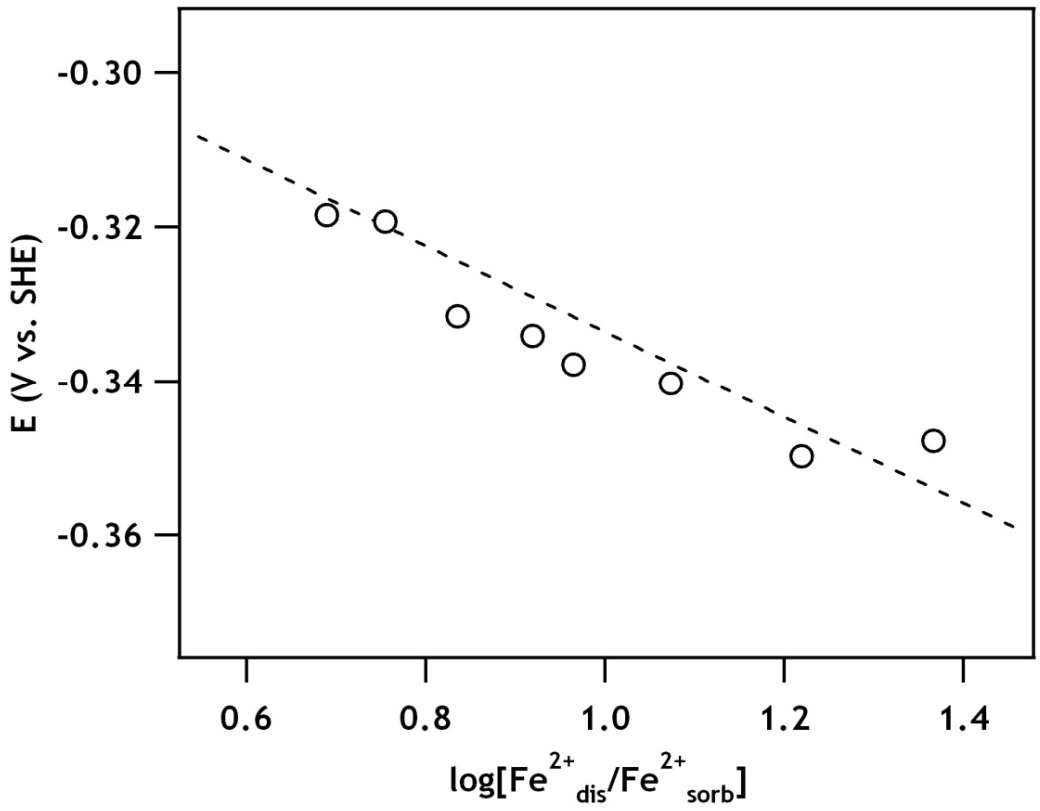

Figure 5.8. The measured potential using viologen vs. log ratio of the equilibrium dissolved Fe^{2+} concentration and the sorbed Fe^{2+} concentration after sorption (same data set as Figure 5.6). The fitted line yields E = -0.0556[Fe^{2+}_{dis}] - 0.278; R^2 = 0.85. Experimental conditions: 2 g/L hematite, pH 7.8.

CHAPTER VI: MÖSSBAUER SPECTROSCOPY OF Fe^{2+} SORBED ON ENVIRONMENTALLY RELEVANT SURFACES: A CRITICAL REVIEW

Abstract

Ferrous iron (Fe^{2+}) readily sorbs to several substrates commonly found in the environment, including bacteria and several mineral species, under anaerobic conditions and neutral pH values. These sorbed species have been shown to influence contaminant fate, metal and nutrient cycling, and microbial respiration. Little spectroscopic data is available characterizing sorbed Fe^{2+}, making it difficult to discern broad trends between samples. Here, we characterized sorbed Fe^{2+} on a suite of environmentally relevant samples (i.e., Fe-free clays, Ti and Al oxides, and cells) using cryogenic ^{57}Fe Mössbauer spectroscopy. Collected hyperfine parameters for sorbed Fe^{2+} were identical to several structural Fe^{2+} forms, making it impossible to fingerprint sorbed Fe^{2+} using the hyperfine parameters alone. Nearly all samples analyzed exhibited spectral asymmetry, however, which is hypothesized here to be an indicator of sorbed Fe^{2+} in environmental samples. Fe^{2+} sorbed to functionalized beads was used as an analog for more complex cell surfaces, and was consistent with Fe^{2+} sorbing preferentially to carboxyl and phosphate functional groups, although it was not conclusive. Mössbauer spectra were collected for $^{57}Fe^{2+}$ exposed to γ-Al_2O_3 at several pH values and Fe^{2+} concentrations to discern trends between bulk solution conditions and Mössbauer hyperfine parameters.

Introduction

At neutral pHs, ferrous iron (Fe^{2+}) will readily sorb to several substrates commonly found in the environment, including clay minerals, metal oxides, and bacteria (21, 23, 164-173). Under anaerobic conditions, sorbed Fe^{2+} forms a stable Fe^{2+} surface complex for some substrates (e.g., Al and Ti oxides) (24, 164, 165), while for others, a more complex reaction occurs, which involves electron transfer between the Fe^{2+} atom

and the underlying solid phase (e.g., Fe^{3+} oxides, clay minerals) (23, 24, 29, 30, 74). This work focuses only on redox inactive substrates (i.e., a stable, sorbed Fe^{2+} species) and our ability to spectroscopically characterize these phases.

Sorbed Fe^{2+} is a critical groundwater substituent to several processes including redox buffering, contaminant fate, microbial respiration, and microbial metabolism (166-169). Previous studies have shown that sorbed Fe^{2+} on clay minerals as well as Al and Ti oxides is capable of reducing and degrading environmental contaminants which are not reactive with dissolved Fe^{2+} alone, including nitroaromatics, Se^{6+}, and Tc^{7+} (165, 169-172). Two recent works have confirmed that Fe^{2+} sorbed on Al and Ti oxides is a stronger reductant (lower E_h) than dissolved Fe^{2+} (172, 173). For dissimilatory iron reducing bacteria (DIRB), Fe^{2+} sorbed on cells was shown to diminish the ability of the cells to respire on Fe^{3+} oxides and nitrate (166, 167), and other works have argued that sorbed Fe^{2+} on cells significantly influences the mineralogy of Fe in the environment (e.g., 174).

Despite the importance of Fe^{2+} sorption to biogeochemistry, sorbed Fe^{2+} is largely uncharacterized using spectroscopic methods, which is likely due to its amorphous structure and low abundance within the sample. For example, sorbed Fe^{2+} is completely invisible to powder X-ray diffraction. In most studies, Fe^{2+} sorption is examined only indirectly, by measuring the amount of dissolved Fe^{2+} removed from solution after addition of the solid phase (21, 164, 172, 175). Spectroscopic techniques have been used in some systems, including XAFS and Mössbauer spectroscopy, but these techniques are so rarely used that it is difficult to discern if the conclusions drawn in each study can be applied to broader scopes (23, 176, 177). This lack of spectroscopic data presents a gap in our understanding of Fe^{2+} sorption and its environmental implications.

Instead of spectroscopy, surface complexation modeling (SCM) is used more commonly to describe Fe^{2+} sorption behavior on environmental surfaces (21, 164, 172, 175). SCM is a valuable technique, and can aid in understanding what is occurring at the

molecular solid-solution interface. The application of SCM can be presumptuous in some cases, however, and is troubling in that it will provide an answer that is often unchecked with complementary techniques. For example, SCM has produced well-fitting models for Fe^{2+} sorption of Fe^{3+} oxides (20-22, 178, 179), yet spectroscopic data indicates that a stable, sorbed Fe^{2+} complex does not exist under these conditions (22, 24, 26, 74). In two studies that used SCM coupled with Mössbauer spectroscopy for Fe^{2+} sorption on an Fe-free montmorillonite and goethite (α-FeOOH), significant oxidation of Fe^{2+} was observed in the absence of oxygen or an aqueous electron acceptor, yet SCM produced excellent model fits assuming the formation of stable, sorbed Fe^{2+} (22, 23). In general, the precision with which SCM can model experimental data is not indicative that it is an accurate descriptor of molecular scale reactions.

In this study, our goal was to rigorously characterize sorbed Fe^{2+} on a suite of environmentally-relevant surfaces using Mössbauer spectroscopy, with subsequent interpretation of measured hyperfine parameters. We aimed to (*i*) determine in Mössbauer spectroscopy could be used to fingerprint samples by their hyperfine parameters, (*ii*) access if additional information could be extracted from the hyperfine parameters (e.g., bond strength to the surface), and (*iii*) to provide the community with a collection of data for reference in future studies aiming to characterize sorbed Fe^{2+}.

We examined Fe^{2+} sorbed on three primary surfaces: (*i*) Fe-free clay minerals, (*ii*) Al and Ti oxides, and (*iii*) cell surfaces and functionalized bead surfaces. The hyperfine parameters grouped into two different ranges: one containing Fe^{2+} sorbed on Al and Ti oxides and clays, and the other containing the cells and functionalized bead surfaces. Positive correlations were observed between the center shifts and quadrupole splitting for the clay and oxide samples was in agreement with previous findings for structural Fe^{2+} (180, 181). From the data sets, we concluded that the hyperfine parameters for sorbed Fe^{2+} overlap with those found for structural Fe^{2+} in many commonly occurring minerals.

The appearance of asymmetry within the spectra, however, is a rarely observed phenomenon, and may be used as an indicator for sorbed Fe^{2+} in the future.

We characterized Fe^{2+} adsorbed to cell surfaces to elucidate the relevant functional groups present at the cell interface. It has been proposed in the literature that Fe^{2+} primarily bonds to amine, phosphate, and carboxyl groups at the cell surface based on titration data (182-184). To probe this hypothesis, we exposed Fe^{2+} to four species of DIRB (*Shewanella puterfaciens* CN32, *Shewanella oniedensis* MR1, *Shewanella alga* BrY, and *Geobacter sulfurreducens*), the soil bacterium *Bacillus subtilis*, and polystyrene beads labeled with six different functional groups: amine (≡R-NH_2), hydroxyl (≡R-OH), phosphate (≡ROP(=O)$(OH)_2$), carboxyl (≡R-C(=O)OH), suflate (≡R-SO_3H), and sulfonate (≡R-SO_2R'). Mössbauer spectra were then collected and fitted for all samples, allowing for comparison of the collected hyperfine parameters.

For the oxides and Fe-free clay samples, we gained a better understanding of how Fe^{2+} interacts with the substrate using the collected Mössbauer hyperfine parameters; for example, the relative strength of the ligand bond can be elucidated using the center shift (CS) and quadrupole splitting (QS) (8, 65, 67, 68, 185). To explore the relationship of bulk observations to spectroscopic data, we collected a Fe^{2+} sorption isotherm and a pH-edge using γ-Al_2O_3, with Mössbauer spectra collected for each point. This allowed for comparison of hyperfine parameters to bulk experiment techniques (e.g., CS vs pH). The trends observed between the CS and QS and the bulk solution conditions (i.e., concentration of Fe^{2+} and pH) were consistent with predictions, such as stronger bonds were observed when more Fe^{2+} was taken up from solution, although some hyperfine-bulk correlations could not be explained.

Materials and Methods

Sorption Experiments

All experiments were conducted within a N_2/H_2 (94/6) anaerobic glovebox with the atmospheric oxygen concentration below 1 ppm. All aqueous solutions were made from deionized (> 18 Ω) water, and were degassed by purging with N_2 gas for at least one hour, followed by equilibration within the anaerobic glovebox atmosphere for several days. All solids were weighed outside the glovebox, then allowed to equilibrate in the anaerobic atmosphere several weeks prior to use in sorption experiments. A $^{57}Fe^{2+}$ solution was prepared from acidic dissolution of 57-enriched Fe^0 (96%) in 1 M HCl in the anaerobic chamber. The pH was then raised with 10 M NaOH until slight precipitation occurred, then the filtered through a 0.2 µm filter to remove trace Fe^{3+}, followed by lowering the pH with 5 M HCl to a pH below 1.

Sorption experiments were done using a solution buffered to the desired pH with 25 mM either 3-(*N*-morpholino)propaesulfonic acid (MOPS; pKa = 7.2), piperazine-*N*,*N'*-bis(2-ethanesulfonic acid) (PIPES; pKa 7.1), or piperazine-*N*,*N*"-bis(3-propanesulfonic acid) (PIPPS; pKa = 8.0). Control experiments with carboxyl beads indicated that the buffer selected had no influence on the measured hyperfine parameters. For sorption experiments, the buffered solution was spiked with the $^{57}Fe^{2+}$ stock to reach the desired concentration, followed by an addition of 1 M NaOH to the desired pH. The solution was mixed at least two hours and was subsequently filtered (0.2 µm) to remove trace precipitates. The degassed solids were then added to the solution to reach the desired concentration, and allowed to mix in the absence of light (10 hours for Al_2O_3 and cell experiments, 24 hours for all others). The solids were then filtered using a filtering housing with a removable filter paper. The filter paper was sealed between two pieces of 5 mm Kapton tape to avoid inadvertent oxidation when transferring the sample to the

Mössbauer spectrometer. Aqueous Fe^{2+} measurements were taken before and after the addition of the solids using the 1-10-phenanthroline method (89).

Polystyrene Bead Samples

Functionalized polystyrene beads were purchased from three vendors: Magsphere (Pasadena, CA, US; www.magsphere.com), Bangs Laboratories, Inc (Fishers, IN, US; www.bangslabs.com), and Kisker (Germany; www.kisker-biotech.com), with the details for each functional group shown in Table 6.1. The diameter of the beads ranged from 0.50 to 1.26 µm. For all experiments, the beads were washed in 25 mM PIPPS four times to remove surfactants from the solution, with supernatant separated after centrifugation and the final amount of volume added to reach a solids concentration of 12 g/L using the mass/volume value provided by the suppliers. The beads were then purged with N_2 gas for approximately one hour, then were taken into an N_2/H_2 glovebox, and allowed to equilibrate in the atmosphere for at least one day prior to using.

For sorption experiments, 5 mL of 12 g/L bead solution was added to 10 mL of buffered $^{57}Fe^{2+}$ solution to achieve a final volume of 15 mL, with 4 g/L beads, and 1 mM Fe^{2+}. The solution was allowed to equilibrate 24 hours, followed by filtration and Mössbauer sample preparation. The final Fe^{2+} concentration was measured, but because the experiment involved dilution by adding two solutions, the measured concentration was not as precise as in other experiments.

Oxide and clay samples

Aluminum oxides (γ-Al_2O_3 and α-Al_2O_3) were purchased from Alfa Aesar (Ward Hill, MA). TiO_2 were purchased from Nanostructured and Amorphous Materials, Inc. (Houston, TX) (5 nm) and Alfa Aesar (Ward Hill, MA) (32 nm); both were characterized as anatase by the supplier, and are described in more detail elsewhere (186).

The three clay samples used for sorption experiments were synthetic, and free of Fe and other redox active elements. All were purchased from the Clay Mineral Society

Source Clays Repository (US; www.clays.org). Montmorillonite (SYn-1 Barasym SSN-100 synthetic mica-montmorillonite) was produced by NL Industries, laponite (SYnL-1) is from Southern Clay Products, Inc., and hecotrite (SynH-1) was synthesized by Optigel-SH United Catalysis, Inc. All clays were used as provided with no further treatment or characterization.

Cell samples

Shewanella putrefaciens CN32, *Shewanella oniedensis* MR1, *Shewanella alga* BrY, and *Bacilis subtilis* were kindly provided from Dr. Michael Leonardo (Coe College). These cells were grown aerobically in trypic soy broth and mineral medium. *Geobacter sulfurreducens* was grown under anaerobic conditions and was kindly provided from Dr. Eric Roden (University of Wisconsin). The density of all cell suspensions was on the order of 10^{10} cells mL^{-1} (personal communication, Dr. Michael Leonardo, Coe College).

Mössbauer spectroscopy

Transmission Mössbauer spectroscopy was performed with a variable temperature He-cooled system with a 1024 channel detector. The ^{57}Co source used (~50 mCi) was in a Rh matrix at room temperature. All center shifts reported are relative to α-Fe foil at room temperature. Samples were prepared by sealing the powder specimen between two pieces of 5 mL Kapton Tape to avoid oxidation while mounting the sample. Spectra were collected on ±6 mm/s velocity scale for all samples to increase precision in fitting. 4.2 K spectra were collected by Aaron Williams (USEPA).

Spectral fitting was done using Recoil Software (University of Ottawa, Ottawa, Canada). Voigt-based fitting was selected as the most appropriate modeling technique as described in the Results and Discussion. For fits, all spectral parameters were floated with the exception of the spectrum background and relative peak areas within a doublet. It was found that only a single quadrupole splitting component was needed, and

additional components did not significantly increase the spectral fitting. The linewidth was floated in addition to the Voigt distribution broadening to account for instrumental broadening (e.g., vibrations) and thickness effects. If the linewidth became unrealistically large (> 0.12 mm/s), then the value was fixed at 0.12 mm/s.

In some cases, an Fe^{3+} doublet was apparent in the spectra, and modeling of this component was done to increase the accuracy of the whole fit. The Fe^{3+} component was likely due to inadvertent oxidation, as extrapolation from fits suggested that the same absolute concentration was observed in every sample, and was observed only when low amounts of Fe^{2+} sorbed. We have no reason to suspect that the Fe^{3+} was due to electron transfer was occurring from the Fe^{2+} to the solid because of the observance of a fixed amount of Fe^{3+} in all samples. Samples where a trace Fe^{3+} signal was used for fitting are denoted in Table 6.2.

Background

Mössbauer Spectroscopy

In this Chapter, we present a sufficient background in Mössbauer spectroscopy such that a reader understands the basic phenomenon, and the information which can be extracted. This work focuses on high spin octahedrally coordinated (VI) Fe^{2+} atoms, which largely narrows the scope of discussion. Several excellent review articles and books exist which thoroughly explore the theory, instrumentation , fitting, and applications in much greater depth than here (8, 65, 66, 185, 187). Mössbauer spectroscopy is predominantly done on the ^{57}Fe isotope, and the background presented will focus on this isotope.

Mössbauer spectroscopy is a nuclear spectroscopy that provides information regarding the hyperfine interactions (i.e., nucleus-electron interactions). The Mössbauer effect relies upon the resonant absorption and subsequent recoilless emission of γ-rays of a very specific energy by the ^{57}Fe nucleus. The energy at which a γ-ray will be absorbed

is dependent upon how the nucleus interacts with its surrounding electrons (i.e., the hyperfine interactions), and the subsequent peak localities in the spectrum are determined by these hyperfine interactions. For recoilless emission of a γ-ray, a ^{57}Fe nucleus must be sufficiently rigid in its surrounding matrix such that when the nucleus emits the γ-ray, it does not recoil in the opposite direction; instead, the recoil energy is distributed out across the crystal lattice, which effectively dampens the movement to a negligible amount. The recoilless emission is necessary to produce an interpretable spectrum, as the recoil energy is several orders of magnitude larger than the hyperfine energy (65). The percentage of ^{57}Fe atoms that undergo recoilless emission is denoted as the recoilless fraction (*f*), a value that becomes larger with increasing rigidity of the ^{57}Fe atoms, and is often increased by lowering the temperature of the sample to reduce thermal energy.

Hyperfine interactions are typically very difficult to probe spectroscopically because the energy shifts that occur between samples due to slight changes in the local environment are usually so minute that they cannot be detected. Mössbauer spectroscopy is fortuitous in that respect, as it measures incredibly slight changes in what energy a γ-ray is resonantly absorbed by the ^{57}Fe atom. In a typical spectrum, the x-axis is velocity on the scale of ±12 mm/s for ^{57}Fe which arises from moving a γ-ray emitting source forward and backward on an oscillating motor. The velocity is the speed with which the source is moving towards or away from the sample. ^{57}Co is a typical source, with the 14.4 keV γ-ray used as the probe, and the velocity with which it is moving to and from the sample slightly modifies this energy via the Doppler effect. The energy shifts which can be detected are on the order of 10^{-12} the energy of the γ-ray (66).

Mössbauer spectroscopy offers several unique advantages for characterizing Fe in samples: (*i*) it provides accurate site populations, allowing for quantification of several co-existing phases; (*ii*) it allows for characterization of impure, "dirty" samples, as it only examines the ^{57}Fe isotope; (*iii*) it provides quantitative analysis of local distortions and chemical environments; (*iv*) amorphous samples can be easily characterized; and (*v*) only

a small amount of ^{57}Fe is required to achieve a meaningful spectrum (approx. 2 µg ^{57}Fe, 100 µg ^{NA}Fe) (8). In this work, we used an isotopically-enriched $^{57}Fe^{2+}$ stock (95.95%) to allow for spectra to be collected when extremely low concentrations of Fe^{2+} uptake were observed (~10 µM uptake from solution for some experiments).

There are also limitations to Mössbauer spectroscopy, however, which may be partially responsible for its somewhat narrowed scope of applications in geosciences: (*i*) spectra can only be collected on solid phase samples (which can often be overcoming by freezing solutions); (*ii*) hyperfine parameters cannot be derived theoretically, and can be empirically interpreted; (*iii*) only certain isotopes are "Mössbauer active;" and (*iv*) spectral interpretation requires considerable training (8). The lack of theoretically derivable parameters is the largest hindrance in the field today, although significant efforts are being made in this area, specifically with semi-empirical density functional theory (DFT) modeling (e.g., 188) and purely theoretical studies (67, 68).

Mössbauer Spectral Interpretation

If a collected Mössbauer spectrum is of sufficient intensity and is well resolved, it can be fit to extract the hyperfine parameters. The three primary hyperfine parameters which are typically extracted are the center shift (CS; mm/s), the quadrupole splitting or shift (QS; mm/s), and the hyperfine field interaction (H; Teslas). The CS is the best understood of the three, and is consequently the easiest to interpret. The observed CS is actually a combination of two effects, the isomer shift (IS), which is temperature independent, and a second order Doppler shift (SOD), which is temperature dependent (65, 189). These values can be decoupled with sufficient theoretical and experimental data, but the reported value is typically the CS. It is simply important to know that the CS will become larger upon lowering the temperature of the sample due to the SOD. Throughout this paper, we will refer to the relative values of the CS among samples, but the IS is typically the true hyperfine parameter being analyzed.

The observed CS is proportional to the s-electron density within the nucleus. As a result, the CS is often used to elucidate the electron density of the ^{57}Fe atom, which can then be applied to compare relative bonding environments and bond strengths. Because the ^{57}Fe isotope becomes smaller upon excitation by the γ-ray, the expected trend between electron density and the CS is reversed: an increase in CS indicates a decrease in s-electron density (8, 71). When comparing high spin (HS) $^{VI}Fe^{3+}$ and $^{VI}Fe^{2+}$ atoms, the CS values are markedly different ($^{VI}Fe^{2+}$: ~0.8-1.3 mm/s; $^{VI}Fe^{3+}$: ~0-0.5 mm/s) (8); the higher CS observed for Fe^{2+} atoms is due to the extra d-electron having a probability of being closer to the nucleus than the s-electrons, which shields the s-electrons, and consequently reduces the s-electron density at the nucleus.

The QS, or the electric field gradient (EFG), is caused by the nucleus having a non-spherical shape. For atoms with a nuclear spin (I) of ½ or greater (½ for ^{57}Fe), the nucleus can be elongated (rod-shaped) or flattened (pancake), with the QS being the measured deviation from spherical symmetry (71, 190). Anisotropic effects in electron distributions, such as the increase in the strength of a bond, will increase the observed QS if it is increasing the distortion, or it will decrease the QS if it is counteracting the other distortions. When comparing HS $^{VI}Fe^{2+}$ to $^{VI}Fe^{3+}$, the extra d-electron in $^{VI}Fe^{2+}$, which has an opposite spin of the other five d electrons, will occupy the lowest energy orbital, causing increased asymmetry in the electron density distribution, so the QS is typically much larger for HS $^{VI}Fe^{2+}$ (~1.8-3.8 mm/s) than $^{VI}Fe^{3+}$ (~0-1.0 mm/s) (71, 185). It has been stated previously that the QS for HS $^{VI}Fe^{2+}$ and $^{VI}Fe^{3+}$ are temperature independent (185), although increasing QS with decreasing temperatures were observed in this study. For a fitted spectrum, the distribution of QS environments can be derived by the width of the peaks (70); this value corresponds to the distribution of unique sites within the samples, which will vary slightly between nuclei in unique local environments. In this work, this distribution is referred to as the quadrupole splitting distribution (QSD; mm/s).

H is related to the strength of the internal magnetic field, which occurs when the electrons spins of neighboring atoms order. H is directly proportional to the strength of the internal field, and is commonly reported in Teslas. This interaction is very dependent upon structure and temperature, as thermal energy must be sufficiently reduced to inhibit electron spin flipping (65). The temperature for which magnetic ordering occurs is valuable in fingerprinting phases, as well as understanding more fundamental characteristics, such as crystalline defects and doping. To observe an internal magnetitic field in a sample (i.e., H), sufficient interatomic interactions must occur, which would be unexpected for sorbed Fe^{2+}. This information can be used advantageously because most mineral phases order at very low temperatures (13 K and below), but we would expect no signs of ordering here, as there should be neglibigle Fe-Fe interactions.

Figure 6.1 contains the spectral representation of CS, QS, and H. The CS of samples is usually referenced to α-Fe^0 foil at room temperature. All samples will contain a CS value relative to α-Fe^0, and may contain QS and H contributions. The number of peaks observed for a given phase in the spectrum (i.e., singlet (1), doublet (2), and sextet (6)) arise from the allowed nuclear transitions (65). An octet (8 peaks) is also possible in magneticially ordered HS Fe^{2+} samples where spin-forbidden transitions can occur, with interpretation being complex (65). The CS value is the offset of the phase spectrum from zero, the QS is the distance between the two peaks of a doublet, and H is the width of the sextet, or the distance between the two outermost peaks (Figure 6.1).

To model spectra, fitting is typically done using computer software with a least-squares fitting approach (71). Individual parameters can be floated or fixed to allow for the most realistic fit. Fitting of spectra is nontrivial, and is dependent upon the model assumed for fitting. The ideal lineshape in a Mossbauer spectrum is Lorentzian, which arises from the excitation time and the Heisenberg uncertainty principle. Spectra typically display linewidths broader than the predicted ones, which has been accounted for using different models. The broadening can occur by a sample which is too thick, or by

distributions of sites (i.e., different stresses and strains for each atom) (69, 70). It has been concluded previously that for samples with a distribution of sites, a broader Lorentzian line is not an accurate descriptor by several researchers; instead, it is common to assume a Gaussian distribution of Lorentzian peaks, which is referred to as a Voigt distribution (70). Here, the Voigt model is used for all modeling parameters reported (70). Similar Voigt-based modeling techniques have been used in the past to fit similar spectra of $^{57}Fe^{2+}$ sorbed on montmorillonite (23).

Results and Discussion

Spectral Interpretation of Sorbed Fe^{2+}

Spectra were collected at three temperatures (140 K, 13 K, 4.2 K) for sorbed Fe^{2+} on a series of substrates. Spectra collected for $^{57}Fe^{2+}$ sorbed on cell, oxide, and clay surfaces are all very similar at 13 K (Figure 6.2). The spectra all contain doublets which have the characteristic peak localities for HS $^{VI}Fe^{2+}$ (8). There is no indication of magnetic ordering (i.e., no appearance of the doublet broadening to a sextet or octet). In spectra collected at lower temperatures (4.2 K; Table 6.2), no ordering was observed. Most ferrous minerals will order above 4 K, including siderite, green rusts, vivianite, and in some cases, Fe^{2+} in clay minerals (191-193); the lack of ordering is indicative that there is negligible metallic bonding and Fe-Fe interactions (65, 71, 194). Note that upon careful inspection, the doublets appear to be slightly asymmetrical; this is discussed in greater depth later.

A primary goal of this work was to determine if sorbed Fe^{2+} could be distinguished from other forms of Fe^{2+}, such as structural Fe^{2+} in minerals. To do this, the hyperfine parameters (i.e., CS and QS) were compared between literature values for other forms of Fe^{2+} and the sorbed Fe^{2+} samples from this study. Here, the 13 K data is presented for the sorbed Fe^{2+} samples, but it should be noted that similar trends are also observed for the 140 K spectral parameters (Table 6.2). The data from previous studies

was collected at 77 K, 16 K, and 4.2 K; the change in temperature will slightly influence the hyperfine parameters, although it will likely be fairly minor (< 0.05 mm/s).

To compare hyperfine parameters, the values are typically plotted with QS vs. CS (Figure 6.3) (8, 180, 181). Two clear groupings exist within this data set; the oxide and clay samples cluster together in a narrow CS and QS range, while the cell data samples have significantly larger CS and QS values. For the Fe^{2+} sorbed on oxide and clay samples, the hyperfine parameters overlap with samples containing structural Fe^{2+}, including green rust, ferrous phosphates, and Fe^{2+} found structurally within clays. As a result, the parameters indicate that sorbed Fe^{2+} cannot be fingerprinted using the hyperfine parameters. In a previous work examining Fe^{2+} sorption on hematite (α-Fe_2O_3), the hyperfine parameters were used to attempt to discriminate a sorbed Fe^{2+} signal from a mineral species, and it was also concluded that the hyperfine parameters could not be used to differentiate between the possible phases (26).

As mentioned above, the spectra in Figure 6.2 appear to be slightly asymmetrical; this is a telling observation, and can be used to gain insight into the hyperfine interactions of sorbed Fe^{2+}. In the spectra, the left peaks appear to be narrower and deeper, while the right peaks are broader and shorter. The presence of asymmetry is abnormal in a spectrum, although it can arise from multiple sources. Fitting of the spectrum determined that the two peaks had the same spectral area, which narrows down the potential explanations. Note that if the peak areas were different, it would likely be due to an unaccounted for Fe^{3+} phase contained within the left peak, preferential orientation of the sample, or the Goldanskii-Karyagin effect, where a sample has orientation-dependent *f* values (8). Asymmetrical doublet peaks have been reported in the literature, and usually arise when a sample is poorly structured, such as in metallic glasses and heterogenic samples, where there are negligible Fe-Fe interactions (70, 194-197). For sorbed Fe^{2+}, the fairly low Fe^{2+} uptake as compared to the amount of substrate and lack of crystallinity in a frozen sorbed sample suggest that the sample is indeed heterogenic and poorly ordered.

It has been previously argued that in amorphous samples, CS-QS coupling is observed because a considerably large range of CS and QS values exist due to different binding environments of the individual ^{57}Fe atoms (e.g., bond lengths, distortions). In a more crystalline solid, however, while distortions still exist, the bulk Fe-Fe and magnetization interactions dominate the effects of the local changes, effectively washing out any potential coupling (71). The implications of this are significant: *the observed hyperfine parameters for crystalline solids and amorphous samples (i.e., sorbed Fe^{2+}) manifest from fundamentally different effects, and can therefore not be compared on an interpretative level* (71, 198). This means that if a sorbed Fe^{2+} sample and a crystalline Fe^{2+} sample (e.g., green rust) exhibit similar or identical hyperfine parameters, one cannot conclude that the ^{57}Fe atoms have similar local environments. Furthermore, this suggests that a range of hyperfine parameters is likely not a good indicator for sorbed Fe^{2+}, but instead the appearance of CS-QS coupling may be a better indicator.

Spectral Asymmetry of Sorbed Fe^{2+}

Since asymmetry is rarely observed in environmentally relevant samples, we aimed to determine if it could be used to fingerprint sorbed Fe^{2+} samples. To model and interpret asymmetrical doublets with the same area under each peak, researchers have invoked the use of a coupling factor (CF), with is a modeling technique which assumes that a distribution of local ^{57}Fe environments exist within a sample (i.e., sample heterogeneity). The CF modeling observes that there is a correlation between the distribution of CS and QS values within a spectrum (195 and refs. therein). Typically, a first-order trend between the CS and QS is assumed, with the CS expressed relative to QS:

$$\mathrm{CS}(\mathrm{QS}) = \mathrm{CF} \times (\mathrm{QS} - \mathrm{QS}_{\mathrm{min}}) + \mathrm{CS}_{\mathrm{min}} \qquad (6.1)$$

Using equation 6.1, a simple linear trend is produced, with the slope (CF) being the degree of correlation; it can be seen that if the CF is assumed to be zero, the CS will

simply be a constant value (i.e., CS_{min}). In the literature, both positive and negative CF values have been reported (70, 194-197), indicating that the CS and QS can relate to one another in fundamentally different ways. Despite our ability to model coupling observed in spectra, it still remains unclear as to why the CS and QS should be coupled, or why the relationship would be linear (197). It has been proposed that a change in a bond or the local environment would affect both the CS (i.e., electron density) and the QS (i.e., electron distribution and distortion) in a systematic way among ^{57}Fe isotopes (70, 197).

Figure 6.4 shows a model fit of the $^{57}Fe^{2+}$ sorbed on α-Al_2O_3 spectra shown in Figure 6.2 where a CF was used to model the data, with the Voigt model doing an excellent job of capturing all the character of the spectrum (i.e., peak shape and intensity). Within Figure 6.4, there is an inset of theoretical spectra with varied coupling factors to illustrate the effects of the CF on the left and right peak. Positive CF values lead to a narrow left peak and a broad right peak, while negative CF values result in a broad left peak and a narrow right peak.

In most of the sorbed Fe^{2+} spectra collected in this study (89%), a positive CF value was observed (Table 6.2). To better gauge the relationship between the CF and the sample type, histograms were created for the CF values observed with each substrate (Figure 6.5). For the oxide samples, an apparent normal distribution of CF values is observed, with the mean CF value being approximately 0.04. CF values greater than zero were also observed for the clay and cell surfaces, although the smaller number of samples makes meaningful interpretation difficult. When the data is collected together (Figure 6.5, bottom-right panel), the collection of CF values indicates that CFs may be good indicators of sorbed Fe^{2+} within a sample, although the absence of a coupling in a spectrum cannot rule out the possibility of sorbed Fe^{2+}.

It is difficult to access if the observation of asymmetry is consistent with previous work. In a previous study which examined Fe^{2+} sorption on Al and Ti oxides, the spectra appear very similar to those in this study, with significant asymmetry observed between

the doublet peaks at 4.2 K (24). In other studies examining sorbed Fe^{2+} on clay and cells (23, 199), the spectra all contain significant amounts of Fe^{3+} which overlaps with the left peak. As a result, it would be challenging to discern between the influence of the Fe^{3+} signal and potential coupling effects.

Fe^{2+} sorption on cell surfaces and functional groups

Fe^{2+} sorption on cell surfaces is a widely studied topic, as the process controls the ability for cells to interact with surrounding substates, and can influence the mineralogy of Fe in the environment. As a result, several studies have examined which functional groups on a cell surface interact with dissolved metals, and specifically Fe^{2+}, due to its abundance in the environment (182-184). To determine if the hyperfine parameters could elucidate which functional groups were responsible for Fe^{2+} sorption, sorption experiments were conducted for polystyrene beads activated with six unique functional groups (Table 6.1). Note that in this study, significantly more uptake was observed on the carboxyl and phosphate functional beads (~100 µM) than the others (i.e., amine, sulfate, and sulfonate; ~10 µM), although no trend exists between the extent of uptake and the observed hyperfine parameters. It is possible that the comparison of the extent of sorption may be somewhat biased, as each bead had varying functional group densities, and it is unclear how washing the beads influenced the functional site densities.

To determine if the functionalized beads could be used as an environmental analog, we compared the bead hyperfine parameters with those found for the environmentally relevant surfaces (Figure 6.6). When the functional group markers are plotted along with the other data sets, the hyperfine parameters appear to be markedly different that those found for the clay and oxide surfaces, but they do appear to cluster around the cell data; in fact, the bead data seems to surround the cell samples. In literature regarding Fe^{2+} sorption on cell surfaces, carboxyl and phosphate functional groups are typically thought to be the two dominate sites of sorption on the cell surface

(184 and refs. therein). The data appears to be consistent with this possibility, although it does not offer conclusive evidence.

The deviation of the hyperfine parameters for the cells as compared to the beads could result from several causes such as a combination of sites being used in cell samples, with the observed spectra resulting from an averaging of the hyperfine parameters. Another possibility is that the sorption sites on cell surfaces are not identical to the simplified functional group analogs used here. Both explanations are plausible and could be concurrent. The similarity in the hyperfine parameters, however, is indicative that similar reactions are occurring between the bead and cell samples. The oxide QS-CS parameters are significantly different, however, which suggests that the bonding environment at the oxide surface is somewhat dissimilar to sorption at functional groups.

The one outlier in the functional bead data is the amine sample, which exhibits a significantly smaller CS than for the other beads (Figure 6.6). The amine group (≡R-NH_2) is fundamentally different than the other functional groups in that the amine group is a Fe-N bond, whereas the others have Fe-O bond. The lower CS indicates that the Fe-N bond is weaker than for the Fe-O bonds, which is inconsistent with the spectrochemical series (i.e., amine having a weaker binding strength than hydroxyl); note that previous work has shown that there is good agreement between the spectrochemical series and CS (189). Very little uptake was observed for the amine beads, which may demonstrates that there is not a strong affinity by Fe^{2+} for the beads. A previous study examining Fe^{2+} uptake on cell surface came to a conclusion that the amine group was not a significant sorption site for Fe^{2+} (184).

The Relationship Between Bulk Solution Conditions and Hyperfine Parameters

To further our understanding of the effect of the solution conditions (i.e., pH, the amount of total Fe^{2+}, the amount of sorbed Fe^{2+}) and surface site characteristics influence

the hyperfine parameters (i.e., CS, QS, and CF), a sorption isotherm and pH-edge were performed for $^{57}Fe^{2+}$ uptake on γ-Al_2O_3. The isotherm and pH edge are shown in Figure 6.7. The Fe^{2+} sorption behavior is typical for uptake on a redox inactive surface: the sorption isotherm shows increased Fe^{2+} uptake with higher Fe^{2+} dissolved concentrations until the isotherm appears to plateau at approximately 3 mM Fe^{2+} dissolved Fe^{2+}. For the pH edge, the extent of Fe^{2+} uptake increases with increasing pH, a common observation for Fe^{2+} uptake on clay and oxide substrates, which is typically attributed to the surface becoming increasingly negatively charged (e.g., 200).

At each point of the isotherm and pH edge, a Mössbauer spectrum was collected. Each spectrum was then fit to determine the hyperfine parameters. In order to discern general trends between the bulk conditions and the hyperfine parameters, the CS, QS, and CF were plotted against the typical relevant bulk conditions (i.e., pH, the equilibrium dissolved Fe^{2+} concentration, and the amount of Fe^{2+} sorbed) for the isotherm and pH edge (Figure 6.8).

Prior to examining the data, the expected trends should be outlined. Significant previous work has been done examining the relationship of the CS to several physiochemical parameters (189 and refs. therein). For instance, observed CS values of Fe atoms bound to ligands appear to agree well with the spectrochemical series (i.e., the t_{2g}-e_g energy gap) (189). Experiments have also shown that the center shift increases with electronegativity of ligands (e.g., FeF_2 has a significantly larger CS than FeI_2 (~0.35 mm/s)) (189). As discussed above, the CS is related to the electron density at the nucleus, and an increase in CS is caused by a decrease in the electron density at the ^{57}Fe atom. For a terminal oxygen atom (σ acceptor) at the oxide surface, we would expect that as the ≡R-O-Fe bond strengthened, and shortened as a result, the CS would decrease as a result (assuming no change in the other ligands attached to the Fe^{2+} atom).

Interpreting and predicting the behavior of the QS is more difficult. When a spectrum is fit, the sign of the QS (i.e., negative or positive) cannot be derived, meaning

one cannot determine if the electron field gradient (EFG) shape is flattened (pancake) or stretched (rod-shaped). Because of this, it is not possible to predict if the QS should increase or decrease as a bond changes. Recent theoretical work has shown that the QS should change with a shift in a ligand bond length, but any other changes in the EFG would also influence the observed QS (67, 68). The CF has never been interpreted in a quantitative manner to our knowledge. We should note, however, that the mere presence of a CF suggests that bulk crystalline hyperfine interactions are negligible when compared to the local electronic environment of the atom, although it is unclear how the CF relates to the degree of local environments dictating the spectrum.

These expected correlations can now be compared with the experimental trends (Figure 6.8). For several of the panels in Figure 6.8, strong linear trends are observed between the bulk and hyperfine parameters. Note that the presented data was collected at 13 K, with identical trends observed in spectra collected 140 K (data in Table 6.2). For the pH edge, the CS decreases with increased pH (panel A), which would be indicative of a stronger bond forming between the Fe^{2+} and the ligand as the pH increases. For the isotherm data, the CS increases with more Fe^{2+} sorbed (panel C); this can be rationalized by the increasing Fe^{2+} uptake occurring at progressively weaker binding sites, which would exhibit a higher CS.

It is much more difficult to discern trends between the QS and bulk parameters (panels D-F). From inspection, nearly identical trends are seen for both the CS and QS. The observed similarities between the CS and QS are in agreement with the apparent positive trend observed in Figure 6.6 between the two values. This trend is not related to the CF values observed in spectra however, as these trends exist between multiple samples collected, and the CF is only used to interpret individual samples. Positive CS-QS trends between samples have been observed previously for structural Fe^{2+} in clays as well as several other sample types, although the underlying cause remains unknown (180, 181). What can be said is that the positive correlation between the two parameters

suggests that the change in binding environment which affects the CS is also affecting the QS.

The coupling factors are also presented in relation to the bulk conditions (panels G-I). For the pH-edge, the CF decreasing with increasing pH and uptake, but for the isotherm, the CF remains constant. The decrease in CF is not indicative of a narrowing of the QS distributions (width of peaks), as this value remains relatively constant for all samples (mean = 0.45±0.02 (σ), n = 6; Table 6.2); instead, the decrease in CF means that whatever is causing the coupling is somehow affected by the solution conditions, which could be a result of the changing of the other ligand's bonds.

Final Comments

The interpretation of this data set is admittedly speculative. Because Mössbauer spectra cannot be derived a priori, progress must be made gradually, with experiments used to validate and question existing conclusions. Hypotheses must be formulated empirically, which requires additional experiments to validate or reject them. With this in mind, the following hypotheses have are proposed here, with the goal of furthering progress and discussion regarding characterization of environmental samples at a deeper level:

1. Sorbed Fe^{2+} can be distinguished from other forms of Fe^{2+} found in the environment by the presence of CS-QS coupling, or spectral asymmetry where the two peaks have equal areas.
2. Sorption of Fe^{2+} on complex surfaces (e.g., cells) can be interpreted on a molecular level by collecting Mössbauer hyperfine parameters of simplified analogs.
3. Observed relative trends between observed CS values and expected ^{57}Fe electron densities exhibit good agreement.

4. The CS and QS appear to follow a general positive linear correlation for sorbed Fe^{2+} samples.

Table 6.1. Supplier, lot, and particle size information of the functionalized polystyrene beads used.

Type	Functional Group	Diameter (μm)	Source	Lot No.
Amine	≡R-NH2	0.66	Bangs Laboratories	847
Carboxyl	≡R-C(=O)OH	1.05	Bangs Laboratories	6151
Hydroxyl	≡R-OH	0.86	Magsphere	HY3087B
Phosphate	≡R-OP(=O)(OH)2	0.50	Kisker	GK0480743T
Sulfate	≡R-OSO3H	1.26	Bangs Laboratories	6060
Sulfonate	≡R-SO2R'	0.88	Magsphere	S3088

Table 6.2. Mössbauer hyperfine parameters (CS, QS, QSD, and CF) for sorbed Fe^{2+} data collected at 13 K and 140 K. The solution conditions (pH, [Fe^{2+}]) are provided for each experiment. Reference values are also shown for similar experiments.

	Sorption Conditions					Mössbauer Parameters					
Sample	pH	Fe^{2+}_{init} (µM)	Fe^{2+}_{sorb} (µM)	$Fe^{2+}_{eq.}$ (µM)	Solids conc. (g/L)	Temp. (K)	CS (mm/s)	QS (mm/s)	QSD (mm/s)	CF	Trace Fe^{3+}
Beads											
Amine	7.5	~1000	~10	990	4	13	1.29	2.92	0.39	0.06	N
						140	1.25	2.86	0.45	0.06	Y
Carboxyl	7.5	~1000	59	940	4	13	1.36	2.97	0.42	0.04	Y
						140	1.31	2.84	0.47	0.04	Y
		~1000	b.d.	~1000	4	13	1.36	2.97	0.43	0.03	Y
						140	1.32	2.82	0.50	0.02	Y
Hydroxyl	7.5	~1000	b.d.	~1000	4	140	1.32	2.96	0.41	0.13	Y
Phosphate	7.5	~1000	110	890	4	13	1.38	2.96	0.45	0.05	N
						140	1.33	2.83	0.49	0.04	N
Sulfate	7.5	~1000	b.d.	~1000	4	13	1.39	3.18	0.33	-0.01	N
						140	1.33	2.94	0.57	-0.02	Y
		~1000	~9	990	4	13	1.38	3.20	0.44	0.07	N

Table 6.2 Continued

	Sorption Conditions					Mössbauer Parameters					
Sample	**pH**	**Fe^{2+}_{init} (µM)**	**Fe^{2+}_{sorb} (µM)**	**$Fe^{2+}_{eq.}$ (µM)**	**Solids conc. (g/L)**	**Temp. (K)**	**CS (mm/s)**	**QS (mm/s)**	**QSD (mm/s)**	**CF**	**Trace Fe^{3+}**
						140	1.33	3.04	0.58	-0.03	Y
Sulfonate	7.5	~1000	b.d.	~1000	4	13	1.39	3.13	0.45	0.09	N
						140	1.28	2.92	0.53	0.07	Y
Cells											
S. putrefaciens CN32	7.4	2127	1483	689	*a	4.2	1.37	3.19	0.30	0.00	N
						13	1.36	3.07	0.46	0.01	N
	7.0	991	787	204	*	13	1.36	3.08	0.42	0.01	N
						140	1.32	2.92	0.45	0.01	N
S. ojiedensis MR1	7.4	2127	1264	908	*	4.2	1.37	3.17	0.39	0.01	N
						13	1.37	3.08	0.43	0.02	N
	7.0	860	586	274	*	140	1.32	2.88	0.47	0.02	N

Table 6.2 Continued

	Sorption Conditions					Mössbauer Parameters					
Sample	pH	Fe^{2+}_{init} (µM)	Fe^{2+}_{sorb} (µM)	$Fe^{2+}_{eq.}$ (µM)	Solids conc. (g/L)	Temp. (K)	CS (mm/s)	QS (mm/s)	QSD (mm/s)	CF	Trace Fe^{3+}
S..alga BrY	7.0	1016	751	265	*	140	1.33	2.88	0.40	0.02	N
B. subtilis	7.4	2130	484	1646	*	4.2	1.38	3.18	0.29	0.05	N
G. Sulfurreducens	7.4	2070	424	1646	*	13	1.36	3.10	0.53	0.01	N
						140	1.32	3.00	0.54	0.01	N
B. substlis **(199)**	4.0					4.2	1.2	3.3	0.2		Y
	4.0					4.2	1.3	3.4	0.2		Y
	4.3					4.2	1.15	3.23	0.35		Y
	4.3					4.2	1.3	3.1	0.34		Y
	2.6					4.2	1.2	3.4	0.35		Y
	2.6					4.2	1.2	3.4	0.39		Y
Oxides											
TiO_2 (32nm)	7.2	1013	82	931	2	13	1.31	2.71	0.40	0.01	Y

Table 6.2 Continued

	Sorption Conditions					Mössbauer Parameters					
Sample	pH	Fe^{2+}_{init} (μM)	Fe^{2+}_{sorb} (μM)	$Fe^{2+}_{eq.}$ (μM)	Solids conc. (g/L)	Temp. (K)	CS (mm/s)	QS (mm/s)	QSD (mm/s)	CF	Trace Fe^{3+}
						140	1.25	2.65	0.38	0.04	Y
	7.5	985	116	869	2	13	1.30	2.73	0.41	0.02	Y
						140	1.27	2.57	0.40	0.00	Y
TiO_2 (5 nm)	7.5	1009	661	348	2	13	1.30	2.75	0.45	0.01	N
						140	1.26	2.65	0.45	0.01	N
γ-Al_2O_3	7	101	86	15	20	13	1.31	2.67	0.42	0.05	N
						140	1.27	2.62	0.41	0.04	N
	7	489	310	179	20	13	1.32	2.73	0.43	0.05	N
						140	1.28	2.67	0.42	0.04	N
	7.1	1044	554	490	20	13	1.32	2.75	0.44	0.04	N
						140	1.28	2.69	0.43	0.04	N
	7	3889	861	3028	20	13	1.33	2.78	0.48	0.04	N
						140	1.29	2.71	0.47	0.03	N

Table 6.2 Continued

	Sorption Conditions					Mössbauer Parameters					
Sample	pH	Fe^{2+}_{init} (µM)	Fe^{2+}_{sorb} (µM)	$Fe^{2+}_{eq.}$ (µM)	Solids conc. (g/L)	Temp. (K)	CS (mm/s)	QS (mm/s)	QSD (mm/s)	CF	Trace Fe^{3+}
	6.9	9138	762	8376	20	13	1.33	2.80	0.50	0.04	N
						140	1.29	2.72	0.48	0.03	N
	5.9	939	65	874	20	13	1.33	2.83	0.44	0.07	N
						140	1.30	2.76	0.46	0.05	N
	6.2	996	139	857	20	13	1.33	2.79	0.44	0.06	N
						140	1.29	2.72	0.44	0.06	N
	6.6	994	296	698	20	13	1.33	2.77	0.43	0.06	N
						140	1.28	2.70	0.43	0.05	N
	7.1	1044	554	490	20	13	1.32	2.75	0.44	0.04	N
						140	1.28	2.69	0.43	0.04	N
	7.5	981	612	369	20	13	1.31	2.75	0.45	0.03	N
						140	1.27	2.69	0.44	0.02	N
	7.9	930	847	83	20	4.2	1.32	2.73	0.41	0.05	N

Table 6.2 Continued

	Sorption Conditions					Mössbauer Parameters					
Sample	pH	Fe^{2+}_{init} (μM)	Fe^{2+}_{sorb} (μM)	$Fe^{2+}_{eq.}$ (μM)	Solids conc. (g/L)	Temp. (K)	CS (mm/s)	QS (mm/s)	QSD (mm/s)	CF	Trace Fe^{3+}
						13	1.30	2.74	0.44	0.02	N
						140	1.26	2.68	0.43	0.02	N
α-Al_2O_3	7.0	991	204	788	20	4.2	1.33	2.77	0.35	0.06	N
						13	1.31	2.75	0.37	0.04	N
						140	1.28	2.69	0.36	0.03	N
α-Al_2O_3 (24)	7.4				10	4.2	1.31	2.68			Y
TiO_2 (24)	7.4				10	4.2	1.32	2.79			Y
Clays											
Montmorillonite	7.8	716	457	259	1	13	1.30	2.79	0.38	0.10	Y
						140	1.26	2.77	0.34	0.08	Y
Hectorite	7.8	768	527	241	1	13	1.31	2.70	0.72	0.02	N
						140	1.28	2.57	0.48	0.00	N

Table 6.2 Continued

	Sorption Conditions					Mössbauer Parameters					
Sample	pH	Fe^{2+}_{init} (µM)	Fe^{2+}_{sorb} (µM)	$Fe^{2+}_{eq.}$ (µM)	Solids conc. (g/L)	Temp. (K)	CS (mm/s)	QS (mm/s)	QSD (mm/s)	CF	Trace Fe^{3+}
Laponite	7.8	623	452	171	1	13	1.31	2.68	0.69	0.01	N
						140	1.28	2.57	0.46	0.00	N
Montmorillonite	4.03	650	n.r.	n.r.	10	77	1.34	3.18	n.d.	n.r.	Y
(23)	5.01	650	n.r.	n.r.	10	77	1.32	3.08	n.d.	n.r.	Y
	6.1	650	n.r.	n.r.	10	77	1.30	3.05	n.d.	n.r.	Y
	7.08	650	n.r.	n.r.	10	77	1.31	2.92	n.d.	n.r.	Y
	8.66	650	n.r.	n.r.	10	77	1.27	2.93	n.d.	n.r.	Y
	4.91	650	n.r.	n.r.	10	77	1.29	2.81	n.d.	n.r.	Y
Illite (177)	~7					77	1.26	3.02			

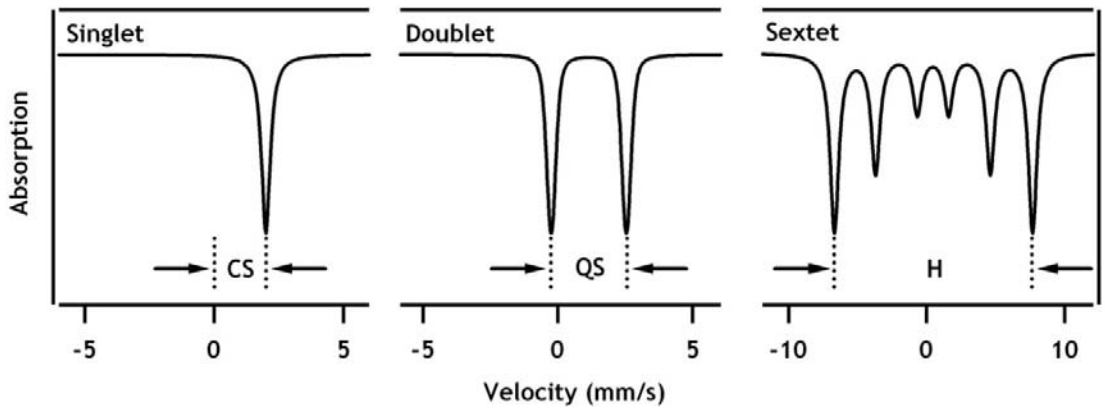

Figure 6.1. Mössbauer spectral diagrams for single-line source (single), a quadrupole split source (doublet), and a hyperfine split source (sextet). The hyperfine variables (i.e., CS, QS, and H) are illustrated on each spectrum.

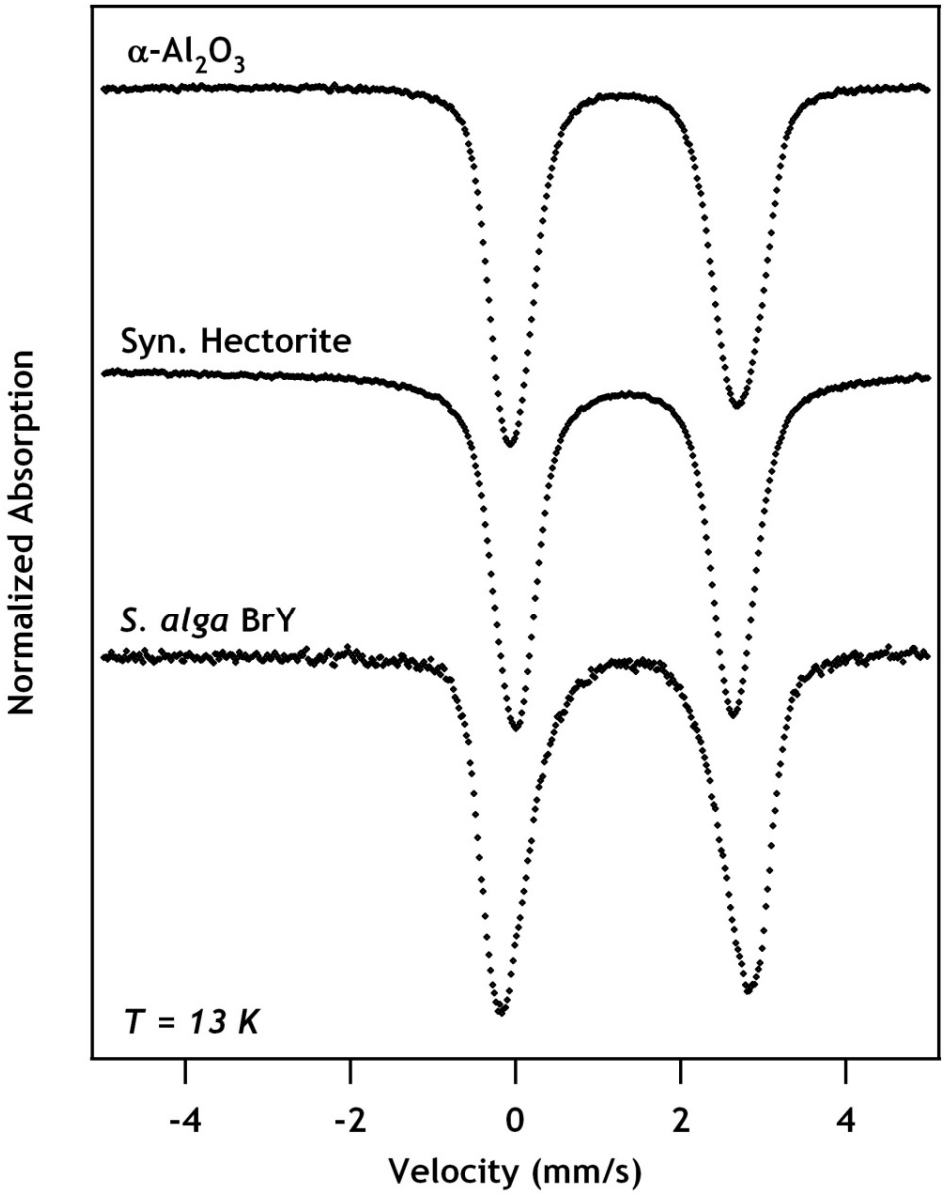

Figure 6.2. Mössbauer spectrum of $^{57}Fe^{2+}$ sorbed on α-Al_2O_3, a synthetic hectorite, and *Shewanella alga* BrY at 13 K. Experimental conditions: α-Al_2O_3: [α-Al_2O_3] = 20 g/L, $[Fe^{2+}]_{init}$ = 1 mM, pH 7.1, 25 mM PIPES, 10 hr eq. 554 µM Fe^{2+} sorbed; hectorite: [hectorite] = 1 g/L, $[Fe^{2+}]_{init}$ = 0.8 mM, pH 7.8, 25 mM PIPPS, 24 hr eq. 527 µM Fe^{2+} sorbed; *S. alga* BrY: [cells] ≈ 10^{10} mL^{-1}, $[Fe^{2+}]_{init}$ = 1 mM, pH 7.0, 10 hr eq. 750 µM Fe^{2+} sorbed.

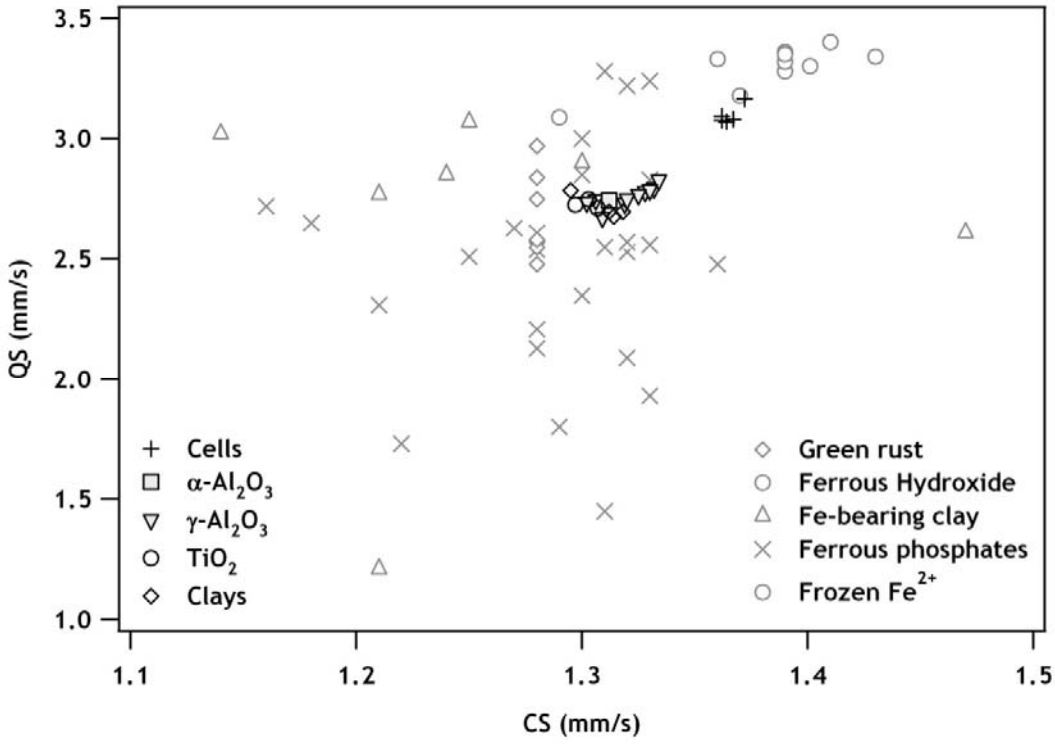

Figure 6.3. Hyperfine parameters for sorbed $^{57}Fe^{2+}$ (dark markers) compared to structural and frozen Fe^{2+} (grey markers). Sorbed Fe^{2+} data was collected at 13 K, the values are provided Table 6.2. The structural and frozen Fe^{2+} data were taken from: Green rust, 77 K (201); ferrous hydroxide, 77 K (23); Fe-bearing clays, 77 K, 16 K, 4 K (8, 195); ferrous phosphates, 77 K (202); and frozen Fe^{2+}, 4.2 K (203).

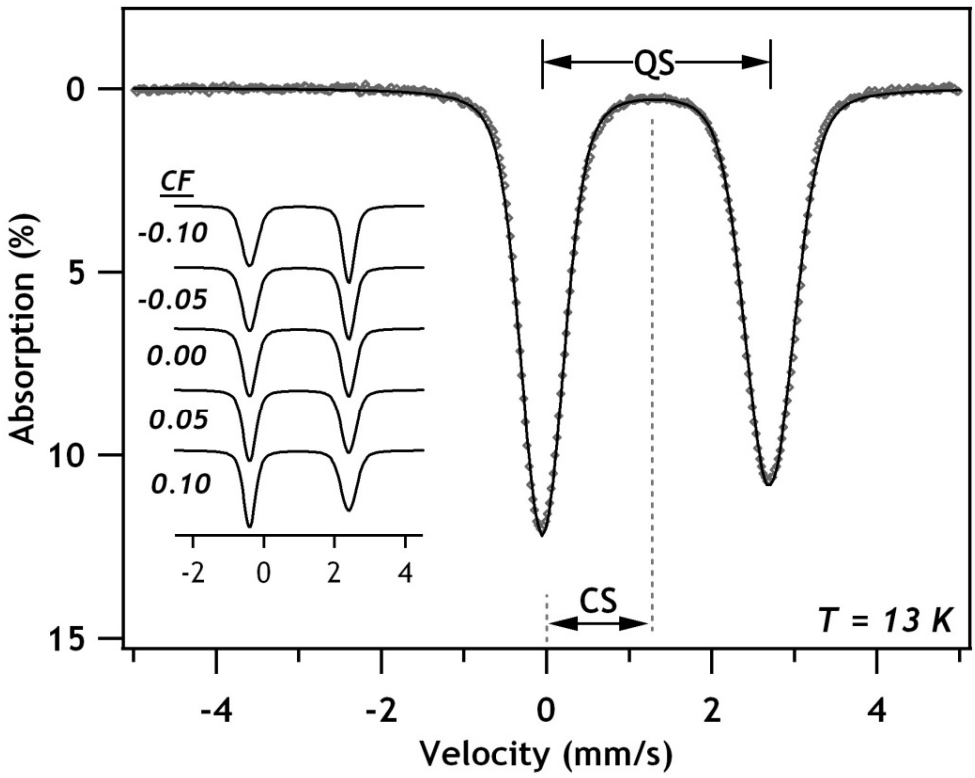

Figure 6.4. Mössbauer spectrum of $^{57}Fe^{2+}$ sorbed on α-Al_2O_3 at 13 K. Raw data is shown (◇) with the model fit (—) overlaid. Experimental conditions: [α-Al_2O_3] = 20 g/L, $[Fe^{2+}]_{init}$ = 1 mM, pH 7.1, 25 mM PIPES, 10 hr eq. 554 µM Fe^{2+} was taken up by the particles.

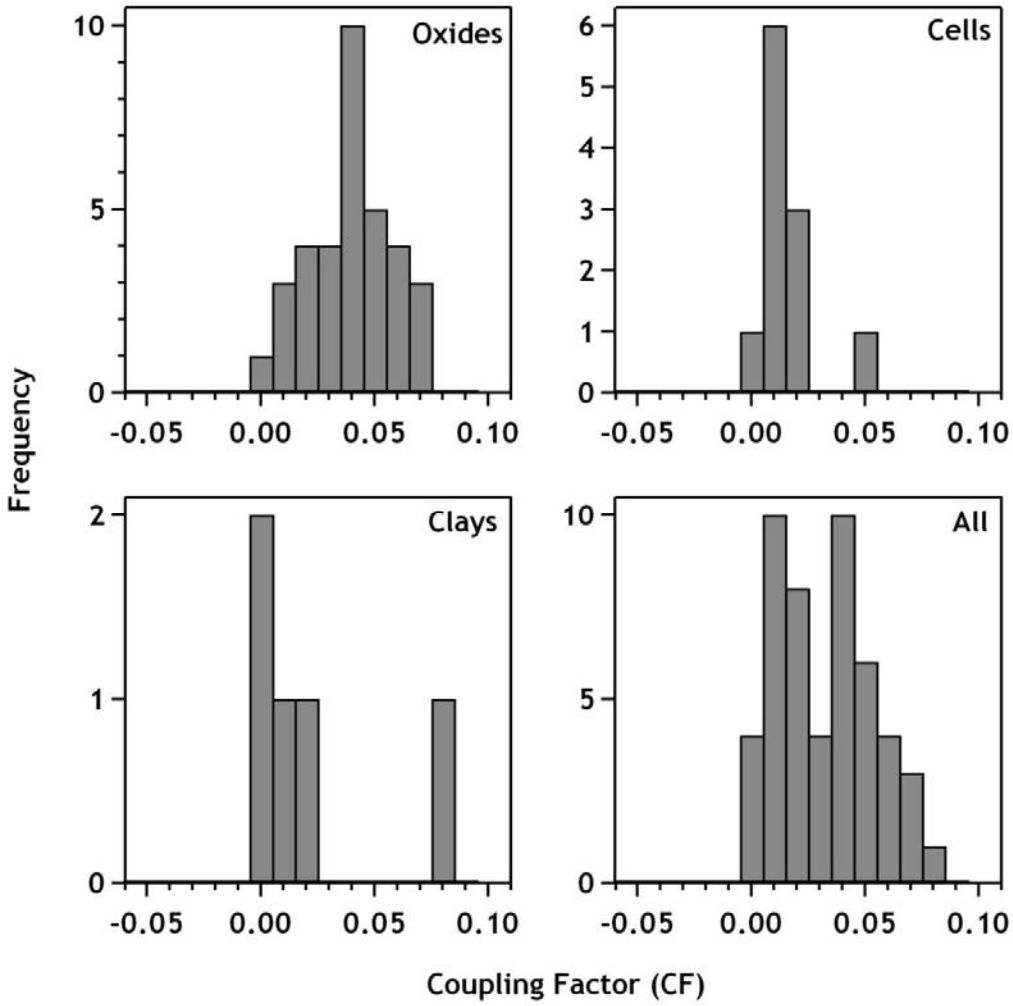

Figure 6.5. Frequencies of coupling factors observed in Mössbauer spectra of sorbed Fe^{2+} separated by substrate type (data also in Table 6.2).

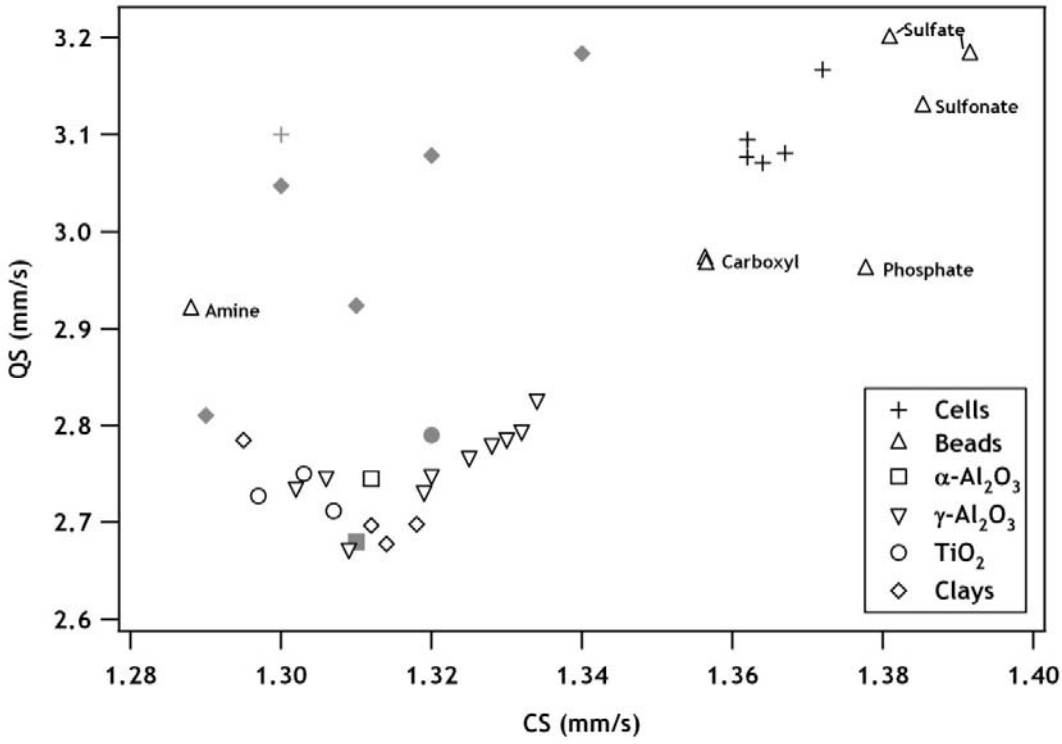

Figure 6.6. Hyperfine parameters for sorbed Fe^{2+} at 13 K (black markers). Grey markers are for reference data: cells, 4.2 K (199); α-Al_2O_3 and TiO_2, 4.2 K (24); clays, 77 K (23).

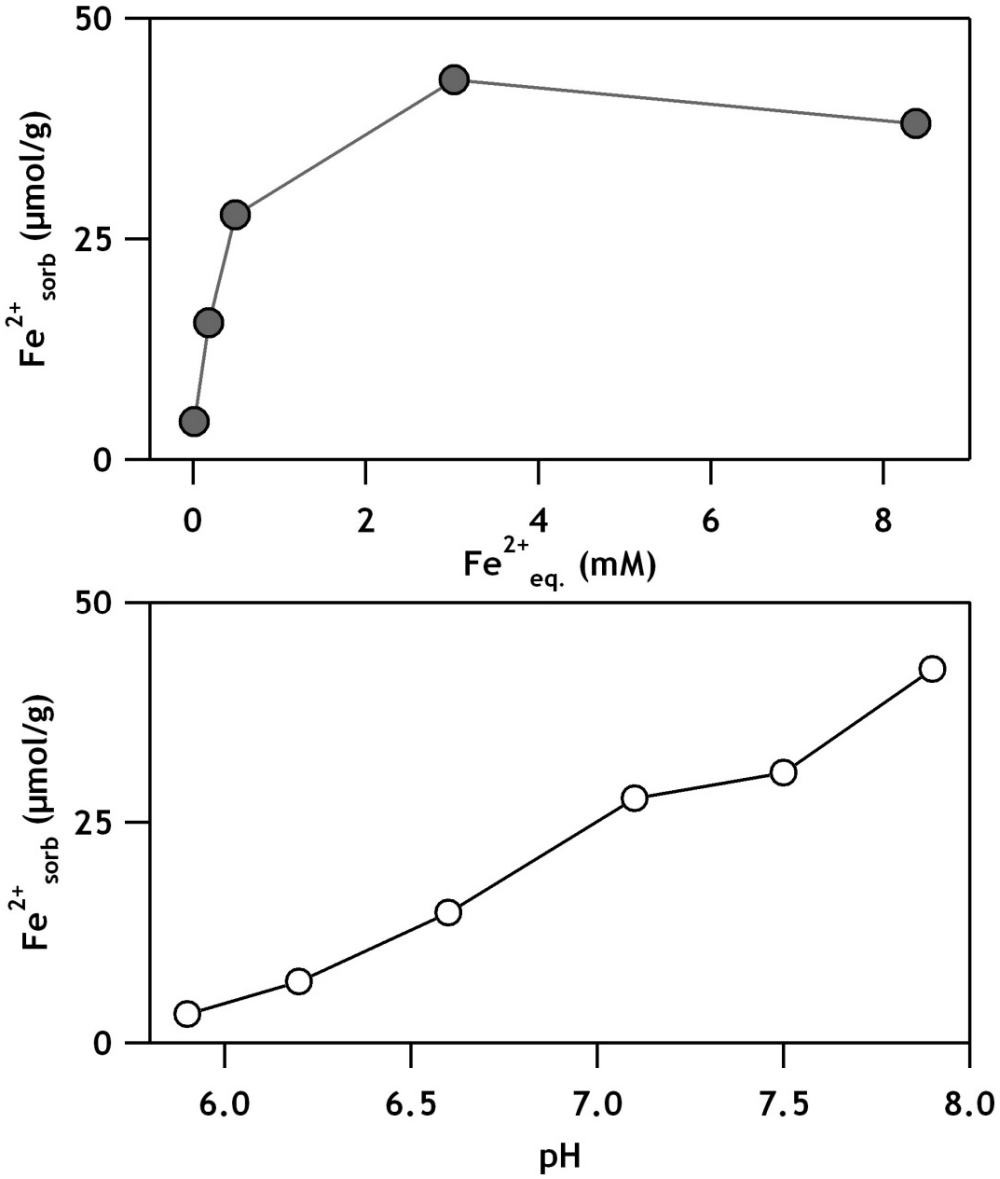

Figure 6.7. An Fe^{2+} sorption isotherm (top) and pH edge (bottom) for $^{57}Fe^{2+}$ exposed to γ-Al_2O_3. Isotherm experimental conditions: [γ-Al_2O_3] = 20 g/L, pH 7.0, 25 mM PIPES, 10 hr eq. pH-edge experimental conditions: [γ-Al_2O_3] = 20 g/L, $[Fe^{2+}]_{init}$ = 1 mM, 25 mM PIPES , 10 hr eq.

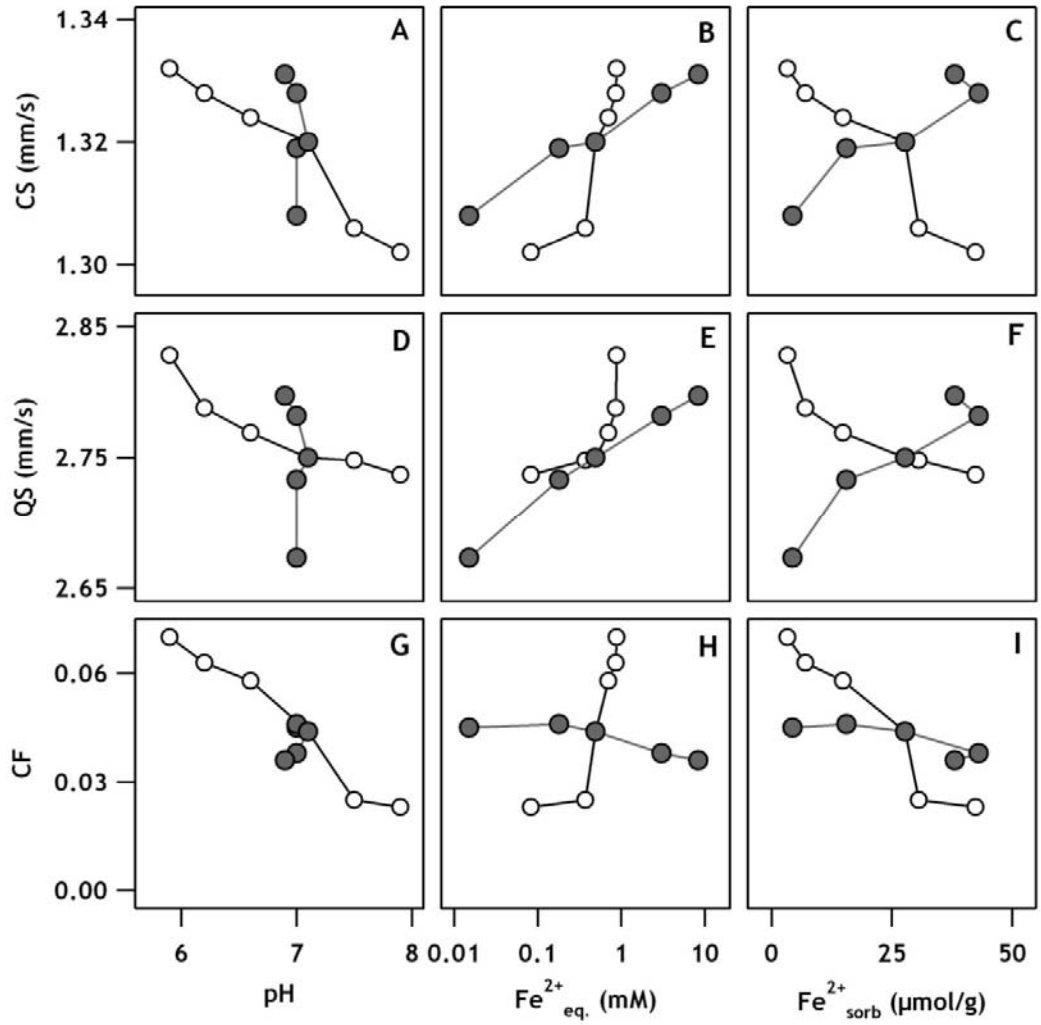

Figure 6.8. Scatter plot matrix comparing measured hyperfine parameters (y-axes) and bulk solution conditions (x-axes). Filled markers are data from the sorption isotherm. Open markers are data from the pH-edge.

CHAPTER VII: ENGINEERING AND SCIENTIFIC SIGNIFICANCE

Summary

This work sheds new light on the redox reactions which occur between iron oxides and groundwater constituents. Previous studies of magnetite contained several discrepancies regarding the measured redox potential and reactions with dissolved Fe^{2+} and several environmental contaminants. This work was able to reproduce and explain these results by finding the contradictions rooted to the magnetite stoichiometry ($x = Fe^{2+}/Fe^{3+}$), which can vary between $x = 0.5$ (i.e., stoichiometric) to $x = 0$ (i.e., completely oxidized). Here, we showed that stoichiometry is a critical parameter to consider in environmental studies, and should be measured in future work. The three most common techniques used to measure stoichiometry and their relative agreements are reviewed in Chapter II of this thesis.

The observation that Fe^{2+} uptake by magnetite is controlled by the stoichiometry has interesting implications for the uptake of Fe^{2+} by other oxides. Recent work by several groups has shown that Fe^{2+} uptake on other iron oxides also involves electron transfer reactions, which may be controlled by a 'capacity' for structural Fe^{2+} as observed for magnetite. The fate of a transferred electron to the underlying oxide phase is less understood for other minerals, making the potential capacity difficult to access. The apparent Nernstian relationship between the redox conditions of the Fe^{2+}-iron oxide suspensions observed in Chapter V offers an additional step to making progress in this area.

In Chapter IV, it was shown that redox measurements of magnetite made using a powder disk electrode (PDE) setup could be used to accurately predict the reduction rates of substituted nitroaromatics using a quantitative structure-activity relationship (QSAR). To our knowledge, this is the first example of contaminant reduction rates being predicted using only redox measurements for reduced iron oxide suspensions. This

technique may aid in the ability for regulators to better access the fate of contaminants in the environment.

Work using Mössbauer spectroscopy was also carried out to characterize several samples of sorbed Fe^{2+} on Al and Ti oxides, clay minerals, cells, and functionalized beads. Sorbed Fe^{2+} is often difficult to characterize due to its amorphous structure and low relative atomic abundance within a sample. Within the literature, there are very few reported hyperfine parameters for sorbed Fe^{2+}, making it difficult to compare values between studies. Chapter VI provides an extensive collection of measured parameters collected under various conditions which can be used in future works. Furthermore, the observed asymmetry for sorbed Fe^{2+} Mössbauer spectra may be used as an indicator for a sample being fingerprinted as sorbed Fe^{2+}.

Recommendation of Future Work

Using the data presented in Chapters III-V, a conceptual semiconductor model can be developed which is based on the photoexcitation of an electron (Figure 7.1). Here, sorption of Fe^{2+} on an oxide surface results in interfacial electron transfer, with a structural Fe^{3+} atom being subsequently reduced to structural Fe^{2+}. The valence electron will then undergo promotion from the valence band (VB) to the conduction band (CB) as described in Chapter I. The additional electron on the structural Fe^{2+} atom has three possible fates: (*i*) it can become trapped in a structural defect known as a trapping site (t), which exists due to slight imperfections in bonding environments (149); (*ii*) the electron can reduce an aqueous species, such as a contaminant (nitrobenzene shown), or (*iii*) the electron may have a sufficiently low potential that reductive dissolution occurs at the surface. This model is consistent with the paradigm shift that has recently occurred for Fe^{2+} sorption of Fe^{3+} oxides which have been outlined in Chapter I, yet validating or disproving this model will require further work.

The implications of magnetite stoichiometry are likely to impact several biogeochemical processes which were not explored in this work. The stoichiometry of magnetite found in the environment remains entirely unexplored; in the few studies were stoichiometry can be extracted, precaution was not taken to avoid oxidation. For microbial iron reduction and oxidation, processes thought to be important in iron redox cycling, it is unclear how stoichiometry influences the extent and rate of biological respiration. Additionally, it is unclear if the synthesis method, particle size, and probe contaminant will influence conclusions presented in this work. For example, it has been hypothesized that large particulate magnetite does not oxidize to maghemite, and instead directly transforms to hematite (204).

The utilization of the quantitative structure-activity relationship (QSAR) in Chapter IV is the first study to our knowledge that accurately predicted contaminant reduction rates using only electrochemical measurements. Reduction of additional contaminants still needs to be explored with this model to determine the scope of the QSAR. Additionally, measurements made using powder disk electrodes can easily be applied to other oxide systems equilibrated with dissolved Fe^{2+}, which will aid in our ability to understand and potentially predict contaminant fate in the environment.

In addition to biogeochemical processes, the importance of stoichiometry in determining the redox processes of magnetite expands to several fields of research. Magnetite, a semiconductor with an incredibly low band gap (~0.1 eV), has several industrial applications which can be foreseen due to the adjustable properties of magnetite: (*i*) the size can range from a few nanometers to several microns, and can be coated onto surfaces; (*ii*) the redox potential can range over 500 mV as shown in Chapter IV; (*iii*) the particles can be easily "recharged" by a reductant or dissolved Fe^{2+} (Chapter III); (*iv*) the conductivity and band gap are strongly correlated to the stoichiometry; and (*v*) several works have shown that functional groups can be readily sorbed to the surface to further control their reactivity and properties (cite).

Other iron oxides, such as hematite and goethite, also have potential industrial applications. Leland and Bard previously studied the photochemistry of several iron oxide polymorphs (158), and is often cited for demonstrating that iron oxides are poor photochemical catalysts (cite). They argued that surface trapping sites are the most likely reason for lower than expected electron recoveries. The work presented here, and work by other groups (30, 33, 149, 159), indicates that the presence of aqueous Fe^{2+} can fill trapping sites, and may result in significantly more efficient photocatalysis by hematite, and potentially other iron oxides. Like magnetite, nanoparticulate and micron-scale iron oxides can easily be synthesized and do not involve expensive trace metals, making them ideal candidates for green chemistry applications including synthesis of compounds, photocatalysis in energy cells and batteries, and several more possibilities which remain currently unforeseen.

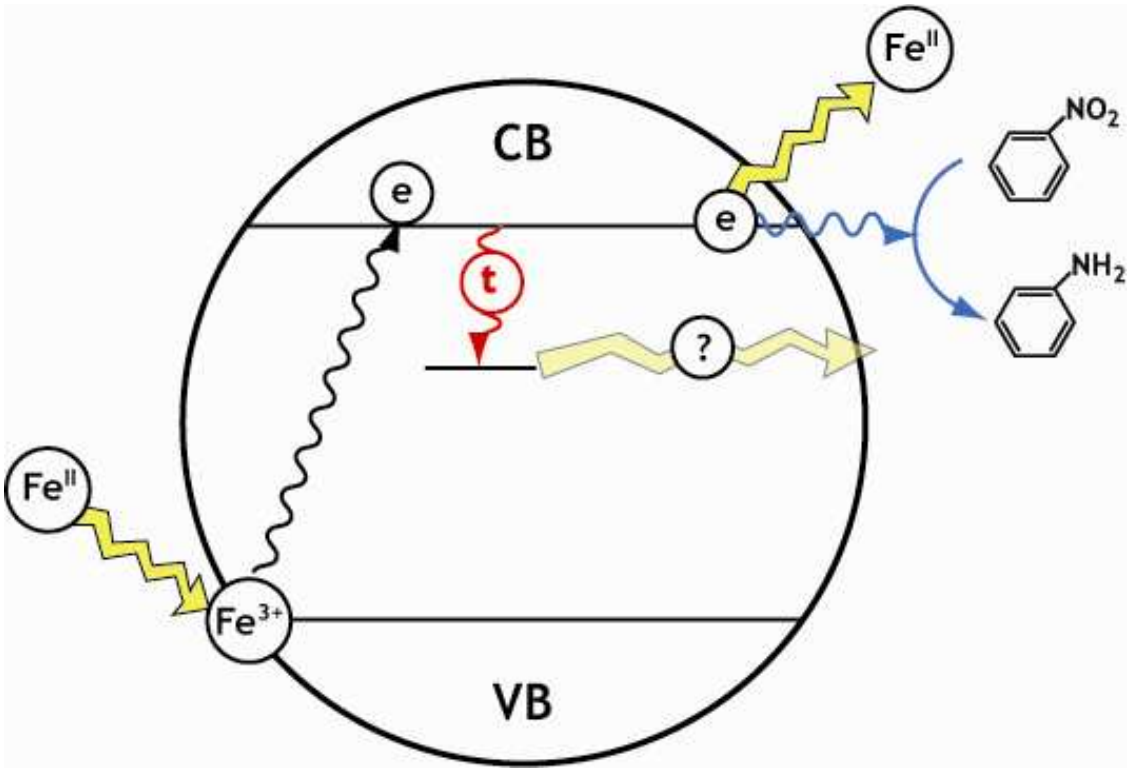

Figure 7.1. Conceptual semiconductor model of iron oxide suspensions in the presence of aqueous Fe^{2+}. Here, a sorbed aqueous Fe^{2+} atom subsequently reduces a structural Fe^{3+} atom, which promotes the additional electron from the valence band (VB) to the conduction band (CB). The electron can then become trapped in a crystalline defect (t), undergo reductive dissolution as aqueous Fe^{2+}, or reduce an aqueous reductant such as nitrobenzene ($ArNO_2$).

APPENDIX A: SUPPLEMENTAL INFORMATION

Supplemental Information for Chapter III

Figures and Tables

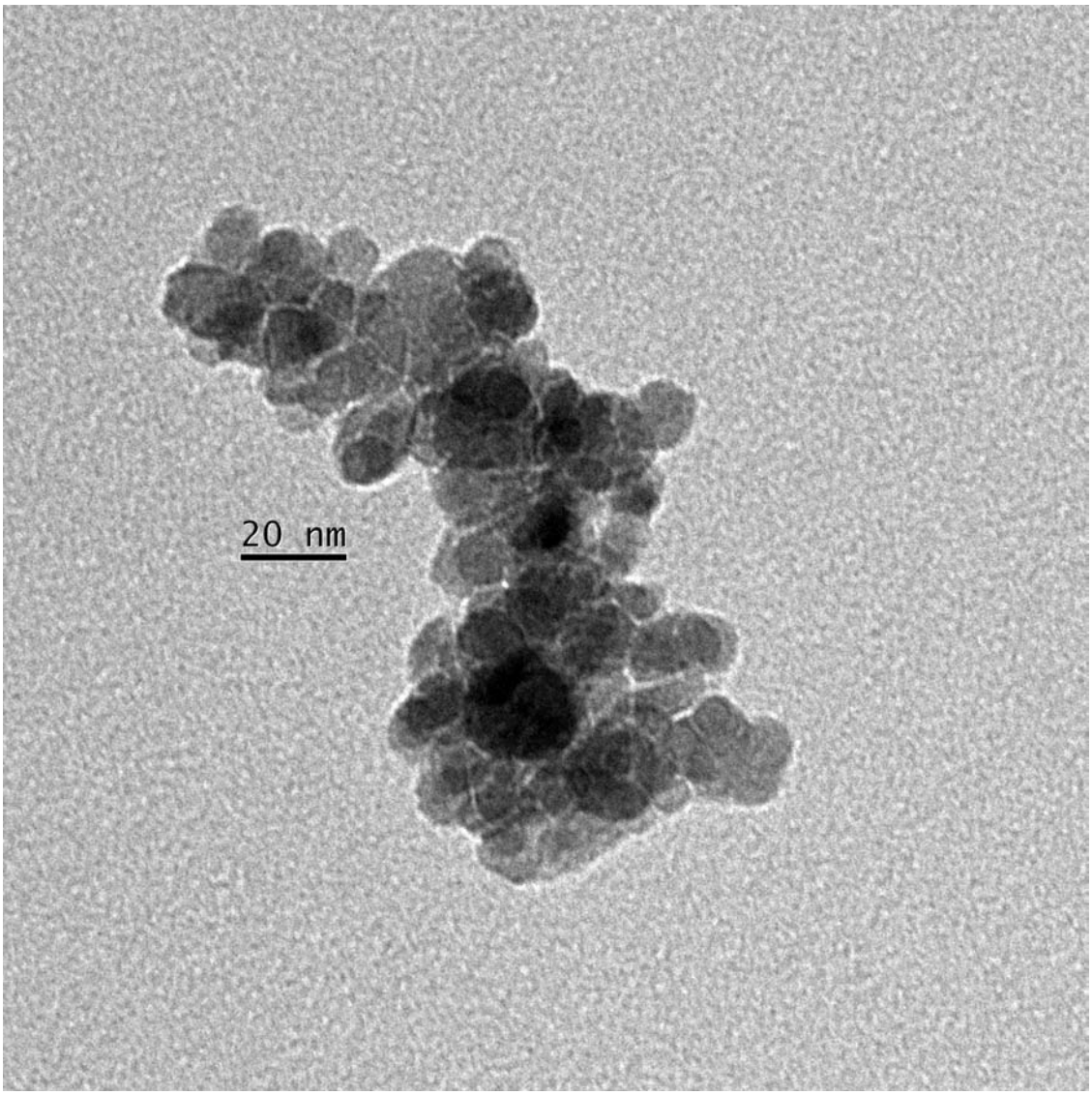

Figure A.1. A representative transmission electron microscopy (TEM) of the magnetite used in this study, with the particles typically ~ 20 nm in size, with spherical morphology.

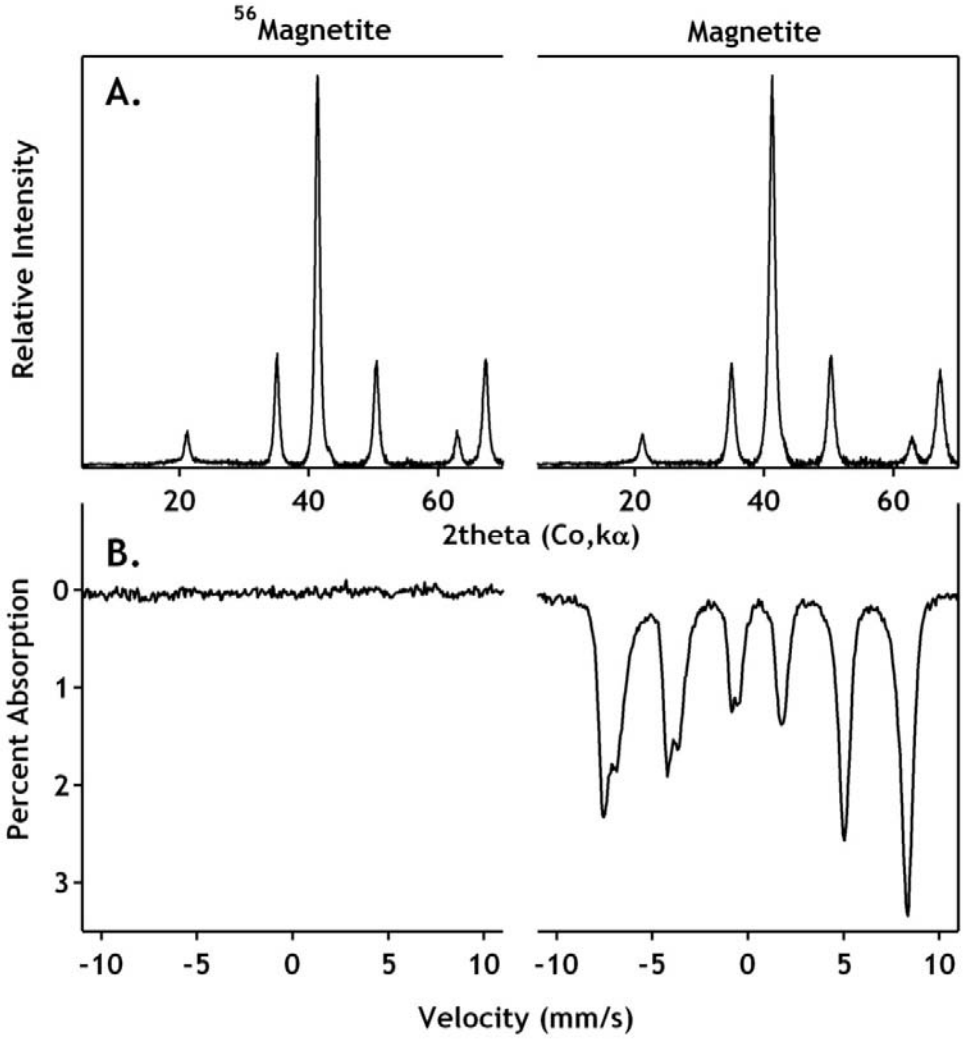

Figure A.2. (A) Powder X-ray diffraction patterns of magnetite synthesized from ^{56}Fe metal and naturally abundant Fe-salts. All the observed peaks corresponded to magnetite, with no observable difference between the two patterns. (B) Mössbauer spectra of 20 mg of ^{56}magnetite and ^{IN}magnetite collected at 140 K.

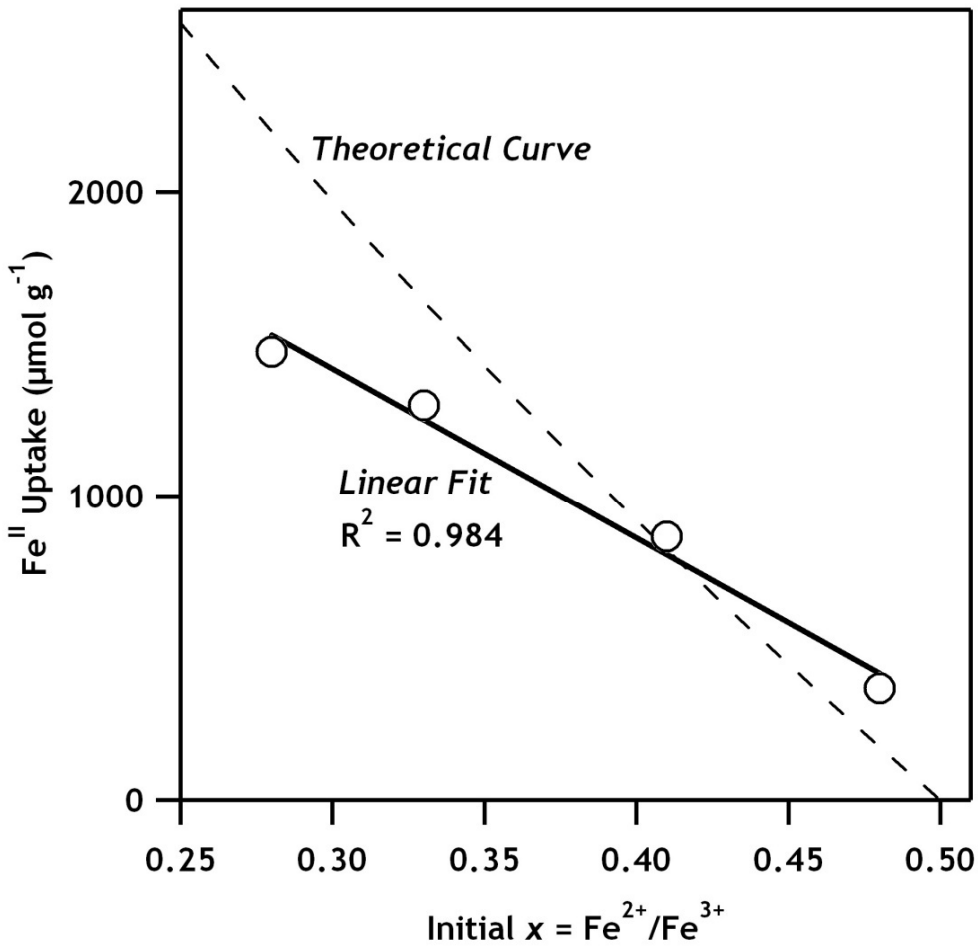

Figure A.3. Fe^{II} uptake reported for magnetite batches of varying stoichiometries from Figure 3.1. The data shown was collected with an initial aqueous Fe^{II} concentration of 3 mM. The theoretical fit model was calculated assuming that the particle would go to stoichiometric magnetite (x = 0.5), using a mass balance approach with 1 g/L initial solids.

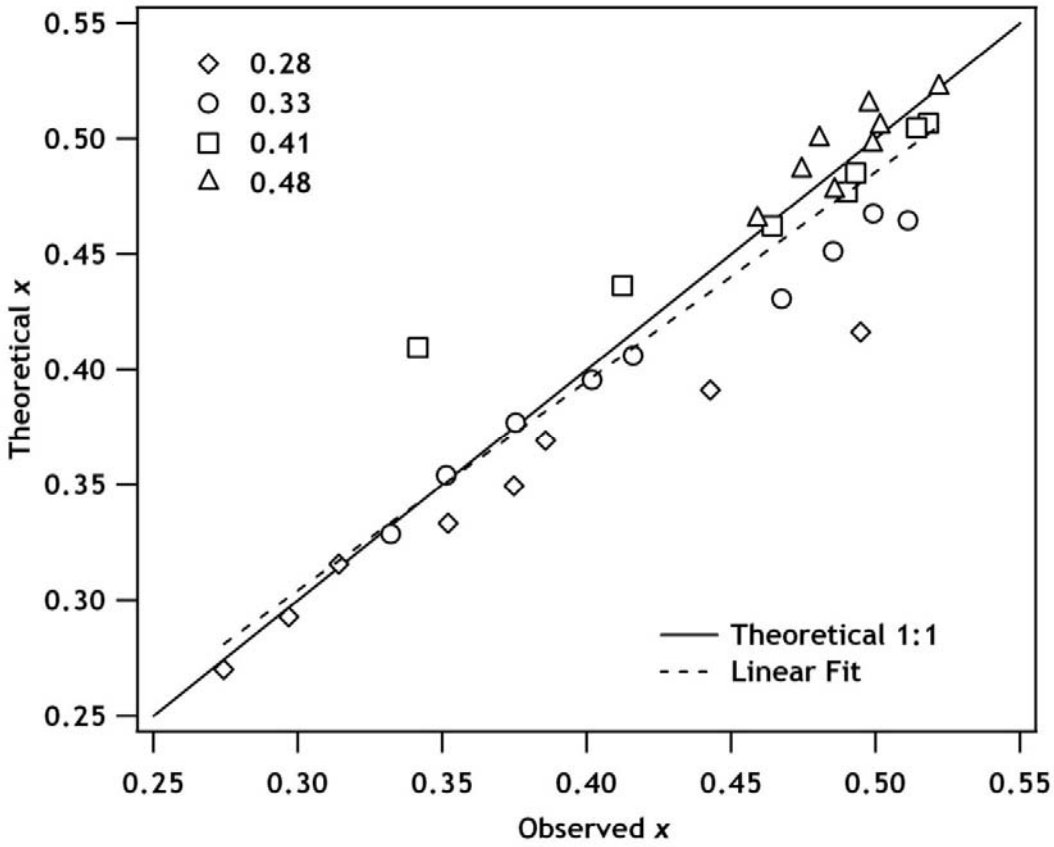

Figure A.4. Observed trend of the calculated *x* values after Fe^{II} uptake to the *x* value measured from dissolution in Figure 3.4. For the linear fit, m= 0.91; R^2 = 0.88; n = 32.

Table A.1. Data shown in Figures 3.3, 3.4, and A.3. Experimental conditions: 50 mM MOPS buffer at pH 7.2, 24 hour equil, 1 g/L solids. *x theor.* was calculated using the method shown in Calculation A.2.

Initial (µM)	Final (µM)	Sorbed (µM)	*x meas*	*x theor.*	Initial (µM)	Final (µM)	Sorbed (µM)	*x meas*	*x theor.*	Initial (µM)	Final (µM)	Sorbed (µM)	*x meas*	*x theor.*	Initial (µM)	Final (µM)	Sorbed (µM)	*x meas*	*x theor.*
0	0	0	0.28	0.28	0	0	0	0.33	0.33	0	0	0	0.41	0.41	0	0	0	0.48	0.48
15	14	1	0.27	0.28	12	26	-14	0.33	0.33	12	16	-4	0.34	0.41	24	156	-132	0.46	0.46
242	12	230	0.30	0.30	258	26	232	0.35	0.35	263	20	243	0.41	0.44	263	286	-22	0.49	0.48
474	14	460	0.31	0.33	510	56	454	0.38	0.38	536	58	478	0.46	0.46	518	462	55	0.47	0.49
690	52	637	0.35	0.34	782	148	634	0.40	0.40	771	157	614	0.49	0.48	767	615	152	0.50	0.50
912	112	801	0.37	0.36	1028	293	735	0.42	0.41	1011	323	688	0.49	0.49	1027	854	173	0.48	0.50
1379	380	1000	0.39	0.38	1489	517	973	0.47	0.43	2056	1170	886	0.52	0.51	1520	1299	221	0.50	0.51
1845	623	1222	0.44	0.40	1989	817	1172	0.49	0.45	3011	2144	867	0.51	0.50	2047	1743	303	0.50	0.51
2786	1310	1476	0.49	0.43	2456	1126	1329	0.50	0.47						2989	2622	367	0.52	0.52
					3855	2555	1300	0.51	0.46										

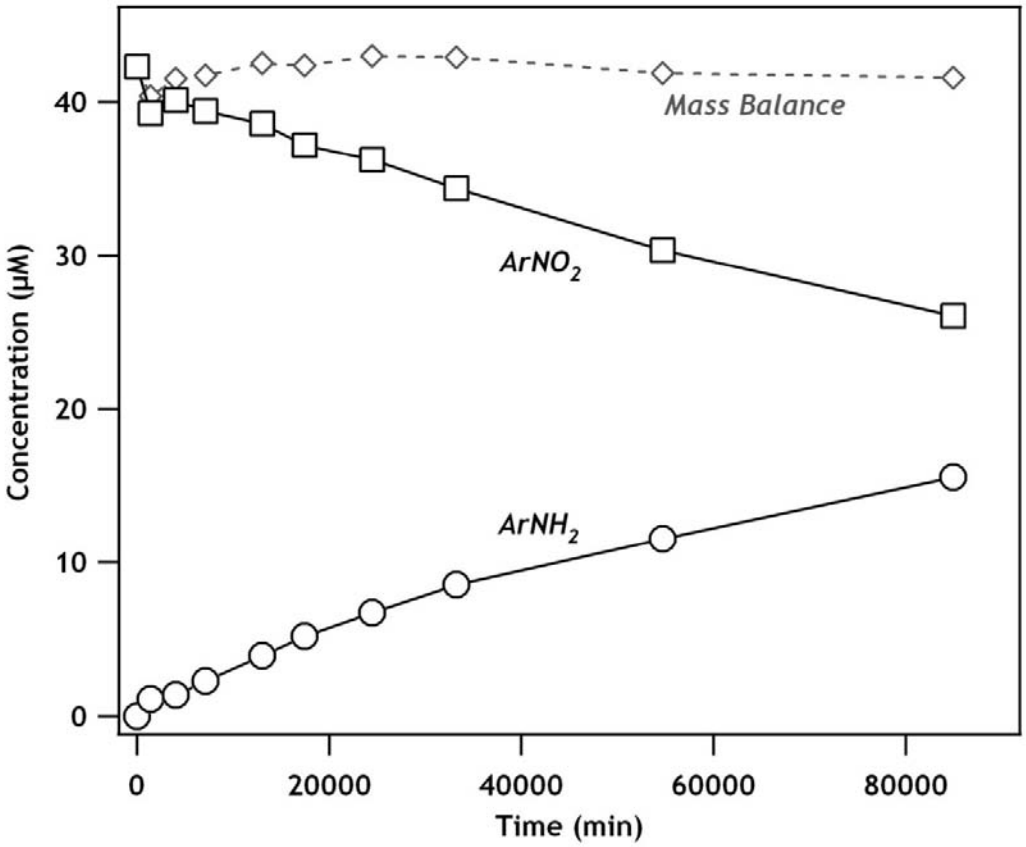

Figure A.5. Reduction of nitrobenzene to aniline by non-stoichiometric magnetite (x = 0.31). Experimental conditions: 50 mM MOPS buffer at pH 7.2, 1 g/L solids, 40 μM nitrobenzene.

Mössbauer Fitting Notes

Samples were prepared by filtering suspensions onto 13 mm filter disks in an anaerobic glove box. Air was then passed through the filter housing several times to remove excess moisture prior to mounting the sample between two pieces of Kapton tape to avoid oxidation when the sample was removed from the glove box. Spectra were then collected in transmission mode with a constant acceleration drive system, with a ^{57}Co source ranging from 30-50 mCi. Data were calibrated against α-Fe metal foil collected at room temperature. Spectral fitting was done using the Recoil software package, as described in detail below (University of Ottawa, Ottawa, Canada). Spectra were collected at room temperature, with the sample subsequently cooled to lower temperatures (typically 140 K, 77 K, and 13 K) for data collection.

Spectra collected at all temperatures suggested only the presence of magnetite and maghemite in the signal, but only the 140 K spectra are presented, as lowering the temperature maximized the clarity due to size and surface effects diminished the quality of higher temperature spectra (205). Spectra collected below the Verwey transition (121 K) produce very complex spectra, with five to six sextets used to model the signal, making quantitative interpretation virtually impossible (206-208). The challenge with this technique was that little literature existed on modeling magnetite at this temperature, but due to the small particulate magnetite used, room temperature spectra could only be used qualitatively due to collapsing of the observed signal.

Magnetite spectra at 140 K manifests in the observation of two sextets, one corresponding to the $^{Oct}Fe^{2.5+}$ signal, and the other representing the $^{Oct}Fe^{3+}$ and $^{Tet}Fe^{3+}$ signals. One can then model the magnetite in order to determine the Fe^{2+} content of the magnetite by the formula:

$$x_{Mössbauer} = \frac{\frac{1}{2}{}^{Oct}Fe^{2.5+}}{\frac{1}{2}{}^{Oct}Fe^{2.5+} + {}^{Tet}Fe^{3+}} = \frac{Fe^{2+}}{Fe^{3+}} \qquad (A.1)$$

Fitting of these two sextets is non-trivial, as the underlying assumptions of model type produces significantly different results. In this study, the magnetite spectra were fit using three model types: Lorentzian, Voigt-based fitting (VBF), and Extended Voigt-based fitting (xVBF) using Recoil software package. Previous work has shown that a solid contains probe nuclei in several different local environments, with each local environment having slightly different hyperfine parameters (70). In a Lorentzian fit, only one local environment is assumed, with the natural line-width of Mössbauer signal (an intrinsic constant, 0.097 mm/s) is broadened to account for this distribution, which is an inaccurate physical model. VBF, however, uses a Gaussian distribution of Lorentzian lines to account for the distribution of local environments, which more accurately describes the likely environment on a physical level. xVBF is a more complex fitting method, which allows for the linear coupling of unique parameters (center shift, quadrupole shift, hyperfine field), and provides a more rigorous fit due to the addition of adjustable parameters (99).

xVBF fitting was chosen as the final fit type due to the accuracy of the final fit that could be achieved based on the χ^2 value and the appearance. Fits were achieved using two sextets ($^{Oct}Fe^{2.5+}$ and $^{Tet}Fe^{3+}$,$^{Oct}Fe^{3+}$). Each sextet was fit using two components for the hyperfine field, with one component accounting for interline broadening that was observed in spectrum. Additional components were attempted, but the fit was not significantly improved, and in some cases unrealistic values were produced. No coupling parameters were allowed to float in the fitting process, but relative areas of peak intensities did float, with minor shifts from the ideal 3:2:1 ratio observed. The $x = 0.48$ magnetite was fit initially, with the fit saved and applied to other spectra, floating all variables. The linewidth and background were also held constant through the fitting process.

Calculations

Calculation A.1. Theoretical calculation for Figure 3.2

For 1 g/L magnetite:

$$1\ {}^{g}/_{L}\ Fe3O4 \times \frac{mol}{231.54g} \times \frac{3\ Fe}{mol\ Fe3O4} = 12.96\ mM\ Fe$$

1.5 mM $^{56}Fe^{2+}$ sorbed from solution

Assume $^{2}/_{3}$ of the sorbed Fe^{2+} undergoes electron transfer, with the other $^{1}/_{3}$ remaining Fe^{2+} to form stoichiometric magnetite in the growth phase. As a result, 1.0 mM electrons transferred to the underlying magnetite.

1.0 mM/12.96 mM = 7.7% of the underlying oxide reduced.

For every one electron transferred, two $^{Oct}Fe^{3+}$ are reduced to two $^{Oct}Fe^{2.5+}$ atoms.

Expected increase in $^{Oct}Fe^{2.5+}$ = 2*7.7% = 15.4%

The observed spectral $^{Oct}Fe^{2.5+}$ change from Figure 3.2A to 3.2B = 12.4% (Table 3.1).

Calculation A.2. Theoretical *x* values

The stoichiometry of the magnetite particles measured by dissolution ($x_{dissolution}$) is used to determine the percentage of maghemite in the particle. From that we can determine how much Fe^{2+} would be required to reduce the phase to stoichiometric magnetite.

For 1 g/L magnetite (Fe_3O_4):

$$1\ {}^{g}\!/_{L}\ Fe3O4 \times \frac{mol}{231.54g} \times \frac{3\ Fe}{mol\ Fe3O4} = 12.96\ mM\ Fe$$

4.32 mM Fe^{2+}

8.64 mM Fe^{3+}

12.96 mM Total Fe

For 1 g/L maghemite (Fe_2O_3)

$$1\ {}^{g}\!/_{L}\ Fe2O3 \times \frac{mol}{159.69g} \times \frac{2\ Fe}{mol\ Fe2O3} = 12.52\ mM\ Fe$$

Variables

M = % Magnetite

Mh = % Maghemite

x = Fe^{2+}/Fe^{3+}

Calculations

The calculation of the Fe^{2+} and Fe^{3+} concentrations can be made in relation to percent magnetite and maghemite (in mM):

$[Fe^{2+}] = M*4.32$

$[Fe^{3+}] = 12.52*Mh + 8.64*M$

$M = 1 - Mh$ (Mass balance, $M + Mh = 1$ assuming all iron is either maghemite or magnetite)

$[Fe^{3+}] = 12.52*(1-M) + 8.64*M$

$[Fe^{3+}] = 12.52 - 3.88*M$

x can then be expressed relative to the 'percent magnetite' of the sample:

$$x = \frac{Fe^{2+}}{Fe^{3+}} = \frac{4.32 \times M}{12.52 - 3.88 \times M}$$

Using algebra, the equation can also be expressed as:

$$M = \frac{12.52}{4.32/x + 3.88}$$

For Figure A.2, the amount of Fe^{2+} needed to reach $x = 0.5$ was calculated.

$$x = \frac{4.32 \times M + Sorbed\ Fe^{II}}{12.52 - 3.88 \times M}$$

Plugging in $x = 0.5$:

$$0.5 = \frac{4.32 \times M + Sorbed\ Fe^{II}}{12.52 - 3.88 \times M}$$

$0.5*(12.52-3.88*M) = 4.32*M + Sorbed\ Fe^{II}$

The amount of Fe^{II} needed can be expressed relative to the percent magnetite or x:

$$Sorbed\ Fe^{II} = 6.26 \times (1-M) = 6.26 \times (Mh)$$

$$Sorbed\ Fe^{II} = 6.26 \times \left(1 - \frac{12.52}{4.32/x + 3.88}\right)$$

Supplemental Information for Chapter IV

Chemicals and Instrumentation Used

Chemicals used:

MOPS buffer: Research Product International Corporation, >99%

Ferrous chloride (anyhydrous): Fisher Scientific, 99.99%

Ferric chloride (anhydrous, lump): Fisher Scientific, >97%

H_2O_2: Fisher Scientific, 30%

Methanol: Burdick and Jackson, >99.9%

Aniline, Fisher Scientific, 99.9%

Nitrobenzene, Fisher Scientific, 99.9%

2-Me-Aniline, Acros Organics, 99%

2-Me-Nitrobenzene, Acros Organics, 99%

3-Cl-Aniline, Acros Organics, 99%

3-Cl-Nitrobenzene, Acros Organics, 98%

Instruments used:

TEM: Joel 1230 TEM

pXRD: Rigaku Miniflex II, equipped with a Co source

^{57}Fe Mössbauer spectrometer: 13 K He system equipped with a ~30 mCu ^{57}Co source from Science Engineering and Education Co.

HPLC: Agilent 1100 Series HPLC

BET: Automated surface area analyzer, Quantachrome BET Nova 4200e

Figures and Tables

Table A.2. Measured E_{OCP} of magnetites with varying stoichiometries after 60 minutes equilibration; data shown in Figure 4.5. Measurements reported are of single specimens; when sufficient material was available, duplicate E_{OCP} measurements were done, and the results generally agreed within 5%. σ_x < 0.01 for all batches.

$x = Fe^{2+}/Fe^{3+}$	E_{OCP}[a] (V vs. SHE)
0.50	-0.477
0.49	-0.464
0.42	-0.298
0.36	-0.258
0.31	-0.253
0.28	-0.182
0.33	-0.262
0.22	-0.010
0.17	+0.047

[a] Open-circuit potential.

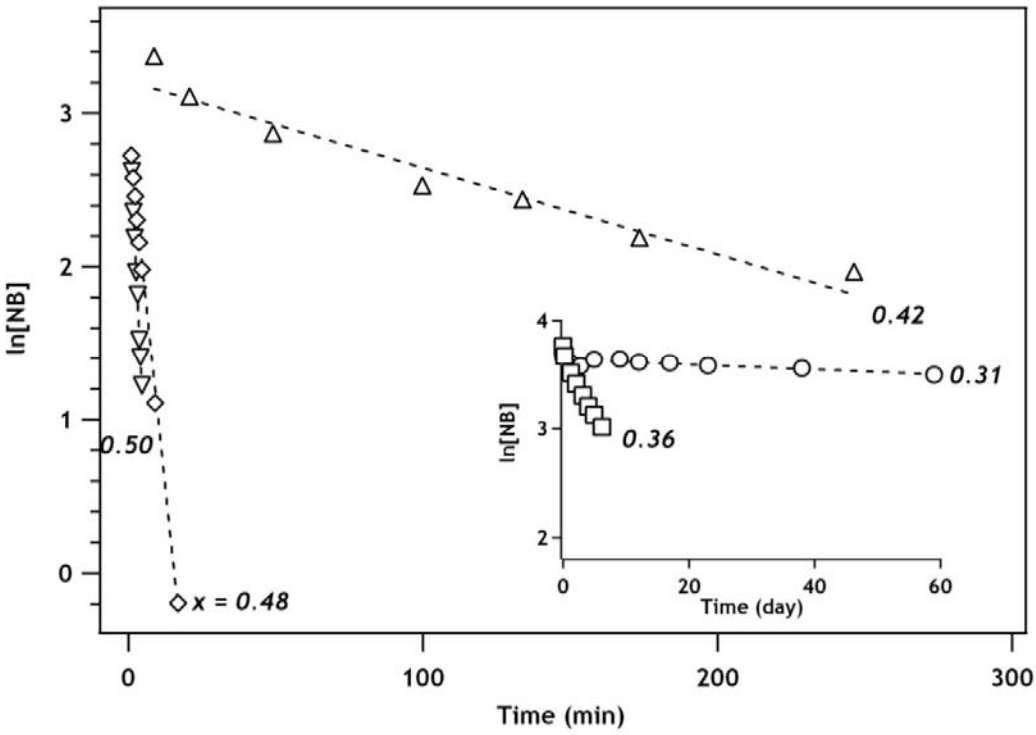

Figure A.6. First-order plot for 2-Me-$ArNO_2$ reduction by magnetite with different stoichiometries ($x = Fe^{2+}/Fe^{3+}$). Legend: ▽ x = 0.50, ◇ x = 0.48, △ x = 0.42, □ x = 0.36, ○ x = 0.31. Experimental conditions: 1 g/L magnetite, pH 7.2, 50 mM MOPS buffer, 1 hour equilibration prior to addition of 2-Me-$ArNO_2$, [2-Me-$ArNO_2$]$_0$ = 40 µM.

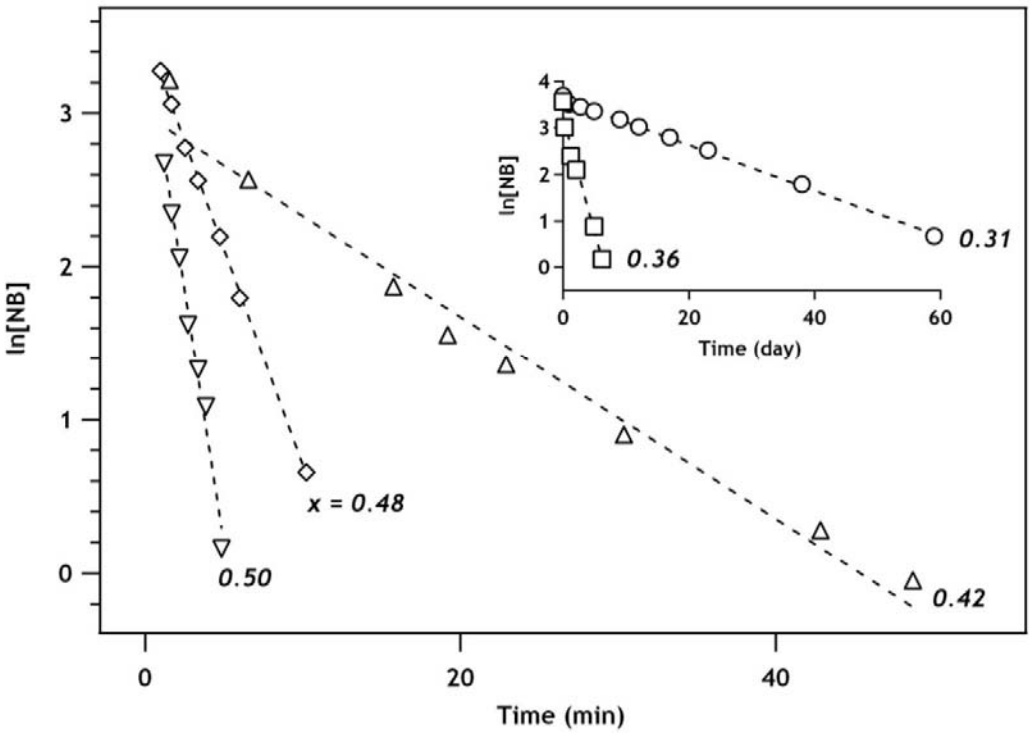

Figure A.7. First-order plot for 3-Cl-$ArNO_2$ reduction by magnetite with different stoichiometries ($x = Fe^{2+}/Fe^{3+}$). Legend: ▽ x = 0.50, ◇ x = 0.48, △ x = 0.42, □ x = 0.36, ○ x = 0.31. Experimental conditions: 1 g/L magnetite, pH 7.2, 50 mM MOPS buffer, 1 hour equilibration prior to addition of 3-Cl-$ArNO_2$, [3-Cl-$ArNO_2$]$_0$ = 40 µM.

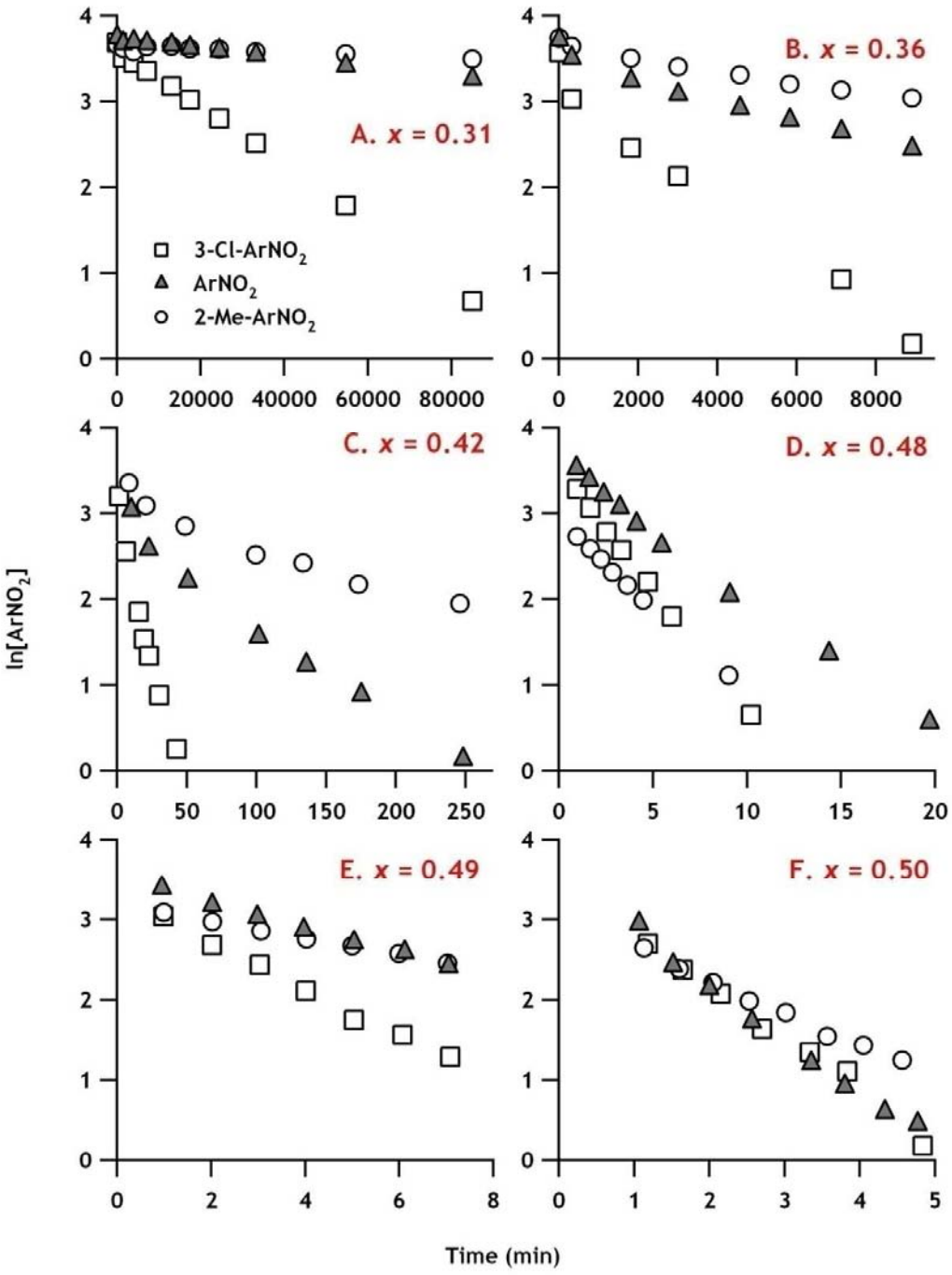

Figure A.8. First-order kinetics of substituted nitrobenzene compounds by magnetites of varying stoichiometries (x = Fe^{2+}/Fe^{3+}). Experimental conditions: pH 7.2, 50 mM MOPS, 1 g/L magnetite, 40 µM nitrobenzene. First-order linear fits are presented in Table 4.1.

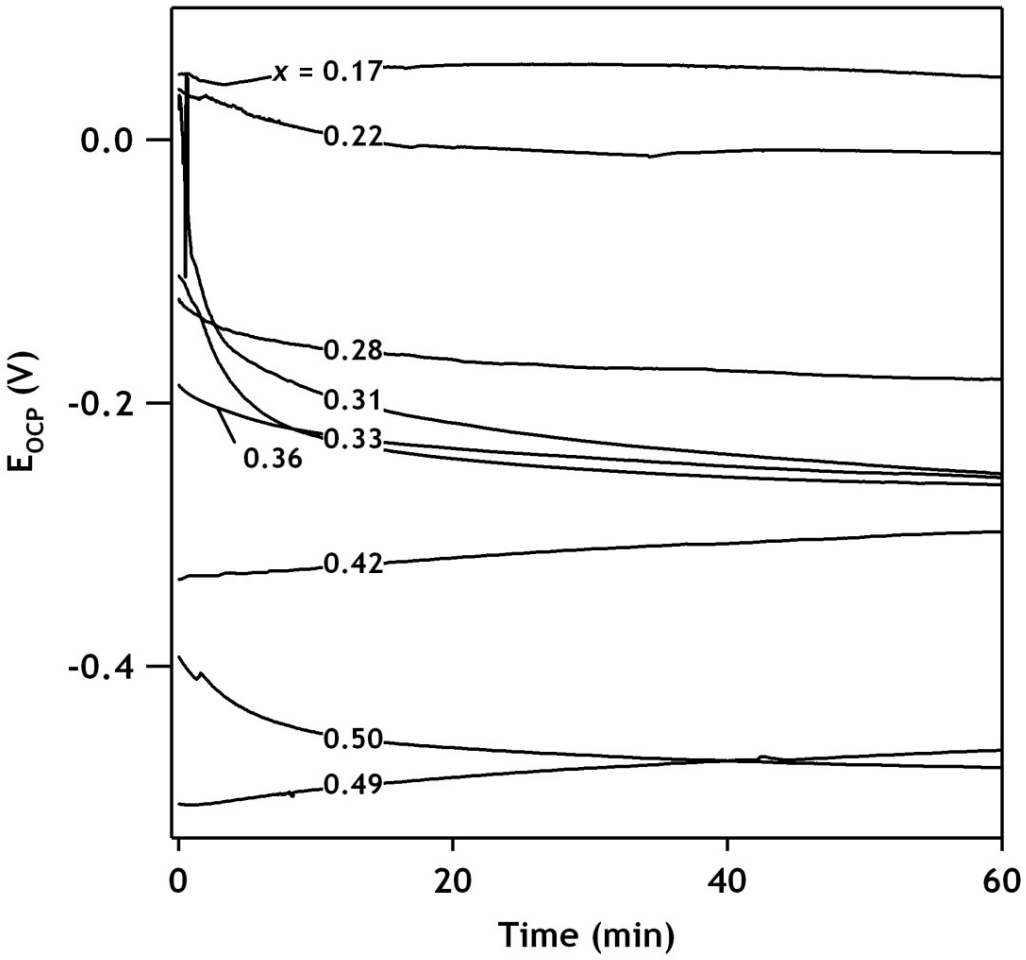

Figure A.9. The measured open-circuit potentials (E_{OCP}) of magnetite-packed electrodes in N_2 purged 50 mM MOPS, pH 7.2. The written values on the Figure are the stoichiometry ($x = Fe^{2+}/Fe^{3+}$) for each sample. Values shown are in reference to SHE.

Calculations

Calculation A.3**.** Production of the calculated rates in Figure 4.7.

Example calculation for $ArNO_2$ reduction by magnetite. Note for substituted nitroaromatics (or other contaminants), $E_h^{1'}$ will be the only variable that changes; thus, the y-intercept will shift, but the slope will still be dependent only on $E_{OCP}(x)$.

$$E_{cell}(x) = E_h^{1'} - E_{OCP}(x)$$

For $ArNO_2$: ($E_h^{1'}$ = -0.485 V)

$$E_{cell}(x) = [-0.485\ V — (-1.52(x) + 0.28\ V)]$$

$$E_{cell}(x) = [-0.765\ V + 1.52(x)]$$

$$\ln[k(x)] = \alpha\frac{-nF}{RT}[E_{cell}(x)] + \beta$$

n = 1; F = 96.485 kC; R = Ideal gas constant, T = absolute temperature (298 K here)

Assume α = 1 (adiabatic); β = 0 (allow E_a to determine intercept)

$$\ln[k(x)] = -29.8 + 59.2(x)$$

APPENDIX B: CONNECTING OBSERVATIONS OF HEMATITE (α-Fe_2O_3) GROWTH CATALYZED BY Fe(II)

Abstract

Electron exchange between aqueous Fe(II) and structural Fe(III) in iron oxides and oxyhydroxides is important for understanding degradation of environmental pollutants through its apparent constitutive role underlying highly reactive "sorbed Fe(II)" and by catalyzing phase interconversion among these minerals. Although a mechanistic understanding of relationships between interfacial $Fe(II)_{ads}$-$Fe(III)_{oxide}$ electron transfer, bulk electron conduction, Fe(II) release, and phase transformation behavior is emerging, much remains unclear in part due to poorly interconnected investigations. The focus of this study is on reconciling two mutually similar observations of Fe(II)-catalyzed hematite growth documented spectroscopically and microscopically under substantially different chemical conditions. Here we employ iron isotopic labeling to demonstrate that hematite grown on the (001) surface in Fe(II)-oxalate solution at pH 2.10 and 348 K has temperature-dependent magnetic properties that closely correspond to those of hematite grown in Fe(II) solution at pH 7.4 and room temperature. The temperature evolution and extent of the Morin transition displayed in these two materials strongly suggest a mechanistic link between the two studies, and that this mechanism involves in part trace structural Fe(II) incorporation into the growing hematite. Our findings indicate that Fe(II) catalyzed growth of hematite on hematite can occur under environmentally relevant conditions and may be due to bulk electron conduction previously demonstrated for hematite single crystals.

K.M. Rosso, S.V. Yanina, C.A. Gorski, P. Larese-Casanova, and M.M. Scherer. Connecting observations of hematite (α-Fe_2O_3) growth catalyzed by Fe(II). *Environmental Science and Technology.* 2009, *In press.*

Introduction

Electron exchange between aqueous Fe(II) and structural Fe(III) in iron oxides and oxyhydroxides is a natural process capable of important direct and indirect linkages to the degradation or mobility of environmental pollutants. For example, it appears to comprise a key characteristic of highly reactive putatively "sorbed Fe(II)" pools on these minerals that yield kinetically enhanced reduction of redox-active contaminants (13, 20, 143). Electron exchange between aqueous Fe(II) and structural Fe(III) is also fundamental to redox transformations of iron oxide and oxyhydroxide minerals from one phase to another, which impacts the nature and availability of the reactive surface sites provided by this widespread class of high specific surface area subsurface sorbents (1).

The electron transfer step, entailing reduction of lattice Fe(III) to Fe(II) through a surface adduct with adsorbed Fe(II) – the electron donor, was deduced in early research (85, 209, 210) and more recently has been directly implicated (24, 26-30). Also, because many iron oxides and oxyhydroxides are electrical semiconductors with significant charge carrier mobilities (158, 211, 212), electron transfer into the solid has long been speculated or known to couple with spontaneous electron conduction, such that injected electrons are somewhat free to move about in the solid or solid surface to remote locations (30, 85, 149, 154, 157, 213, 214). The dynamics of diffusive mobility of injected electrons and its relationship to crystalline structure for these materials has been examined in detail with computational methods from first principles, and generally validates this picture (215-221).

The relationship between interfacial $Fe(II)_{ads}$-$Fe(III)_{oxide}$ electron transfer, bulk electron conduction, and phase transformation behavior remains poorly understood. They appear intimately linked in the topotactic transformation between maghemite and magnetite (29, 54, 85). Recent studies of Fe(II) interaction with fine-grained hematite and goethite powder, under circumneutral pH and low [Fe(II)] where conversion to magnetite is avoided, provide strong evidence for interfacial $Fe(II)_{ads}$-$Fe(III)_{oxide}$ electron

transfer without change in mineralogy (22, 24, 26-29, 140, 222). In these instances, Fe(II) appears to catalyze recrystallization of the solid. Ostensibly, this occurs by oxidative adsorption of Fe(II) coupled to remote reductive dissolution of Fe(III) by surface or bulk conduction, yielding a combined electron and iron atom exchange process. However, a complete picture is yet to emerge. Current findings are not without some apparent contradictions, and the existing set of observations remain poorly interconnected due to significant differences in approach, experimental conditions, and degree of conclusiveness.

Two recent studies involving Fe(II)/hematite interaction performed with very different approaches and conditions have intriguingly similar conclusions. Larese-Casanova and Scherer (26) used the ^{57}Fe specificity of Mössbauer spectroscopy to examine the interaction of ^{57}Fe(II) with synthetic α-$^{56}Fe_2O_3$ powder (hereafter ^{56}hematite) anoxically at room temperature over a range of Fe(II) concentrations and pH values. At pH 7.4 with sorbed Fe(II) concentrations estimated to be lower than site saturation, these workers spectroscopically documented growth of a ^{57}Fe-bearing hematite surface layer formed from ^{57}Fe(II) oxidation by structural ^{56}Fe(III) at the ^{56}hematite surface. By examining the temperature dependence of the Mössbauer spectra, the hematite surface layer was found to have a partially suppressed Morin transition. Pure bulk hematite is weakly ferromagnetic (WF) above the Morin transition temperature T_M ~ 265 K (223, 224), and antiferromagnetic (AF) below. The WF phase entails alignment of unpaired spins contributed by high-spin Fe $3d^5$ electrons along the basal (001) plane in a nearly antiparallel fashion, whereas the AF phase entails antiparallel spin alignment along the [001] direction with no net magnetic moment. With decreasing temperature, the spin-flip transition to the AF phase is complete; the WF phase is gone typically within a few degrees of T_M. However, certain impurities and structural defects are known to suppress T_M even in low concentrations (225). In the study by Larese-Casanova and Scherer (26), the Fe(II)-catalyzed hematite surface layer never completes the Morin transition, that is,

the WF phase persists down to 13 K. In a follow-up Mössbauer study using reversed Fe isotopes, Larese-Casanova and Scherer (27) examined the magnetic properties of ^{57}hematite after exposure to ^{56}Fe(II). Suppression of T_M to below 13 K was also observed for this system using equivalent conditions. Lattice ^{57}Fe(II) was not directly observed, attributed to valence interchange and electron hopping mobility faster than observable by Mössbauer spectroscopy, consistent with theoretical predictions (221).

The second study of interest was reported by Yanina and Rosso (30). Macroscopic single crystals of hematite with oriented surfaces and synthetic tabular hematite platelets were exposed to a variety of anoxic, low pH, Fe(II) solutions that included oxalate anions to achieve conditions consistent with ligand-assisted dissolution "catalytically enhanced" by Fe(II) (214, 226). Fe(II) was the only available reductant and was present at concentrations similar to those in Larese-Casanova and Scherer (26). The structure, composition, and morphology of basal and edge surfaces was examined before and after reaction, which showed that while most surfaces dissolve, the basal (001) surface grows large amounts of additional hematite. Using controlled exposure of specific surface types, and measurements of surface potential differences and bulk electrical conductivity, the interaction of Fe(II) with hematite was deduced to initiate two distinct but coupled surface-specific interfacial processes: i.) hematite growth on (001) by net Fe(II) oxidative adsorption at this surface, and ii.) dissolution of edge surfaces by net internal reduction of lattice Fe(III) at edge surfaces yielding Fe(II) release. Edge surface Fe(III) effectively serves as the oxidant for Fe(II) adsorbed on the (001) surface, and electron exchange between these sites is facilitated by bulk electrical conduction (30).

The focus of the present study is on the mutually similar conclusions in Larese-Casanova and Scherer (26) and in Yanina and Rosso (30) that Fe(II) interaction with hematite causes hematite deposition by $Fe(II)_{ads}$-$Fe(III)_{oxide}$ interfacial electron transfer into the solid. While similar Fe(II) concentrations were used in both studies, different pH regimes, the presence of iron chelating ligands, and hematite materials that differ

substantially in their origin, preparation, crystal sizes and morphologies make it unclear whether the observations were due to similar mechanisms. Here we address this issue by applying the surface-specific methods and conditions of Yanina and Rosso (30) to yield Fe(II)-catalyzed hematite growth on the (001) surface, and we use iron isotopes and Mössbauer characterization similar to Larese-Casanova and Scherer (26) to characterize the magnetic properties of the deposited hematite alone. The hypothesis is that if the hematite growth mechanism observed in both studies is similar, hematite grown on the (001) surface will also display Morin transition suppression with characteristics close to that documented in Larese-Casanova and Scherer (26). Because the temperature dependence of the Morin transition is sensitive to the degree of hematite crystal perfection, close correspondence in the temperature dependence would be a compelling argument that the deposited hematite in the two studies has similar mechanistic origins despite the different conditions and materials used. Specifically, the Fe(II) oxidative adsorption process causing hematite deposition observed by Larese-Casanova and Scherer (26) could be driven by preferential Fe(II) adsorption and electron transfer to lattice Fe(III) at specific crystallographic surfaces or sites, with bulk electron conduction flowing down a surface potential gradient to remote electron accepting Fe(III) sites of relatively high oxidation potential favoring Fe(II) release, as deduced by Yanina and Rosso (30).

Materials and Methods

Synthetic tabular hematite powders were grown similar to those used in Yanina and Rosso (30) following a hydrothermal recipe (227). ^{57}Fe is the signal-generating isotope for Mössbauer measurements. Two hematite samples were synthesized: (1) non-isotopically selective hematite containing iron isotopes at natural abundance (~2.2% ^{57}Fe; hereafter termed ^{NA}hematite), and (2) isotopically enriched ^{56}hematite (>99% ^{56}Fe) (Supporting Information, Appendix A) intended as a Mössbauer-transparent sample. In

both cases, resulting hematite platelets had a euhedral platy hexagonal habit with large smooth (001) surfaces bounded by (012) edge terminations. X-ray diffraction (XRD) showed that both materials so obtained consisted primarily of hematite with trace deposits of nanocrystalline goethite. Trace goethite was eliminated by conversion to hematite from annealing in air at 873 K overnight. This step also eliminates trapped H_2O/OH^- (228)

The anoxic reaction of hematite with Fe(II) in oxalate results in the preferential growth of hematite on the (001) surface (30), presumably towards a new equilibrium crystal morphology under these conditions. The present study utilizes ^{57}Fe(II)-oxalate reaction mixtures with 1 mM $^{57}FeCl_2$ and 10 mM oxalic acid; the pH was adjusted to 2.10 using HCl (see Supporting Information, Appendix A). Reaction runs were performed using a digestion bomb setup (30), where ~ 10 mg of hematite and 125 mL of the ^{57}Fe(II)-oxalate solution were placed in a cylindrical Teflon™ vessel (~ 125 mL capacity) within the glove box and tightly covered with a Teflon™ lid. The covered vessel was placed inside the digestion bomb (Parr Instrument Co., Moline, IL, USA) which was then sealed. Reaction runs were performed with precisely controlled temperature (75±2ºC) and shaking (~ 150 rpm) for 24 h as described in Supporting Information, Appendix A.

XRD and scanning electron microscopy (SEM) analyses of hematite before and after reaction were performed at Pacific Northwest National Laboratory, while Mössbauer analyses were performed at the University of Iowa on samples from parallel runs, with sample handling as described in Supporting Information, Appendix A. Mössbauer spectra were collected in the 13-298 K temperature range using methods described earlier (26). All spectra are reported in reference to α-Fe foil calibration room temp spectrum. Spectra were fit using Recoil software package (University of Ottawa, Ottawa, Canada). Three unique models were used to fit spectra to attempt to minimize model-bias and provide a range of plausible parameters. The models used were the

Lorentzian, Voigt (70), and extended-Voigt (99). Parameters were set initially to references values, then allowed to vary using a least-squares optimization. For all fits, the 3:2:1 peak ratio was held constant, and the linewidth was fixed at 0.12 for the Voigt and extended-Voigt fits, as it was determined to be the instrumental linewidth. Here, we report the Lorentzian fits, as they were the most conservative estimates of relative areas; the Voigt and extended-Voigt parameters and fitting standard deviations can be found in Tables B.3 and B.4 in Supporting Information, Appendix A. Fitting of ^{57}Fe(II) spectra typically showed the following standard deviations in parameters 0.01 mm/s (CS), 0.04 mm/s (QS), 0.1 T (H), and 0.5% (relative area). For the natural abundance samples, the standard deviations were below the significant Figures presented here.

All solutions were prepared from deionized anoxic H_2O from boiling Milli-Q water under vacuum (resistance >18 MΩ) with the residual dissolved oxygen content determined to be below 1 ppb based upon Rhodazine D™ colorimetric analysis (CHEMetrics, Inc., Calverton, VA, USA). Solutions were prepared in the dark under nitrogen atmosphere from liquid N_2 evaporation inside an oxygen-monitored glove box (nominal $pO_2 \leq 1.0$ ppm) using oxalic acid (99.999%, purified), and HCl (ACS reagent grade) for pH adjustment to 2.10. Isotopically pure ^{57}Fe(II)-oxalate solutions were produced as follows: A weighed amount of metallic ^{57}Fe was placed into 5 mL of a concentrated solution of oxalic acid and HCl prepared with anoxic H_2O, which was left to fully digest overnight inside the glove box. The next day, the solution was filtered with cellulose Millipore™ filters (20 μm pore size) and diluted to yield a solution of 1 mM ferrous iron chloride and 10 mM oxalate. Isotopically pure (>99%) metallic ^{56}Fe and ^{57}Fe was obtained from Cambridge Isotopes (Cambridge, MA). All solutions were prepared immediately prior to the experiments. All glassware, plastic bottles and Teflon™ parts used in the experiments were cleaned in 5 M HCl, 10% HNO_3 and deionized H_2O prior to experiments.

Reaction runs in the digestion bomb were performed as follows. For the purpose of monitoring the internal temperature, a K-type thermocouple (Omega Engineering, Stamford, CT, USA) was placed in contact with the lid of the vessel in the interior of the bomb. The bomb was tightly sealed and enclosed in a heating mantle (Barnstead International, Dubuque, IA, USA) that was placed on an orbital shaker moving at a rate of ~ 150 rpm. The temperature of the external bomb sheath was monitored separately with a K-type thermocouple attached to the body of the bomb. The bomb was heated for 45 minutes up to 75±2ºC and held at this temperature for 24 hours. During a run, the temperature inside the reaction vessel did not deviate from the temperature of the external bomb sheath by more than ± 2 K. Upon completion of a run, the bomb was cooled in an ice bath for two to five minutes.

For XRD and SEM analyses of reacted samples, the vessels were opened in air with no concern for oxidation, the reaction solution was decanted, and the powders were washed with deionized H_2O and placed onto glass dishes to dry. Previous work has shown that the grown material is hematite (13) and therefore insensitive to oxidation. Fe(II) was found to be sufficiently stable with respect to oxidation at low pH such that the rinsing and drying treatment did not deposit unwanted Fe(III) solids on the sample surfaces detectable by XRD, SEM, nor Mössbauer analysis. For Mössbauer characterization, samples from parallel runs were sent in their sealed reaction vessels to the University of Iowa. At the University of Iowa, the vessels were opened in air, powders were collected and mounted on Kapton™ tape for analysis.

Results and Discussion

The conceptual model for these experiments can be illustrated as shown in Figure B.1. The objective of the present study is to catalytically grow hematite on hematite parent crystals by reaction in Fe(II)-oxalate solution (30) and to characterize the magnetic properties of the deposited hematite alone without significant contribution from the

underlying hematite. The underlying hematite must be Mössbauer-transparent, and the deposited hematite must be sufficiently enriched in ^{57}Fe and present in sufficient amounts for detection. To accomplish this, a tabular platelet morphology of ^{56}hematite was exposed to ^{57}Fe(II)-oxalate solution. The hematite platelets are bounded at their edges by (012) surfaces (1), which under our conditions are expected to dissolve as the (001) surface grows. The reaction of interest is net oxidative adsorption of ^{57}Fe(II) at the (001) surface of ^{56}hematite platelets. This process is expected to be simultaneously coupled to release of ^{56}Fe(II) from (012) edge surfaces by capture of electrons being injected into the (001) surface, in principle in a one-for-one atom exchange fashion (30). The solution, although initially pure in ^{57}Fe(II), progressively becomes a mixture of ^{57}Fe/^{56}Fe over the course of the reaction. However, as long as the amount of ^{57}Fe in solution remains much greater than the amount of contributed ^{56}Fe, the hematite deposited on the (001) surface should at all times be isotopically enriched in ^{57}Fe, while the underlying original hematite remains composed of Mössbauer-transparent ^{56}Fe. The presence of oxalate also provides a means for ^{56}Fe release, in this case by chelation of surface Fe(III) or Fe(II) (221). The apparent one-for-one iron atom exchange process described above can be considered a "sub-system" within an overall process that entails net iron release into solution by ligand-assisted dissolution. Nonetheless, because the solid to solution ratio (0.08 g/L) was chosen to be small enough such that any released ^{56}Fe over the time frame of the experiment would remain at least 2x less concentrated than ^{57}Fe, ^{57}Fe enrichment of the grown hematite is the expectation.

The two hematite samples, ^{56}hematite and ^{NA}hematite, were pre-characterized by SEM for crystal morphology, XRD for phase identification and to assess phase purity and crystallinity, and electron microprobe spectrometry for compositional purity. SEM showed that initial platelets had a euhedral tabular hexagonal habit with large flat (001) surfaces (Figure B.2a). Lateral dimensions ranged between approximately 2-15 μm and platelet thickness ranged between approximately 0.5-2.0 μm; the samples were not

monodisperse. The morphology and (001) surface details of hematite platelets synthesized in the same fashion were earlier characterized in detail by atomic force microscopy in (221). Powder XRD Rietveld structure refinement of these materials confirmed that they consisted of pure hematite with hexagonal unit cell parameters *a*=5.032 Å and *c*=13.739 Å. Electron microprobe analysis showed that these hematites had ideal Fe_2O_3 stoichiometry within measurement error.

To establish a reference for characterizing the deposited hematite, the magnetic properties of unreacted ^{NA}hematite were assessed by collecting spectra at temperatures ranging from room temperature to 13 K (Figure B.3). The spectra displayed the characteristic sextet of high-spin octahedral Fe(III) with spectral parameters (center shift (CS), quadrupole splitting (QS), and hyperfine magnetic field (H) values consistent with those of pure bulk hematite (26, 27) (Table B.1). At 298 K, ^{NA}hematite was found to be fully in the WF state. Upon cooling, the ^{NA}hematite is observed to start the Morin transition between 270-230 K and is fully in the AF state by 140 K. The measured T_M for ^{NA}hematite, taken as the temperature at which the two magnetic phases exist in equal proportions according to integrated peak areas, was ~ 250 K. Although pure bulk hematite nominally has a T_M ~ 265 K, the measured value is within the range of a survey of reported T_M values on a variety of hematite samples (225), which suggests our synthesis protocol yields relatively pure hematite without significant defect. Hence, the chosen synthesis route yields a material not only with the desired tabular morphology but one that behaves close to ideal α-Fe_2O_3.

We now turn our attention to ^{56}hematite reaction with ^{57}Fe(II)-oxalate solution. Mössbauer spectra at 13 K for ^{56}hematite before reaction showed a very weak signal due to trace ^{57}Fe initially present (Figure B.1). This material was synthesized from elemental iron that contained >99% ^{56}Fe, therefore a trace amount of ^{57}Fe impurity was expected to be present with initially uncertain spectroscopic detectability. Although this ^{57}Fe impurity signal was too weak for detailed spectral fitting, fitting one sextet to the data

shows that it is consistent with an AF phase (from the QS value, Table B.1). The ^{56}hematite sample was then reacted in 1 mM ^{57}Fe(II) + 10 mM oxalic acid (pH = 2.10, temperature = 348 K, duration 24 h). SEM of the reacted material confirmed that most of (001) basal surfaces of the platelets developed pyramidal overgrowths, consistent with Yanina and Rosso (30) (Figure B.2b). Mössbauer spectra at 13 K showed that ^{57}Fe-enriched hematite was indeed deposited from the reaction based on an increase in the intensity of the sextet peaks (Figure B.1). The spectra are consistent with ^{57}Fe occupation of octahedral lattice sites in the hematite structure. Our identification of hematite as the sole phase to comprise the pyramids using Mössbauer spectroscopy is consistent with previous identification of the pyramids as hematite using a variety of techniques (30).

The pyramidal hematite, however, shows markedly different magnetic behavior compared to bulk ^{NA}hematite. Although pure bulk hematite is antiferromagnetic at 13 K (e.g., the ^{NA}hematite and unreacted ^{56}hematite samples, Table B.1), there is a significant presence of the WF phase as well as the AF phase at this temperature in the reacted ^{56}hematite sample. The WF phase is not statistically resolvable in the low temperature spectra of ^{56}hematite before reaction, nor is it present at 13 K for ^{NA}hematite. Persistence of the WF phase at low temperature in the reacted sample suggests strong Morin transition suppression in the hematite deposited on the (001) surface. The temperature series from room temperature to 13 K is shown in Figure B.3 with accompanying parameter fitting values given in Table B.1. Similar to ^{NA}hematite, the reacted sample starts the Morin transition between 270-230 K. Equal proportions of the WF and AF phases are present in the reacted sample at ~ 230 K, somewhat lower than T_M ~ 250 K measured for ^{NA}hematite. However, unlike the ^{NA}hematite, the reacted sample never completes the full transition into the AF state. The WF phase is retained by the reacted sample to a significant degree on cooling to 140 K and persists down to 13 K.

The amount of retained WF phase is difficult to quantify due to the low signal to noise ratio and the background signal from the ^{57}Fe impurity in the ^{56}Fe hematite (shown

in Figure B.3 for the 13K data**)**. We chose to use multiple models to fit the data with and without background subtraction to determine a reasonable estimate of the range of WF phase present. The fitting parameters estimated from the models are all consistent with the WF and AF phase identifications, but the relative areas vary by about 20% as shown by the error bars in Figure B.4. Despite the 20% variation in the relative areas, it is still clear that the WF phase is retained by the reacted sample to a significant degree (about 20-40%) on cooling to 140 K and persists down to 13 K.

The suppression of Morin transition observed here, and the temperature range over which the transition evolves, shows good correspondence to that reported by Larese-Casanova and Scherer (26, 27) for ^{57}Fe-enriched hematite deposited on ^{56}hematite from exposure to ^{57}Fe(II) solutions under substantially different reaction conditions (e.g., no oxalate, circummeutral pH, room temperature, 10 hours of reaction, different hematite particle sizes and crystal morphologies). In that study, much smaller hematite crystallites with a mixture of acicular 200×20 nm crystals and rounded hexagonal plates 100–200 nm in diameter were used. Reacted material showed equal proportions of the WF and AF phases at approximately 13 K, although spectra were recorded for only two temperatures (Table B.2). Furthermore, our findings are consistent with the behavior of ^{57}hematite "doped" with Fe(II) to levels between ~ 0.3-0.5% by electron injection from oxidatively adsorbed ^{56}Fe(II) (27). That reversed isotope experiment, also involving the smaller hematite crystals, showed an equal proportion of the WF and AF phases occurs at approximately 180 K, 52 K below the reported T_M of the unreacted ^{57}hematite (232 K) (Table B.2). Hematite reacted in this manner does not complete the Morin transition by 13 K. Instead it retains a mixture of WF (~ 30%) and AF phases (~ 70%) in proportions very similar to those reported here (~ 20-40% WF and ~ 60-80% AF) for the ^{57}Fe-enriched hematite grown on (001) surfaces of tabular ^{56}hematite.

Suppression of the Morin transition has been linked to a wide range of hematite characteristics including incomplete stoichiometry, certain impurities, lattice strain,

particle size and morphology, and the thermal history of the particles. However, many of these characteristics are intertwined, and debate remains because of inadequate or impossible separation of effects (228, 229). Given that the spectroscopic findings of the present study, which is based on the chemical conditions of Yanina and Rosso (30), are strongly reminiscent of those of Larese-Casanova and Scherer (26, 27), and given the numerous differences in growth conditions used, certain characteristics can be eliminated from consideration if they are not relevant to both sets of studies simultaneously. For example, particle size effects do not appear to be relevant because in the present study grown hematite crystallite sizes are generally much larger (micron scale) than those where size effects become important (nanometer scale) (229). Also, thermal history appears irrelevant because the hematite overlayer in Larese-Casanova and Scherer (26) was grown at room temperature and analyzed at room temperature and below.

Hence, characteristics of the grown hematite that appear most relevant to both sets of studies entail possible incorporation of structural and/or compositional defects. Hematites grown in hydrothermal conditions often incorporate molecular water into interstitial sites at a level of several mole percent, i.e., "protohematite" (230), or charged structural defects, such as Fe(III)-vacancies coupled to structural OH^- creation (i.e., by exchange of a lattice Fe(III) cation for three protons bound to lattice oxygen anions near the vacancy), i.e., "hydrohematite" (231). However, in the studies under consideration hematite was grown under sub-hydrothermal conditions which alone typically does not yield significant T_M suppression (232). A related charged defect is incorporation of lattice Fe(II), which is conceptually feasible by either coupling to oxygen anion vacancy creation (e.g., exchange of lattice O^{2-} for reduction of two lattice Fe(III) cations to Fe(II) (233)), or to structural OH^- creation (e.g., reduction of a lattice Fe(III) cation to Fe(II) with charge compensation by protonation of a nearby lattice oxygen anion). Fe(II) is the one key solution component common to the studies under consideration, and its incorporation in the hematite lattice has a long precedent (38). Furthermore, small

amounts of Fe(II) doping in hematite have been shown to yield dramatic T_M suppression (225, 234). Therefore, the strongest candidate to explain T_M suppression behavior in Fe(II)-catalyzed hematite growth is incorporation of lattice Fe(II), as originally concluded by Larese-Casanova and Scherer (27).

Spectroscopic (26) and microscopic (30) observations of Fe(II)-catalyzed hematite growth therefore appear mechanistically related despite substantial differences in reaction conditions. The magnetic properties of the ^{57}Fe-enriched hematite grown on the (001) surface in the present study is very well described by that of the 0.3-0.5% Fe(II)-doped ^{57}hematite in Larese-Casanova and Scherer (27). The deposited hematite in both studies is likely driven by preferential Fe(II) adsorption and electron transfer to lattice Fe(III) at specific crystallographic surfaces or sites, with bulk electron conduction flowing down a surface potential gradient to remote electron accepting Fe(III) sites of relatively high oxidation potential favoring Fe(II) release. The same process was recently invoked to explain complete atom exchange observed between goethite and aqueous Fe(II) (29). It requires transient occupation of surface sites by adsorbed Fe(II) preceding electron transfer into the solid at sites favorable for this forward reaction. Occupation of sites consistent with infilling or extension of the metal sublattice would be consistent with recent atomic-level surface structural investigations of Fe(II) interaction with crystallographically oriented hematite surfaces (142). Hence, random incorporation of small amounts of residual Fe(II) bound at incipient lattice sites by inclusion in the growing overlayer of deposited Fe(III) electron transfer reaction products would be one chemically reasonable explanation. Our findings suggest that the process of Fe(II)-catalyzed electron and atom exchange is operative over a wide range of conditions in the Fe(II)-hematite system. With respect to fundamental understanding of the degradation and mobility of environmental pollutants, the collective observations point to the need for a greatly improved conceptual model of iron oxides and oxyhydroxides in contact with aqueous Fe(II).

Table B.1. Fit spectral parameters of samples in this study[a]. The spectra are shown in Figure B.3.

		Weakly ferromagnetic phase				Antiferromagnetic phase			
	Temp	CS	QS	H	RA	CS	QS	H	RA
sample	(K)	(mm s^{-1})	(mm s^{-1})	(T)	(%)	(mm s^{-1})	(mm s^{-1})	(T)	(%)
$^{NA}Fe_2O_3$	298	0.37	-0.21	51.6	100	-	-	-	0
	270	0.39	-0.2	51.7	100	-	-	-	0
	230	0.43	-0.2	52.3	10	0.41	0.4	52.8	90
	140	-	-	-	0	0.46	0.41	53.5	100
	77	-	-	-	0	0.48	0.4	53.6	100
	13	-	-	-	0	0.49	0.4	53.7	100
$^{57/56}Fe_2O_3$	298	0.37	-0.21	51.4	100	-	-	-	0
	270	0.38	-0.2	51.6	100	-	-	-	0
	230	0.42	-0.18	51.9	48	0.41	0.4	52.8	52
	200	0.4	-0.16	51.8	31	0.43	0.41	53	69
	140	0.46	-0.28	52.5	19	0.46	0.43	53.4	81
	77	0.51	-0.21	52.9	25	0.48	0.4	53.6	75
	13	0.51	-0.27	52.8	21	0.5	0.39	53.5	79
$^{56}Fe_2O_3$	13	-	-	-	-	0.5	0.39	53.7	~100

[a] Parameters are from Lorentzian model fits. CS = center shift. QS = quadrupole splitting. H = hyperfine magnetic field. RA = relative spectral area from fits.

Table B.2. Fit spectral parameters[a] from Larese-Casanova and Scherer (26) for ^{56}hematite reacted with ^{57}Fe(II), and from Larese-Casanova and Scherer (27) for ^{57}hematite and ^{57}hematite reacted with ^{56}Fe(II).

		Weakly ferromagnetic phase				Antiferromagnetic phase			
	Temp	CS	QS	H	RA	CS	QS	H	RA
sample	(K)	(mm s^{-1})	(mm s^{-1})	(T)	(%)	(mm s^{-1})	(mm s^{-1})	(T)	(%)
^{57}hematite	295	0.37	-0.21	51.2	100	--	--	--	--
	239	0.41	-0.20	52.0	100	--	--	--	--
	229	0.41	-0.21	52.1	40.4	0.42	0.44	52.9	59.6
	219	--	--	--	--	0.42	0.42	53.1	100
	77	--	--	--	--	0.48	0.42	53.9	100
	13	--	--	--	--	0.49	0.42	54.0	100
^{57}hematite +	270	0.39	-0.21	51.4	98.5[c]	--	--	--	--
^{56}Fe(II) ~0.5%[b]	140	0.45	-0.23	52.6	27.0	0.46	0.45	53.4	73.0
	13	0.47	-0.21	53.1	29.4	0.49	0.44	53.7	70.6
^{57}hematite	140	0.44	-0.22	52.5	21.4	0.46	0.45	53.4	78.6
+ ^{56}Fe(II) ~0.3%[b]	13	0.47	-0.19	53.1	26.1	0.49	0.46	53.7	73.9
^{57}Fe(II)	140	0.46	-0.20	51.6	57.2	0.45	0.38	52.4	42.8
+ ^{56}hematite	13	0.48	-0.16	53.2	48.8	0.49	0.40	53.4	51.2

[a]Parameters are from Lorentzian model fits for ^{57}hematite and are from Voigt model fits for ^{56}hematite. CS = center shift. QS = quadrupole splitting. H = hyperfine magnetic field. RA = relative area from fits.

[b]Percentage value is amount of ^{56}Fe(II) sorbed in atom %.

[c]The remaining 1.5% was due to an unmodeled (super)paramagnetic phase.

Table B.3. Fit parameters for ^{57}Fe(II) reacted with ^{56}hematite using three unique models at a series of temperatures.

		Weakly ferromagnetic phase				Antiferromagnetic phase			
		CS	QS	H	RA	CS	QS	H	RA
Temp (K)	Model	(mm s^{-1})	(mm s^{-1})	(T)	(%)	(mm s^{-1})	(mm s^{-1})	(T)	(%)
270	Lor[a]	0.38	-0.20	51.6	100	-	-	-	0
	VBF[b]	0.38	-0.20	51.6	100	-	-	-	0
	xVBF[c]	0.38	-0.21	51.6	100	-	-	-	0
230	Lor	0.42	-0.18	51.9	48	0.41	0.40	52.8	52
	VBF	0.42	-0.16	51.8	50.0	0.40	0.40	52.9	50.0
	xVBF	0.43	-0.16	51.8	50.3	0.40	0.40	52.9	49.7
200	Lor	0.40	-0.16	51.8	31	0.43	0.41	53	69
	VBF	0.42	-0.11	51.6	39.4	0.42	0.40	53.2	60.6
	xVBF	0.43	-0.14	51.4	34.1	0.42	0.39	53.2	65.9
140	Lor	0.46	-0.28	52.5	19	0.46	0.43	53.4	81
	VBF	0.52	-0.15	52.7	30.5	0.45	0.42	53.5	69.5
	xVBF	0.48	-0.30	52.6	23.6	0.46	0.42	53.4	76.4
77	Lor	0.51	-0.21	52.9	25	0.48	0.40	53.6	75
	VBF	0.52	-0.20	52.9	29.9	0.48	0.41	53.7	70.1
	xVBF	0.52	-0.27	52.8	24.9	0.48	0.40	53.6	75.1
13	Lor	0.51	-0.27	52.8	21	0.50	0.39	53.5	79
	VBF	0.53	-0.16	52.8	34.6	0.49	0.42	53.7	65.4
	xVBF	0.51	-0.28	52.7	24.8	0.50	0.40	53.6	75.2

[a]Lor = Lorentzian fit [b]VBF = Voight based fitting [c]xVBF = extended Voigt based fitting.

Table B.4. Fit spectral parametersa for ^{56}hematite reacted with ^{57}Fe(II) at 13 K assuming different model types.

	Weakly ferromagnetic phase				Antiferromagnetic phase			
Model	CS (mm s^{-1})	QS (mm s^{-1})	H (T)	RA (%)	CS (mm s^{-1})	QS (mm s^{-1})	H (T)	RA (%)
Lorentzian	0.51	-0.28	52.8	21.3	0.50	0.38	53.5	78.7
	(0.02)[b]	(0.05)	(0.2)	(0.7)	(0.01)	(0.02)	(0.1)	(0.7)
Voigt	0.53	-0.16	52.8	34.6	0.49	0.42	53.7	65.4
	(0.03)	(0.08)	(0.2)	(0.5)	(0.01)	(0.02)	(0.1)	(0.5)
Extended-Voigt	0.51	-0.28	52.7	24.8	0.50	0.40	53.6	75.2
	(0.03)	(0.06)	(0.2)	(0.5)	(0.01)	(0.03)	(0.1)	(0.5)
Voigt[c]	0.55	-0.26	52.8	40.4	0.53	0.36	53.5	59.6
	(0.01)	(0.01)	(0.1)	(0.2)	(0.01)	(0.01)	(0.02)	(0.2)

[a]CS = center shift. QS = quadrupole splitting. H = hyperfine magnetic field. RA = relative area from fits.

[b]Standard deviation provided by fitting software.

[c]Fit by subtracting out the ^{56}hematite spectrum from the ^{57}Fe(II) reacted with ^{56}hematite spectrum to remove background signal.

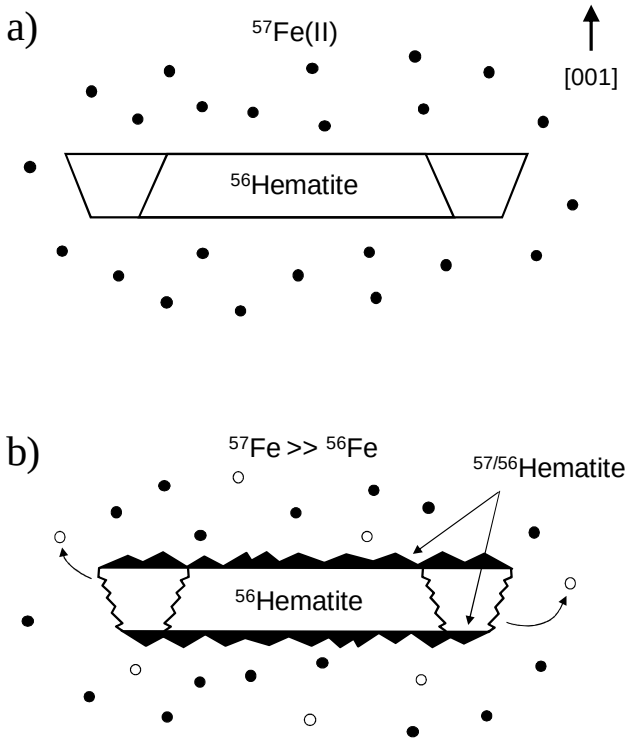

Figure B.1. Conceptual design for the Fe(II)-catalyzed growth of ^{57}Fe isotopically enriched hematite on the (001) surface of synthetic tabular hematite platelets, with a) initial conditions before reaction, and b) during reaction. Edge surfaces bounding the platelets are (012). Closed circles are ^{57}Fe(II) species present in the aqueous solution and open circles represent aqueous ^{56}Fe(II) species created from reduction of ^{56}Fe(III) atoms initially in the hematite structure.

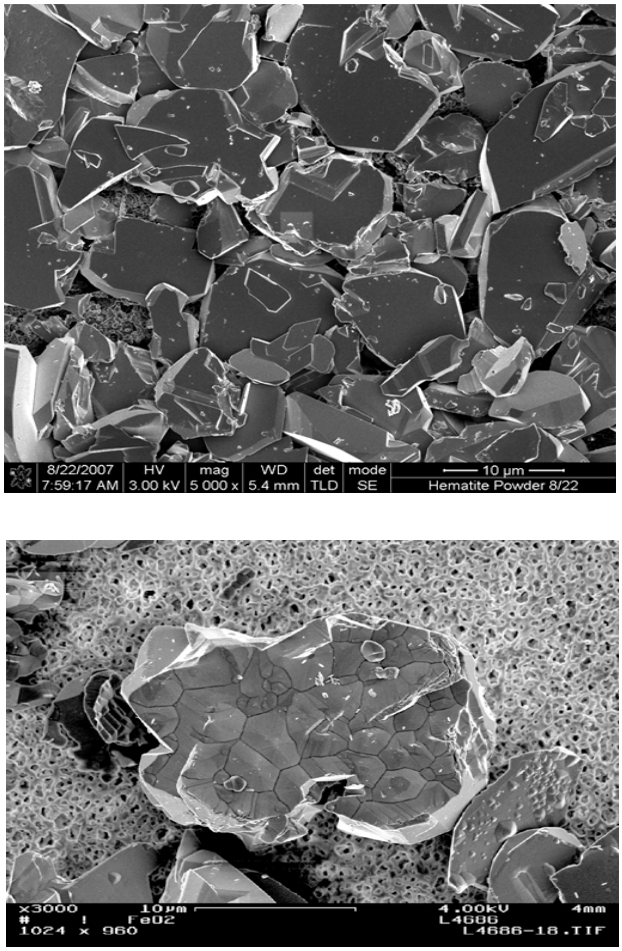

Figure B.2. Scanning electron micrographs of synthetic tabular [NA]hematite powder before (a, top) and after (b, bottom) reaction in 1 mM $FeCl_2$ + 10 mM oxalic acid at pH 2.10, temperature = 348 K, for 24 hours. Before reaction the powder consists of flat hexagonal platelets with (001) surface expression dominant. After reaction, the (001) surfaces of the platelets are covered by pyramidal hematite island overgrowths.

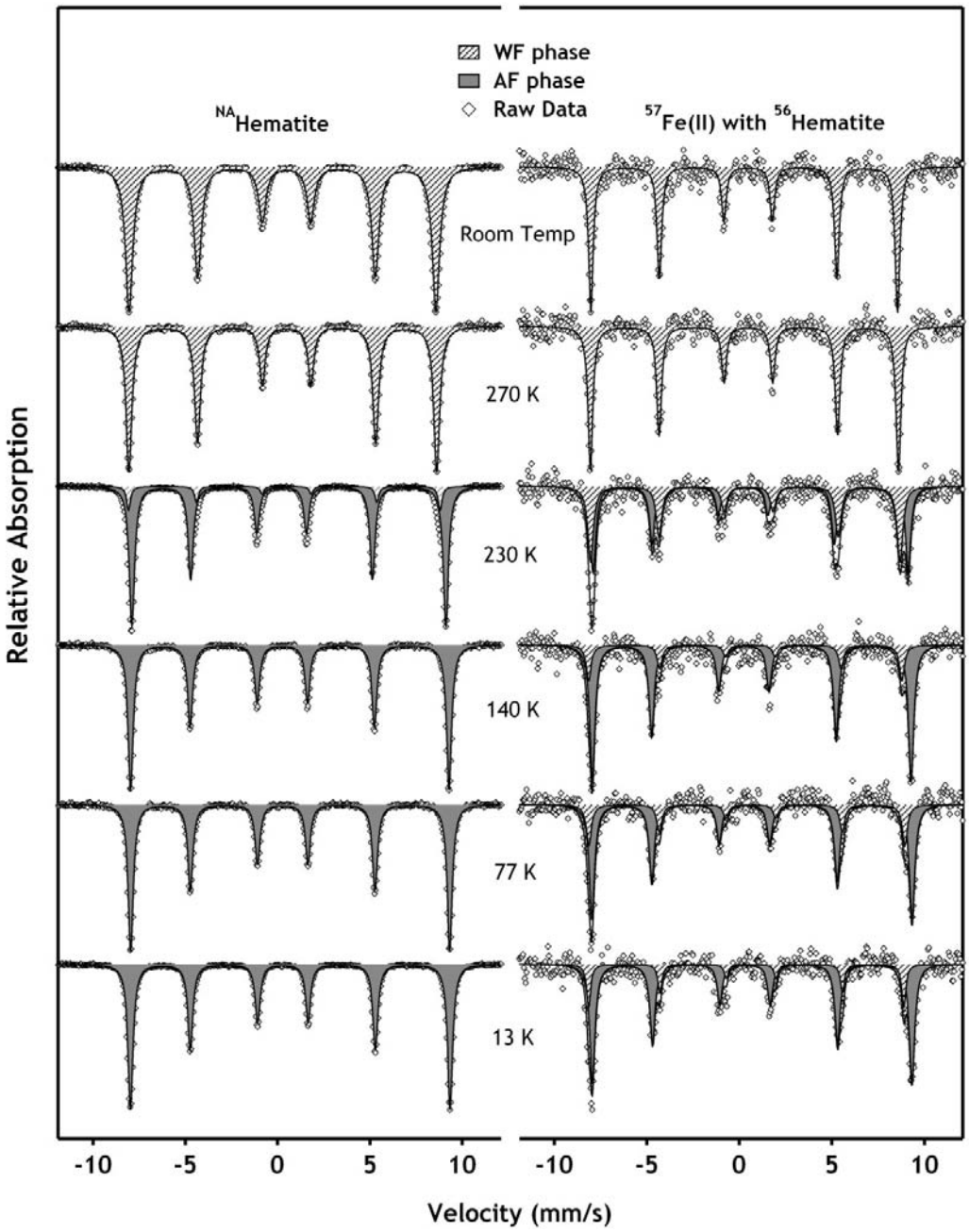

Figure B.3. Variable temperature Mössbauer spectra of ^{NA}hematite (left stack), and ^{56}hematite reacted with ^{57}Fe(II) (right stack), with Lorentzian fitting as described in the text. The ^{NA}hematite is fully in the AF state at low temperature. For the reacted sample, the WF state can be observed even at low temperatures, far below the literature value of the Morin transition for hematite.

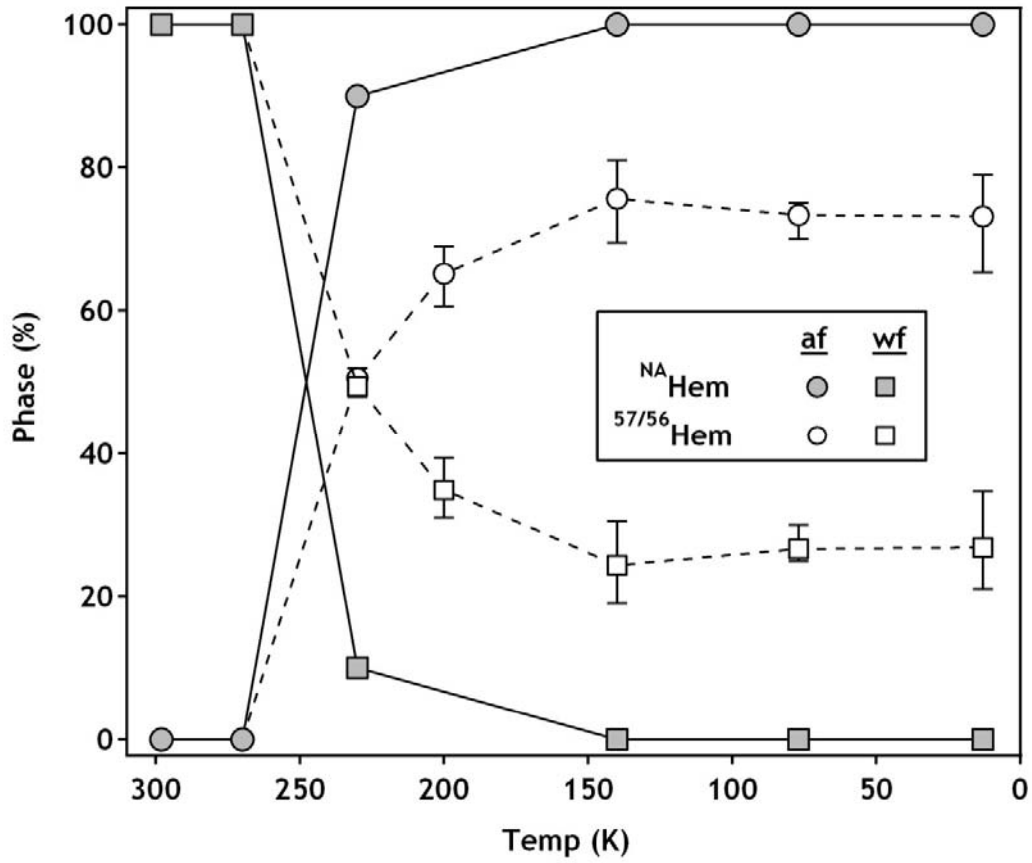

Figure B.4. The relative abundance of antiferromagnetic (af, ○) and weakly ferromagnetic (wf, □) phases in the Mössbauer spectra (Figure B.3) presented as a function of temperature for ^{NA}hematite (filled markers) and ^{56}hematite reacted with ^{57}Fe(II) (open markers). The ^{56}hematite reacted with ^{57}Fe(II) sample exhibits a partial suppression of the Morin transition, where approximately 20-40% of the reacted sample does not complete the transition to the antiferromagnetic phase. The error bars shown represent the range of relative areas found with three different fitting models, with the markers representing the average area.

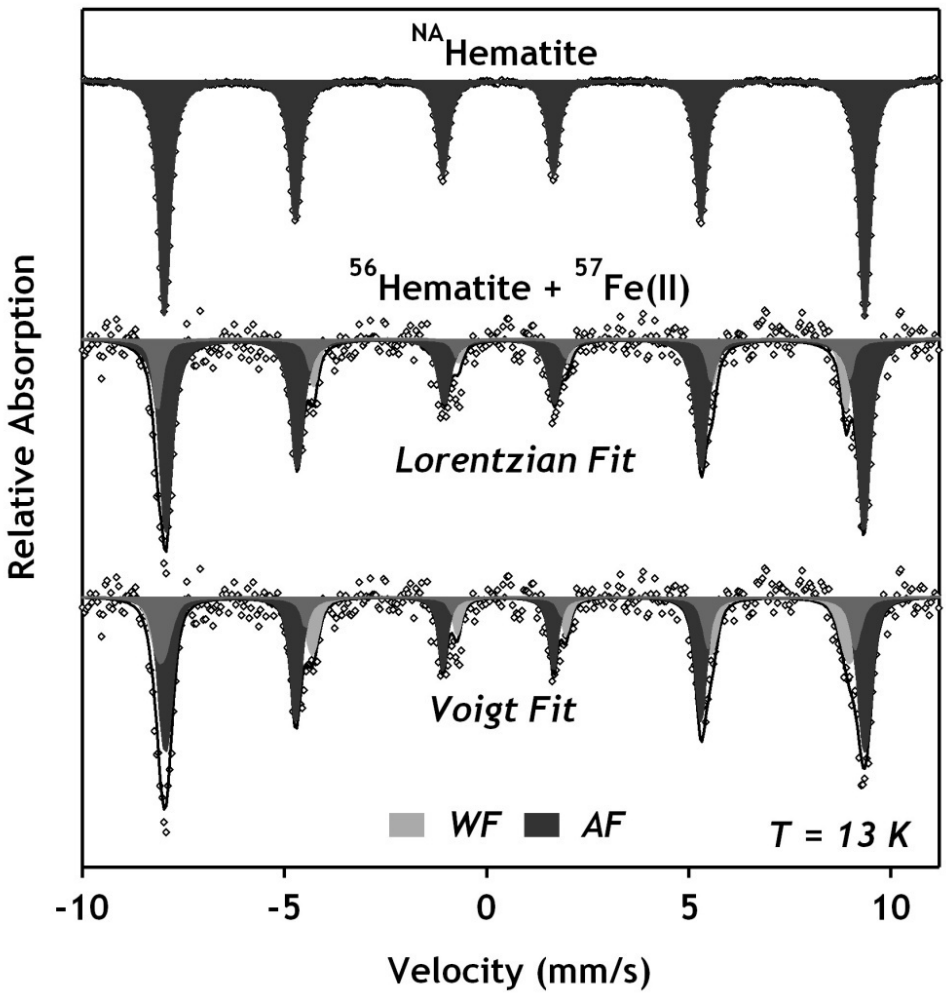

Figure B.5. The relative intensities of ^{56}hematite compared to ^{56}hematite reacted with ^{57}Fe(II) fit using two unique models. The intensity increases upon reaction, which is attributed to the uptake of ^{57}Fe(II) from solution.

REFERENCES

1. Cornell, R. M.; Schwertmann, U., *The iron oxides: Structure, properties, reactions, occurrence, and uses*. VCH: New York, 2003.

2. Xin, Y.; Huang, Z. H.; Peng, L.; Wang, D. J., Photoelectric performance of poly(p-phenylene vinylene)/Fe3O4 nanofiber array. *Journal of Applied Physics* **2009,** 105, 3.

3. Hradil, D.; Grygar, T.; Hradilova, J.; Bezdicka, P., Clay and iron oxide pigments in the history of painting. *Applied Clay Science* **2003,** 22, 223-236.

4. Weiss, W.; Ranke, W., Surface chemistry and catalysis on well-defined epitaxial iron-oxide layers. *Progress in Surface Science* **2002,** 70, 1-151.

5. Raj, K.; Moskowitz, R., Commercial applications of ferrofluids. *Journal of Magnetism and Magnetic Materials* **1990,** 85, 233-245.

6. Pankhurst, Q. A.; Connolly, J.; Jones, S. K.; Dobson, J., Applications of magnetic nanoparticles in biomedicine. *Journal of Physics D-Applied Physics* **2003,** 36, R167-R181.

7. Yavuz, C. T.; Mayo, J. T.; Yu, W. W.; Prakash, A.; Falkner, J. C.; Yean, S.; Cong, L. L.; Shipley, H. J.; Kan, A.; Tomson, M.; Natelson, D.; Colvin, V. L., Low-field magnetic separation of monodisperse Fe_3O_4 nanocrystals. *Science* **2006,** 314, 964-967.

8. Murad, E.; Cashion, J., *Mossbauer Spectroscopy of Environmental Materials and their Industrial Utilization*. Kluwer Academic Publishers: 2004.

9. Lovely, D. R., Microbial Fe(III) reduction in subsurface environments. *FEMS Microbiology Reviews* **1997,** 20, 305-313.

10. Li, Y.; Vali, H.; Yang, J.; Phelps, T. J.; Zhang, C. L., Reduction of Iron Oxides Enhanced by a Sulfate-Reducing Bacterium and Biogenic H2S. *Geomicrobiology Journal* **2006,** 23, 103-117.

11. Chun, C. L.; Hozalski, R. M.; Arnold, W. A., Degradation ot drinking water disinfection byproducts by synthetic goethite and magnetite. *Environmental Science & Technology* **2005,** 39, 8525-8532.

12. Elsner, M.; Schwarzenbach, R. P.; Haderlein, S., Reactivity of Fe(II)-bearing minerals toward reductive transformation of organic contaminants. *Environmental Science and Technology* **2004,** 38, 799-807.

13. Pecher, K.; Haderlein, S. B.; Schwarzenbach, R. P., Reduction of polyhalogenated methanes by surface-bound Fe(II) in aqueous suspensions of iron oxides. *Environmental Science and Technology* **2002,** 36, 1734-1741.

14. Klausen, J.; Trober, S. P.; Haderlein, S. B.; Schwarzenbach, R. P., Reduction of substituted nitrobenzenes by Fe(II) in aqueous mineral suspensions. *Environmental Science and Technology* **1995,** 29, 2396-2404.

15. Hofstetter, T. B.; Heijman, C. G.; Haderlein, S. B.; Holliger, C.; Schwarzenbach, R. P., Complete reduction of TNT and other (poly)nitroaromatic compounds under iron-reducting subsurface conditions. *Environmental Science and Technology* **1999,** 33, 1479-1487.

16. Strathmann, T. J.; Stone, A. T., Abiotic reduction of oxime carbacmate pesticideds by Fe(II): Catalytic role of mineral surfaces. *National Meeting of the American Chemical Society: Division of Environmental Chemistry* **2000,** 40, 141-144.

17. White, A. F.; Peterson, M. L., Reduction of aqueous transition metal species on the surfaces of Fe(II)-containing oxides. *Geochimica et Cosmochimica Acta* **1996,** 60, 3799-3814.

18. Scott, T. B.; Allen, G. C.; Heard, P. J.; Randell, M. G., Reduction of U(VI) to U(IV) on the surface of magnetite. *Geochimica et Cosmochimica Acta* **2005,** 69, 5639-5646.

19. Zachara, J. M.; Heald, S. M.; Jeon, B.-H.; Kukkadapu, R. K.; Liu, C.; McKinley, J. P.; Dohnalkova, A. C.; Moore, D. A., Reduction of pertechnetate [Tc(VII)] by aqueous Fe(II) and the nature of solid phase redox products. *Geochimica et Cosmochimica Acta* **2007,** 71, 2137-2157.

20. Liger, E.; Charlet, L.; Van Cappellen, P., Surface catalysis of uranium(VI) reduction by iron(II). *Geochimica et Cosmochimica Acta* **1999,** 63, 2939-2955.

21. Hiemstra, T.; van Riemsdijk, W. H., Adsorption and surface oxidation of Fe(II) on metal (hydr)oxides. *Geochimica et Cosmochimica Acta* **2007,** 71, 5913-5933.

22. Silvester, E.; Charlet, L.; Tournassat, C.; Gehin, A.; Greneche, J. M.; Liger, E., Redox potential measurements and Mossbauer spectrometry of Fe(II) adsorbed onto Fe(III) (oxyhydr)oxides. *Geochimica et Cosmochimica Acta* **2005,** 69, 4801-4815.

23. Gehin, A.; Greneche, J. M.; Tournassat, C.; Brendle, J.; Rancourt, D. G.; Charlet, L., Reversible surface-sorption-induced electron-transfer oxidation of Fe(II) at reactive sites on a synthetic clay mineral. *Geochimica et Cosmochimica Acta* **2007,** 71, 863-876.

24. Williams, A. G. B.; Scherer, M. M., Spectroscopic evidence for Fe(II)-Fe(III) electron transfer at the Fe oxide-water interface. *Environmental Science and Technology* **2004,** 38, 4782-4790.

25. Cwiertny, D. M.; Baltrusaitis, J.; Hunter, G. J.; Laskin, A.; Scherer, M. M.; Grassian, V. H., Characterization and acid-mobilization study of iron-containing mineral dust source materials. *Journal 0f Geophysical Research-Atmospheres* **2008,** 113, D05202.

26. Larese-Casanova, P.; Scherer, M. M., Fe(II) sorption on hematite: New insights based on spectroscopic measurements. *Environmental Science and Technology* **2007,** 41, 471-477.

27. Larese-Casanova, P.; Scherer, M. M., Morin transition suppression in polycrystalline ^{57}hematite (α-Fe_2O_3) exposed to ^{56}Fe(II). *Hyperfine Interactions* **2007,** 174, 111-119.

28. Pedersen, H. D.; Postma, D.; Jakobsen, R.; Larsen, O., Fast transformation of iron oxyhydroxides by the catalytic action of aqueous Fe(II). *Geochimica et Cosmochimica Acta* **2005,** 69, 3967-3977.

29. Handler, R. M.; Beard, B. L.; Johnson, C. M.; Scherer, M. M., Atom exchange between aqueous Fe(II) and goethite: An Fe isotope tracer study. *Environmental Science and Technology* **2009,** 43, 1102-1107.

30. Yanina, S. V.; Rosso, K. M., Linked reactivity at mineral-water interfaces through bulk crystal conduction. *Science* **2008,** 320, 218-222.

31. Chun, C. L.; Hozalski, R. M.; Arnold, T. A., Degradation of drinking water disinfection byproducts by synthetic goethite and magnetite. *Environmental Science and Technology* **2005,** 39, 8525-8532.

32. Williams, B. G.; Patrick, J., W.H., Effect of Eh and pH on the dissolution of strengite. *Nature Physical Science* **1971,** 234, 16-17.

33. Park, B.; Dempsey, B. A., Heterogeneous oxidation of Fe(II) on ferric oxide at neutral pH and a low partial pressure of O_2. *Environmental Science and Technology* **2005,** 39, 6494-6500.

34. Barnes, A.; Sapsford, D. J.; Dey, M.; Williams, K. P., Heterogeneous Fe(II) oxidation and zeta potential. *Journal of Geochemical Exploration* **2009,** 100, 192-198.

35. Becker, U.; Rosso, K. M.; Hochella, M. F., The proximity effect on semiconducting mineral surfaces: A new aspect of mineral surface reactivity and surface complexation theory? *Geochimica et Cosmochimica Acta* **2001,** 65, 2641-2649.

36. Dare-Edwards, M. P.; Goodenough, J. B.; Hamnett, A.; Trevellick, P. R., Electrochemistry and Photoelectrochemistry of Iron(III) Oxide. *Journal of the Chemical Society, Faraday Transactions 1: Physical Chemistry in Condensed Phases* **1983,** 79, 2027-41.

37. Stratmann, M.; Bohnenkamp, K.; Engell, H.-J., An electrochemical study of phase-transitions in rust layers. *Corrosion Science* **1983,** 23, 969-985.

38. Balko, B. A.; Clarkson, K. M., The effect of doping with Ti(IV) and Sn(IV) on oxygen reduction at hematite electrodes. *Journal Of The Electrochemical Society* **2001,** 148, E85-E91.

39. Goss, C. J., Saturation magnetization, coercivity, and lattice parameter changes in the system Fe_3O_4-γFe_2O_3, and their relationship to structure. *Physics and Chemistry of Minerals* **1988,** 16, 164-171.

40. Sherman, D. M., Molecular orbital (SCF-Xα-SW) theory of metal-metal charge transfer processes in minerals. *Physics and Chemistry of Minerals* **1987,** 14, 355-363.

41. Walz, F., The Verwey transition - A topical review. *Journal of Physics: Condensed Matter* **2002,** 14, R285-R340.

42. Garcia, J.; Subias, G., The Verwey transition - A new perspective. *Journal of Physics: Condensed Matter* **2004,** 16, R145-R178.

43. McCormick, M. L.; Bouwer, E. J.; Adriaens, P., Carbon tetrachloride transformation in a model iron-reducing culture: Relative kinetics of biotic and abiotic reactions. *Environmental Science and Technology* **2002,** 36, 403-410.

44. Tamaura, Y.; Ito, K.; Katsura, T., Transformation of γ-FeO(OH) to Fe_3O_4 by adsorption of iron(II) ion on γ-FeO(OH). *Journal of the Chemical Society Dalton Transactions* **1983,** 2, 189-194.

45. Hansel, C. M.; Benner, S. G.; Fendorf, S., Competing Fe(II)-induced mineralization pathways of ferrihydrite. *Environmental Science and Technology* **2005,** 39, 7147-7153.

46. Vikesland, P. J.; Heathcock, A. M.; Rebodos, R. L.; Makus, K. E., Particle size and aggregation effects on magnetite reactivity toward carbon tetrachloride. *Environmental Science and Technology* **2007,** 41, 5277-5283.

47. Danielsen, K. M.; Hayes, K. F., pH dependence of carbon tetrachloride reductive dechlorination by magnetite. *Environmental Science and Technology* **2004,** 38, 4745-4752.

48. Peterson, M. L.; White, A. F.; Brown, G. E.; Parks, G. A., Surface passivation of magnetite by reaction with aqueous Cr(VI): XAFS and TEM results. *Environmental Science and Technology* **1997,** 31, 1573-1576.

49. Charlet, L.; Silvester, E.; Liger, E., N-compound reduction and actinide immobilization in surficial fluids by Fe(II): the surface Fe(III)OFe(II)OH degrees species, as major reductant. *Chemical Geology* **1998,** 151, 85-93.

50. Ferrey, M.; Wilkin, R.; Ford, R.; Wilson, J., Nonbiological removal of cis-dichloroethylene and 1,1-dichlorethylene in aquifer sediment containing magnetite. *Environmental Science and Technology* **2004,** 38, 1746-1752.

51. Gregory, K. B.; Larese-Casanova, P.; Parkin, G. F.; Scherer, M. M., Abiotic transformation of hexahydro-1,3,5-trinitro-1,3,5-triazine by Fe^{II} bound to magnetite. *Environmental Science and Technology* **2004,** 38, 1408-1414.

52. Tronc, E.; Jolivet, J.-P.; Lefebvre, J.; Massart, R., Ion adsorption and electron transfer in spinel-like iron oxide colloids. *Journal of the Chemical Society, Faraday Transactions* **1984,** 80, 2619-2629.

53. Gallagher, K. J.; Feitknecht, W.; Mannweiler, U., Mechanism of oxidation of magnetite to γ-Fe_2O_3. *Nature* **1968,** 217, 1118-1121.

54. White, A. F.; Peterson, M. L.; Hochella, M. F., Electrochemistry and dissolution kinetics of magnetite and ilmenite. *Geochimica et Cosmochimica Acta* **1994,** 58, 1859-1875.

55. Sidhu, P. S.; Gilkes, R. J.; Posner, A. M., Mechanism of the low temperature oxidation of magnetite. *Journal of Inorganic and Nuclear Chemistry* **1977,** 39, 1953-1958.

56. Tang, J.; Myers, M.; Bosnick, K. A.; Brus, L. E., Magnetite Fe_3O_4 nanocrystals: Spectroscopic observation of aqueous oxidation kinetics. *Journal of Physical Chemistry: B* **2003,** 107, 7501-7506.

57. Chen, C.-T.; Cahan, B. D., The nature of the passive film on iron. I. Automatic ellipsometric spectroscopy studies. *Journal of the Electrochemical Society* **1982,** 129, 17-26.

58. Cahan, B. D.; Chen, C.-T., The nature of the passive film on iron. II. A-C impedance studies. *Journal of the Electrochemical Society* **1982,** 129, 474-480.

59. Cahan, B. D.; Chen, C.-T., The nature of the passive film on iron. III. The chemi-conductor model and further supporting evidence. *Journal of the Electrochemical Society* **1982,** 129, 921-925.

60. Castro, P. A.; Vago, E. R.; Calvo, E. J., Surface electrochemical transformations on spinel iron oxide electrodes in aqueous solutions. *Journal of the Chemical Society, Faraday Transactions* **1996,** 92, 3371-3379.

61. Pang, S. C.; Chin, S. F.; Anderson, M. A., Redox equilibria of iron oxides in aqueous-based magnetite dispersions: Effect of pH and redox potential. *Journal of Colloid and Interface Science* **2007,** 311, 94-101.

62. Itai, R.; Shibuya, M.; Matsumura, T.; Ishi, G., Electrical resistivity of magnetite anodes. *Journal of the Electrochemical Society* **1971,** 118, 1709-11.

63. Verwey, E. J. W.; Haayman, P. W., Electronic conductivity and transition point of magnetite (Fe_3O_4). *Physica* **1941,** 8, 979-987.

64. Stockbridge, C. D.; Sewell, P. B.; Cohen, M., Cathodic behavior of iron single crystals and the oxides Fe_3O_4 , γ-Fe_2O_3, and α-Fe_2O_3. *Journal of the Electrochemical Society* **1961,** 108, 928-933.

65. Rancourt, D. G., Mossbauer spectroscopy in clay science. *Hyperfine Interactions* **1998,** 117, 3-38.

66. Dyar, M. D.; Agresti, D. G.; Schaefer, M. W.; Grant, C. A.; Sklute, E. C., Mossbauer spectroscopy of earth and planetary elements. *Annual Review of Earth and Planetary Sciences* **2006,** 34, 83-125.

67. Evans, R. J.; Rancourt, D. G.; Grodzicki, M., Hyperfine electric field gradients and local distortion environments of octahedrally coordinated Fe2+. *American Mineralogist* **2005,** 90, 187-198.

68. Evans, R. J.; Rancourt, D. G.; Grodzicki, M., Hyperfine electric field gradient tensors at Fe^{2+} sites in octahedral layers: Toward understanding oriented single-crystal Moessbauer spectroscopy measurements of micas. *American Mineralogist* **2005,** 90, 1540-1555.

69. Rancourt, D. G.; McDonald, A. M.; Lalonde, A. E.; Ping, J. Y., Mossbauer absorber thicknesses for accurate site populations in Fe-bearing minerals. *American Mineralogist* **1993,** 78, 1-7.

70. Rancourt, D. G.; Ping, J. Y., Voigt-based methods for arbitrary-shape static hyperfine parameter distributions in Mössbauer spectroscopy. *Nuclear Instruments and Methods in Physics Research B* **1991,** B58, 85-97.

71. Campbell, S. J.; Aubertin, F., Evaluation of Distributed Hyperfine Parameters. In *Mössbauer spectroscopy applied to inorganic chemistry*, Long, G. J.; Grandjean, F., Eds. Plenum Press: New York, 1989; Vol. 3, pp 183-242.

72. Long, G. J., *Mossbauer Spectroscopy Applied to Inorganic Chemistry*. Plenum Press: New York, 1984; Vol. 1.

73. Lee, W.; Batchelor, B., Abiotic reductive dechlorination of chlorinated ethylenes by iron-bearing soil minerals. 1. Pyrite and Magnetite. *Environmental Science and Technology* **2002,** 36, 5147-5154.

74. Gorski, C. A.; Scherer, M. M., Influence of magnetite stoichiometry on Fe^{II} uptake and nitrobenzene reduction. *Environmental Science and Technology* **2009,** 43, 3675-3680.

75. Tronc, E.; Jolivet, J. P.; Massart, R., Defect spinel structure in iron oxide colloids. *Materials Research Bulletin* **1982,** 17, 1365-1369.

76. da Costa, G. M.; De Grave, E.; Vandenberghe, R. E., Mossbauer studies of magnetite and Al-substituted maghemites. *Hyperfine Interactions* **1996,** 117, 207-243.

77. Gorski, C. A.; Nurmi, J. T.; Tratnyek, P. G.; Hofstetter, T. B.; Scherer, M. M., Redox behavior of magnetite: Implications for contaminant reduction. *Environmental Science and Technology* **2009,** In Press.

78. Annersten, H.; Hafner, S. S., Vacancy distribution in synthetic spinels of the series magnetite-γ-iron(III) oxide. *Zeitschrift fuer Kristallographie* **1973,** 137, 321-340.

79. Volenik, K.; Seberini, M.; Neid, J., Mossbauer and X-ray-diffraction study of nonstoichiometry in magnetite. *Czechoslovak Journal of Physics* **1975,** 25, 1063-1071.

80. da Costa, G. M.; De Grave, E.; de Bakker, P. M. A.; Vandenberghe, R. E., Influence of nonstoichiometry and the presence of maghemite on the Moessbauer spectrum of magnetite. *Clays and Clay Minerals* **1995,** 43, 656-668.

81. Vandenberghe, R. E.; de Grave, E., Mossbauer Effect Studies of Oxidic Spinels. In *Mossbauer Spectroscopy Applied to Inorganic Chemistry, Volume 3*, Long, G. J., Ed. 1989; pp 59-182.

82. Daniels, J. M.; Rosencwaig, A., Moessbauer spectroscopy of stoichiometric and nonstoichiometric magnetite. *Journal of Physics and Chemistry of Solids* **1969,** 30, 1561-1571.

83. Yang, J. B.; Zhou, X. D.; Yelon, W. B.; James, W. J.; Cai, Q.; Gopalakrishnan, K. V.; Malik, S. K.; Sun, X. C.; Nikles, D. E., Magnetic and structural studies of the Verwey transition in $Fe_{3-\delta}O_4$ nanoparticles. *Journal of Applied Physics* **2004,** 95, 7540-7542.

84. Tronc, E.; Belleville, P.; Jolivet, J. P.; Livage, J., Transformation of ferric hydroxide into spinel by Fe(II) adsorption. *Langmuir* **1992,** 8, 313-319.

85. Jolivet, J. P.; Tronc, E., Interfacial electron transfer in colloidal spinel iron oxide. Conversion of Fe_3O_4-γFe_2O_3 in aqueous solution. *Journal of Colloid and Interface Chemistry* **1988,** 125, 688-701.

86. Gotic, M.; Koscec, G.; Music, S., Study of the reduction and reoxidation of substoichiometric magnetite. *Journal of Molecular Structure* **2009,** 924-26, 347-354.

87. Carvallo, C.; Sainctavit, P.; Arrio, M.-A.; Menguy, N.; Wang, Y.; Ona-Nguema, G.; Brice-Profeta, S., Biogenic vs. abiogenic magnetite nanoparticles: A XMCD study. *American Mineralogist* **2008,** 93, 880-885.

88. Schwertmann, U.; Cornell, R. M., *Iron oxides in the laboratory*. VCH: Weinheim, 1991; p 137.

89. Tamura, H.; Goto, K.; Yotsuyan.T; Nagayama, M., Spectrophotometric determination of iron(II) with 1,10-phenanthroline in presence of large amounts of iron(III). *Talanta* **1974,** 21, 314-318.

90. Hansen, H. C. B., Composition, stabilization, and light-absorption of Fe(II)Fe(III) hydroxy-carbonate (green rust). *Clay Minerals* **1989,** 24, 663-669.

91. Howard, S. A.; Preston, K. D., Profile fitting of powder diffraction patterns. In *Modern Powder Diffraction*, Bish, D. L. P., J.E. , Ed. Mineralogical Society of America: 1989; Vol. 20, pp 217-275.

92. Vandenberghe, R. E.; Barrero, C. A.; da Costa, G. M.; Van San, E.; De Grave, E., Mossbauer characterization of iron oxides and (oxy)hydroxides: the present state of the art. *Hyperfine Interactions* **2000,** 126, 247-259.

93. Morrish, A. H.; Haneda, K.; Schurer, P. J., Surface magnetite structure of small γ-Fe_2O_3 particles. *Journal de Physique* **1976,** 12, 301-305.

94. Lotgering, F. K.; Vandiepen, A. M., Electron exchange between Fe^{2+} and Fe^{3+} ions on octahedral sites in spinels studied by means of paramagnetic Mossbauer-spectra and susceptibility measurements. *Journal of Physics and Chemistry of Solids* **1977,** 38, 565-572.

95. Degrave, E.; Persoons, R. M.; Vandenberghe, R. E.; Debakker, P. M. A., Mossbauer study of the high-temperature phase of Co-substituted magnetites, $Co_xFe_{3-x}O_4$ .1. $x \leq 0.04$. *Physical Review B* **1993,** 48, 3581-3581.

96. Tronc, E.; Jolivet, J. P.; Belleville, P.; Livage, J., Redox phenomena in spinel iron-oxide colloids induced by adsorption. *Hyperfine Interactions* **1989,** 46, 637-643.

97. Jolivet, J. P.; Belleville, P.; Tronc, E.; Livage, J., Influence of Fe(II) on the formation of the spinel iron oxide in alkaline medium. *Clays and Clay Minerals* **1992,** 40, 531-539.

98. Ozdemir, O.; Dunlop, D. J.; Moskowitz, B. M., The effect of oxidation on the Verwey transition in magnetite. *Geophysical Research Letters* **1993,** 20, 1671-1674.

99. Lagarec, K.; Rancourt, D. G., Extended Voigt-based analytic lineshape method for determining N-dimensional correlated hyperfine parameter distributions in Mossbauer spectroscopy. *Nuclear Instruments and Methods in Physical Research B* **1997,** 129, 266-280.

100. Ping, J. Y.; Rancourt, D. G., An effective method of direct QSD extraction using combined partial deconvolution. *Hyperfine Interactions* **1994,** 92, 1203-1207.

101. Ping, J. Y.; Rancourt, D. G., Failure of the direct HFD extraction method. *Hyperfine Interactions* **1994,** 92, 1209-1212.

102. Haggstrom, L.; Annersten, H.; Ericsson, T.; Wappling, R.; Karner, W.; Bjarman, S., Magnetic dipolar and electric quadrupolar effects on the Mossbauer spectra of magnetite above the Verwey transition. *Hyperfine Interactions* **1978,** 5, 201-214.

103. Sawatzky, G. A.; Coey, J. M. D.; Morrish, A. H., Mössbauer study of electron hopping in octahedral Sites of Fe_3O_4. *Journal of Applied Physics* **1969,** 40, 1402-1403.

104. Ramdani, A.; Steinmetz, J.; Gleitzer, C.; Coey, J. M. D.; Friedt, J. M., Perturbation de l'echange electronique rapide par les lacunes cationiques dans $Fe_{3-x}O_4$ ($x < 0,09$). *Journal of Physics and Chemistry of Solids* **1987,** 48, 217-228.

105. Cullen, J. R.; Callen, E., Collective electron theory of metal-semiconductor transition in magnetite. *Journal of Applied Physics* **1970,** 41, 879-880.

106. Ihle, D.; Lorenz, B., Small-polaron band versus hopping conduction in Fe_3O_4. *Journal of Physics C-Solid State Physics* **1985,** 18, L647-L650.

107. Cullen, A. C.; Vorhees, D. J.; Altshul, L. M., Influence of harbor contamination on the level and composition of polychlorinated biphenyls in produce in greater New Bedford, Massachusetts. *Environmental Science and Technology* **1996,** 30, 1581-1588.

108. Nakagiri, N.; Manghnani, M. H.; Ming, L. C.; Kimura, S., Crystal-structure of magnetite under pressure. *Physics and Chemistry of Minerals* **1986,** 13, 238-244.

109. Feitknecht, W.; Brunner, P.; Oswald, H. R., Uber Den Einfluss Der Feuchtigkeit Auf Die Oxydation Von Manganhydroxid Durch Molekularen Sauerstoff. *Zeitschrift Fur Anorganische Und Allgemeine Chemie* **1962,** 316, 154-160.

110. Kuhn, L. T.; Bojesen, A.; Timmermann, L.; Nielsen, M. M.; Morup, S., Structural and magnetic properties of core-shell iron-iron oxide nanoparticles. *Journal of Physics-Condensed Matter* **2002,** 14, 13551-13567.

111. Vandenberghe, R. E.; Hus, J. J.; de Grave, E., Evidence from Mossbauer spectroscopy of neo-formation of magnetite/maghemite in the soils of loess/paleosol sequences in China. *Hyperfine Interactions* **1998,** 117, 359-369.

112. Jung, Y.; Choi, J.; Lee, W., Spectroscopic investigation of magnetite surface for the reduction of hexavalent chromium. *Chemosphere* **2007,** 68, 1968-1975.

113. Regazzoni, A. E.; Urrutia, G. A.; Blesa, M. A.; Maroto, A. J. G., Some observations on the composition and morphology of synthetic magnetites obtained by different routes. *Journal of Inorganic and Nuclear Chemistry* **1981,** 43, 1489-1493.

114. Nedkov, I.; Merodiiska, T.; Slavov, L.; Vandenberghe, R. E.; Kusano, Y.; Takada, J., Surface oxidation, size and shape of nano-sized magnetite obtained by co-precipitation. *Journal of Magnetism and Magnetic Materials* **2006,** 300, 358-367.

115. Zhang, J. Z., Interfacial charge carrier dynamics of colloidal semiconductor nanoparticles. *Journal of Physical Chemistry B* **2000,** 104, 7239-7254.

116. McCormick, M. L.; Adriaens, P., Carbon tetrachloride transformation on the surface of nanoscale biogenic magnetite particles. *Environmental Science and Technology* **2004,** 38, 1045-1053.

117. Peterson, M. L.; Brown, G. E.; Parks, G. A., Direct XAFS evidence for heterogeneous redox reaction at the aqueous chromium/magnetite interface. *Colloids and Surfaces A: Physicochemical and Engineering Aspects* **1996,** 107, 77-88.

118. Sun, Z.; Su, F.; Forsling, W.; Samskog, P., Surface characteristics of magnetite in aqueous suspension. *Journal of Colloid and Interface Science* **1998,** 197, 151-159.

119. Dixit, S.; Hering, J. G., Comparison of arsenic(V) and arsenic(III) sorption onto iron oxide minerals: implications for arsenic mobility. *Environmental Science and Technology* **2003,** 37, 4182-4189.

120. Lippert, C. P., Big discovery for biogenic magnetite. *Proceedings of the National Academy of Sciences of the United States of America* **2008,** 105, 17595-17596.

121. Nagayama, M.; Cohen, M., The anodic oxidation of iron in neutral solution: 1. The nature and composition of the passive film. *J. Electrochem. Soc.* **1962,** 109, 781-790.

122. Schwarzenbach, R. P.; Stierli, R.; Lanz, K.; Zeyer, J., Quinone and iron porphyrin mediated reduction of nitroaromatic compounds in homogeneous aqueous solution. *Environmental Science and Technology* **1990,** 24, 1566-1574.

123. Tratnyek, P. G.; Weber, E. J.; Schwarzenbach, R. P., Quantitative structure-reactivity relationships for chemical reductions of organic contaminants. *Environmental Toxicology and Chemistry* **2003,** 22, 1733-1742.

124. Colon, D.; Weber, E. J.; Anderson, J. L.; Suarez, L. A., Reduction of nitrosobenzenes and *N*-hydroxylanilines by Fe(II) species: Elucidation of the reaction mechanism. *Environmental Science and Technology* **2006,** 40, 4449-4454.

125. Haderlein, S.; Hofstetter, T.; Schwarzenbach, R. P., Subsurface chemistry of nitroaromatic compounds. In *Biodegradation of Nitroaromatic Compounds and Explosives*, Spain, J. C.; Hughes, J. B.; Knackmuss, H.-J., Eds. Lewis Publishers: Boca Raton, Florida, 2000; pp 311-357.

126. Hartenbach, A. E.; Hofstetter, T. B.; Aeschbacher, M.; Sander, M.; Kim, D.; Strathmann, T. J.; Arnold, W. A.; Cramer, C. J.; Schwarzenbach, R. P., Variability of nitrogen isotope fractionation during the reduction of nitroaromatic compounds with dissolved reductants. *Environmental Science and Technology* **2008,** 42, 8352-8359.

127. Nurmi, J. T.; Bandstra, J. Z.; Tratnyek, P. G., Packed powder electrodes for characterizing the reactivity of granular iron in borate solutions. *Journal of the Electrochemical Society* **2004,** 151, B347-B353.

128. Nurmi, J. T.; Tratnyek, P. G., Electrochemical studies of packed iron powder electrodes: Effects of common constituents of natural waters on corrosion potential. *Corrosion Science* **2008,** 50, 144-154.

129. Hofstetter, T. B.; Neumann, A.; Arnold, W. A.; Hartenbach, A. E.; Bolotin, J.; Cramer, C. J.; Schwarzenbach, R. P., Substituent effects on nitrogen isotope fractionation during abiotic reduction of nitroaromatic compounds. *Environmental Science and Technology* **2008,** 42, 1997-2003.

130. Berg, M.; Bolotin, J.; Hofstetter, T. B., Compound-specific nitrogen and carbon isotope analysis of nitroaromatic compounds in aqueous samples using solid-phase microextraction coupled to GC/IRMS. *Analytical Chemistry* **2007,** 79, 2386-2393.

131. Neumann, A.; Hofstetter, T. B.; Skarpeli-Liati, M.; Schwarzenbach, R. P., Reduction of polychlorinated ethanes and carbon tetrachloride by structural Fe(II) in smectites. *Environmental Science and Technology* **2009,** 43, 4082-4089.

132. Neumann, A.; Hofstetter, T. B.; Lussi, M.; Cirpka, O. A.; Petit, S.; Schwarzenbach, R. P., Assessing the redox reactivity of structural iron in smectites using nitroaromatic compounds as kinetic probes. *Environmental Science and Technology* **2008,** 42, 8381-8387.

133. Grygar, T., Dissolution of pure and substituted goethites controlled by the surface reaction under conditions of abrasive stripping voltammetry *Journal of Solid State Electrochemistry* **1997,** 1, 77-82.

134. Grygar, T.; Marken, F.; Schroder, U.; Scholz, F., Electrochemical analysis of solids. A review. *Collection of Czechoslovak Chemical Communications* **2002,** 67, 163-208.

135. Buerge, I. J.; Hug, S. J., Influence of mineral surfaces on chromium(VI) reduction by iron(II). *Environmental Science and Technology* **1999,** 33, 4285-4291.

136. Jeon, B. H.; Dempsey, B. A.; Burgos, W. D.; Royer, R. A., Sorption kinetics of Fe(II), Zn(II), Co(II), Ni(II), Cd(II), and Fe(II)/Me(II) onto hematite. *Water Research* **2003,** 37, 4135-4142.

137. Zhang, Y.; Charlet, L.; Schindler, P. W., Adsorption of protons, Fe(II) and Al(III) on lepidocrocite (γ-FeOOH). *Colloids and Surfaces* **1992,** 63, 259-268.

138. Dixit, S.; Hering, J. G., Sorption of Fe(II) and As(III) on goethite in single- and dual-sorbate systems. *Chemical Geology* **2006,** 228, 6-15.

139. Vikesland, P. J.; Valentine, R. L., Iron oxide surface-catalyzed oxidation of ferrous iron by monochloramine: Implications of oxide type and carbonate on reactivity. *Environmental Science and Technology* **2002,** 36, 512-519.

140. Jeon, B. H.; Dempsey, B. A.; Burgos, W. D., Kinetics and mechanisms for reactions of Fe(II) with iron(III) oxides. *Environmental Science and Technology* **2003,** 37, 3309-3315.

141. Cwiertny, D. M.; Handler, R. M.; Schaefer, M. V.; Grassian, V. H.; Scherer, M. M., Interpreting nanoscale size-effects in aggregated Fe-oxide suspensions: Reaction of Fe(II) with goethite. *Geochimica et Cosmochimica Acta* **2008,** 72, 1365-1380.

142. Tanwar, K. S.; Petitto, S. C.; Ghose, S. K.; Eng, P. J.; Trainor, T. P., Strucutral study of Fe(II) adsorption on hematite (11(bar)02). *Geochimica et Cosmochimica Acta* **2008,** 72, 3311-3325.

143. Amonette, J. E.; Workman, D. J.; Kennedy, D. W.; Fruchter, J. S.; Gorby, Y. A., Dechlorination of carbon tetrachloride by Fe(II) associated with goethite. *Environmental Science and Technology* **2000,** 34, 4606-4613.

144. Strathmann, T. J.; Stone, A. T., Mineral surface catalysis of reactions between Fe(II) and oxime carbamate pesticides. *Geochimica et Cosmochimica Acta* **2003,** 67, 2775-2791.

145. Vikesland, P. J.; Valentine, R. L., Reaction pathways involved in the reduction of monochloramine by ferrous iron. *Environmental Science and Technology* **2000,** 34, 83-90.

146. Cwiertny, D. M.; Young, M. A.; Grassian, V. H., Chemistry and photochemistry of mineral dust aerosol. *Annual Review Of Physical Chemistry* **2008,** 59, 27-51.

147. Rosso, K. M.; Yanina, S. V.; Gorski, C. A.; Larese-Casanova, P.; Scherer, M. M., Connecting observations of hematite (α–Fe_2O_3) growth catalyzed by Fe(II). *Environmental Science and Technology* **2009,** In Press.

148. Cwiertny, D. M.; Handler, R. M.; Ali, H.; Grassian, V. H.; Scherer, M. M., Reactivity of ferrous iron associated with nanoparticle iron oxides. *Abstracts of Papers of the American Chemical Society* **2006,** 231.

149. Mulvaney, P.; Cooper, R.; Grieser, F.; Meisel, D., Charge trapping in the reductive dissolution of colloidal suspensions of iron(III) oxides. *Langmuir* **1988,** 4, 1206-1211.

150. Li, T.; Farrell, J., Reductive dechlorination of trichloroethene and carbon tetrachloride using iron and palladized-iron cathodes. *Environmental Science and Technology* **2000,** 34, 173-179.

151. Logue, B. A.; Westall, J. C., Kinetics of reduction of nitrobenzene and carbon tetrachloride at an iron-oxide coated gold electrode. *Environmental Science and Technology* **2003,** 37, 2356-2362.

152. Sarathy, V.; Tratnyek, P. G.; Nurmi, J. T.; Baer, D. R.; Amonette, J. E.; Chun, C.; Penn, R. L.; Reardon, E. J., Aging of iron nanoparticles in aqueous solution: Effects of structure and reactivity. *Journal of Physical Chemistry, C* **2008,** 112, 2286-2293.

153. Nurmi, J. T.; Tratnyek, P. G.; Sarathy, V.; Baer, D. R.; Amonette, J. E.; Pecher, K.; Wang, C.; Linehan, J. C.; Matson, D. W.; Penn, R. L.; Driessen, M. D., Characterization and properties of metallic iron nanoparticles: Spectroscopy, electrochemistry, and kinetics. *Environmental Science and Technology* **2005,** 39, 1221-1230.

154. Buxton, G. V.; Rhodes, T.; Sellers, R. M., Radiation-induced dissolution of colloidal haematite. *Nature* **1982,** 295, 583-585.

155. Michaelis, L.; Hill, E. S., The viologen indicators. *Journal of General Physiology* **1933,** 16, 859-873.

156. Buxton, G. V.; Rhodes, T.; Seller, R. M., Radiation chemistry of colloidal haematite and magnetite in water. Reductive dissolution by $(CH_3)_2C$•OH radicals and Fe^{II}EDTA. *Journal of the Chemical Society, Faraday Transactions I* **1983,** 79, 2961-2974.

157. Dimitrijevíc, N. M.; Savíc, D.; Mícíc, O. I.; Nozik, A. J., Interfacial electron-transfer equilibria and flat-band potentials of α-Fe_2O_3 and TiO_2 colloids studied by pulse radiolysis. *Journal of Physical Chemistry* **1984,** 88, 4278-4283.

158. Leland, J. K.; Bard, A. J., Photochemistry of colloidal semiconducting iron oxide polymorphs. *Journal of Physical Chemistry* **1987,** 91, 5076-5083.

159. Mulvaney, P.; Swayambunathan, V.; Grieser, F.; Meisel, D., Dynamics of interfacial charge-transfer in iron(III) oxide colloids. *Journal of Physical Chemistry* **1988,** 92, 6732-6740.

160. Bird, C. L.; Kuhn, A. T., Electrochemistry of the viologens. *Chemical Society Reviews* **1981,** 10, 49-82.

161. Yu, Q.; Kandegedara, A.; Xu, Y.; BRorabacher, E. B., Avoiding interferances from Good's buffers: A contiguous series of noncomplexing tertiary amine buffers covering the entire range of pH 3-11. *Analytical Biochemistry* **1997,** 253, 50-56.

162. Pourbaix, M., *Atlas of Electrochemical Equilibria in Aqueous Solutions.* Pergamon: Oxford, 1966; p 644.

163. Bard, A. J.; Faulkner, L. R., *Electrochemical Methods. Fundamentals and Applications.* Second Edition ed.; Wiley: New York, 2001; p 833.

164. Nano, G. V.; Strathmann, T. J., Ferrous iron sorption by hydrous metal oxides. *Journal of Colloid and Interface Science* **2006,** 297, 443-454.

165. Peretyazhko, T.; Zachara, J. M.; Heald, S. M.; Kukkadapu, R. K.; Liu, C.; Plymale, A. E.; Resch, C. T., Reduction of Tc(VII) by Fe(II) sorbed on Al (hydr)oxides. *Environmental Science and Technology* **2008,** 42, 5499-5506.

166. Coby, A. J.; Picardal, F. W., Inhibition of NO_3^- and NO_2^- reduction by microbial Fe(III) reduction: Evidence of a reaction between NO_2^- and cell surface-found Fe^{2+}. *Applied and Environmental Microbiology* **2005,** 71, 5267-5274.

167. Fakih, M.; Chatellier, X.; Davranche, M.; Dia, A., *Bacillus subtilis* bacteria hinder the oxidation and hydrolysis of Fe^{2+} ions. *Environmental Science and Technology* **2008,** 42, 3194-3200.

168. Grenthe, I.; Stumm, W.; Laaksuharju, M.; Nilsson, A.-C.; Wikberg, P., Redox potentials and redox reactions in deep groundwater systems. *Chemical Geology* **1992,** 98, 131-150.

169. Nano, G. V.; Strathmann, T. J., Application of surface complexation modeling to the reactivity of iron(II) with nitroaromatic and oxime carbamate contaminants in aqueous TiO_2 suspensions. *Journal of Colloid and Interface Science* **2008,** 321, 350-359.

170. Charlet, L.; Scheinost, A. C.; Tournassat, C.; Greneche, J. M.; Gehin, A.; Fernandez-Martinez, A.; Coudert, S.; Tisserand, D.; Brendle, J., Electron transfer at the mineral/water interface: Selenium reduction by ferrous iron sorbed on clay. *Geochimica et Cosmochimica Acta* **2007,** 71, 5731-5749.

171. Schultz, C. A.; Grundl, T. J., pH dependence on reduction rate of 4-Cl-nitrobenzene by Fe(II)/montmorillonite systems. *Environmental Science and Technology* **2000,** 34, 3641-3648.

172. Tao, L.; Li, F. B.; Feng, C. H.; Sun, K. W., Reductive transformation of 2-nitrophenol by Fe(II) species in gamma-aluminum oxide suspension. *Applied Clay Science* **2009,** 46, 95-101.

173. Li, F. B.; Tao, L.; Feng, C. H.; Li, X. Z.; Sun, K. W., Electrochemical evidences for promoted interfacial reactions: The role of Fe(II) adsorbed onto γ-Al_2O_3 and TiO_2 in reductive transformation of 2-nitrophenol. *Environmental Science and Technology* **2009,** 43, 3656-3661.

174. Chatellier, X.; West, M. M.; Rose, J.; Fortin, D.; Leppard, G. G.; Ferris, F. G., Characterization of iron-oxides formed by oxidation of ferrous ions in the presence of various bacterial species and inorganic ligands. *Geomicrobiology Journal* **2004,** 21, 99-112.

175. Hiemstra, T.; DeWit, J. C. M.; VanRiemsdijk, W. H., Multisite oroton adsorption modeling at the solid/solution interface of (hydr)oxides: A new approach, II. Application to barious important (hydr)oxides. *Journal of Colloid and Interface Science* **1989,** 133, 105-117.

176. Boyanov, M. I.; O'Loughlin, E. J.; Roden, E. E.; Fein, J. B.; Kemner, K. M., Adsorption of Fe(II) and U(VI) to carboxyl-functionalized microspheres: The influence of speciation on uranyl reduction studied by titration and XAFS. *Geochimica et Cosmochimica Acta* **2007,** 71, 1898-1912.

177. Dong, H. L.; Kukkadapu, R. K.; Zachara, J. M.; Kennedy, D. W.; Kostandarithes, H. M., Microbial reduction of structural Fe(III) in illite and goethite. *Environmental Science and Technology* **2003,** 37, 1268-1276.

178. Appelo, C. A. J.; Van der Weiden, M. J. J.; Tournassat, C.; Charlet, L., Surface complexation of ferrous iron and carbonate on ferrihydrite and the mobilization of arsenic. *Environmental Science and Technology* **2002,** 36, 3096-3103.

179. Limousin, G.; Gaudet, J.-P.; Charlet, L.; Szenknect, S.; Barthes, V.; Krimissa, M., Sorption isotherms. A review on physical bases, modeling and measurement. *Applied Geochemistry* **2007,** 22, 249-275.

180. Griffen, D. T.; Nelson, W. R., Mossbauer spectroscopy of Zn-poor and Zn-rich rhodonite. *American Mineralogist* **2007,** 92, 1486-1491.

181. Burns, R. G., Mineral Mössbauer-Spectroscopy - Correlations between chemical-shift and quadrupole splitting parameters. *Hyperfine Interactions* **1994,** 91, 739-745.

182. Chatellier, X.; Fortin, D., Adsorption of ferrous ions onto *Bacillus subtilis* cells. *Chemical Geology* **2004,** 212, 209-228.

183. Martinez, R. E.; Smith, D. S.; Pedersen, K.; Ferris, F. G., Surface chemical heterogeneity of bacteriogenic iron oxides from a subterranean environment. *Environmental Science and Technology* **2003,** 37, 5671-5677.

184. Beveridge, T. J.; Murray, R. G. E., Sites of Metal-Deposition in the Cell-Wall of Bacillus-Subtilis. *Journal of Bacteriology* **1980,** 141, 876-887.

185. Amthauer, G.; Groczicki, M.; Lottermoser, W.; Redhammer, G., Mössbauer spectroscopy: Basic Principles. In *Spectroscopic Methods in Mineralogy*, Beran, A.; Libowitzky, E., Eds. 2004; Vol. 6, pp 345-367.

186. Pettibone, J. M.; Cwiertny, D. M.; Scherer, M.; Grassian, V. H., Adsorption of organic acids on TiO_2 nanoparticles: Effects of pH, nanoparticle size, and nanoparticle aggregation. *Langmuir* **2008,** 24, 6659-6667.

187. Campbell, S. J.; Aubertin, F., Evaluation of Distributed Hyperfine Parameters. In *Mössbauer spectroscopy applied to inorganic chemistry*, Long, G. J.; Grandjean, F., Eds. 1984; Vol. 3, pp 183-242.

188. Vrajmasu, V.; Munck, E.; Bominaar, E. L., Density functional study of the electric hyperfine interactions and the redox-structural correlations in the cofactor of nitrogenase. Analysis of general trends in Fe-57 isomer shifts. *Inorganic Chemistry* **2003,** 42, 5974-5988.

189. Shenoy, G. K., Mössbauer-Effect Isomer Shifts. In *Mössbauer Spectroscopy Applied to Inorganic Chemistry*, Long, G. J.; Grandjean, F., Eds. Plenum Press: New York, 1989; Vol. 1, pp 57-74.

190. Spiering, H., The Electric Field Gradient and the Quadrupole Interaction. In *Mössbauer Spectroscopy Applied to Inorganic Chemistry*, Long, G. J.; Grandjean, F., Eds. Plenum Press: New York, 1989; Vol. 1, pp 79-169.

191. Rusch, B.; Genin, J. M. R.; Ruby, C.; Abdelmoula, M.; Bonville, P., Mossbauer study of magnetism in Fe^{II}-^{III} (oxy-)hydroxycarbonate green rusts; ferrimagnetism of Fe^{II}-^{III} hydroxycarbonate. *Hyperfine Interactions* **2008,** 187, 7-12.

192. Ok, H. N., Relaxation effects in antiferromagnetic ferrous carbonate. *Physical Review* **1969,** 185, 472-476.

193. Ribeiro, F. R.; Fabris, J. D.; Kostka, J. E.; Komadel, P.; Stucki, J. W., Comparisons of structural iron reduction in smectites by bacteria and dithionite: II. A variable-temperature Mössbauer spectroscopic study of Garfield nontronite. *Pure and Applied Chemistry* **2009,** 81, 1499-1509.

194. Fries, S. M.; Wagner, H. G.; Campbell, S. J.; Gonser, U.; Blaes, N.; Steiner, P., Hydrogen in Amorphous $Zr_{76}Fe_{24}$. *Journal of Physics F-Metal Physics* **1985,** 15, 1179-1193.

195. McCammon, C., Mossbauer Spectroscopy of Minerals. In *Mineral Physics and Crystallography- A Handbook of Physical Constants*, American Geophysical Union: 1995.

196. Czjzek, G., Magnetism and structure of metallic glasses. *Hyperfine Interactions* **1985,** 25, 667-680.

197. Wivel, C.; Morup, S., Improved computational-rrocedure for evaluation of overlapping hyperfine parameter distributions in Mössbauer-spectra. *Journal of Physics E-Scientific Instruments* **1981,** 14, 605-610.

198. Fries, G. F., Degradation of chlorinated hydrocarbons under anaerobic conditions. In *Fate of Organic Pesticides in the Aquatic Environment*, Faust, S. D., Ed. American Chemical Society: Washington, D.C., 1972; Vol. 111, pp 256-270.

199. Rancourt, D. G.; Thibault, P. J.; Mavrocordatos, D.; Lamarche, G., Hydrous ferric oxide precipitation in the presence of nonmetabolizing bacteria: Constraints on the mechanism of a biotic effect. *Geochimica et Cosmochimica Acta* **2005,** 69, 553-577.

200. Jaisi, D. P.; Liu, C. X.; Dong, H. L.; Blake, R. E.; Fein, J. B., Fe^{2+} sorption onto nontronite (NAu-2). *Geochimica et Cosmochimica Acta* **2008,** 72, 5361-5371.

201. Géhin, A.; Ruby, C.; Abdelmoula, M.; Benali, O.; Ghanbaja, J.; Refait, P.; Génin, J. M. R., Synthesis of Fe(II-III) hydroxysulphate green rust by coprecipitation. *Solid State Sciences* **2002,** 4, 61-66.

202. Mattievich, E.; Danon, J., Hydrothermal Synthesis and Mossbauer Studies of Ferrous Phosphates of Homologous Series $Fe_3^{2+}(PO_4)_2(H_2O)_N$. *Journal of Inorganic and Nuclear Chemistry* **1977,** 39, 569-580.

203. Vertes, A.; Nagy, D. L., *Mossbauer Spectroscopy of Frozen Solutions*. H. Stillman Publishers: Boca Raton, FL, 1990.

204. Colombo, U.; Fagherazzi, G.; Gazzarrini, F.; Lanzavecchia, G.; Sironi, G., Mechanism of low-temperature oxidation of magnetites. *Nature* **1968,** 219, 1036-1037.

205. Rancourt, D. G.; Daniels, J. M., Influence of unequal magnetizaton direction probabilities on the Mossbauer spectra of superparamagnetic particles. *Physical Review B* **1984,** 29, 2410-2414.

206. Harker, S. J.; Pollard, R. J., A stuy of magnetite at 4.2 K and subject to strong applied magnetic fields. *Nuclear Insturments and Methods in Physical Research* **1993,** B76, 61-63.

207. Berry, F. J.; Skinner, S.; Thomas, M. F., ^{57}Fe Mossbauer spectroscopic examination of a single crystal of Fe_3O_4. *Journal of Physics: Condensed Matter* **1998,** 10, 215-220.

208. Hargrove, R. S.; Kundig, W., Mossbauer measurements of magnetite below the Verwey transition. *Solid State Communications* **1970,** 8, 303-308.

209. Stimming, U.; Schultze, J. W., A semiconductor model of the passive layer on iron electrodes and its application to electrochemical reactions. *Electrochimica Acta* **1979,** 24, 858-869.

210. Wehrli, B., Redox reactions of metal ions at mineral surfaces. In *Aquatic Chemical Kinetics: Reaction Rates of Processes in Natural Waters,* Stumm, W., Ed. Wiley-Interscience: New York, 1990; pp 311-336.

211. Parker, R., Electrical Transport Properties. In *Magnetic Oxides Part 1,* Craik, D. J., Ed. Wiley and Sons: 1975; pp 421-482.

212. Shuey, R. T., *Semiconducting Ore Minerals*. Elsevier: Amsterdam, 1975; Vol. 4.

213. White, A. T., Hetergeneous electrochemical reactions associated with oxidation of ferrous oxide and silicate surfaces. In *Mineral-Water Interface Geochemistry,* Hochella, M. F., Jr.; White, A. F., Eds. Mineralogical Society of America: Washington, DC, 1990; Vol. 23, pp 467-509.

214. Zinder, B.; Furrer, G.; Stumm, W., The coordination chemistry of weathering: II. Dissolution of Fe(III) oxides. *Geochimica et Cosmochimica Acta* **1986,** 50, 1861-1869.

215. Iordanova, N.; Dupuis, M.; Rosso, K. M., Charge transport in metal oxides: A theoretical study of hematite α-Fe_2O_3. *Journal Of Chemical Physics* **2005,** 122.

216. Rosso, K. M.; Dupuis, M., Reorganization energy assoicated with small polaron mobility in iron oxide. *Journal of Chemical Physics* **2004,** 122, 7059-7054.

217. Wang, J. W.; Rustad, J. R., A simple model for the effect of hydration on the distribution of ferrous iron at reduced hematite (012) surfaces. *Geochimica et Cosmochimica Acta* **2006,** 70, 5285-5292.

218. Kerisit, S.; Rosso, K. M., Charge transfer in FeO: A combined molecular-dynamics and ab initio study. *Journal of Chemical Physics* **2005,** 123, 224712.

219. Kerisit, S.; Rosso, K. M., Computer simulation of electron transfer at hematite surfaces. *Geochimica et Cosmochimica Acta* **2006,** 70, 1888-1903.

220. Kerisit, S.; Rosso, K. M., Kinetic Monte Carlo model of charge transport in hematite (α-Fe_2O_3). *Journal of Chemical Physics* **2007,** 127, 124706.

221. Rosso, K. M.; Smith, D. M. A.; Dupuis, M., An *ab initio* model of electron transport in hematite (α-Fe_2O_3) basal planes. *Journal of Chemical Physics* **2003,** 118, 6455-6466.

222. Jang, J. H.; Mathur, R.; Liermann, L. J.; Ruebush, S.; Brantley, S. L., An iron isotope signature related to electron transfer between aqueous ferrous iron and goethite. *Chemical Geology* **2008,** 250, 40-48.

223. Legall, H.; Leycuras, C.; Minerlla, D.; Rudashewsky, E. G.; Merkoulov, V. S., Anamalous evolution of magnetic and magneto-optical properties of hematite at temperature near and lower than Morin phase-transition. *Physica B & C* **1977,** 86, 1223-1225.

224. Morin, F. J., Electrical properties of α-Fe_2O_3. *Physical Review* **1954,** 93, 1195-1199.

225. Morrish, A. H., *Canted Antiferromagnetism: Hematite*. World Scientific Publishing Co.: Singapore, 1994.

226. Suter, D.; Siffert, C.; Sulzberger, B.; Stumm, W., Catalytic dissolution of iron(III) (Hydr)oxides by oxalic-acid in the presence of Fe(II). *Naturwissenschaften* **1988,** 75, 571-573.

227. Sapieszko, R. S.; Matijevic, E., Preperation of well-defined colloidal particules by thermal-decomposition of metal chelates 1. Iron-oxides. *Journal of Colloid and Interface Science* **1980,** 74, 405-422.

228. Dang, M. Z.; Rancourt, D. G.; Dutrizac, J. E.; Lamarche, G.; Provencher, R., Interplay of surface conditions, particle size, stoichiometry, cell parameters, and magnetism in synthetic hematite-like materials. *Hyperfine Interactions* **1998,** 117, 271-319.

229. De Grave, E.; vandenberghe, R. E.; Dauwe, C., ILEEMS: Methodology and application to iron oxides. *Hyperfine Interactions* **2005,** 161, 147-160.

230. Serna, C. J.; Iglesias, J. E., Nature of protohematite and hydrohematite. *Journal of Materials Science Letters* **1986,** 5, 901-902.

231. Wolska, E.; Szajda, W., Structural and spectroscopic characteristics of synthetic hydrohematite. *Journal of Materials Science* **1985,** 20, 4407-4412.

232. Shinjo, T.; Kiyama, M.; Sugita, N.; Watanabe, K.; Takada, T., Surface magnetism of α-Fe_2O_3 by Mössbauer spectrocopy. *Journal of Magnetism and Magnetic Materials* **1983,** 35, 133-135.

233. Atkinson, K. J.; Grimes, R. W.; Levy, M. R.; Coull, Z. L.; English, T., Accomodation of impurities in α-Al_2O_3, α-Cr_2O_3, α-Fe_2O_3. *Journal of the European Ceramic Society* **2003,** 23, 3059-3070.

234. Lamykin, E. V.; Fabrichn, P. B.; Babeshki, A. M.; Nesmeyan, A. N., Effect of small Sn addition on Morin transition temperature in hematite (α-Fe_2O_3). *Fizika Tverdogo Tela (S. -Peterburg)* **1973,** 15, 874-877.